KINETIC AND MECHANISTIC INSIGHTS INTO THE THREE-PHASE STRUCTURE MODEL AND CHAIN SCISSION MECHANISM OF POLY(LACTIC ACID) DURING HYDROLYSIS

By

Wanwarang Limsukon

A DISSERTATION

Submitted to
Michigan State University
in partial fulfillment of the requirements
for the degree of

Packaging—Doctor of Philosophy

2023

ABSTRACT

Poly(lactic acid) - PLA - is one of the most promising biobased and biodegradable polymers able to replace several fossil-based plastics for packaging and other applications. However, PLA is subjected to hydrolytic degradation, affecting its service performance, end-of-life, and environmental sustainability. This dissertation investigated the hydrolytic degradation of PLA to elucidate how the three-phase semicrystalline structure model of a polymer is responsible for the kinetic and mechanistic insights into the hydrolysis of PLA.

Modifying a polymer crystallinity is the simpler and more practical approach for enhancing the properties of materials. The crystalline structure exhibits high stability and impermeability to water, consequently reducing the hydrolysis process throughout the entire materials. According to the three-phase structure model, a rigid amorphous fraction (RAF), the interphase between the crystal fraction (CF) and the mobile amorphous fraction (MAF), has more geometrical constraints, causing unique characteristics. So, the amount of RAF may be responsible for some of the discrepancies between the theoretical prediction and the experimental results in PLA hydrolysis.

Molecular weight and three-phase fraction analyses were performed during hydrolysis at an elevated temperature of 85 °C to evaluate the morphological change and estimate the kinetic rates using phenomenological models. The different L-lactide content and crystallization methods significantly affected the three-phase fractions, consequently affecting the hydrolysis behavior. The amorphous PLA film with higher L-lactide content had more potential to crystallize, leading to a higher degree of crystallinity. Moreover, the specific structure of the nano-confined crystals from the melt-stretching method provided a high CF and less RAF, demonstrating the lowest hydrolysis rates among the samples. For cold-crystallized samples, a higher initial amount of RAF resulted in accelerated hydrolysis, effectively counterbalancing the crystallinity effect.

The influence of varying hydrolysis temperatures on the three-phase structure of PLA was studied, providing insights into the temperature-dependent three-phase behavior. PLA films were crystallized by melt-crystallization at 120 °C with variations in crystallization time to achieve a desirable quantity level of the three-phase structure. Results revealed that temperature significantly impacted PLA degradation. Above the glass transition temperatures (75 and 85 °C), the hydrolysis rates of PLA were comparable among samples with different crystallinity. In contrast, the higher crystallinity sample exhibited a faster hydrolysis rate below and near the glass transition temperatures (45 and 65 °C). These findings highlight the impact of RAF under various temperature conditions. The amount of RAF shows less significant impact at higher temperatures and exhibits similar characteristics to MAF. While at lower temperatures, the chains in RAF were immobilized and retained their defects. This study provides insights into the complex interplay among temperature, crystallinity, and hydrolysis kinetics, establishing a predictive framework to comprehend PLA degradation behavior fully.

Finally, a population balance was introduced to describe the evolution of the entire molecular weight distribution (MWD) during the hydrolysis. Our predictions show a promising agreement in the weight location and distribution shape with the experimental MWDs. The evolution of the MWDs by hydrolysis can be explained by considering it as a random process with noncatalytic and autocatalytic reactions, along with specific chain scission of a particular length. The simulation of the evolution of MWD was constructed for real-life hydrolytic degradation to provide comprehensive guideline information for degradation under various applications.

ACKNOWLEDGEMENTS

I would like to express my deepest gratitude and appreciation to all those who have contributed to achieving my Ph.D. journey.

First and foremost, I am profoundly grateful for the unwavering guidance and support of my advisor, Dr. Rafael Auras. His mentorship not only propelled me toward the achievement of my academic goals but also fostered a profound understanding of the research pursuit I undertook. Additionally, I would like to express my sincere appreciation to my committee members, Dr. Loong-Tak Lim, Dr. Muhammad Rabnawaz, and Dr. Maria Rubino, for their invaluable guidance, support, and generous time throughout this journey.

I am deeply grateful for the RAA research group. Our collective sharing and learning experiences have been invaluable. Importantly, our group meetings have consistently provided an energizing source, motivating me to work diligently throughout each week.

Special thanks go to Dr. Puttha Sakkaplangkul from King Mongkut's Institute of Technology Ladkrabang for his invaluable assistance in the development of my modeling.

I would also like to acknowledge Mr. Aaron Walworth for his exceptional dedication and kind assistance in the laboratory. My special thanks go to Tracy Lorenz, Cathie Allison, and Susan Barnaby for their kindness and responsive assistance.

I am thankful to the Royal Thai Government and Rajamangala University of Technology Tawan-ok for the honor scholarship and financial support during my studies, as well as CANR and the School of Packaging for the generous fellowship opportunities.

Finally, I am grateful for the support and encouragement provided by my friends in the School of Packaging. I am truly fortunate to have such a supportive and understanding group of friends by my side who are always ready to help and support each other during challenging times. Thanks, of course, to my family and long-standing friends for their support and always encouraging me to pursue my dreams.

TABLE OF CONTENTS

LIST OF ABBREVIATIONS

PLA	poly(lactic acid)
PLLA	poly(L-lactic acid)
PDLA	poly(D-lactic acid)
PET	poly(ethylene terephthalate)
PS	polystyrene
CF	crystalline fraction
MAF	mobile amorphous fraction
RAF	rigid amorphous fraction
X_C	degree of crystallinity – amount of CF
X_{C0}	initial X_C
X_{MAF}	amount of MAF
X_{RAF}	amount of RAF
MWD	molecular weight distribution
$Đ$	polydispersity
M_n	number-average molecular weight
M_w	weight-average molecular weight
Sc-PLA	Stereocomplex PLA
D	diffusion coefficient
WAXD	wide angle X-ray diffraction
AFM	atomic force microscopy
POM	polarized-light optical microscopy
SEC	size exclusion chromatography
DMA	dynamic-mechanical analysis
SEM	scanning electron microscopy

DSC	differential scanning calorimetry
MDSC	modulated DSC
T_m	melting temperature
T_g	glass transition temperature
T_{cc}	cold-crystallization temperature
HF	total heat flow
C_p	specific heat capacity
H_m	enthalpy of fusion
T_c	crystallization temperature
t_c	crystallization time
CC	cold-crystallization method
MC	melt-crystallization method
L_c	crystalline thickness
G	spherulite growth rate
K_c	crystallization rate constant
K_p	crystallization rate constant of the primary crystallization
K_s	crystallization rate constant of the secondary crystallization
X_p	X_C of the primary crystallization
CRR	cooperative rearranging regions
T_α	T_g of the subvolume
ξT_α	CRR length
δT	mean temperature fluctuation
K_{deg}	degradation model rate constant
r_s	total number of chain scissions per unit volume of the amorphous polymer
c_{ol}, C_{ol}	number of ester units of all the short chain per unit volume of the amorphous polymer, the semicrystalline polymer

$c_{E,}$ C_E	number of ester units of all the long chain per unit volume of amorphous polymer, semicrystalline polymer
R_s	total number of chain scissions per unit volume
ω	number of ester units of the crystalline phase per unit volume
a, β	dimensionless constants
r_s	total number of chain scissions per unit volume of amorphous polymer
R_s	total number of chain scissions per unit volume of semicrystalline polymer
N_{chain0}	number of polymer chains per unit volume
m	average degree of polymerization of oligomers
PBM	population balance model
VTF	Vogel–Tammann–Fulcher model
T_0	Vogel temperature
$\beta(L_i, L_j)$	daughter size distribution for the scission
ΔL	size of a category
NM	number of moments
NC	number of catergories

CHAPTER 1: INTRODUCTION

1.1 Background and motivation

Over the past decade, the worldwide growing environmental awareness has been a driving force to the development of sustainable materials to minimize the dependence on fossil-based resources and produce materials for the new circular economy [1]. Poly(lactic acid) – PLA – a compostable polymer, could be one of the most suitable alternative materials developed to overcome these issues. PLA is produced by the fermentation of plant-derived carbohydrates such as corn starch, beets, and sugar cane [1]. It can be recyclable through mechanical and chemical recycling, and alternatively, it can be composted under industrial composting conditions to yield water, carbon dioxide, and inorganic compounds that are not harmful to the environment [2]. PLA has been developed for various applications, including packaging [3]. It can be processed with widely converting methods such as injection molding, thermoforming, cast film/sheet extrusion, blow molding, and foaming [4]. PLA, as a packaging material, exhibits comparable properties as conventional plastics such as poly(ethylene terephthalate) (PET) and polystyrene (PS) with analogous mechanical properties, gas barriers, and processability [3]. On the other hand, PLA has several drawbacks, including its low toughness, low heat resistance, and poor water barrier properties limiting its use in certain applications. Additionally, PLA is susceptible to hydrolytic degradation, especially in high humidity and high temperature, which can also be advantages and disadvantages in specific situations. While this degradation can lead to a reduction in molecular weight and deterioration of some properties [5], it reduces the molecular weight to a level suitable for microorganisms able to degrade PLA chains [6]. Thus, it is important to understand the hydrolytic degradation of PLA to parallelly improve both stability and biodegradability and expand its commercial use.

Hydrolytic degradation of PLA can be divided into three general stages: (1) the diffusion of water; (2) the hydrolytic cleavage of the ester bonds; and (3) the production of small oligomers, resulting in a decrease in molecular weight and weight loss [5]. The hydrolysis kinetics of PLA can be effectively described by considering a decrease in molecular weight over time, which allows for the calculation of degradation rates. The hydrolysis behavior of PLA is affected by several parameters related to the material, such as molecular structures, order structures, and morphology, and surrounding media factors such as temperature and *pH*.

Crystallinity is one of the significant parameters affecting the hydrolytic degradation of PLA, potentially promoted by the polymer productions, crystallization procedures and the rearrangement of the molecular chains occurring in response to specific environmental conditions[5,7]. Hydrolysis-induced crystallization can take place due to the reduced entanglement of shorter chain segments and the plasticizer effect of water molecules [8]. The chains within the crystalline region exhibit greater resistance to hydrolysis compared to those in the amorphous region [5]. The presence of crystalline structure in the matrix can decrease mass transfer by reducing the diffusion of molecules by increasing a tortuous pathway for the water molecules to penetrate in the amorphous region, thus slowing down the hydrolysis process [9]. On the other hand, increasing crystallinity can lead to a higher density of hydrophilic terminal groups in the amorphous region, resulting in increased water content within the amorphous and enhancing the autocatalytic effect [5,10]. The findings highlight the complex relationship between crystallinity and hydrolysis degradation in PLA.

According to the three-phase structure model, the semicrystalline PLA not only consists of the crystalline fraction (CF), the mobile amorphous fraction (MAF), but also the interphase between CF and MAF called the rigid amorphous fraction (RAF), which could lead to worsen thermomechanical and barrier properties [11–13]. Naturally, RAF is associated

with the restriction of the amorphous chain fixed to the basal plane of the crystals leading to a higher constraint compared to MAF. Del Rio et al. [14] showed that the formation of RAF leads to an excess free volume in annealed samples. The effect of RAF during crystallization on the mechanical and barrier properties of PLA has been reported in several studies [12–15]. In the case of hydrolytic degradation, Tsuji et al. [16] reported the fast hydrolysis rate in high crystallinity PLA films, which could be attributed to the increase of the hydrophilic end chains and the free volume of RAF [17,18]. However, the specific effect of RAF on hydrolytic degradation of PLA remains unclear, as no studies have tracked and measured this process concurrently with its relation to environmental conditions.

Mathematical models are useful tools to provide comparative analysis and lifetime prediction and to improve the understanding of the hydrolysis behavior based on theoretical background [19–22]. Traditionally, zero- or first-order kinetics have been used to describe the simple hydrolysis process of organic materials [23,24]. However, in specific cases, higher-order reactions have been applied, highlighting the need for a comprehensive understanding of the various processes involved in accurate hydrolysis description [25]. Regarding the hydrolysis of semicrystalline PLA, the kinetic rates can be achieved by using phenomenological models proposed by Pan [26]. These models comprise a series of mathematical equations simultaneously considering the chain scission and crystallization processes, which have been successfully applied in studies on the hydrolysis of semicrystalline PLA [27,28].

Another limitation of the current method is the lack of molecular interpretation derived from the number- and weight-average molecular weight, which is often not a good representative for an understanding of the true characteristic of polymers. The evolution of the molecular weight distribution (MWD), instead of average molecular weight, could provide an accurate prediction of the entire molecular system during hydrolysis and a better

understanding of the hydrolysis behavior [29,30]. In this regard, a population balance approach will be applied to derive the simulation of the entire MWD during hydrolysis [31].

1.2 Overall goal and objectives

The overall goal of this dissertation is to investigate the hydrolytic degradation of amorphous and semicrystalline PLA to elucidate how the three-phase structure model is responsible for the kinetic and mechanistic insights into the hydrolytic degradation of PLA. To achieve this goal, this dissertation aims to address four specific objectives, which are:

1) To implement an efficient method for determining the evolution of the three-phase structure of PLA throughout the process of hydrolysis.

2) To examine the impact of different crystallization methods on the three-phase structure of PLA during hydrolysis.

3) To evaluate the effect of the temperature on the three-phase structure evolution during hydrolytic degradation of PLA.

4) To investigate the hydrolysis rate of the three-phase structure of PLA and provide a theoretical model for the molecular weight distribution simulation.

1.3 Dissertation overview

This dissertation is organized as follows.

The current chapter, Chapter 1, provides an exploration of the background, the underlying motivation and justification behind of this dissertation. Additionally, this chapter outlines the overall goal of the dissertation, elucidates the specific objectives that guide our investigation, and establishes the context for the subsequent chapters.

Chapter 2 provides a critical literature review, serving as a crucial key element within this dissertation. This chapter addresses the essential subjects, starting with the fundamental aspects of PLA, delving into its crystallization behavior, elucidating the complexities of its three-phase structures, and providing a detailed examination of its

hydrolytic behavior, including key parameters and a comprehensive overview of the hydrolysis studies of semicrystalline PLA. Finally, it explores mathematical models employed to enhance our understanding of PLA's hydrolytic degradation.

Chapter 3 presents the investigation the effects of the three-phase structure of PLA (i.e., MAF, RAF, and CF) during hydrolytic degradation in water. Physical and morphological characteristics of the two commercial PLA with different L-lactide content and crystallized by the two crystallization methods, cold-crystallization and melt-stretching crystallization, were investigated using modulated differential scanning calorimetry (MDSC), wide-angle X-ray diffraction, scanning electron microscopy, and size exclusion chromatography to correlate with the hydrolytic processes.

Chapter 4 provides a holistic understanding of the three-phase structure model–temperature relationship on the hydrolysis of PLA by investigating the hydrolytic degradation of PLA from 45 to 85 °C. PLA films were crystallized by melt-crystallization at 120 °C for different levels of the three-phase structure. The molecular weight of the samples and their three-phase structure were assessed during the hydrolysis to obtain the appropriate interpretation of the PLA hydrolysis. Finally, the kinetic constants of hydrolysis were estimated using modified phenomenological models.

Chapter 5 presents a method for simulating the molecular weight distribution using the population balance method. This method aims to enable the prediction of the time evolution of the entire molecular weight distribution. This method could help identify the mechanistic behavior of the entire system by monitoring the progression of hydrolysis. To validate the model, experimental data obtained in Chapter 4 were utilized.

Chapter 6 summarizes all the works in this dissertation and concludes with future work recommendations.

REFERENCES

[1] Sudesh K. and Iwata T., Sustainability of biobased and biodegradable plastics, *Clean - Soil, Air, Water*, vol. 36, no. 5–6, pp. 433–442, 2008, doi: 10.1002/clen.200700183.

[2] Kale G., Kijchavengkul T., Auras R., *et al.*, Compostability of bioplastic packaging materials: An overview, *Macromol. Biosci.*, vol. 7, no. 3, pp. 255–277, 2007, doi: 10.1002/mabi.200600168.

[3] Auras R., Harte B., and Selke S., An overview of polylactides as packaging materials, *Macromol. Biosci.*, vol. 4, no. 9, pp. 835–864, 2004, doi: 10.1002/mabi.200400043.

[4] Lim L. T., Auras R., and Rubino M., Processing technologies for poly(lactic acid), *Prog. Polym. Sci.*, vol. 33, no. 8, pp. 820–852, 2008, doi: 10.1016/j.progpolymsci.2008.05.004.

[5] Tsuji H., Hydrolytic Degradation, in *Poly(Lactic Acid)*, Hoboken, NJ, USA: John Wiley & Sons, Inc., 2010, pp. 343–381.

[6] Hamad K., Kaseem M., Yang H. W., *et al.*, Properties and medical applications of polylactic acid: A review, *Express Polym. Lett.*, vol. 9, no. 5, pp. 435–455, 2015, doi: 10.3144/expresspolymlett.2015.42.

[7] Li H. and Huneault M. A., Effect of nucleation and plasticization on the crystallization of poly(lactic acid), *Polymer (Guildf).*, vol. 48, no. 23, pp. 6855–6866, 2007, doi: 10.1016/j.polymer.2007.09.020.

[8] Naga N., Yoshida Y., Inui M., *et al.*, Crystallization of amorphous poly(lactic acid) induced by organic solvents, *J. Appl. Polym. Sci.*, vol. 119, no. 4, pp. 2058–2064, Feb. 2011, doi: 10.1002/app.32890.

[9] Gorrasi G., Anastasio R., Bassi L., and Pantani R., Barrier properties of PLA to water vapour: Effect of temperature and morphology, *Macromol. Res.*, vol. 21, no. 10, pp. 1110–1117, 2013, doi: 10.1007/s13233-013-1144-0.

[10] Huang Y., Chen F., Pan Y., *et al.*, Effect of hydrophobic fluoropolymer and crystallinity on the hydrolytic degradation of poly(lactic acid), *Eur. Polym. J.*, vol. 97, pp. 308–318, 2017, doi: 10.1016/j.eurpolymj.2017.09.044.

[11] Righetti M. C., Amorphous fractions of poly(lactic acid), *Adv. Polym. Sci.*, vol. 279, pp. 195–234, 2018, doi: 10.1007/12_2016_14.

[12] Fernandes Nassar S., Guinault A., Delpouve N., *et al.*, Multi-scale analysis of the impact of polylactide morphology on gas barrier properties, *Polymer (Guildf).*, vol. 108, pp. 163–172, 2017, doi: 10.1016/j.polymer.2016.11.047.

[13] Sonchaeng U., Iñiguez-Franco F., Auras R., *et al.*, Poly(lactic acid) mass transfer properties, *Prog. Polym. Sci.*, vol. 86, pp. 85–121, 2018, doi: 10.1016/j.progpolymsci.2018.06.008.

[14] del Río J., Etxeberria A., López-Rodríguez N., *et al.*, A PALS Contribution to the

Supramolecular Structure of Poly(L-lactide), *Macromolecules*, vol. 43, no. 10, pp. 4698–4707, May 2010, doi: 10.1021/ma902247y.

[15] Aliotta L., Gazzano M., Lazzeri A., and Righetti M. C., Constrained amorphous interphase in poly(l-lactic acid): Estimation of the Tensile elastic modulus, *ACS Omega*, vol. 5, no. 33, pp. 20890–20902, 2020, doi: 10.1021/acsomega.0c02330.

[16] Tsuji H. and Ikada Y., Properties and morphology of poly(L-lactide): IV. Effects of structural parameters on long-term hydrolysis of poly(L-lactide) in phosphate-buffered solution, *Polym. Degrad. Stab.*, vol. 67, no. 1, pp. 179–189, 2000, doi: 10.1016/S0141-3910(99)00111-1.

[17] Tsuji H., Mizuno A., and Ikada Y., Properties and morphology of poly(L-lactide). III. Effects of initial crystallinity on long-term in vitro hydrolysis of high molecular weight poly(L-lactide) film in phosphate-buffered solution, *J. Appl. Polym. Sci.*, vol. 77, no. 7, pp. 1452–1464, 2000, doi: 10.1002/1097-4628(20000815)77:7<1452::AID-APP7>3.0.CO;2-S.

[18] Sangroniz A., Chaos A., Iriarte M., *et al.*, Influence of the Rigid Amorphous Fraction and Crystallinity on Polylactide Transport Properties, *Macromolecules*, vol. 51, no. 11, pp. 3923–3931, Jun. 2018, doi: 10.1021/acs.macromol.8b00833.

[19] Rodriguez E. J., Marcos B., and Huneault M. A., Hydrolysis of polylactide in aqueous media, *J. Appl. Polym. Sci.*, vol. 133, no. 44, pp. 1–11, 2016, doi: 10.1002/app.44152.

[20] Van Nostrum C. F., Veldhuis T. F. J., Bos G. W., and Hennink W. E., Hydrolytic degradation of oligo(lactic acid): A kinetic and mechanistic study, *Polymer (Guildf).*, vol. 45, no. 20, pp. 6779–6787, 2004, doi: 10.1016/j.polymer.2004.08.001.

[21] Pan J., *Modelling Degradation of Bioresorbable Polymeric Medical Devices*. Elsevier, 2015.

[22] Laycock B., Nikolić M., Colwell J. M., *et al.*, Lifetime prediction of biodegradable polymers, *Prog. Polym. Sci.*, vol. 71, pp. 144–189, 2017, doi: 10.1016/j.progpolymsci.2017.02.004.

[23] Siparsky G. L., Voorhees K. J., and Fudu M., Hydrolysis of Polylactic Acid (PLA) and Polycaprolactone (PCL) in Aqueous Acetonitrile Solutions: Autocatalysis, *J. Environ. Polym. Degrad.*, vol. 6, no. 1, pp. 31–41, 1998, doi: 10.1023/A:1022826528673.

[24] Bruschi M. L., Ed., Mathematical models of drug release, in *Strategies to Modify the Drug Release from Pharmaceutical Systems*, Elsevier, 2015, pp. 63–86.

[25] Lyu S. P., Schley J., Loy B., *et al.*, Kinetics and time-temperature equivalence of polymer degradation, *Biomacromolecules*, vol. 8, no. 7, pp. 2301–2310, 2007, doi: 10.1021/bm070313n.

[26] Pan J., Modelling degradation of semi-crystalline biodegradable polyesters, in *Modelling Degradation of Bioresorbable Polymeric Medical Devices*, Elsevier, 2015, pp. 53–69.

[27] Gleadall A., Pan J., and Atkinson H., A simplified theory of crystallisation induced by polymer chain scissions for biodegradable polyesters, *Polym. Degrad. Stab.*, vol. 97, no. 9, pp. 1616–1620, 2012, doi: 10.1016/j.polymdegradstab.2012.06.023.

[28] Han X. and Pan J., A model for simultaneous crystallisation and biodegradation of biodegradable polymers, *Biomaterials*, vol. 30, no. 3, pp. 423–430, 2009, doi: 10.1016/j.biomaterials.2008.10.001.

[29] Ahmad W., Kuitunen S., Sixta H., and Alopaeus V., Population balance based modeling of changes in cellulose molecular weight distribution during ageing, *Cellulose*, vol. 22, no. 1, pp. 151–163, 2015, doi: 10.1007/s10570-014-0529-3.

[30] Kuen Y., Kirse C., Briesen H., *et al.*, Towards improved predictions for the enzymatic chain-end scission of natural polymers by population balances : The need for a non-classical rate kernel, *Chem. Eng. Sci.*, vol. 176, pp. 329–342, 2018, doi: 10.1016/j.ces.2017.10.027.

[31] Ramkrishna D. and Singh M. R., Population Balance Modeling : Current Status and Future Prospects Population Balance Modeling : Current Status and Future Prospects, no. March, 2014, doi: 10.1146/annurev-chembioeng-060713-040241.

CHAPTER 2: LITERATURE REVIEW

2.1 Poly(lactic acid) – PLA

Poly(lactic acid), PLA, is considered a bio-based material produced by the fermentation of renewable resources such as cassava, corn starch, beets, and sugar cane to convert carbohydrates to lactic acid by microorganisms [1]. It has been extensively studied as a potential alternative to petrochemical-based plastics due to its thermal plasticity, high stiffness, reasonable strength, good processability, and biocompatibility, which can be used in various fields, including packaging applications [2,3]. With the specific process developing, PLA can be economically processed into a range of forms, including films, sheets, molded parts, foams, and nanofibers, providing the versatility needed to meet a wide array of packaging demands [4,5]. Furthermore, numerous research endeavors have been dedicated to PLA-based technologies, with an emphasis on achieving chemical, mechanical, and biological properties that either match or surpass those of conventional polymers. This pursuit aims to establish the suitable properties and appropriate service life-time for their intended consumer applications [6]. For the end-of-life process, PLA can be recovered through recycling and composting. Currently, the recycling of PLA material can be accomplished through both chemical and mechanical processes, which require effective sorting and thorough cleaning procedures [7]. Alternatively, it can be recovered under industrial composting conditions through the action of microorganisms to yield water, carbon dioxide, and inorganic compounds at temperatures around 58 °C and over 80% relative humidity [3,7,8]. Similarly, home composting condition, typically conducted at lower temperatures within the mesophilic range of 10 to 46 °C, undergoes a slower process that extends over a period of up to two years [7].

2.2 Chemical and chain structure

PLA belongs to a family of aliphatic polyesters. Its basic building block is lactic acid (2-hydroxy propionic acid), which is the simplest occurring carboxylic acid in nature with an asymmetric carbon atom and exists in two optically active forms, the dextrorotary form called L-(+)-lactic acid and the levorotatory form called D-(–)-lactic acid [3] (**Figure 2.1**). The pure form of the two optical isomers have the comparable properties, for example, melting point, hygroscopicity, water and ethanol solubility, and density [9,10]. In the typical ROP process, PLA pre-polymers produced by condensation polymerization are converted into cyclic dimer lactide (3,6-dimethyl-1,4-dioxane-2,5-dione) through cyclization depolymerization. The lactide combines two lactic acids and exists the three stereoisomeric forms, L-lactide, D-lactide, and D, L-lactide or *meso*-lactide (**Figure 2.1**). PLA can be polymerized in a wide variety of molecular structures, for example, homopolymers–poly(L-lactide) (PLLA) and poly(D-lactide) (PDLA) synthesized from the pure L-lactide and D-lactide, respectively, and copolymers of D-lactide and L-lactide. The distinct properties of PLA are influenced by the chain stereochemistry, which may be controlled by altering the fraction ($X_{\text{D-lactide}}$ or $X_{\text{L-lactide}}$) and sequence length ($\bar{\xi}$) of the major monomer units [11–13]. A higher $\bar{\xi}$ value leads to a higher chain order, which directly affects the crystallization behavior [13,14].

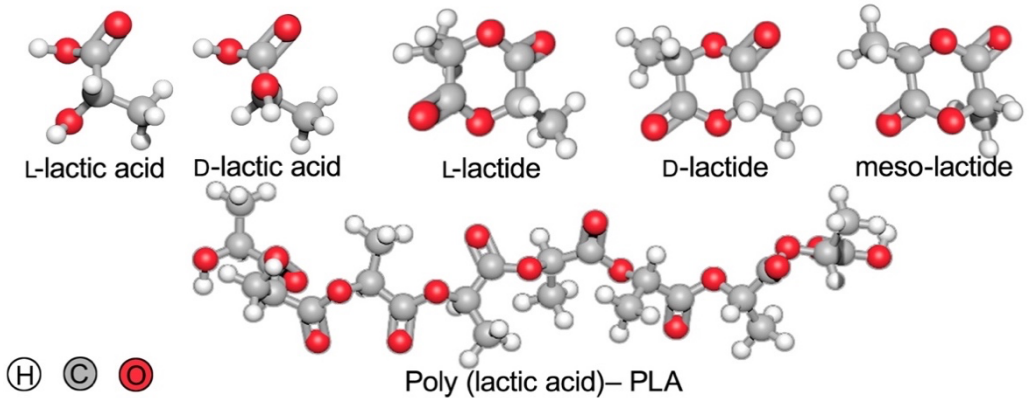

Figure 2.1 Chemical structure of L-lactide, D-lactide, and meso-lactide.

2.3 Crystallization behavior of PLA

The transformation of an amorphous phase into an ordered crystalline phase can occurs under appropriate conditions such as temperature, pressure, mechanical stress, and the influence of surrounding solvent. In the case of the crystalline structure of polymer, the polymeric chains are never entirely crystalline and typically exhibit a semicrystalline nature, influenced by factors such as the material's structures, crystallization conditions, and the presence of foreign particles within the polymer matrix. This is because polymer crystalline structures tend to be smaller and less perfect compared to the crystalline structures found in non-polymeric pure compounds [15,16]. The crystallization of polymers occurs at a temperature below the equilibrium melting temperature (T_m^0). The general crystallization processes can be defined into three major steps: (1) nucleation process; (2) crystal growth; and (3) secondary crystallization/perfection [17,18].

Crystal nucleation is an initial formation of supercritical nuclei by random thermal fluctuations that do not disappear with time [19,20]. The nucleation in the polymer can be homogeneous nucleation in the pure supercooled melt or heterogeneous nucleation on the pre-existing nuclei or by the presence of insoluble impurities. It typically reduces the energy needed to generate the formation of nuclei. The nucleation rate can be quantified from the number of spherulitic crystals growing at a later stage by polarized-light optical microscopy (POM) and atomic force microscopy (AFM) [18,21–23]. The nucleation kinetics of PLA was observed as the spherulite density (the number per unit area) in the wide range of temperature from below the glassy to melt state, approximately 60–140 °C. The decreasing crystallization temperature leads to an increase in the number of spherulites with the maximum rate of crystal nucleation at around 100 °C [23–27].

The crystal growth occurs after the primary nucleation process. The crystal structure originates from the parallel rearrangement of the chains to form the lamellar with the thickness of 5–50 nanometers and the lateral size ranging from nanometers to several micrometers [20]. The lamellar often grows radially from a nucleus to a spherulite. However, the growth of lamellae can be constrained by the high nucleation density and high concentration of chain defects, resulting in reduced lateral size and the absence of lamellar structure. Instead, fringed micelles, nodular structures, or particle-like crystals can be formed [19,20]. In other cases, PLA thin films with thickness ranging from 50–200 nm have exhibited features like rod-like structures [28] and flat-on crystals [29]. The kinetic crystal growth rate of semicrystalline polymers has mainly been analyzed by POM and AFM. POM can be precise and reliable in the cases of low spherulite growth rate and low nucleation density. While AFM is very efficient in obtaining the nanoscale structural information. In particular, AFM can be equipped with a hot stage for tracking the real-time crystalline morphology as a function of temperature and time. The crystal growth rate can be evaluated from the slope of the spherulite radius and time curve [30,31]. The crystal growth of PLA, (i.e., spherulite growth rate and size) is influenced by several factors, such as crystallization temperature, molecular mass, and stereoregularity, all of which can mutually affect one another [19,32]. During the isothermal crystal growth process, the radius of the spherulites increases linearly with time. The higher temperatures (120–160 °C) result in the formation of a smaller number of spherulites, which, in turn, leads to the development of larger spherulites. The crystallization temperature also influences on the spherulite growth rate, as noted by various researchers [29,33–39]. In those studies, the spherulite growth rates were evaluated across a wide temperature range, spanning from T_g and T_m, revealing two local maxima, occurring at approximately 105–115 °C and 125–135 °C. This phenomenon could be

due to the differences in the crystal growth rates of α and δ crystals (mentioned later in Section 2.3.1.1), which are favored below and above 120 °C, respectively. The dependence of growth rate on the molecular weight of PLA was studied by Tsuji et al. [39], Di Lorenzo et al. [40], and Abe et al. [29]. They found that an increase of chain length results in a lower growth rate. Moreover, the long molecular chains could lead to more entanglement and higher irregular structures [40]. Lastly, the effects of stereoregularity on crystal growth rate can be described as the presence of the concentration of D-lactide in the molecular chains of PLLA. The maximum growth rate decreases with an increasing amount of D-lactide fraction due to the segregation of non-crystallizable units, which leads to a lower crystallinity and eventually lower achievable crystallinity [26].

The degree of crystallinity derived from the measurement is used to estimate the kinetic parameters of crystallization by fitting the Avrami equation [41,42] and later developed by several authors [43–45]:

$$X_c = 1 - \exp(-V_t) \qquad (2.1)$$

where X_c is the crystallinity and V_t is the volume of the crystalline material at time, t. The crystalline volume is increased during the spherical nucleation can be expressed as:

$$dV_t = 4\pi r^2 N\, dr \qquad (2.2)$$

where N are the number of nuclei with radius, r. The crystallinity occurred in the material can form during both nucleation and crystal growth processes. The increase of V_t during the time interval from $t = 0$ to t can be estimated from the constant growth of spherulite (G) as $r = Gt$. Equation (2.2) can result in:

$$V_t = \int_0^t 4\pi G^2 t^2 \cdot N \cdot G\, dt \qquad (2.3)$$

$$V_t = \frac{4}{3}\pi G^3 N t^3 \qquad (2.4)$$

The crystal nucleation is followed by the crystal growth at time t_i. The increase of V_t during the time interval from t_i to $t_i + dt$ can be estimated from the constant nucleation rate (l) as $N = lt$. Eq. (2.3) can result in:

$$dV_t = 4\pi G^2 (t - t_i)^2 \cdot lt \cdot G\, dt \tag{2.5}$$

$$V_t = \frac{2}{3}\pi G^3 l t^4 \tag{2.6}$$

Eqs. (2.4) and (2.6) expresses the volume of the crystalline fraction as a function of time. Eq. (2.1) can then be written as:

$$X_c = 1 - \exp(-kt^n) \tag{2.7}$$

which can be rearranged in the natural logarithmic form:

$$ln(1 - X_c) = -kt^n \tag{2.8}$$

where k and n are the constants, referred to the crystallization rate constant, Avrami exponent, respectively. These constants depend on the mechanism of nucleation and crystal growth summarized in **Table 2.1** [46]. The Avrami exponent of PLA is typically between 2.5 and 3.5 for the isothermal crystallization at around 90–130 °C [47–53]. There is a discrepancy in the literature about the low n values of the crystallization of PLA. The low n can be found in the crystallization in organic liquid over the wide range of temperature above T_g [54–56]. This phenomenon could be due to the restriction by the diffusion-controlled growth rate of the crystals. Hence, the crystallization found in solution does not follow a constant crystal growth [56].

Table 2.1 The Avrami parameters for crystallization of polymers [46].

Crystal Geometry	Nucleation Mechanism	Avrami Constants		Restrictions
		K_c	n	
Spheres	Sporadic [1]	$\frac{2}{3}\pi G^3 l$	4	3 dimensions
	Predetermined [2]	$\frac{4}{3}\pi G^3 N$	3	3 dimensions
Discs	Sporadic	$\frac{\pi}{3} G^2 l t^4$	3	2 dimensions
	Predetermined	$\pi G^3 N d$	2	2 dimensions
Rods	Sporadic	$\frac{\pi}{4}\pi \mathrm{G} l d^2$	2	1 dimension
	Predetermined	$\frac{1}{2}\pi \mathrm{G} N d^2$	1	1 dimension

[1] *Sporadic nucleation has the constant nucleation rate*
[2] *Predetermined has the constant number of nuclei*

The crystallization kinetics can be evaluated using a differential scanning calorimetry (DSC) to quantify the transition temperatures and the enthalpies during isothermal and non-isothermal procedures [32]. In general, the crystalline weight fraction in the polymer can be determined from the heating scan using:

$$X_C = \frac{\Delta H_f - \sum \Delta H_c}{\Delta H_f^0} \tag{2.9}$$

where ΔH_f is the enthalpy of fusion from the integration of the heat flow in the melting region, $\sum \Delta H_c$ is the sum of the exothermic peak enthalpies, and ΔH_f^0 is the calculated fusion enthalpy of 100% crystalline. ΔH_f^0 represents the amount of energy needed to change a solid substance to a liquid at a specific temperature. This value is indeed dependent on the stability of the crystal and can vary with the crystal form. The standard ΔH_f^0 value of 93.1 J g^{-1} for PLA was reported by Fischer et al. as [57]. Righetti et al. [58] reported a variation of literature values of the ΔH_f^0 in a wide range of 82–203 J g^{-1} which can be due to the different ΔH_f^0 for the δ- and α-crystals. According to Avrami model, a typical crystallinity-versus-time plot exhibits a sigmoidal shape which can be explained by the three-step crystallization rate

process: a lag phase, a log phase (or exponential phase of rapid growth), and a stationary or plateau phase [17] .

The final step of the crystallization process is secondary crystallization (or crystal perfection), involving an increase of the thermodynamic stability of crystals by internal rearrangement. It is much slower than the primary step depending on the temperature and mobility of chain segments, including the thickening of lamellae, removal of lattice defects, and insertion of lamellae within existing stacks [17,20]. The secondary crystallization can be visually determined by POM observing after the impingement event where the radius of spherulite remains constant. Moreover, it can be identified by the deviation of an Avrami curve at the end of primary crystallization and the further annealing process of uncrystallized chains [22,59].

The kinetic of the secondary crystallization has been shown to fit a root-time dependence ($t^{1/2}$) [60–62]. Then, Eq. (2.7) can be adjusted to:

$$X_c = X_p + X_s = X_{p\infty}\left(1 + K_s t^{1/2}\right) \tag{2.10}$$

where $X_{p\infty}$ is the crystallinity at the end of the primary crystallization, X_s is the crystallinity forming during the secondary crystallization at time t, and K_s is the secondary crystallization rate constant.

2.3.1 A three-phase structure model of PLA

Semicrystalline polymers are conventionally considered as heterogeneous two-phases structures, which consist of crystalline and amorphous phases. Suzuki et al. [63] first proposed the existence of two types of amorphous called a mobile amorphous fraction (MAF) and a rigid amorphous fraction (RAF) in semicrystalline poly(oxymethylene)s by the difference in heat capacity. The RAF is a region between the crystalline and amorphous phases, having more order and more constraint from adjacent crystal lamellae, with a much

higher stiffness than the bulk amorphous phase. The formation of RAF has later been investigated in various semicrystalline polymers, including poly(ethylene terephthalate) (PET) [64–68], poly(trimethylene terephthalate) (PTT) [69], Nylon-6 [70], isotactic polystyrene (iPS) [71] and PLA [67,72–78]. It has been widely accepted that the three-phase structure model provides a much better prediction for the relevant physical mechanism of the highly ordered structures of semicrystalline polymers. Schematic representation of the arrangement of CF, RAF, and MAF is shown in **Figure 2.2**.

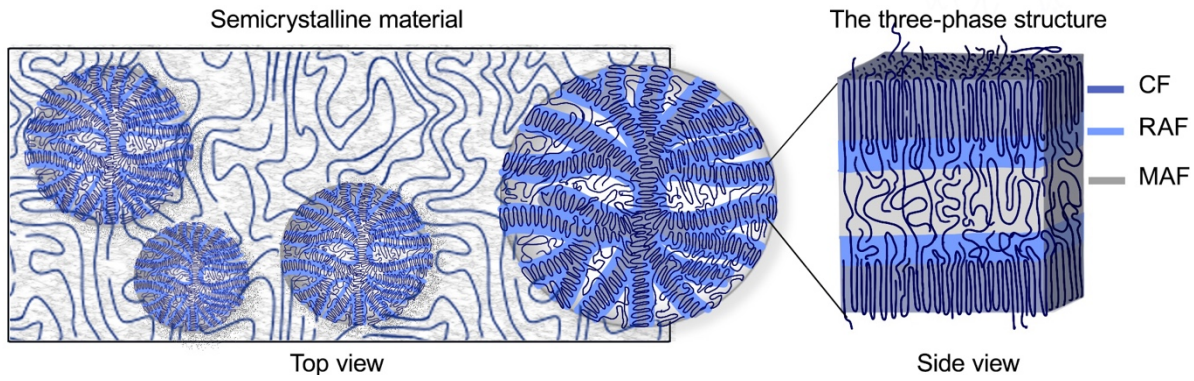

Figure 2.2 Schematic representation of the arrangement of crystalline (CF), rigid amorphous (RAF), and mobile amorphous fractions (MAF).

2.3.1.1 Crystalline region

Homopolymer PLA exists in different crystal structures and morphology affecting the properties of semicrystalline polymers. Based on the main-chain chirality of PLA, the chains can rotate and exhibit different helical conformations, which are always left-handed for PLLA and right-handed for PLDA; however, they have similar crystallization behavior [79–81]. PLA can crystallize in different crystalline modifications, such as, α, δ (previously known as the α'), β, and γ forms, and a stereocomplex (sc) between PLLA and PLDA mixture [79]. The homopolymer PLA helices generally have the helical conformations of three units in one turn (3_1) or ten units in three turns (10_3) and pack into an orthorhombic or a trigonal unit cell as described in **Table 2.2**.

The variation in the crystal modification of PLA can be achieved through crystallization preparation, depending on specific conditions, including melt, cold, and solution crystallization. The α crystal is the most common and stable modification formed during melt- and cold-crystallization at by a temperature (T_c) starting from around 110 ºC [19,82]. While the more disordered form, δ crystal, is obtained by the melt-crystallization at T_c below 110–120 ºC and the cold-crystallization at the 70–110 ºC [79,82–85]. Correspondingly, the formation of two polymorphic crystals can concurrently form at the temperature range of 100–140 ºC [84,85]. Moreover, the δ transfers into the more stable α crystal during the subsequent annealing at T_c around 120 ºC [79,86]. Additionally, the ordered structures are prepared by the orientation method. The mesophase state can be induced by stretching PLA film at the temperature below or slightly above T_g [87]. The degree of order of the mesophase depends on the draw a temperature and ratio [88,89]. By a combination of the two methods, melt-crystallization and orientation, the occurrence of mesophase–δ and mesophase–α transitions are found at around 70–90 ºC [90] and 150 ºC [91], respectively. The β crystal can be formed by a specific stretching condition. The formation of the β crystal originates from the melt-stretching near T_m at high drawing rates [91,92]. Moreover, it can be prepared by the deformation of α crystal by melt-stretching of pre-annealed α-form film at 170 ºC [92].

Table 2.2 The crystal unit cell parameters for homopolymer PLA.

Crystal modification	Crystal system	Helical conformation	Crystal unit cell parameters			Ref.
			a, Å	b, Å	c, Å	
α	Orthorhombic	10_3	10.68	6.17	28.86	[93]
			10.86	6.16	28.86	[94]
			10.50	6.10	28.80	[95]
	Pseudo-orthorhombic	Distorted 10_3	10.60	6.10	28.80	[96]
			10.07	5.95	27.80	[97]
			10.70	6.45	27.80	[98]
δ	Orthorhombic	10_3	10.80	6.20	28.80	[94]
β	Orthorhombic	3_1	10.31	18.21	9.00	[96]
			10.40	17.70	9.00	[99]
	Trigonal	3_1	10.52	10.52	8.80	[100]
sc	Trigonal	3_1	14.98	14.98	8.70	[101]
	Triclinic	3_1	9.16	9.16	8.70	[101,102]

The sc-PLA between PLLA and PLDA can be formed via melt-, cold-crystallization, and in solution. It is achieved at the 1:1 L and D-lactide ratio, which are packed side by side with strong van der Waals interaction leading to the high thermal and mechanical properties [103]. In the isothermal crystallization, the low molecular weight PLLA/PLDA can be achieved at T_c of 130 ºC from the melt. While the stereocomplex formation between the high molecular weight mixtures has been challenged and tends to form α or δ crystal of homo-crystal structure [103,104]. To enhance the formation of the high molecular weight sc-PLA, crystallization processes have been reported elsewhere [104–106].

In general, the crystallite structure can affect the barrier properties of polymeric materials. It tends to act as a filler dispersing in the polymer matrix. Therefore, the crystallite zone is considered impermeable in which the gas and liquid penetrants cannot

diffuse [107]. The crystal structure can affect the diffusivity because it forces a tortuous diffusive pathway of the permeants depending on the degree of crystallinity [107].

2.3.1.2 Mobile amorphous region

Mobile amorphous fraction (MAF), a free or bulk amorphous region, is described as an orderless and structureless mass with random interchain entanglements and free volume. At the temperature below its T_g, the MAF in the glassy state is a solid obtained by quenching PLA from the melt [108]. The amount of MAF (X_{MAF}) in the semicrystalline sample can be quantitated by the specific heat capacity (C_p) step during glass transition compared with the C_p step of the fully amorphous polymer:

$$X_{MAF} = \frac{\Delta C_p}{\Delta C_p^0} \tag{2.11}$$

where ΔC_p is the measured heat capacity increment at T_g of the sample, and ΔC_p^0 is the heat capacity increment of a 100% amorphous PLA.

The rearrangement of the amorphous PLA can be associated with the isothermal aging or cooling processes showing the enthalpy recovery endotherm at the late stage of the glass transition. As a result, the quenched polymer with the loose packing can rearrange to the more dense packing of the local structural orientation depending on aging and cooling [109]. Furthermore, the chains in the amorphous regions can undergo rearrangement into more ordered structures through uniaxial drawing, a process referred to as the mesophase in stretching crystallization. The ordered amorphous could be devitrified/vitrified at a temperature higher than the T_g of the untreated amorphous PLA [110].

For semicrystalline PLA, the two MAFs, intra-spherulitic and inter-spherulitic amorphous regions can exist either between lamellae in spherulites or in the spaces where adjacent spherulites grow and impinge on one another [111]. Righetti et al. [78] explained that the inter-spherulitic MAF, defined as the amorphous region outside spherulite, has

mobility close to the fully amorphous fraction. In comparison, the MAF located in intra-spherulitic areas has more restricted mobility. Delpouve and coworkers [112–114] used the cooperative rearranging regions (CRR) concept to differentiate each phase and to assess their T_g and fraction of the two MAFs.

2.3.1.3 Rigid amorphous region

The RAF can be generated during the crystallization process due to the lack of mobility of the amorphous fraction linked with the crystals by covalent interaction resulting in constraints in geometrically restricted areas. RAF could also be induced from the internal stresses of the amorphous region that cannot be released during crystal growth and accumulated at the interface between the crystal and amorphous [109]. Additionally, it can be generated by the repulsive interactions between the growth faces of the crystals referred to as "the rigid wall effect" [109,115]. However, it has been reported that RAF is located at only the crystal basal planes (fold-surface) and does not affect crystal growth in the lateral direction [116].

Ma et al. [69] investigated the vitrification and devitrification of RAF during crystallization. They reported that the vitrification of RAF proceeds from the fold-surface of the lamellae, which acts as fixed constraints. Hence, the amorphous layer adjacent to the crystal lamellae has the highest restriction devitrified at a temperature higher than T_g of the MAF. The next layer that does not attach to the crystal phase has slightly lower experiences slightly lower restriction compared to the attached layer. The successive layers undergo devitrification at the lower temperature until they reach T_g of the MAF due to its relatively greater mobility. Due to the distinct characteristics of RAF, the temperature that the RAF vitrifies/devitrifies is related to the level of constraint, as shown schematically in **Figure 2.3a**. Recently, Sangroniz et al. [74] proposed the dedensification effect of the RAF of crystallized PLLA. They described that the increase of RAF can lead to a significant excess

free volume in the amorphous phases trapped between the crystals. The proposed schematic structure of the PLLA and free volume associated with RAF is shown in **Figure 2.3b.**

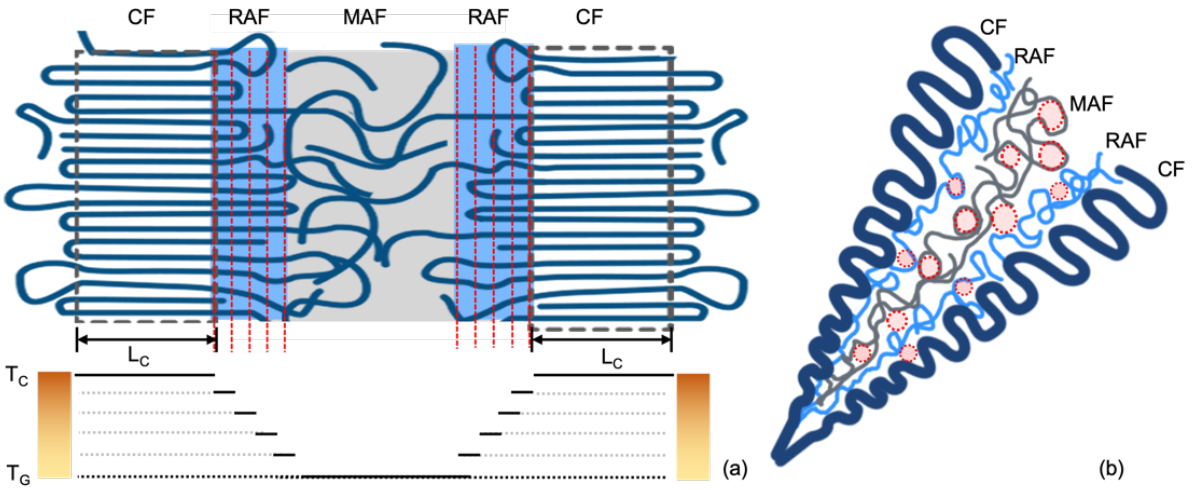

Figure 2.3 Schematic representation of (a) the arrangement of rigid amorphous (RAF), which corresponds to the level of constraints, adapted from [69], (b) the dedensification effect of the RAF, adapted from [74].

The RAF can be estimated based on DSC using heating scan by considering the temperature range between the glass transition of MAF and the melting stage of the CF. To achieve more accurate determination of RAF, modulated DSC (MDSC) can be used due to its higher resolution, sensitivity, and capability of distinguishing overlapping thermal events as observing from the conventional DSC [117].

Once the CF and MAF are determined by using Eqs. (2.9) and (2.11), respectively, the amount of RAF (X_{RAF}) is obtained as the remaining fraction as follows:

$$X_{RAF} = 1 - X_{CF} - X_{MAF} \tag{2.12}$$

Besides the DSC analysis, dynamic-mechanical analysis (DMA) can also be used to identify the existence of RAF. Kolesov and Androsch [118] estimated the RAF by the remaining fraction, apart from MAF obtained from the integration of loss-factor curve and CF obtained from the other sources (e.g., wide-angle X-ray scattering (WAXS) and DSC). As

the result, the RAF can be developed with an increase of annealing temperature due to an increasing CF. Furthermore, the devitrification of RAF can significantly enhance the storage modulus. Similarly, Zuza et al.[119] analyzed the cold-crystallization of PLLA at 50 ºC for different times and found that the loss factor appeared as double peaks at around 60 and 75 ºC, which were assigned by the researchers as the T_g of MAF and RAF, respectively. The advantage of the DMA technique is to obtain the mechanical characteristics based on the different behavior of amorphous structures in the transition region of glassy and rubbery states. More details regarding the investigation of RAF with increasing annealing temperature crystallization using DMA analysis can be found elsewhere [118,119].

As a general rule, the evolution of the RAF during crystallization is greatly influenced by T_c, in which the crystal structures are developed. Righetti and Tombari [120] measured the evaluation of the three-phase structure of PLLA during quasi-isothermal from the melt at 90, 130, and 135 ºC. According to the finding, at a low T_c of 90 ºC, the RAF developed in parallel with the CF. The molecular chains had low mobility leading to the strong coupling between crystalline and amorphous phases and high stress accumulated in the amorphous. It can result in a profound increase in RAF and the development of irregular chain structures. Conversely, at a high T_c of 130–135 ºC, the formation of RAF started increasing at a later period due to the high mobility, which facilitated the organization of the chain to form a perfect crystal structure. The RAF could increase simultaneously with secondary crystallization after spherulite impingement.

Several studies have reported that the morphological structure has an effect on the properties of PLA [121,122]. The diffusion of water molecules is one of the critical phenomena in the hydrolytic degradation process that could be affected by the degree of crystallinity [123]. Sonchaeng et al. [75] provided a critical review on the mass transfer properties of PLA and summarized the discrepancy in the effect of crystallinity on the diffusion, which could be

attributed to the presence of RAF. **Table 2.3** summarizes the diffusion coefficient (*D*) of PLA film with the specific conditions from the studies of Siparsky et al. [124] and Gorrasi et al.[125]. It is apparent that the water vapor diffusion into the PLA film varied depending on the optical purity and X_C. Siparsky et al. [124] reported the D values of PLA at 40 and 50 ºC at 90% relative humidity. They found that amorphous PLA film with a lower L-lactide content exhibited a higher *D* value at 40 ºC, attributable to the larger free volume in the chain packing under the glassy state, in contrast to those with a higher L-lactide content, which showed the higher crystallinity. The *D* of PLA seems to decrease with increased crystallinity at the temperature of 50 ºC which is above its T_g. Similarly, Gorrasi et al. [125] reported the *D* values of PLA at 30 ºC. They noted that the *D* of PLA tends to decrease with increased crystallinity. However, when the crystallinity surpasses 40%, the diffusion may either remain constant or begin to increase due to the high free volume associated with the effect of RAF. Indeed, the properties of RAF could depend on various crystallization conditions, methods, time, temperature, and crystal modifications [74,124,125].

Table 2.3 A summary of the diffusion coefficient of PLA film with the specific conditions in the literature.

Ref.	PLA (L/ D)	Crystallization			Diffusion coefficient (D, $cm^2/s \times 10^6$)		
		Condition[1]	X_C	Crystal form	Temperature (°C)		
					30	40	50
Siparsky et al. [124]	95/5	–	–	–	–	0.150	0.200
	100/0	–	11%	–	–	0.051	0.250
	100/0	MC–160 °C, 15m	39%	–	–	0.067	0.320
Gorrasi et al. [125]	98.6/1.4	Q	0%	–	0.078	–	–
	98.6/1.4	AN–110 °C, 30m	12%	δ	0.066	–	–
	98.6/1.4	MC–110 °C, 5h	38%	δ	0.040	–	–
	98.6/1.4	CC–110 °C, 5h	45%	δ	0.060	–	–

1 Crystallization condition: Q is melt-quenching; AN is annealing; MC and CC are melt- and cold-crystallization.

2.4 Hydrolysis degradation of PLA

One of the great advantages of PLA is its ability to be gradually hydrolyzed under normal environmental conditions, facilitating the subsequent composting process when dispose in industrial composting facilities. However, this could be a significant drawback when the hydrolytic degradation occurs during its service lifetime, leading to a decrease in the molecular weight, deterioration of the properties, and material failure [126].

Hydrolytic degradation of PLA generally proceeds in several steps [126,127]:

(1) Diffusion of water into the amorphous phase of polymer material

(2) Hydrolysis of the ester bonds by the chain scission and molecular weight reduction

(3) Production of the water-soluble oligomers and monomers and mass loss

(4) Partial hydrolysis of crystalline region

In real-life scenarios, more or fewer concurrent processes can coincide. For example, crystallization can simultaneously occur after the diffusion of water in the matrix and the cleavage of molecular chains. This process enhances the molecular segment's mobility, leading to rearrangement into a more orderly structure [126,128]. This hydrolysis process results in a reduction in molecular weight, an increase in the degree of crystallinity, and weight loss. **Figure 2.4** shows the flow diagram of hydrolysis processes and their interrelationships.

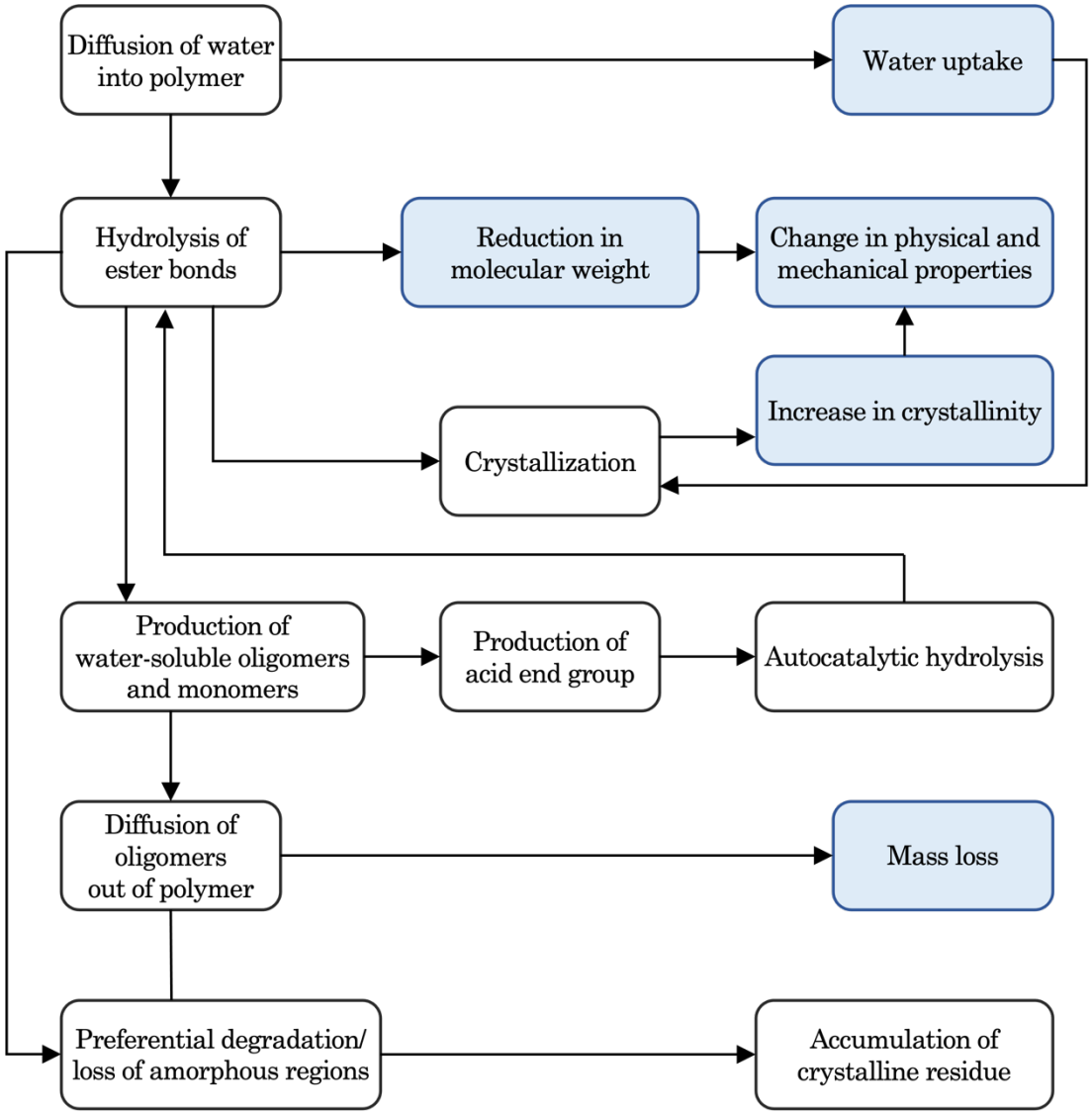

Figure 2.4 Flow diagram showing PLA hydrolytic degradation adapted from [129]. Shaded boxes represent the measured properties.

In general, the hydrolytic degradation of neat PLA film in water is a bulk-erosion process which assumes that the water diffusion rate is very high compared to the degradation rate. Therefore, the overall hydrolytic degradation of PLA considers only the chain scission reaction occurring in the presence of water given by:

$$R–C(CH_3)COO–R' + H_2O \rightarrow R–C(CH_3)COOH + HO–R' \quad (2.13)$$

in which R and R' denote the repeating units of the initial PLA chains. (R – C(CH_3) – COOH) and (R' – OH) represent the hydrolyzed PLA with carboxylic acid and hydroxyl ends, respectively. Typically, the hydrolysis rate depends on the concentration of the ester bonds and acidic products, while water molecules are abundant and remain constant [130]. In certain cases, if the hydrolysis reaction rate is faster with respect to the water diffusion, the surface will be hydrolyzed before water diffuses into the material matrix, leading to a gradual erosion from the surface inwards. As a result, it can result in weight loss and a decrease in material thickness; this suggests a surface-erosion mechanism [126,131]. In contrast, the bulk erosion mechanism can lead to mass loss in the late-stage degradation.

2.4.1 Hydrolysis of PLA and related parameters

The hydrolysis behavior is affected by several parameters, which can be media-related factors such as pH and temperature and polymer-related factors such as crystallinity, optical purity, and molecular weight and distribution. Specific details for the main parameter are discussed below.

2.4.1.1 pH

pH plays a very crucial role in the hydrolysis of PLA. It affects both the hydrolysis mechanisms and reaction kinetics. Therefore, according to the environment where the reactions occur, the hydrolysis behavior could be altered by changing nature of the medium.

The hydrolysis of PLA follows a bulk erosion degradation mechanism when it is immersed in neutral aqueous media (e.g., distilled water, phosphate-buffer solution, and

alcoholic solution, *pH* 7.4) and acid aqueous media (e.g., hydrochloric acid, phosphoric acid, acetate buffer solution, *pH* 1–6) [132]. On the other hand, PLA undergoes mainly surface erosion in alkaline media (sodium hydroxide solution, *pH* 10–13) [133]. This behavior can be explained by the water absorption of PLA, which decreases by increasing *pH*. Hence, the hydroxyl ions are entrapped on the surface; as a result, the surface erosion mechanism becomes dominant [134].

The chain scission reaction that occurs during hydrolytic degradation of PLA can be catalyzed by a high concentration of hydroxide (OH^-) and hydronium (H_3O^+) ions in the alkaline and acidic media, respectively [126]. Jung et al. [135] studied the accelerated hydrolysis of PLA in varying pH and summarized that the degradation rate constant was faster under strongly alkaline media than in the strong acid.

2.4.1.2 Optical purity

As mentioned in Section 2.3.1, the properties of PLA, such as the thermal properties and crystallization behavior, are strongly affected by the nature of the optical purity with respect of the fraction and sequence length of the major monomer units. In a hydrolytic process, Tsuji [14] studied the effect optical purity and tacticity on the autocatalytic hydrolysis of by using the high optical purity of L-lactide (PLLA), D-lactide (PDLA), the mixture of PLLA and PDLA (PDLLA) and well-stereocomplexed blending of PLLA and PDLA (PLLA/PDLA). According to their results, all the PLA films remained amorphous for 16 months. They concluded that the low tacticity of the PDLLA chains increased the interaction between PDLLA chains and water molecules as compared with the high optical purity PLA. The stereocomplex crystallites formed from the blended PLLA/PDLA might have reduced the hydrolysis rate. In another study, the same group of authors [136] studied the hydrolysis of PLA with different grades (small amounts of D-lactide unit of 0.2–1.2%), and reported that the incorporation of small amounts of D-lactide can enhance the hydrolysis of PLA, due to

decreased chain interactions. While X_C of PLA film could increase with a reduced amount of D-lactide. This leads to a subsequent decrease in the rate of the late stage of hydrolysis.

2.4.1.3 Temperature

The rate constant of the PLA hydrolysis kinetics is highly affected by the environmental temperatures. Increasing temperature can accelerate the hydrolysis of PLA. Therefore, many hydrolysis studies have been carried at elevated temperatures to accelerate the reaction and extrapolate the hydrolysis behaviors to the end-use temperatures [137–139]. Assuming the relationship between the hydrolysis constant and the inverse of temperature follows the Arrhenius relationship. The activation energy values are obtained from the slope of Arrhenius plot and then used to estimate the rate constant at the temperature of interest. However, if the temperature conditions are below the T_g, the hydrolysis of amorphous chains existing in the glassy state much slower due to the lack of chain mobility. Another prediction approach, such as Vogel–Tammann–Fulcher (VTF) model, can be used to assess the hydrolysis of PLA over a wide range of temperature across the T_g as presented by Lyu et al. [140] and Limsukon et al. [141].

2.4.1.4 Crystallinity

According to the two-phase structural model, the hydrolytic degradation of PLA occurs only in the amorphous region since the water molecules can penetrate easier than the tightly packed crystal structure [126]. As a result, the hydrolysis predominantly occurs in the amorphous regions, subsequently leaving the crystalline residue intact. As mentioned in **Section 2.3.1**, the properties of the semicrystalline polymer are strongly affected by the three-phase structures. Many researchers reported that the increase in the crystallinity of semicrystalline PLA could retard the alkaline [142–144] and enzymatic [145–148] hydrolytic degradation. These phenomena are correlated with the surface erosion mechanism that the degradation initiates from the surface. Tsuji et al. [142] considered not only the crystalline

phase but also the rigid amorphous regions, RAF (or alternatively called the restricted amorphous phase in their hydrolysis study). The researchers concluded that in the alkaline solution, the hydrolysis rate of the MAF and RAF were similar. While in the enzymatic hydrolysis of PLA, the hydrolysis rate of the film is much lower of RAF than that of MAF.

In the case of bulk erosion hydrolysis, commonly found in neutral and acid media, the RAF could be attributed to adverse effects on hydrolysis [126]. According to the literature [74,142,149,150], the characteristic of RAF in the bulk erosion hydrolysis is predicted to be (1) more hydrophilic with increasing densities of terminal carboxyl and hydroxyl groups of PLA; (2) accelerated by an increase in the carboxylic acid ends in the area through the autocatalytic reaction; and (3) more disorder in restricted chain packing leading to the excess free volume related to a higher number of nano-size holes or cavities. However, some contradictions in the effect of crystallinity on the hydrolysis behavior of amorphous and semicrystalline PLA in the literature are observed, which could be attributed to the different behavior of RAF. The hydrolysis conditions and findings reported by researchers are summarized in **Table 2.4**.

Table 2.4 A summary of the hydrolysis behavior of amorphous and semicrystalline PLA in the literature.

Reference	PLA (L/D)	Crystallization [1]			Hydrolysis [2]			Effect [3] of X_C
		Condition	Initial X_C	Final X_C	Media	Temp.	Rate (d^{-1})	
Li et al. [131]	PLLA–plate	Amorphous	0%	49%	PBS (pH 7.4)	37 °C	0.0066	ns
		CC–130 °C, 2h	73%	73%			0.0064	
Duek et al. [151]	PLLA–rod	Amorphous	0%	55.80%	PBS (pH 7.4)	38 °C	0.0134	Dec.
		MC–slow-cooled	48%	67.27%			0.0110	
Tsuji [152]	PLLA	Amorphous	0%	0%	PBS (pH 7.4)	37 °C	0.0040	Dec.
	PDLA	Amorphous	0%	0%			0.0042	
	Blended (50/50)	Blending	35%	46%			0.0014	
Harris and Lee [153]	98.6/1.4	Amorphous	10.8%	51%	90%RH	50 °C	0.0310	Dec.
		AN–80 °C, 1h	42.3%	48%			0.0270	

Table 2.4 (cont'd)

Reference	PLA (L/D)	Crystallization [1]			Hydrolysis [2]			Effect [3] Of X_C
		Condition	Initial X_C	Final X_C	Media	Temp.	Condition	
Gorrasi et al. [154]	88/12	Amorphous	0%	40.8%	Distilled water	58 °C	0.1264	Dec.
	96/4	Amorphous	0%	51.6%			0.1170	
	95/5	Amorphous	0%	53.0%			0.1138	
	95/5	CC–110 °C, 5h	52.4%	74.6%			0.0716	
Rodriguez [155]	98/2	Amorphous	0%	75%	Distilled water	60 °C	0.1810	Dec.
	90/10	Amorphous	0%	54%			0.3000	
	98/2	Amorphous	0%	75%	Distilled water	70 °C	0.5040	Dec.
	90/10	Amorphous	0%	54%			0.7220	
	98/2	Amorphous	0%	75%	Distilled water	80 °C	1.2540	Dec.
	90/10	Amorphous	0%	54%			1.5220	
Zhang et al. [156]	96/4	MC–80 °C, 1h	26.4%	–	Distilled water	50 °C	0.0453	Dec.
		MC–80 °C, 6h	47.3%	57.5%			0.0316	
		MC–140 °C, 1h	18.8%	–	Distilled water	50 °C	0.0428	Dec.
		MC–140 °C, 6h	51.9%	64.5%			0.0237	

Table 2.4 (cont'd)

Reference	PLA (L/D)	Crystallization [1]			Hydrolysis [2]			Effect [3] of X_C
		Condition	Initial X_C	Final X_C	Media	Temp.	Rate (d^{-1})	
Tsuji et al. [149]	98/2	Amorphous	0%	29%	PBS (pH 7.4)	37 °C	0.0031	Inc.
		MC–140 °C, 15m	2%	34%			0.0037	
		MC–140 °C, 30m	30%	63%			0.0045	
		MC–140 °C, 45m	45%	76%			0.0045	
		MC–140 °C, 60m	54%	78%			0.0046	
Tsuji and Ikada [157]	98/2	MC–100 °C, 10h	40%	75%	PBS (pH 7.4)	37 °C	0.0031	Inc.
		MC–120 °C, 10h	47%	82%			0.0035	
		MC–140 °C, 10h	54%	92%			0.0039	
		MC–160 °C, 10h	56%	95%			0.0045	
Tsuji and Nakahara [158]	PLLA	Amorphous	0%	3%	HCl (pH 2.0)	37 °C	0.0030	Inc.
		MC–140 °C, 10h	32%	49%			0.0046	
		Amorphous	0%	3%	DLLA (pH 2.0)	37 °C	0.0024	–
		MC–140 °C, 10h	32%	45%			0.0023	
		Amorphous	0%	3%	PBS (pH 7.4)	37 °C	0.0026	Inc.
		MC–140 °C, 10h	37%	43%			0.0035	

Table 2.4 (cont'd)

Reference	PLA (L/D)	Crystallization [1]			Hydrolysis [2]			Effect [3] of X_C
		Condition	Initial X_C	Final X_C	Media	Temp.	Rate (d^{-1})	
Tsuji [159]	PLLA	MC–140 °C, 10h	39%	59%	PBS (pH 7.4)	37 °C	0.0043	Inc.
	PDLA	MC–140 °C, 10h	40%	61%			0.0047	
	Nonblended 50/50	MC–140 °C, 10h	30%	32%			0.0052	
Huang et al. [160]	95.75/4.25	Amorphous	0%	<2.5%	88%RH	39 °C	0.0048	Inc.
		MC–90 °C, 3h	32%	45%			0.0060	
		MC–120 °C, 2h	43%	50%			0.0072	

[1] Crystallization condition: Q is melt quenching, AN is annealing, MC and CC are melt- and cold-crystallization.
[2] Hydrolysis rate constants were calculated from the first-order reactions: $M_n = M_{n_0} e^{-kt}$.
[3] Effect of X_C on the hydrolysis of PLA: The hydrolysis of PLA Inc. (= increases) or Dec. (= decreases) as increasing of X_C. ns is not significant.

2.5 Population balance modeling (PBM)

2.5.1 Introduction to PBM

PBM is a widely used modeling technique that describes the properties of a continuous or discrete number of particles in systems where they interact with their environment. Each system of states represents a unique combination of properties (e.g., particle size, length, mass, and any other quantitative descriptors) and position of the particle in the three-dimensional space that depict the entity's condition in the particular process using a finite dimensional vector [161,162]. In general, this vector includes both *internal coordinates*, which signify selected properties representing the entity, as well as *external coordinates* typically utilized to depict its physical position. PBM plays a critical role in the principles of a number conservation of mass, momentum, and energy. By comprehensively tracking the distribution and evolution of entities within a system, PBM can provide insights into how quantities are preserved or transformed as processes unfold to elucidate specific behaviors observed within the system [161,163].

In most instances, the Population Balance Equation (PBE) includes mathematical components known as *accumulation, convection,* and *diffusion terms* with respect to each dimension of the phase space, and *sink*/*source term* that takes into account the birth and death of the entities. The birth and death processes are influenced by the specific states of the entities that are either created or eliminated, each having its associated characteristics or properties that define its behavior and interactions of the system. For instance, the birth process could involve coalescence, agglomeration, coagulation, and aggregation events. In contrast, the death process could be influenced by breakup, fragmentation, rupture, and breakage events [162].

According to Solsvik and Jakobsen [162], the continuous phase variables are represented by a vector field that depends on internal coordinates (X) and external coordinates (r) with respect of time (t). The general form of PBE is given by Eq. (2.14):

$$\frac{\partial f_n^1(r,X,t)}{\partial t} + \nabla_r \cdot [f_n^1(r,X,t)\, v_r(r,X,t)] + \nabla_x \cdot [f_n^1(r,X,t)\, v_X(r,X,t)] = J(r,X,t) \tag{2.14}$$

where $f_n^1(\mathrm{r},\mathrm{X},\mathrm{t})$ dr dX dt represents the number of particles per unit volume of the particle phase with an internal coordinate between [X, X+dX], an external coordinate between [r, r+dr] during the time interval [t, t+dt]. v_r and v_X are the velocity in the external and internal coordinates, respectively. $J(r,X,t)$ is a source term considering death and birth of particles.

2.5.2 PBM for the hydrolytic degradation

Generally, the hydrolytic degradation model can be utilized to track the evolution of average molecular weights, implying that all entities behave in a similar manner. However, this assumption often falls short in accurately representing the properties of macromolecules. The molecular weight distribution (MWD) serves as a more appropriate approach to capture the intricacies of a complex process. PBM has been applied to polymer material degradation processes not only to uncover degradation behavior but also to simulate the evolution of MWDs throughout the process. PBM offers a comprehensive insight into the degradation phenomenon and provides a robust tool for evaluating the intricate changes in molecular weight distribution [164–166].

In the context of hydrolysis degradation, the PBM focuses solely the breakage phenomenon attributed to chain scission reactions. It captures the intricacies of molecular transformations during the hydrolysis process, specifically the fragmentation of molecular chains resulting in changes to the overall molecular weight distribution without taking into

account physical spatial influences as well as growth and shrinkage effects. Then, Eq. (2.14) can be simplified as follows [167]:

$$\frac{\partial f_n^1(\mathrm{X},\mathrm{t})}{\partial t} = J(X,t) = J^+(x,t) - J^-(x,t) \tag{2.15}$$

The sink term, $J^-(x,t)$, is the breakage of particles of size X into smaller fragments. This can be mathematically expressed as:

$$J^-(x,\mathrm{t}) = k(x,t)\, f_n(x,\mathrm{t}) \tag{2.16}$$

The source term, $J^+(\mathrm{x},\mathrm{t})$, is the breakage of particles of sizes greater than x undergoing breakage and transitioning to size x. This relationship of a daughter particle with a length of x is produced by the breakage of a mother particle with a length of y can be formulated mathematically as:

$$J^+(x,\mathrm{t}) = \int_x^\infty v(y,t)\, k(y,t)\ \Omega(x|y,t)\, f_n(y,\mathrm{t})dy \tag{2.17}$$

where $k(x,t)$ and $k(y,t)$ represent the hydrolysis rates of the breakage and production of x, respectively.$f_n(x,t)$ and $f_n(y,t)$ are the number density function. $v(y,t)$ is the average number of daughter particles that are formed per breakage event. $\Omega(x|y,t)$ is the probability density function for particle of state y to x.

Assuming the hydrolysis of PLA occurs randomly along the polymer chains, where a macromolecule P with a molecular weight of x undergoes hydrolysis at a random position along the main chain, with a rate coefficient of random chain scission denoted as k_r. This process results in the formation of the products x' and x - x':

$$P(x) \overset{k_r}{\rightarrow} P(x') + P(x-x') \tag{2.18}$$

The rate of change of the macromolecule P can be mathematically represented within the framework of the PBM as follows:

$$\frac{\partial P(\mathrm{x},\mathrm{t})}{\partial t} = -k_r(\mathrm{x})\,\mathrm{P}(x,t) + 2\int_x^{\infty} k_r(\mathrm{y})\,\Omega(x|y,t)\,P(y,t)\,dy \tag{2.19}$$

In this equation, $\Omega(x,y)$ represents a stoichiometric kernel, which serves to describe the probability density function representing the likelihood that a daughter particle x is produced by the breakage of a mother particle y. Specifically, for the scenario of random scission, this kernel is defined as 1/y, and it aligns with binary breakage as indicated by $v(y,t) = 2$ [168].

In the context of the specific case of polymer degradation reactions, Kostoglou [169] introduced the concept of a breakage population balance equation to analyze the evolution of MWDs for chain-end polymer degradation. This research presents a continuous model specifically designed to predict the concentration of monomers produced through scission processes. Furthermore, Lazzari et al. [132] proposed a PBM framework tailored to the pH-dependent degradation (pH = 1–7.4) of lactic acid oligomer, ranging from dimer to octamer, in water at 37 ºC. This approach considers various kinetic constants, including the acid-catalyzed ($k_{D,n}$), random and backbiting (k_{RH} and k_{BB}) and non-catalyzed (k_W) degradation machanisms. The proposed framework fitted the experimental data well for short-chain oligomers.

REFERENCES

[1] Groot W., van Krieken J., Sliekersl O., and de Vos S., Production and Purification of Lactic Acid and Lactide, in *Poly(Lactic Acid)*, Hoboken, NJ, USA: John Wiley & Sons, Inc., 2010, pp. 1–18.

[2] Auras R., Harte B., and Selke S., An overview of polylactides as packaging materials, *Macromol. Biosci.*, vol. 4, no. 9, pp. 835–864, 2004, doi: 10.1002/mabi.200400043.

[3] Chen G. Q., *Plastics from Bacteria*, vol. 14. Berlin, Heidelberg: Springer Berlin Heidelberg, 2010.

[4] Lim L. T., Auras R., and Rubino M., Processing technologies for poly(lactic acid), *Prog. Polym. Sci.*, vol. 33, no. 8, pp. 820–852, 2008, doi: 10.1016/j.progpolymsci.2008.05.004.

[5] Ren J., Processing of PLA, in *Biodegradable Poly(Lactic Acid): Synthesis, Modification, Processing and Applications*, Berlin, Heidelberg: Springer Berlin Heidelberg, 2010, pp. 142–207.

[6] Farah S., Anderson D. G., and Langer R., Physical and mechanical properties of PLA, and their functions in widespread applications — A comprehensive review, *Adv. Drug Deliv. Rev.*, vol. 107, pp. 367–392, Dec. 2016, doi: 10.1016/j.addr.2016.06.012.

[7] Kale G., Kijchavengkul T., Auras R., *et al.*, Compostability of bioplastic packaging materials: An overview, *Macromol. Biosci.*, vol. 7, no. 3, pp. 255–277, 2007, doi: 10.1002/mabi.200600168.

[8] Jamshidian M., Tehrany E. A., Imran M., *et al.*, Poly-Lactic Acid: Production, Applications, Nanocomposites, and Release Studies, *Compr. Rev. Food Sci. Food Saf.*, vol. 9, no. 5, pp. 552–571, 2010, doi: 10.1111/j.1541-4337.2010.00126.x.

[9] Jem K. J. and Tan B., The development and challenges of poly (lactic acid) and poly (glycolic acid), *Adv. Ind. Eng. Polym. Res.*, vol. 3, no. 2, pp. 60–70, 2020, doi: 10.1016/j.aiepr.2020.01.002.

[10] Suzanne M. Delong, An efficient Methodology for Analysis of Stochastic Computer Simulation Experiment. Berlin, Heidelberg, 2012.

[11] Urayama H., Kanamori T., and Kimura Y., Microstructure and thermomechanical properties of glassy polylactides with different optical purity of the lactate units, *Macromol. Mater. Eng.*, vol. 286, no. 11, pp. 705–713, 2001, doi: 10.1002/1439-2054(20011101)286:11<705::AID-MAME705>3.0.CO;2-Q.

[12] Jiang X., Luo Y., Tian X., *et al.*, Chemical Structure of Poly(Lactic Acid), in *Poly(Lactic Acid)*, Hoboken, NJ, USA: John Wiley & Sons, Inc., 2010, pp. 67–82.

[13] Tsuji H., Ohsada K., and Arakawa Y., Stereocomplex- and homo-crystallization behavior, polymorphism, and thermal properties of enantiomeric random copolymers of l- and d-lactic acids from the melt, *Polymer (Guildf).*, vol. 228, no. June, p. 123954, 2021, doi: 10.1016/j.polymer.2021.123954.

[14] Tsuji H., Autocatalytic hydrolysis of amorphous-made polylactides: Effects of L-lactide content, tacticity, and enantiomeric polymer blending, *Polymer (Guildf).*, vol. 43, no. 6, pp. 1789–1796, 2002, doi: 10.1016/S0032-3861(01)00752-2.

[15] Arif P. M., Kalarikkal N., and Thomas S., Introduction on Crystallization in Multiphase Polymer Systems, in *Crystallization in Multiphase Polymer Systems*, Elsevier, 2018, pp. 1–16.

[16] Hoffman J. D. and Weeks J., Melting Process and Equilibrium Melting Temperature of Polychlorotrifluoroethylene, vol. 66, no. February, 1962.

[17] Baltá-Calleja F. J. and Ezquerra T. A., Polymer Crystallization: General Concepts of Theory and Experiments, in *Encyclopedia of Materials: Science and Technology*, vol. 6, no. 10, Elsevier, 2001, pp. 7244–7252.

[18] Di Lorenzo M. L., Androsch R., Rhoades A. M., and Righetti M. C., Analysis of Polymer Crystallization by Calorimetry, in *Handbook of Thermal Analysis and Calorimetry*, vol. 6, 2018, pp. 253–299.

[19] Androsch R., Schick C., and Di Lorenzo M. L., Kinetics of Nucleation and Growth of Crystals of Poly(l-lactic acid), in *Synthesis, Structure and Properties of Poly(lactic acid)*, vol. 279, M. L. Di Lorenzo and R. Androsch, Eds. Cham: Springer International Publishing, 2018, pp. 235–272.

[20] Schick C., Androsch R., and Schmelzer J. W. P., Homogeneous crystal nucleation in polymers, *J. Phys. Condens. Matter*, vol. 29, no. 45, p. 453002, Nov. 2017, doi: 10.1088/1361-648X/aa7fe0.

[21] Reiter G. and Sommer J.-U., Polymer Crystallization: Observations, Concepts and Interpretations, *Lect. Notes Phys.*, vol. 608, no. January, 2003, doi: 10.1007/3-540-45851-4.

[22] Drieskens M., Peeters R., Mullens J., *et al.*, Structure versus properties relationship of poly(lactic acid). I. Effect of crystallinity on barrier properties, *J. Polym. Sci. Part B Polym. Phys.*, vol. 47, no. 22, pp. 2247–2258, Nov. 2009, doi: 10.1002/polb.21822.

[23] Di Lorenzo M. L. and Androsch R., Influence of α′-/α-crystal polymorphism on properties of poly(l-lactic acid), *Polym. Int.*, vol. 68, no. 3, pp. 320–334, 2019, doi: 10.1002/pi.5707.

[24] Li H. and Huneault M. A., Effect of nucleation and plasticization on the crystallization of poly(lactic acid), *Polymer (Guildf).*, vol. 48, no. 23, pp. 6855–6866, 2007, doi: 10.1016/j.polymer.2007.09.020.

[25] Sánchez M. S., Mathot V. B. F., Poel G. Vanden, and Ribelles J. L. G., Effect of the cooling rate on the nucleation kinetics of poly(l-lactic acid) and its influence on morphology, *Macromolecules*, vol. 40, no. 22, pp. 7989–7997, 2007, doi: 10.1021/ma0712706.

[26] Androsch R., Di Lorenzo M. L., and Schick C., Crystal nucleation in random l/d-lactide

copolymers, *Eur. Polym. J.*, vol. 75, pp. 474–485, Feb. 2016, doi: 10.1016/j.eurpolymj.2016.01.020.

[27] Androsch R. and Di Lorenzo M. L., Kinetics of crystal nucleation of poly(L-lactic acid), *Polymer (Guildf).*, vol. 54, no. 26, pp. 6882–6885, 2013, doi: 10.1016/j.polymer.2013.10.056.

[28] Li H., Nie W., Deng C., *et al.*, Crystalline morphology of poly(l-lactic acid) thin films, *Eur. Polym. J.*, vol. 45, no. 1, pp. 123–130, 2009, doi: 10.1016/j.eurpolymj.2008.10.008.

[29] Abe H., Kikkawa Y., Inoue Y., and Doi Y., Morphological and Kinetic Analyses of Regime Transition for Poly[(S)-lactide] Crystal Growth, *Biomacromolecules*, vol. 2, no. 3, pp. 1007–1014, Sep. 2001, doi: 10.1021/bm015543v.

[30] Yu C., Xie Q., Bao Y., *et al.*, Crystalline and Spherulitic Morphology of Polymers Crystallized in Confined Systems, *Crystals*, vol. 7, no. 5, p. 147, May 2017, doi: 10.3390/cryst7050147.

[31] Schick C. and Androsch R., *Fast Scanning Chip Calorimetry*, vol. 6. 2018.

[32] Saeidlou S., Huneault M. A., Li H., and Park C. B., Poly(lactic acid) crystallization, *Prog. Polym. Sci.*, vol. 37, no. 12, pp. 1657–1677, 2012, doi: 10.1016/j.progpolymsci.2012.07.005.

[33] Di Lorenzo M. L., The Crystallization and Melting Processes of Poly(L-lactic acid), *Macromol. Symp.*, vol. 234, no. 1, pp. 176–183, Feb. 2006, doi: 10.1002/masy.200650223.

[34] Di Lorenzo M. L., Determination of spherulite growth rates of poly(L-lactic acid) using combined isothermal and non-isothermal procedures, *Polymer (Guildf).*, vol. 42, no. 23, pp. 9441–9446, 2001, doi: 10.1016/S0032-3861(01)00499-2.

[35] Yuryev Y., Wood-Adams P., Heuzey M. C., *et al.*, Crystallization of polylactide films: An atomic force microscopy study of the effects of temperature and blending, *Polymer (Guildf).*, vol. 49, no. 9, pp. 2306–2320, 2008, doi: 10.1016/j.polymer.2008.02.023.

[36] Yasuniwa M., Tsubakihara S., Iura K., *et al.*, Crystallization behavior of poly(l-lactic acid), *Polymer (Guildf).*, vol. 47, no. 21, pp. 7554–7563, Oct. 2006, doi: 10.1016/j.polymer.2006.08.054.

[37] Di Lorenzo M. L., Crystallization behavior of poly(l-lactic acid), *Eur. Polym. J.*, vol. 41, no. 3, pp. 569–575, 2005, doi: 10.1016/j.eurpolymj.2004.10.020.

[38] Pan P., Zhu B., Kai W., *et al.*, Effect of crystallization temperature on crystal modifications and crystallization kinetics of poly(L-lactide), *J. Appl. Polym. Sci.*, vol. 107, no. 1, pp. 54–62, Jan. 2008, doi: 10.1002/app.27102.

[39] Bouapao L., Tsuji H., Tashiro K., *et al.*, Crystallization, spherulite growth, and structure of blends of crystalline and amorphous poly(lactide)s, *Polymer (Guildf).*, vol. 50, no. 16, pp. 4007–4017, 2009, doi: 10.1016/j.polymer.2009.06.040.

[40] Di Lorenzo M. L., Rubino P., Immirzi B., *et al.*, Influence of chain structure on crystal polymorphism of poly(lactic acid). Part 2. Effect of molecular mass on the crystal growth rate and semicrystalline morphology, *Colloid Polym. Sci.*, vol. 293, no. 9, pp. 2459–2467, 2015, doi: 10.1007/s00396-015-3709-2.

[41] Avrami M., Kinetics of Phase Change. I General Theory, *J. Chem. Phys.*, vol. 7, no. 12, pp. 1103–1112, Dec. 1939, doi: 10.1063/1.1750380.

[42] Avrami M., Kinetics of Phase Change. II Transformation-Time Relations for Random Distribution of Nuclei, *J. Chem. Phys.*, vol. 8, no. 2, pp. 212–224, Feb. 1940, doi: 10.1063/1.1750631.

[43] Evans U. R., The laws of expanding circles and spheres in relation to the lateral growth of surface films and the grain-size of metals, *Trans. Faraday Soc.*, vol. 41, pp. 365–374, 1945.

[44] Meares P., *Polymers: Structure and Bulk Properties*. London, Van Nostrand, 1965.

[45] Hay J. N., Application of the modified avrami equations to polymer crystallisation kinetics, *Br. Polym. J.*, vol. 3, no. 2, pp. 74–82, Mar. 1971, doi: https://doi.org/10.1002/pi.4980030205.

[46] Sperling L. H., Introduction to Physical Polymer Science. Wiley, 2005.

[47] Zhou W. Y., Duan B., Wang M., and Cheung W. L., Kinetics of Poly (L-Lactide)/ Carbonated Hydroxyapatite Nanocomposite Microspheres, 2008.

[48] Shieh Y.-T., Twu Y.-K., Su C.-C., *et al.*, Crystallization kinetics study of poly(L-lactic acid)/carbon nanotubes nanocomposites, *J. Polym. Sci. Part B Polym. Phys.*, vol. 48, no. 9, pp. 983–989, May 2010, doi: 10.1002/polb.21986.

[49] Day M., Nawaby A. V., and Liao X., A DSC study of the crystallization behaviour of polylactic acid and its nanocomposites, *J. Therm. Anal. Calorim.*, vol. 86, no. 3, pp. 623–629, 2006, doi: 10.1007/s10973-006-7717-9.

[50] Kolstad J. J., Crystallization kinetics of poly(L-lactide-co-meso-lactide), *J. Appl. Polym. Sci.*, vol. 62, no. 7, pp. 1079–1091, Nov. 1996, doi: 10.1002/(SICI)1097-4628(19961114)62:7<1079::AID-APP14>3.0.CO;2-1.

[51] Iannace S. and Nicolais L., Isothermal crystallization and chain mobility of poly(L-lactide), *J. Appl. Polym. Sci.*, vol. 64, no. 5, pp. 911–919, May 1997, doi: 10.1002/(SICI)1097-4628(19970502)64:5<911::AID-APP11>3.0.CO;2-W.

[52] He Y., Fan Z., Hu Y., *et al.*, DSC analysis of isothermal melt-crystallization, glass transition and melting behavior of poly(l-lactide) with different molecular weights, *Eur. Polym. J.*, vol. 43, no. 10, pp. 4431–4439, Oct. 2007, doi: 10.1016/j.eurpolymj.2007.07.007.

[53] Tsuji H., Takai H., and Saha S. K., Isothermal and non-isothermal crystallization behavior of poly(l-lactic acid): Effects of stereocomplex as nucleating agent, *Polymer*

(Guildf)., vol. 47, no. 11, pp. 3826–3837, 2006, doi: 10.1016/j.polymer.2006.03.074.

[54] Tsai W. C., Hedenqvist M. S., Laiback, *et al.*, Physical changes and sorption/desorption behaviour of amorphous and semi-crystalline PLLA exposed to water, methanol and ethanol, *Eur. Polym. J.*, vol. 76, pp. 278–293, 2016, doi: 10.1016/j.eurpolymj.2016.02.005.

[55] Iñiguez-Franco F., Auras R., Burgess G., *et al.*, Concurrent solvent induced crystallization and hydrolytic degradation of PLA by water-ethanol solutions, *Polymer (Guildf).*, vol. 99, pp. 315–323, Sep. 2016, doi: 10.1016/j.polymer.2016.07.018.

[56] Talukdar M. and Achary P. G. R., Calorimetric Study on Kinetics of Mesophase Transition in Thermotropic Copolyesters, *Ijrras*, vol. 3, no. 1l, pp. 92–99, 2010.

[57] Fischer E. W., Sterzel H. J., and Wegner G., Investigation of the structure of solution grown crystals of lactide copolymers by means of chemical reactions, *Kolloid-Zeitschrift und Zeitschrift für Polym.*, vol. 251, no. 11, pp. 980–990, Nov. 1973, doi: 10.1007/BF01498927.

[58] Righetti M. C., Gazzano M., Di Lorenzo M. L., and Androsch R., Enthalpy of melting of α′- and α-crystals of poly(l-lactic acid), *Eur. Polym. J.*, vol. 70, pp. 215–220, Sep. 2015, doi: 10.1016/j.eurpolymj.2015.07.024.

[59] Wang Z. G., Hsiao B. S., Sauer B. B., and Kampert W. G., The nature of secondary crystallization in poly(ethylene terephthalate), *Polymer (Guildf).*, vol. 40, no. 16, pp. 4615–4627, 1999, doi: 10.1016/S0032-3861(99)00067-1.

[60] Chen Z., Hay J. N., and Jenkins M. J., The effect of secondary crystallization on crystallization kinetics - Polyethylene terephthalate revisited, *Eur. Polym. J.*, vol. 81, pp. 216–223, 2016, doi: 10.1016/j.eurpolymj.2016.05.028.

[61] Marsh J. J., Turner R. P., Carter J., and Jenkins M. J., Thermal diffusivity and secondary crystallisation kinetics in poly(lactic acid), *Polymer (Guildf).*, vol. 179, no. July, p. 121595, Sep. 2019, doi: 10.1016/j.polymer.2019.121595.

[62] Phillipson K., Jenkins M. J., and Hay J. N., The effect of a secondary process on crystallization kinetics – Poly (ε-caprolactone) revisited, *Eur. Polym. J.*, vol. 84, pp. 708–714, 2016, doi: 10.1016/j.eurpolymj.2016.09.037.

[63] Suzuki H., Grebowicz J., and Wunderlich B., Heat capacity of semicrystalline, linear poly(oxymethylene) and poly(oxyethylene), *Die Makromol. Chemie*, vol. 186, no. 5, pp. 1109–1119, 1985, doi: 10.1002/macp.1985.021860521.

[64] Chen H. and Cebe P., Vitrification and devitrification of rigid amorphous fraction of PET during quasi-isothermal cooling and heating, *Macromolecules*, vol. 42, no. 1, pp. 288–292, 2009, doi: 10.1021/ma802104a.

[65] Righetti M. C., Laus M., and Di Lorenzo M. L., Temperature dependence of the rigid amorphous fraction in poly(ethylene terephthalate), *Eur. Polym. J.*, vol. 58, pp. 60–68, 2014, doi: 10.1016/j.eurpolymj.2014.06.005.

[66] Hamonic F., Miri V., Saiter A., and Dargent E., Rigid amorphous fraction versus oriented amorphous fraction in uniaxially drawn polyesters, *Eur. Polym. J.*, vol. 58, pp. 233–244, 2014, doi: 10.1016/j.eurpolymj.2014.06.014.

[67] Arnoult M., Dargent E., and Mano J. F., Mobile amorphous phase fragility in semi-crystalline polymers: Comparison of PET and PLLA, *Polymer (Guildf).*, vol. 48, no. 4, pp. 1012–1019, 2007, doi: 10.1016/j.polymer.2006.12.053.

[68] Righetti M. C., Tombari E., Angiuli M., and Lorenzo M. L. Di, Enthalpy-based determination of crystalline, mobile amorphous and rigid amorphous fractions in semicrystalline polymers. Poly(ethylene terephthalate), *Thermochim. Acta*, vol. 462, no. 1–2, pp. 15–24, 2007, doi: 10.1016/j.tca.2007.06.003.

[69] Ma Q., Georgiev G., and Cebe P., Constraints in semicrystalline polymers: Using quasi-isothermal analysis to investigate the mechanisms of formation and loss of the rigid amorphous fraction, *Polymer (Guildf).*, vol. 52, no. 20, pp. 4562–4570, 2011, doi: 10.1016/j.polymer.2011.08.006.

[70] Chen H. and Cebe P., Investigation of the rigid amorphous fraction in Nylon-6, *J. Therm. Anal. Calorim.*, vol. 89, no. 2, pp. 417–425, 2007, doi: 10.1007/s10973-007-8215-4.

[71] Xu H. and Cebe P., Heat Capacity Study of Isotactic Polystyrene: Dual Reversible Crystal Melting and Relaxation of Rigid Amorphous Fraction, *Macromolecules*, vol. 37, no. 8, pp. 2797–2806, 2004, doi: 10.1021/ma035961n.

[72] Nguyen T. L., Bédoui F., Mazeran P.-E., and Guigon M., Mechanical investigation of confined amorphous phase in semicrystalline polymers: Case of PET and PLA, *Polym. Eng. Sci.*, vol. 55, no. 2, pp. 397–405, Feb. 2015, doi: 10.1002/pen.23896.

[73] Fernandes Nassar S., Guinault A., Delpouve N., *et al.*, Multi-scale analysis of the impact of polylactide morphology on gas barrier properties, *Polymer (Guildf).*, vol. 108, pp. 163–172, 2017, doi: 10.1016/j.polymer.2016.11.047.

[74] Sangroniz A., Chaos A., Iriarte M., *et al.*, Influence of the Rigid Amorphous Fraction and Crystallinity on Polylactide Transport Properties, *Macromolecules*, vol. 51, no. 11, pp. 3923–3931, Jun. 2018, doi: 10.1021/acs.macromol.8b00833.

[75] Sonchaeng U., Iñiguez-Franco F., Auras R., *et al.*, Poly(lactic acid) mass transfer properties, *Prog. Polym. Sci.*, vol. 86, pp. 85–121, 2018, doi: 10.1016/j.progpolymsci.2018.06.008.

[76] Magoń A. and Pyda M., Study of crystalline and amorphous phases of biodegradable poly(lactic acid) by advanced thermal analysis, *Polymer (Guildf).*, vol. 50, no. 16, pp. 3967–3973, 2009, doi: 10.1016/j.polymer.2009.06.052.

[77] Ma Q., Pyda M., Mao B., and Cebe P., Relationship between the rigid amorphous phase and mesophase in electrospun fibers, *Polymer (Guildf).*, vol. 54, no. 10, pp. 2544–2554, 2013, doi: 10.1016/j.polymer.2013.03.019.

[78] Righetti M. C., Gazzano M., Delpouve N., and Saiter A., Contribution of the rigid amorphous fraction to physical ageing of semi-crystalline PLLA, *Polymer (Guildf).*, vol. 125, pp. 241–253, 2017, doi: 10.1016/j.polymer.2017.07.089.

[79] Lotz B., Crystal Polymorphism and Morphology of Polylactides, in *Advances in Polymer Science*, vol. 279, 2017, pp. 273–302.

[80] Maillard D. and Prud'homme R. E., Crystallization of ultrathin films of polylactides: From chain chirality to lamella curvature and twisting, *Macromolecules*, vol. 41, no. 5, pp. 1705–1712, 2008, doi: 10.1021/ma071306u.

[81] Pan P. and Inoue Y., Polymorphism and isomorphism in biodegradable polyesters, *Prog. Polym. Sci.*, vol. 34, no. 7, pp. 605–640, 2009, doi: 10.1016/j.progpolymsci.2009.01.003.

[82] Zhang J., Duan Y., Sato H., *et al.*, Crystal modifications and thermal behavior of poly(L-lactic acid) revealed by infrared spectroscopy, *Macromolecules*, vol. 38, no. 19, pp. 8012–8021, 2005, doi: 10.1021/ma051232r.

[83] Tábi T., Hajba S., and Kovács J. G., Effect of crystalline forms (α′ and α) of poly(lactic acid) on its mechanical, thermo-mechanical, heat deflection temperature and creep properties, *Eur. Polym. J.*, vol. 82, pp. 232–243, 2016, doi: 10.1016/j.eurpolymj.2016.07.024.

[84] Kawai T., Rahman N., Matsuba G., *et al.*, Crystallization and melting behavior of poly (L-lactic acid), *Macromolecules*, vol. 40, no. 26, pp. 9463–9469, 2007, doi: 10.1021/ma070082c.

[85] Zhang J., Tashiro K., Tsuji H., and Domb A. J., Disorder-to-Order Phase Transition and Multiple Melting Behavior of Poly(L-lactide) Investigated by Simultaneous Measurements of WAXD and DSC, *Macromolecules*, vol. 41, no. 4, pp. 1352–1357, Feb. 2008, doi: 10.1021/ma0706071.

[86] Hsu S. T. and Yao Y. L., Effect of film formation method and annealing on morphology and crystal structure of poly (L-Lactic Acid) films, *J. Manuf. Sci. Eng. Trans. ASME*, vol. 136, no. 2, pp. 1–38, 2014, doi: 10.1115/1.4025909.

[87] Wunderlich B., A classification of molecules, phases, and transitions as recognized by thermal analysis, *Thermochim. Acta*, vol. 340–341, pp. 37–52, 1999, doi: 10.1016/s0040-6031(99)00252-x.

[88] Wang Y., Li M., Wang K., *et al.*, Unusual structural evolution of poly(lactic acid) upon annealing in the presence of an initially oriented mesophase, *Soft Matter*, vol. 10, no. 10, pp. 1512–1518, 2014, doi: 10.1039/c3sm52611a.

[89] Stoclet G., Seguela R., Lefebvre J. M., and Rochas C., New insights on the strain-induced mesophase of poly(d, l-lactide): In situ WAXS and DSC study of the thermo-mechanical stability, *Macromolecules*, vol. 43, no. 17, pp. 7228–7237, 2010, doi: 10.1021/ma101430c.

[90] Stoclet G., Seguela R., Lefebvre J. M., *et al.*, Strain-induced molecular ordering in polylactide upon uniaxial stretching, *Macromolecules*, vol. 43, no. 3, pp. 1488–1498, 2010, doi: 10.1021/ma9024366.

[91] Takahashi K., Sawai D., Yokoyama T., *et al.*, Crystal transformation from the α- to the ß-form upon tensile drawing of poly(L-lactic acid), *Polymer (Guildf).*, vol. 45, no. 14, pp. 4969–4976, 2004, doi: 10.1016/j.polymer.2004.03.108.

[92] Wang H., Zhang J., and Tashiro K., Phase Transition Mechanism of Poly(l-lactic acid) among the α, δ, and ß Forms on the Basis of the Reinvestigated Crystal Structure of the ß Form, *Macromolecules*, vol. 50, no. 8, pp. 3285–3300, 2017, doi: 10.1021/acs.macromol.7b00272.

[93] Wasanasuk K., Tashiro K., Hanesaka M., *et al.*, Crystal structure analysis of poly(l-lactic acid) α form on the basis of the 2-dimensional wide-angle synchrotron X-ray and neutron diffraction measurements, *Macromolecules*, vol. 44, no. 16, pp. 6441–6452, 2011, doi: 10.1021/ma2006624.

[94] Wasanasuk K. and Tashiro K., Structural regularization in the crystallization process from the glass or melt of poly(l-lactic acid) viewed from the temperature-dependent and time-resolved measurements of FTIR and wide-angle/small-angle X-ray scatterings, *Macromolecules*, vol. 44, no. 24, pp. 9650–9660, 2011, doi: 10.1021/ma2017666.

[95] Kobayashi J., Ichiki M., Asahi T., *et al.*, Optical Activity In Poly-L-Lactic Acid, *Ferroelectrics*, vol. 151, no. 1, pp. 75–84, 1994, doi: 10.1080/00150199408244725.

[96] Hoogsteen W., Postema A. R., Pennings A. J., and Brinke G., Crystal Structure , Conformation, and Morphology of Solution-Spun Poly (L-lactide) Fibers, pp. 634–642, 1990.

[97] De Santis P. and Kovacs A. J., Molecular conformation of poly(S-lactic acid), *Biopolymers*, vol. 6, no. 3, pp. 299–306, Mar. 1968, doi: 10.1002/bip.1968.360060305.

[98] Kalb B. and Pennings A. J., General crystallization behaviour of poly(l-lactic acid), *Polymer (Guildf).*, vol. 21, no. 6, pp. 607–612, 1980, doi: 10.1016/0032-3861(80)90315-8.

[99] Kazuyo D. S., Aki Sasashige T., Kanamoto T., and Hyon S. H., Preparation of oriented ß-form poly(L-lactic acid) by solid-state coextrusion: Effect of extrusion variables, *Macromolecules*, vol. 36, no. 10, pp. 3601–3605, 2003, doi: 10.1021/ma030050z.

[100] Puiggali J., Ikada Y., Tsuji H., *et al.*, The frustrated structure of poly(L-lactide), *Polymer (Guildf).*, vol. 41, no. 25, pp. 8921–8930, 2000, doi: 10.1016/S0032-3861(00)00235-4.

[101] Cartier L., Okihara T., and Lotz B., Triangular polymer single crystals: Stereocomplexes, twins, and frustrated structures, *Macromolecules*, vol. 30, no. 20, pp. 6313–6322, 1997, doi: 10.1021/ma9707998.

[102] Okihara T., Tsuji M., Kawaguchi A., *et al.*, Crystal Structure of Stereocomplex of

Poly(L-lactide) and Poly(D-lactide), *J. Macromol. Sci. Part B*, vol. 30, no. 1–2, pp. 119–140, 1991, doi: 10.1080/00222349108245788.

[103] Tsuji H., Poly(lactide) stereocomplexes: Formation, structure, properties, degradation, and applications, *Macromol. Biosci.*, vol. 5, no. 7, pp. 569–597, 2005, doi: 10.1002/mabi.200500062.

[104] Tsuji H., Poly(lactic acid) stereocomplexes: A decade of progress, *Adv. Drug Deliv. Rev.*, vol. 107, pp. 97–135, 2016, doi: 10.1016/j.addr.2016.04.017.

[105] Sarasua J. R., Arraiza A. L., Balerdi P., and Maiza I., Crystallization and thermal behaviour of optically pure polylactides and their blends, *J. Mater. Sci.*, vol. 40, no. 8, pp. 1855–1862, 2005, doi: 10.1007/s10853-005-1204-8.

[106] Hirata M. and Kimura Y., Structure and Properties of Stereocomplex-Type Poly(Lactic Acid), *Poly(Lactic Acid) Synth. Struct. Prop. Process. Appl.*, pp. 59–65, Sep. 2010, doi: 10.1002/9780470649848.ch5.

[107] Klopffer M. H. and Flaconneche B., Transport Properties of Gases in Polymers: Bibliographic Review, *Oil Gas Sci. Technol.*, vol. 56, no. 3, pp. 223–244, May 2001, doi: 10.2516/ogst:2001021.

[108] Zanotto E. D. and Mauro J. C., The glassy state of matter: Its definition and ultimate fate, *J. Non. Cryst. Solids*, vol. 471, no. June, pp. 490–495, Sep. 2017, doi: 10.1016/j.jnoncrysol.2017.05.019.

[109] Righetti M. C., Amorphous fractions of poly(lactic acid), *Adv. Polym. Sci.*, vol. 279, pp. 195–234, 2018, doi: 10.1007/12_2016_14.

[110] Chen Y., Zhao L., Pan H., *et al.*, Impact of D-isomer content on the microstructure and mechanical properties of uniaxially pre-stretched poly(lactic acid), *Polymer (Guildf).*, vol. 186, no. August 2019, p. 122022, 2020, doi: 10.1016/j.polymer.2019.122022.

[111] Razavi M. and Wang S.-Q., Why Is Crystalline Poly(lactic acid) Brittle at Room Temperature?, *Macromolecules*, vol. 52, no. 14, pp. 5429–5441, 2019, doi: 10.1021/acs.macromol.9b00595.

[112] Delpouve N., Saiter A., and Dargent E., Cooperativity length evolution during crystallization of poly(lactic acid), *Eur. Polym. J.*, vol. 47, no. 12, pp. 2414–2423, 2011, doi: 10.1016/j.eurpolymj.2011.09.027.

[113] Delpouve N., Saiter A., Mano J. F., and Dargent E., Cooperative rearranging region size in semi-crystalline poly(l-lactic acid), *Polymer (Guildf).*, vol. 49, no. 13–14, pp. 3130–3135, 2008, doi: 10.1016/j.polymer.2008.04.045.

[114] Delpouve N., Arnoult M., Saiter A., *et al.*, Evidence of two mobile amorphous phases in semicrystalline polylactide observed from calorimetric investigations, *Polym. Eng. Sci.*, vol. 54, no. 5, pp. 1144–1150, May 2014, doi: 10.1002/pen.23657.

[115] Aharoni S. M., Increased glass transition temperature in motionally constrained

semicrystalline polymers, *Polym. Adv. Technol.*, vol. 9, no. 3, pp. 169–201, 1998, doi: 10.1002/(SICI)1099-1581(199803)9:3<169::AID-PAT740>3.0.CO;2-Z.

[116] Androsch R. and Wunderlich B., The link between rigid amorphous fraction and crystal perfection in cold-crystallized poly(ethylene terephthalate), *Polymer (Guildf).*, vol. 46, no. 26, pp. 12556–12566, 2005, doi: 10.1016/j.polymer.2005.10.099.

[117] Leyva-Porras C., Cruz-Alcantar P., Espinosa-Solís V., *et al.*, Application of Differential Scanning Calorimetry (DSC) and Modulated Differential Scanning Calorimetry (MDSC) in Food and Drug Industries, *Polymers (Basel).*, vol. 12, no. 1, p. 5, Dec. 2019, doi: 10.3390/polym12010005.

[118] Kolesov I. and Androsch R., The rigid amorphous fraction of cold-crystallized polyamide 6, *Polymer (Guildf).*, vol. 53, no. 21, pp. 4770–4777, 2012, doi: 10.1016/j.polymer.2012.08.017.

[119] Zuza E., Ugartemendia J. M., Lopez A., *et al.*, Glass transition behavior and dynamic fragility in polylactides containing mobile and rigid amorphous fractions, *Polymer (Guildf).*, vol. 49, no. 20, pp. 4427–4432, 2008, doi: 10.1016/j.polymer.2008.08.012.

[120] Righetti M. C. and Tombari E., Crystalline, mobile amorphous and rigid amorphous fractions in poly(L-lactic acid) by TMDSC, *Thermochim. Acta*, vol. 522, no. 1–2, pp. 118–127, 2011, doi: 10.1016/j.tca.2010.12.024.

[121] Aliotta L., Gazzano M., Lazzeri A., and Righetti M. C., Constrained amorphous interphase in poly(l-lactic acid): Estimation of the Tensile elastic modulus, *ACS Omega*, vol. 5, no. 33, pp. 20890–20902, 2020, doi: 10.1021/acsomega.0c02330.

[122] Sato S., Nyuui T., Matsuba G., and Nagai K., Correlation between interlamellar amorphous structure and gas permeability in poly(lactic acid) films, *J. Appl. Polym. Sci.*, vol. 131, no. 16, pp. 1–6, 2014, doi: 10.1002/app.40626.

[123] Gorrasi G. and Pantani R., Hydrolysis and Biodegradation of Poly(lactic acid), in *Advances in Polymer Science*, vol. 279, M. L. Di Lorenzo and R. Androsch, Eds. Cham: Springer International Publishing, 2017, pp. 119–151.

[124] Siparsky G. L., Voorhees K. J., Dorgan J. R., and Schilling K., Water transport in polylactic acid (PLA), PLA/polycaprolactone copolymers, and PLA/polyethylene glycol blends, *J. Environ. Polym. Degrad.*, vol. 5, no. 3, pp. 125–136, 1997, doi: 10.1007/BF02763656.

[125] Gorrasi G., Anastasio R., Bassi L., and Pantani R., Barrier properties of PLA to water vapour: Effect of temperature and morphology, *Macromol. Res.*, vol. 21, no. 10, pp. 1110–1117, 2013, doi: 10.1007/s13233-013-1144-0.

[126] Tsuji H., Hydrolytic Degradation, in *Poly(Lactic Acid)*, Hoboken, NJ, USA: John Wiley & Sons, Inc., 2010, pp. 343–381.

[127] Rodriguez E., Shahbikian S., Marcos B., and Huneault M. A., Hydrolytic stability of polylactide and poly(methyl methacrylate) blends, *J. Appl. Polym. Sci.*, vol. 135, no. 11,

p. 45991, Mar. 2018, doi: 10.1002/app.45991.

[128] Chu C. C., Hydrolytic Degradation of Polyglycolic Acid Sutures., *Trans. Annu. Meet. Soc. Biomater. conjunction with Interna*, vol. 4, p. 65, 1981.

[129] Farrar D., Modelling of the degradation process for bioresorbable polymers, in *Degradation Rate of Bioresorbable Materials: Prediction and Evaluation*, F. B. T.-D. R. of B. M. Buchanan, Ed. Elsevier, 2008, pp. 183–206.

[130] Laura M., Lorenzo D., Gazzano M., *et al.*, The role of the rigid amorphous fraction on cold crystallization of poly(3-hydroxybutyrate), *Macromolecules*, vol. 45, no. 14, pp. 5684–5691, 2012, doi: 10.1021/ma3010907.

[131] Li S., Garreau H., and Vert M., Structure-property relationships in the case of the degradation of massive poly(α-hydroxy acids) in aqueous media - Part 3 Influence of the morphology of poly(l-lactic acid), *J. Mater. Sci. Mater. Med.*, vol. 1, no. 4, pp. 198–206, 1990, doi: 10.1007/BF00701077.

[132] Lazzari S., Codari F., Storti G., *et al.*, Modeling the pH-dependent PLA oligomer degradation kinetics, *Polym. Degrad. Stab.*, vol. 110, pp. 80–90, 2014, doi: 10.1016/j.polymdegradstab.2014.08.012.

[133] Burkersroda F. von, Schedl L., and Göpferich A., Why degradable polymers undergo surface erosion or bulk erosion, *Biomaterials*, vol. 23, no. 21, pp. 4221–4231, Nov. 2002, doi: 10.1016/S0142-9612(02)00170-9.

[134] Shojaei S., Nikuei M., Goodarzi V., *et al.*, Disclosing the role of surface and bulk erosion on the viscoelastic behavior of biodegradable poly(ε-caprolactone)/poly(lactic acid)/hydroxyapatite nanocomposites, *J. Appl. Polym. Sci.*, vol. 136, no. 10, pp. 1–12, 2019, doi: 10.1002/app.47151.

[135] Jung J. H., Ree M., and Kim H., Acid- and base-catalyzed hydrolyses of aliphatic polycarbonates and polyesters, *Catal. Today*, vol. 115, no. 1–4, pp. 283–287, 2006, doi: 10.1016/j.cattod.2006.02.060.

[136] Saha S. K. and Tsuji H., Effects of molecular weight and small amounts of d-lactide units on hydrolytic degradation of poly(l-lactic acid)s, *Polym. Degrad. Stab.*, vol. 91, no. 8, pp. 1665–1673, 2006, doi: 10.1016/j.polymdegradstab.2005.12.009.

[137] Han X., Pan J., Buchanan F., *et al.*, Analysis of degradation data of poly(l-lactide–co-l,d-lactide) and poly(l-lactide) obtained at elevated and physiological temperatures using mathematical models, *Acta Biomater.*, vol. 6, no. 10, pp. 3882–3889, Oct. 2010, doi: 10.1016/j.actbio.2010.05.015.

[138] Weir N. A., Buchanan F. J., Orr J. F., *et al.*, Degradation of poly-L-lactide. Part 2: Increased temperature accelerated degradation, *Proc. Inst. Mech. Eng. Part H J. Eng. Med.*, vol. 218, no. 5, pp. 321–330, 2004, doi: 10.1111/j.1467-8500.1944.tb02025.x.

[139] Buchholz B., Accelerated Degradation Test on Resorbable Polymers, in *Degradation Phenomena on Polymeric Biomaterials*, Berlin, Heidelberg: Springer Berlin

Heidelberg, 1992, pp. 67–76.

[140] Lyu S. P., Schley J., Loy B., *et al.*, Kinetics and time-temperature equivalence of polymer degradation, *Biomacromolecules*, vol. 8, no. 7, pp. 2301–2310, 2007, doi: 10.1021/bm070313n.

[141] Limsukon W., Auras R., and Selke S., Hydrolytic degradation and lifetime prediction of poly(lactic acid) modified with a multifunctional epoxy-based chain extender, *Polym. Test.*, vol. 80, no. September, p. 106108, Dec. 2019, doi: 10.1016/j.polymertesting.2019.106108.

[142] Tsuji H., Tezuka Y., and Yamada K., Alkaline and enzymatic degradation of L-lactide copolymers. II. crystallized films of poly(L-lactide-co-D-lactide) and poly(L-lactide) with similar crystallinities, *J. Polym. Sci. Part B Polym. Phys.*, vol. 43, no. 9, pp. 1064–1075, 2005, doi: 10.1002/polb.20399.

[143] Cam D., Hyon S. hyu, and Ikada Y., Degradation of high molecular weight poly(l-lactide) in alkaline medium, *Biomaterials*, vol. 16, no. 11, pp. 833–843, 1995, doi: 10.1016/0142-9612(95)94144-A.

[144] Tsuji H. and Ikada Y., Properties and Morphology of Poly (L -lactide). II.Hydrolysis in Alkaline Solution, pp. 59–66, 1997.

[145] Tsuji H. and Miyauchi S., Poly(l-lactide): VI Effects of crystallinity on enzymatic hydrolysis of poly(l-lactide) without free amorphous region, *Polym. Degrad. Stab.*, vol. 71, no. 3, pp. 415–424, Jan. 2001, doi: 10.1016/S0141-3910(00)00191-9.

[146] Tsuji H. and Miyauchi S., Poly(L-lactide): 7. Enzymatic hydrolysis of free and restricted amorphous regions in poly(L-lactide) films with different crystallinities and a fixed crystalline thickness, *Polymer (Guildf).*, vol. 42, no. 9, pp. 4463–4467, 2001, doi: 10.1016/S0032-3861(00)00792-8.

[147] Kikkawa Y., Abe H., Iwata T., *et al.*, Crystallization, stability, and enzymatic degradation of poly(L-lactide) thin film, *Biomacromolecules*, vol. 3, no. 2, pp. 350–356, 2002, doi: 10.1021/bm015623z.

[148] Kikkawa Y., Fujita M., Abe H., and Doi Y., Effect of water on the surface molecular mobility of poly(lactide) thin film: An atomic force microscopy study, *Biomacromolecules*, vol. 5, no. 4, pp. 1187–1193, 2004, doi: 10.1021/bm0345007.

[149] Tsuji H., Mizuno A., and Ikada Y., Properties and morphology of poly(L-lactide). III. Effects of initial crystallinity on long-term in vitro hydrolysis of high molecular weight poly(L-lactide) film in phosphate-buffered solution, *J. Appl. Polym. Sci.*, vol. 77, no. 7, pp. 1452–1464, 2000, doi: 10.1002/1097-4628(20000815)77:7<1452::AID-APP7>3.0.CO;2-S.

[150] del Río J., Etxeberria A., López-Rodríguez N., *et al.*, A PALS Contribution to the Supramolecular Structure of Poly(L-lactide), *Macromolecules*, vol. 43, no. 10, pp. 4698–4707, May 2010, doi: 10.1021/ma902247y.

[151] Duek E. A. R., Zavaglia C. A. C., and Belangero W. D., In vitro study of poly(lactic acid) pin degradation, *Polymer (Guildf).*, vol. 40, no. 23, pp. 6465–6473, 1999, doi: 10.1016/S0032-3861(98)00846-5.

[152] Tsuji H., In vitro hydrolysis of blends from enantiomeric poly(lactide)s Part 1. Well-stereo-complexed blend and non-blended films, *Polymer (Guildf).*, vol. 41, no. 10, pp. 3621–3630, May 2000, doi: 10.1016/S0032-3861(99)00545-5.

[153] Harris A. M. and Lee E. C., Heat and humidity performance of injection molded PLA for durable applications, *J. Appl. Polym. Sci.*, vol. 115, no. 3, pp. 1380–1389, Feb. 2010, doi: 10.1002/app.30815.

[154] Gorrasi G. and Pantani R., Effect of PLA grades and morphologies on hydrolytic degradation at composting temperature: Assessment of structural modification and kinetic parameters, *Polym. Degrad. Stab.*, vol. 98, no. 5, pp. 1006–1014, 2013, doi: 10.1016/j.polymdegradstab.2013.02.005.

[155] Rodriguez E. J., Marcos B., and Huneault M. A., Hydrolysis of polylactide in aqueous media, *J. Appl. Polym. Sci.*, vol. 133, no. 44, pp. 1–11, 2016, doi: 10.1002/app.44152.

[156] Zhang N., Yu X., Duan J., *et al.*, Comparison study of hydrolytic degradation behaviors between α'- and α-poly(l -lactide), *Polym. Degrad. Stab.*, vol. 148, pp. 1–9, Feb. 2018, doi: 10.1016/j.polymdegradstab.2017.12.014.

[157] Tsuji H. and Ikada Y., Properties and morphology of poly(L-lactide): IV. Effects of structural parameters on long-term hydrolysis of poly(L-lactide) in phosphate-buffered solution, *Polym. Degrad. Stab.*, vol. 67, no. 1, pp. 179–189, 2000, doi: 10.1016/S0141-3910(99)00111-1.

[158] Tsuji H. and Nakahara K., Poly(L-lactide): IX. Hydrolysis in acid media, *J. Appl. Polym. Sci.*, vol. 86, no. 1, pp. 186–194, 2002, doi: 10.1002/app.10813.

[159] Tsuji H., In vitro hydrolysis of blends from enantiomeric poly(lactide)s. Part 4: well-homo-crystallized blend and nonblended films, *Biomaterials*, vol. 24, no. 4, pp. 537–547, 2003, doi: 10.1016/s0142-9612(02)00365-4.

[160] Huang Y., Chen F., Pan Y., *et al.*, Effect of hydrophobic fluoropolymer and crystallinity on the hydrolytic degradation of poly(lactic acid), *Eur. Polym. J.*, vol. 97, pp. 308–318, 2017, doi: 10.1016/j.eurpolymj.2017.09.044.

[161] Ramkrishna D. and Singh M. R., Population Balance Modeling : Current Status and Future Prospects Population Balance Modeling : Current Status and Future Prospects, no. March, 2014, doi: 10.1146/annurev-chembioeng-060713-040241.

[162] Solsvik J. and Jakobsen H. A., The Foundation of the Population Balance Equation: A Review, *J. Dispers. Sci. Technol.*, vol. 36, no. 4, pp. 510–520, 2015, doi: 10.1080/01932691.2014.909318.

[163] Ramkrishna D. and Mahoney A. W., Population balance modeling. Promise for the future, *Chem. Eng. Sci.*, vol. 57, no. 4, pp. 595–606, 2002, doi: 10.1016/S0009-

2509(01)00386-4.

[164] Nopens I., Torfs E., Ducoste J., *et al.*, Population balance models: A useful complementary modelling framework for future WWTP modelling, *Water Sci. Technol.*, vol. 71, no. 2, pp. 159–167, 2015, doi: 10.2166/wst.2014.500.

[165] Lin S., Yu W., Wang X., and Zhou C., Study on the thermal degradation kinetics of biodegradable poly(propylene carbonate) during melt processing by population balance model and rheology, *Ind. Eng. Chem. Res.*, vol. 53, no. 48, pp. 18411–18419, 2014, doi: 10.1021/ie404049v.

[166] Ahmad W., Kuitunen S., Sixta H., and Alopaeus V., Population balance based modeling of changes in cellulose molecular weight distribution during ageing, *Cellulose*, vol. 22, no. 1, pp. 151–163, 2015, doi: 10.1007/s10570-014-0529-3.

[167] Yeoh G. H., Cheung C. P., and Tu J., Population Balance Approach—A Generic Framework, *Multiph. Flow Anal. Using Popul. Balanc. Model.*, pp. 69–90, 2014, doi: 10.1016/b978-0-08-098229-8.00003-6.

[168] Mehta K. and Madras G., Dynamics of molecular weight distributions for polymer scission, *AIChE J.*, vol. 47, no. 11, pp. 2539–2547, 2001, doi: 10.1002/aic.690471116.

[169] Kostoglou M., Mathematical analysis of polymer degradation with chain-end scission, *Chem. Eng. Sci.*, vol. 55, no. 13, pp. 2507–2513, 2000, doi: 10.1016/S0009-2509(99)00471-6.

CHAPTER 3: EFFECTS OF THE THREE-PHASE CRYSTALLIZATION BEHAVIOR ON THE HYDROLYSIS OF AMORPHOUS AND SEMICRYSTALLINE POLY(LACTIC ACID)S

3.1 Abstract

The hydrolysis of poly(lactic acid)—PLA—was investigated considering the changes in the three-phase model structures, the mobile amorphous (MAF), crystalline (CF), and rigid amorphous fractions (RAF). Amorphous PLA films with different L-lactide were crystallized by cold-crystallization and melt-stretching crystallization to promote the three-phase structural variation in the PLA films. The changes in the phase structure and molecular weight during hydrolysis were investigated. As a result, PLA with higher CF exhibited a slower hydrolysis rate due to limited water diffusion into the crystalline structure. Conversely, the sample with a higher amount of RAF accelerated hydrolysis, influenced by increased water diffusion and a greater presence of hydrophilic end groups. The distinct structure of the nano-confined crystals from the melt-stretching method could limit the diffusion of water molecules into the PLA film and accordingly more stability to the hydrolysis.

3.2 Introduction

Poly(lactic acid) (PLA), a major bio-based and biodegradable commercial polymer, is known to undergo hydrolytic degradation under high humidity and water immersion, leading to a decrease in the molecular weight and deterioration of its properties [1,2]. Water molecules can diffuse into the PLA matrix, causing cleavage of the ester linkages and yielding shorter chains with the presence of two hydrophilic chain end groups, carboxylic and hydroxylic groups [2]. The increase in the concentration of carboxylic groups can result in an acidic environment and contribute to the autocatalytic hydrolytic effect [2–4]. Hydrolysis of PLA occurs predominantly in the amorphous regions compared with the crystalline regions.

During hydrolysis, the water molecules, acting as plasticizers, can enhance the extra mobility of the amorphous chains to rearrange them into higher-ordered structures. The water molecules are unable to penetrate the crystalline region, which remains non-hydrolyzed during the degradation process [5,6]. The hydrolysis of crystalline residue can occur at the late stage of hydrolysis leading to a decrease in the crystalline thickness and the changes at the fold surface observed by the gradual decrease in the melting temperature of the crystallites [7,8].

Overall, crystallinity is one of the most significant parameters affecting the hydrolysis of PLA. The crystallites are the non-permeable region forcing water molecules to diffuse through a tortuous path, which decreases the effective diffusion coefficient, therefore reducing the rate of hydrolysis above the glass transition temperature (T_g) [9–11]. In contrast, Tsuji and coworkers [12–14] studied the effect of PLA films with different crystallinities on the hydrolysis of PLA in phosphate-buffered solutions below T_g and found that the hydrolysis rate increases with an increase in the initial crystallinity. They attributed this effect to the accumulation of hydrophilic terminal groups in the RAF region, which resulted from the rearranging of the crystal chains in the crystalline region. Similar results were also found by Huang et al. [15], who reported a higher hydrolytic rate of those PLA samples below T_g and crystallized by annealing at 90–120 °C when compared with the amorphous PLA.

PLA can crystallize in the $\alpha, \delta, \beta,$ and γ crystalline forms, including the mesophase form obtained under specific crystallization conditions [16–19]. The ordered α form and the less ordered δ form—previously known as the α' form—can develop under normal conditions such as cold- and melt-crystallization [20]. The crystal formation process during hydrolytic degradation has been reported by some authors [19,21]. Zhang et al. [21] studied the

morphological changes of PLA during immersion in water at 60 °C and found that the α crystals were formed in the hydrolysis. However, in their study, the δ form was not differentiated from the α form. Chen et al. [19] reported the presence of the δ form during the hydrolysis of PLA in NaOH solution (pH 13) at 60 °C. In hydrolytic degradation in organic solvents (acetone and water-ethanol solutions at 40 °C), the formation of α crystals was found during the solvent-induced crystallization [22,23].

Evidence of the three-phase model, the crystalline fraction (CF), the mobile amorphous fraction (MAF), and the restricted or rigid amorphous fraction (RAF), has been reported in semicrystalline PLA. The RAF results from the restrictions of amorphous chain mobility due to the fixation to the basal plane of the crystalline lamellae [24–27]. The formation of the RAF depends on the nature of the polymer and the crystallization conditions. The RAF has specific properties, which affect the mechanical and barrier properties of PLA [26,28]. However, the effect of RAF on the hydrolytic degradation of PLA is still unclear and barely explored, requiring further experiments to elucidate its role in PLA hydrolytic degradation.

As well as the three-phase structure of PLA, the optical purity or the L-lactide content can affect the material thermomechanical properties, especially the crystallization rate. The presence of D-lactide content can act as the stereodefect incorporated into crystalline and amorphous regions, reducing the final degree of crystallinity and crystallization kinetics [29–31]. Thus, this work aimed to investigate the development and effects of the three-phase structure of PLA (i.e., MAF, RAF, and CF) during hydrolytic degradation in water at 85 °C. Physical and morphological characteristics of the two commercial PLA grades (with different L-lactide content) extruded as films and crystallized by the two crystallization methods, cold-crystallization and melt-stretching crystallization, were investigated using modulated

differential scanning calorimetry (MDSC), wide angle X-ray diffraction, scanning electron microscopy, and size exclusion chromatography to correlate with the hydrolytic processes.

3.3 Experimental section

3.3.1 Materials and Sample Preparation

Two commercial PLA resins, Ingeo™2003D thermoplastic extrusion-grade resin with L-lactic acid content of 95.7% (PLAL) and Ingeo™6201D thermoplastic fiber-grade resin with the L-lactic acid content of 98.6% (PLAH), were provided by NatureWorks LLC (Minnetonka, MN, USA). PLA resins were dried at 50 °C for 12 h in a vacuum oven and then processed in a Microextruder model RCP-0625 (Randcastle Extrusion Systems, Inc., Cedar Grove, NJ, USA) with a screw diameter of 1.5875 cm, screw L/D of 24/1, and volume of 34 cm^3 using a temperature profile of 195–210 °C. The films were subsequently crystallized by cold-crystallization (PLA–CC) and melt stretching crystallization (PLA–NC) methods. The cold-crystallized PLA samples were prepared by annealing in an oven at 120 °C for 4 h. The melt-stretched samples were prepared by uniaxial melt-stretching with the rate of V/L_0 = 2 min^{-1} at 75 °C to a draw ratio of L/L_0 = 3.5, where V (mm min^{-1}) is the crosshead speed, and L_0 and L (mm) are the initial and final length of the film before and after melt-stretching. The films were subsequently held under constraint for 15 minutes at 75 °C which was 15 °C above the T_g to avoid the large spherulites that occur in the cold-crystallization above 90 °C and 80 °C for PLAL and PLAH, respectively (**Figure A3.2**, Appendix 3B). The melt-stretched PLA was recently developed to enhance mechanical properties and thermal stability by creating nano-sized crystals while preserving the entanglement network; details about the melt-stretched procedure were previously described [32,33]. The sample nomenclature and the final thicknesses of each sample used in this study are listed in **Table 3.1**.

Table 3.1 Sample Nomenclature and Crystallization Methods.

Code	PLA grade (%l-lactide)	Crystallization method	Thickness, mm
PLAL–CT	2003D (95.7%)	None	0.027 ± 0.003
PLAH–CT	6201D (98.6%)	None	0.029 ± 0.001
PLAL–CC	2003D (95.7%)	Cold-crystallization	0.028 ± 0.001
PLAH–CC	6201D (98.6%)	Cold-crystallization	0.030 ± 0.002
PLAL–NC	2003D (95.7%)	Melt-stretching crystallization	0.028 ± 0.001
PLAH–NC	6201D (98.6%)	Melt-stretching crystallization	0.026 ± 0.002

3.3.2 Hydrolysis Experiments

The hydrolysis test method adapted from ASTM D4754–18 [34] was run under an unbuffered condition in water at 85 °C. The hydrolysis cell consists of a glass vial with a cap, a stainless-steel wire, and glass beads. Sample films were cut into 2-cm diameter circles, threaded into the wire with alternating glass beads, and stored in the vial filled with 35 mL of water. Three replicates of each sample were collected and dried before analysis. The pH of the hydrolysis medium was tracked as a function of time using a SevenCompact™ pH/Ion S220 meter equipped with an InLab® Versatile Pro electrode (Mettler-Toledo, Schwerzenbach, Switzerland).

3.3.3 Scanning Electron Microscopy (SEM)

The amorphous structure of the PLA films was etched in a water-methanol (1:2 by volume) solution containing 0.025 mol/L of sodium hydroxide, at 25 °C for 48 h. The etched films were then sputtered with iridium under vacuum. The specimens were observed with a JEOL 7500F scanning electron microscope (JEOL Ltd., Tokyo, Japan). The microscope is equipped with a high-sensitivity secondary electron imaging (SEI) detector operating at a voltage of 3 kV.

3.3.4 Modulated Differential Scanning Calorimetry (MDSC)

Thermal analysis studies were carried out using a differential scanning calorimeter (DSC) (DSC Q100, TA Instruments, New Castle, DE, USA), with the refrigerated cooling system under nitrogen flow of 70 mL min^{-1}. The instrument was calibrated with indium and sapphire standards for the heat flow/temperature and the specific heat capacity, respectively. Samples weighing 5–10 mg were packed and sealed in a standard aluminum pan. The MDSC was performed under the heat-only condition with an oscillation amplitude of 0.318 K, an oscillation period of 60 s, and an underlying heating rate of 1 °C min^{-1}. The MDSC thermograms reported are those of heat capacity (C_p), total heat flow (HF), reversing heat flow, and nonreversing heat flow. T_g was determined as the midpoint of the reversing heat capacity change during the transition. The cold crystallization temperature (T_c) was determined at the exothermic crystallization peak of the nonreversing heat flow. The melting temperature (T_m) was obtained from the endothermic melting peak of the total heat flow.

According to the three-phase model of semicrystalline PLA, the degree of crystallinity (X_C), the mobile amorphous fraction (X_{MAF}), and the rigid amorphous fraction (X_{RAF}) can be determined by the following equations, respectively:

$$X_C = \frac{\Delta H_f - \sum \Delta H_c}{\Delta H_f^0} \tag{3.1}$$

where ΔH_f is the enthalpy of fusion from the integration of the heat flow in the melting region, $\sum \Delta H_c$ is the sum of the exothermic peak enthalpies, and ΔH_f^0 is the calculated fusion enthalpy of 100% crystalline PLA, which is equal to 93.1 J g^{-1} [35]. For clarification, the difference ΔH_f^0 values used in Eq. (3.1) could provide the different degree of crystallinity of PLA.

$$X_{MAF} = \frac{\Delta C_p}{\Delta C_p^0} \tag{3.2}$$

$$X_{RAF} = 1 - X_{MAF} - X_c \quad (3.3)$$

where ΔC_p is the measured heat capacity increment at T_g of the sample, and ΔC_p^0 is the heat capacity increment of a 100% amorphous PLA, which was carefully measured from the PLA film treated by fast cooling from the melting state and a value of 0.527 J g-1 °C^{-1} can be proposed.

3.3.5 Size Exclusion Chromatography (SEC)

The weight average and number average molecular weights (M_w and M_n) and molecular weight distribution (MWD) were measured using an SEC system from Waters (Milford, MA, USA) equipped with an isocratic pump (Waters 1515), an autosampler (Waters 717), a refractive index detector (Waters 2414), and a series of Styragel® GPC columns (Styragel® HR-4/HR-3/HR-2), with a controlled temperature of 35 °C and a flow rate of 1 mL min^{-1}. Tetrahydrofuran (THF) was used as the mobile phase solvent. The Mark-Houwink constants (K and α values) of PLA in THF at 35 °C obtained from the values of the PS standard were 0.0174 mL g^{-1} and 0.736, respectively. The M_w, M_n and MWD were analyzed using the Waters Breeze™ 2 software.

3.3.6 Wide angle X-ray diffraction (WAXD)

Analysis of the wide-angle diffraction was conducted on a Bruker AXS D8 Advance X-ray diffractometer (Bruker Co., Billerica, MA, USA) equipped with a Global Mirror Filter Cu Kα radiation source operating at 40 kV 100 mA. The diffractogram was recorded between a 2θ range from 2 ° and 40 ° at a rate of 0.24 ° min^{-1} and an increment of 0.01 °.

3.3.7 Hydrolytic Degradation Mathematical Modeling.

To estimate the rate of hydrolytic degradation, the molecular weight and crystallinity of the samples were fitted using the phenomenological model proposed by Pan and coworkers [36–40]. The model was simplified to consider only the rate constant of autocatalytic

degradation. It was assumed that only the –COOH chain ends of the short chains can promote hydrolytic degradation. The rate of autocatalytic hydrolytic can be defined by:

$$\frac{\mathrm{d}r_s}{\mathrm{d}t} = k_{\mathrm{deg}} c_E {c_{ol}}^{0.5} \tag{3.4}$$

where r_s (mol m^{-3}) is the total number of chain scissions per unit volume of the amorphous polymer, k_{deg} ([mol^{-1} m^3]0.5 h^{-1}) is the rate of autocatalytic hydrolytic degradation, c_E (mol m^{-3}) is the total number of ester units of all the long chains per unit volume, c_{ol} (mol m^{-3}) is the total number of ester units of the short chains which act as the catalyst, and t (h) is the hydrolysis time. In general, hydrolytic degradation dominantly occurs in the amorphous regions where the polymer chains are much more susceptible to hydrolysis than those in the crystalline region. Therefore, the total number of chain scissions per unit volume in the amorphous phase of semicrystalline polymer (R_s) then becomes:

$$\frac{\mathrm{d}R_s}{\mathrm{d}t} = (1 - X_C)\frac{\mathrm{d}r_s}{\mathrm{d}t} = k_{\mathrm{deg}} C_E \left(\frac{C_{ol}}{1 - X_C}\right)^{0.5} \tag{3.5}$$

where C_E (mol m^{-3}) is the total number of ester units of all the long chains per unit volume of the semicrystalline polymer, and C_{ol} (mol m^{-3}) is the total number of ester units of the short chains per unit volume of the semicrystalline polymer. C_E can be determined as:

$$C_E = C_{E_0} - C_{ol} - \omega\,(X_C - X_{C_0}) \tag{3.6}$$

where C_{E_0} (mol m^{-3}) is the initial number of ester units in the amorphous phase at the beginning of hydrolysis calculated using the initial molecular weight (g mol^{-1}) and the density of MAF and RAF (1.24 and 1.11 g cm^{-3}, respectively), and ω (mol m^{-3}) is the total number of ester units of crystalline phase per unit volume using the density of CF (1.26 g cm^{-3}) [41]. To estimate C_{ol}, the empirical relation between the production of the short chains and the chain scission can be determined as:

$$C_{ol}=C_{E_0}\cdot\alpha\cdot\left(\frac{R_s}{C_{E_0}}\right)^{\beta} \tag{3.7}$$

where α and β are dimensionless parameters indicating the nature of the chain scission of the hydrolysis reaction, which can be adjusted to describe the probability of the chain scission to produce oligomers. Based on the authors' previous work[42] and for simplicity, α and β can be set as 0.4 and 1, respectively, which means one short chain is achieved after ten chain scissions occur, as cited in Sevim and Pan [37] and Han et al. [40]. By replacing (3.6) and (3.7) into (3.5), we obtain:

$$\frac{\mathrm{d}\bar{R}}{\mathrm{d}t}=\left[1-\alpha(\bar{R}_s)^{\beta}-\bar{\omega}\left(X_C-X_{C_0}\right)\right]\left\{k_{deg}\left[C_{E_0}\cdot\alpha(\bar{R}_s)^{\beta}\cdot\left(\frac{1}{1-X_C}\right)\right]^{0.5}\right\} \tag{3.8}$$

where the normalized forms of R_s and ω can be expressed as:

$$\bar{R}_s=\frac{R_s}{C_{E_0}}\ and\ \bar{\omega}=\frac{\omega}{C_{E_0}} \tag{3.9}$$

The average molecular weight of the sample can be assessed by quantifying the weight of all chains in both amorphous and crystalline regions. During hydrolysis, the number of overall chains increases by the number of chain scissions excluding the small oligomers, which can be soluble in the hydrolysis media. The molecular weights of the hydrolyzed sample can be calculated from:

$$M_n=\left(\frac{\left(C_{E_0}+\omega X_{C_0}-C_{ol}\right)M_0}{N_{chain_0}+R_s-\left(\frac{C_{ol}}{m}\right)}\right)=\left(\frac{\left(C_{E_0}+\omega X_{C_0}-\alpha C_{E_0}\left(\frac{R_s}{C_{E_0}}\right)^{\beta}\right)M_0}{N_{chain_0}+R_s-\left(\frac{\alpha}{m}C_{E_0}\left(\frac{R_s}{C_{E_0}}\right)^{\beta}\right)}\right) \tag{3.10}$$

M_n in normalized form can be expressed as:

$$\bar{M}_n=\frac{M_n}{M_{n\,0}}=\left(\frac{1+\bar{\omega}X_{C_0}-\alpha(\bar{R}_s)^{\beta}}{(1+\bar{\omega}X_{C_0})\left[1+\frac{C_{E_0}}{N_{chain0}}\left(\bar{R}_s-\frac{\alpha}{m}(\bar{R}_s)^{\beta}\right)\right]}\right) \tag{3.11}$$

where M_{n0} and M_n (g mol^{-1}) are the initial and time-dependent molecular weight, respectively, M_0 (g mol^{-1}) is the molecular weight of the repeating unit of PLA, and N_{chain0} (mol m^{-3}) is the number of all chains (CF, MAF, and RAF) in the unit volume assessed from the density of each fraction and the initial molecular weight. The rate of autocatalytic hydrolytic degradation, k_{deg}, was estimated using MATLAB® R2019b (MathWorks, Natick, MA, USA) and converted to $\overline{k}_{deg}$ expressed in the units of reciprocal time (h^{-1}).

$$\overline{k}_{deg} = {C_{E_0}}^{0.5} k_{deg} \tag{3.12}$$

3.4 Results and discussion

Figure 3.1 shows sequential images over time of the visual appearance of the PLA films with two different L-lactide contents and crystallization methods during the hydrolysis experiment. The non-crystallized PLA (i.e., PLAL–CT and PLAH–CT) was initially transparent before hydrolysis, then became opaque white within 8 h due to the fast formation of crystals at the early stage. The cold-crystallized films (i.e., PLAL–CC and PLAH–CC) were initially translucent and gradually turned white, after approximately 36 h. On the other hand, the melt-stretching crystallized films (i.e., PLAL–NC and PLAH–NC) remained transparent during the entire hydrolysis. The effect of the crystalline morphology of PLA films on the transparency was evaluated by the transmittance of UV-visible light in the range of 200–800 nm. **Figure A3.1**, Appendix 3A, provides the transmittance values of the initial amorphous and semicrystalline films obtained by the 8-h hydrolysis, cold-crystallization, and melt-stretching crystallization, with X_C values of approximately 0.30–0.33 for PLAL and 0.45–0.50 for PLAH. In general, the formation of crystalline phases provides a higher optical density, affecting the increase of the refractive index and decreasing the speed of light through the crystals. Differences in the refractive index in the film matrix can cause light scattering and reduce the amount of light transmitted through the films [43]. The

transmittance of amorphous PLA films at a reference wavelength of 600 nm was approximately 92% (**Figures A3.1a, b**, 0h). After cold-crystallization, transmittance of PLAL–CC with X_C = 0.31 and PLAH–CC with X_C = 0.50 was reduced to 74% and 54%, respectively (**Figures A3.1c**, **d**, 0h). After hydrolysis for 8 h, PLAL–CT and PLAH–CT were found to have X_C values similar to those of PLAL–CC and PLAH–CC films at 0 h; however, the crystals formed during hydrolysis dramatically reduced the transmittance to 9% and 2%, respectively, (**Figures A3.1a, b**, 8h) due to the inhomogeneities and size of the crystals forming during hydrolysis [44]. For PLAL–NC and PLAH–NC, the crystalline domain did not significantly affect the transparency of the films, due to the small size and the randomly dispersed crystals (**Figures A3.1e**, **f**, 0h). This indicates that the dimensions of the crystals of PLA films obtained from melt-stretching crystallization could be smaller than half the wavelength of visible light (400–800 nm) [32,43].

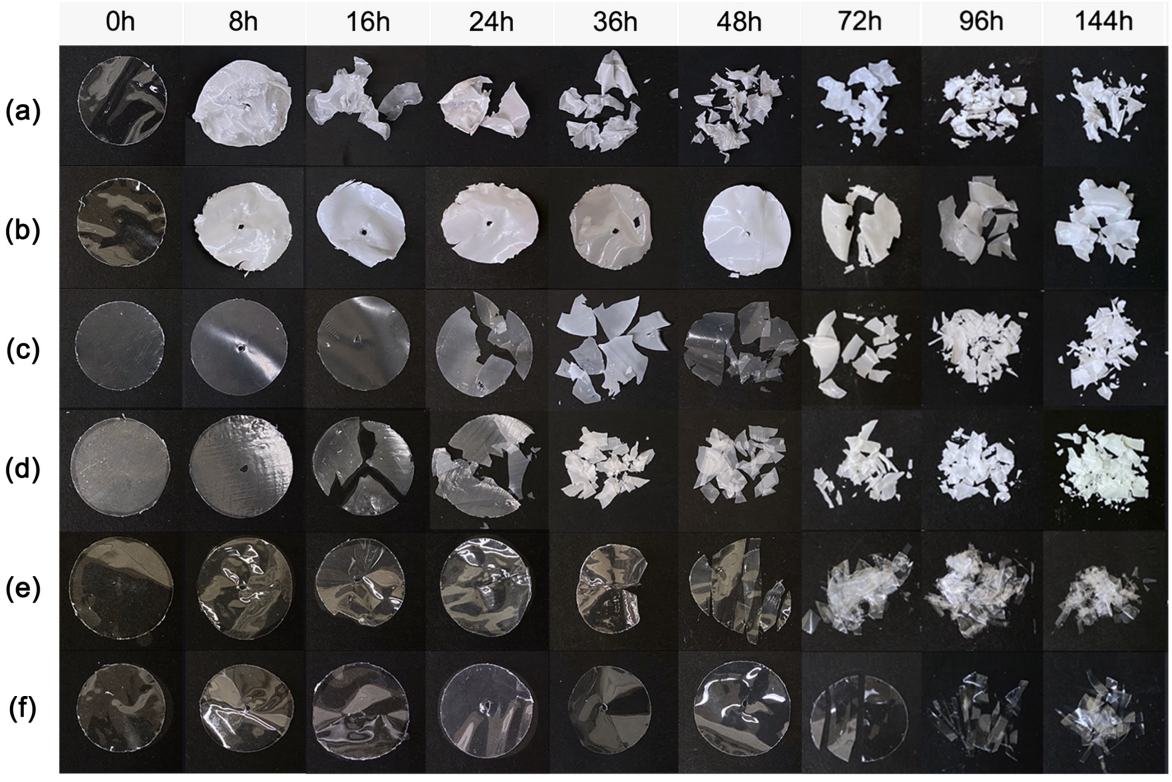

Figure 3.1 Visual appearance of PLA films during hydrolytic degradation: (a) PLAL–CT, (b) PLAH–CT, (c) PLAL–CC, (d) PLAH–CC, (e) PLAL–NC, and (f) PLAH–NC.

The crystal structure of PLA films was examined by SEM before and at 24 h of hydrolysis after chemically etching the film surface to partially remove the amorphous region outside of the spherulite (**Figure 3.2**). For PLAL–CT and PLAH–CT (**Figure 3.2a**, **b**), no crystalline structure was observed in the films at 0 h. The films exhibited only rough surfaces and some shallow hollows from the surface etching. After 24 h of hydrolysis, crystalline structures were formed, substituting the amorphous structure. Cold-crystallization samples, PLAL–CC and PLAH–CC (**Figure 3.2c**, **d**) show that the large spherulites developed radially before hydrolysis and became more tightly packed after hydrolysis. For PLAL–NC and PLAH–NC (**Figure 3.2e**, **f**) a crystalline structure could not be detected under SEM imaging, showing only a flat and smooth surface at 0 and 24 h of hydrolysis. This result also indicates that PLAL–NC and PLAH–NC had more resistance to surface erosion compared with the other samples.

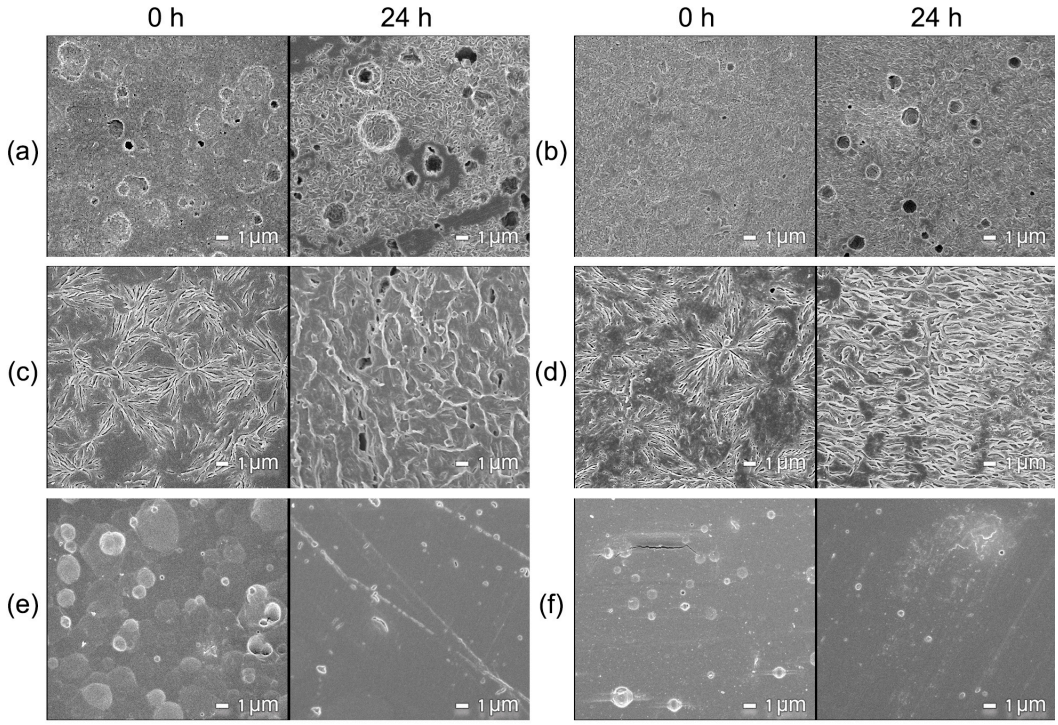

Figure 3.2 Surface crystalline morphology of PLA films by SEM with 4000X magnification after hydrolysis for 0 and 24 h: (a) PLAL–CT, (b) PLAH–CT, (c) PLAL–CC, (d) PLAH–CC, (e) PLAL–NC, and (f) PLAH–NC.

Figure 3.3 shows the MDSC heat flow thermograms at the melting temperature range of the PLA films during hydrolysis. The total heat flow (**Figure 3.3-I**) was separated into two components: the reversing (**Figure 3.3-II**) and nonreversing (**Figure 3.3-III**) heat flows. **Table 3.2** summarizes the thermal properties of PLA samples before the hydrolysis experiment, obtained from the entire temperature range of MDSC thermograms of the PLA films (as shown in **Figure A3.2**, Appendix 3B). WAXD analysis at the hydrolysis time of 0, 24, and 48 h (until samples could be collected) was further performed to identify the crystal modifications of PLA films. The non-crystallized PLA films with different L-lactide contents, PLAL–CT and PLAH–CT, had similar T_g values in the range of 58–59 °C. The T_{cc} of PLAL–CT (99.3 °C) was higher than the T_{cc} of PLAH–CT (94.1 °C) since PLA with higher L-lactide content crystallizes at a lower temperature, while the T_m range of PLAL–CT was 145–155 °C and that of PLAH–CT was 150–175 °C. The difference in the range of melting temperature was attributed to the D-lactide content since a higher amount of D-lactide decreases the averaged L-lactide unit sequence length and decreases the final lamellae thickness and the thermal stability of the crystals. Therefore, the T_m values of PLA shift to a lower temperature range with increasing D-lactide content [31,45]. The multiple melting behavior was observed from non-isothermal crystallization of amorphous films and isothermal crystallization of crystalline films. The T_m peaks of PLAL–CT (**Figure 3.3a**) were observed as a double endotherm at 146.4 and 155.3 °C, denoted as the low-melting peak temperature T_{m1} and the high-melting peak temperature T_{m2}, with no recrystallization peak observed in the nonreversing heat flow. The corresponding WAXD profiles of PLAL–CT in **Figure 3.4**a indicate that the double melting peaks were not due to the presence of polymorphism since only α crystals were observed at this stage. After hydrolysis at 8–16 h, the T_{m2} peak developed primarily while the T_{m1} peak was less evident. The T_{m2} shifted to the lower temperature and

subsequently overlapped with the T_{m1} at the hydrolysis of 24 h. The T_m peaks eventually merged into one peak located at around T_{m1} (146.7 °C), which corresponded to the T_m of the hydrolyzed crystalline residue inducing the decrease of lamellar thickness at the end of hydrolysis. **Figure 3.4a** shows the formation of sharp peaks at 2θ = 14.8°, 16.7°, 19.1°, and 22.3°, corresponding to the plane reflection of the α crystals of (010/104), (110/200), (014/203), and (015), respectively [16,46,47]. For PLAH–CT (**Figure 3.3b**), an exothermic peak was visible at about 152.0 °C prior to the T_m peaks of 170.3 °C, indicating the transition of the δ to α forms, called "the disorder-to-order (δ-to-α)" transition [20]. The overlapping of the T_{m1} of the δ crystal and recrystallization peak can be observed in the reversing and nonreversing heat flow curves, respectively. This corresponds to the WAXD profile of PLAH–CT (**Figure 3.4b**) exhibiting two additional prominent diffraction peaks at 2θ = 16.5° and 18.9°. These peaks are close to the plane reflections of the α and δ of (110/200) and (203), indicating that coexistence of the α and δ crystals occurred during non-isothermal crystallization. During hydrolysis, the δ-to-α transitions were detected. T_{m1} and its recrystallization peaks were shifted to the higher temperature, indicating that the δ crystals reorganized to the more ordered and stable structures. The T_{m2} remained nearly constant up to 48 h. The decrease of T_{m2} was clearly apparent after the hydrolysis of 144 h, at approximately 160 °C (data not shown) due to the partial melting of pre-existing α crystals. By comparing the two amorphous films, PLA with the higher L-lactide content could be more favorable to form δ crystals, especially at the lower crystallization temperature, while α crystals could be observed in PLA with the lower L-lactide content and the higher L-lactide content at higher crystallization temperature [20,48]. Androsch et al. [49] concluded that the maximum growth rate of the different crystal forms is changing as a function of D-lactide content, while a full description of this behavior has not yet been identified.

For the cold-crystallized samples, the T_g was slightly increased with increasing crystallinity. The T_{cc} peaks were absent, while the T_m peaks of PLAL–CC and PLAH–CC (**Figure 3.3c**, **d**) were found at 153.3 °C and 168.6/172.0 °C, respectively. WAXD profiles (**Figure 3.4c**, **d**) show the formation of α crystals from the initial films crystallized by the cold crystallization. During hydrolysis, the T_m peaks of PLAL–CC were found at 152.6 °C and 157.2 °C, which can be observed as a shoulder on the high-temperature side. T_{m2} became more pronounced at 16–24 h. These α crystals were more stable compared with the pre-existing crystals in the initial films. The T_{m2} peaks were merged and shifted to a lower temperature at the late stage of hydrolysis. For PLAH–CC (**Figure 3.3d**), the double melting peaks at the beginning of hydrolysis could be attributed to the presence of different lamellar thickness in the film or the melting–recrystallization–remelting process during the heating scan [50]. The partial degradation of the crystals of PLAH–CC was found at hydrolysis for 16 h, which was attributed to the decrease in lamella thickness. The small amount of δ crystals formed during hydrolysis of PLAH–CC (**Figure 3.4d**) was detected by a slight shifting of the plane reflection of (110/200) and (014/203) towards lower diffraction angles, although the shifting is not clearly visible in **Figure 3.4d**. For PLAL–NC and PLAH–NC, the T_g values shifted to higher temperatures of 67.1 and 69.8 °C, respectively – **Table 3.2**. The high T_g could be associated with the constrained MAF of the PLA film crystallized under certain conditions. It has been reported that a higher T_g of MAF could be found from crystallization at low temperature [24] and the orientation to a more ordered structure after uniaxially pre-stretching [51]. The T_m peaks of PLAL–NC and PLAH–NC were detected at 151.6 °C and 165.5/169.9 °C (**Figure 3.3e, f**). The T_m peak of PLAL–NC shifted toward the high temperature, indicating a change in crystalline thickness with the higher thermal stability during hydrolysis. Like PLAH–CC, the double melting peaks of PLAH–NC could be due to

the difference in crystal thickness. However, T_{m1} of PLAH–NC was more pronounced and shifted to the high temperature. The crystallization behavior of PLAL–NC and PLAH–NC requires further WAXD analysis. The diffraction profiles exhibit only one broad reflection at 2θ = 16.4° of (110/200) reflections (**Figure 3.4e, f**). This diffraction peak could refer to the other disordered forms of α, previously reported as α'' form by Marubayashi et al. [52] and as α' (δ) form by Takasaki et al. [53], which has loose chain packing and lower crystal density compared with the α form. Xu et al. [54] also reported that the broad dispersing diffraction peak could be obtained from the small and dispersed crystals in the film structures. These small crystals were crystallized through a transformation of the mesophase and confined in the chain network during the melt-stretching crystallization. **Figure A3.3**, Appendix 3C, shows the deconvolution of the WAXD profiles of PLAL–NC and PLAH–NC as the three components, namely, amorphous phase, crystalline phase, and mesophase. After hydrolysis, the diffraction peaks around 2θ = 16.4° slightly shifted to 2θ = 16.5°, indicating the slight increase of more ordered forms (the α or δ forms) during the hydrolysis matching the description from the MDSC to a higher T_m.

The content of the three-phase structures, X_C, X_{RAF}, and X_{MAF}, was calculated using Eqs. (3.1–3.3). The initial weight fraction values are summarized in **Table 3.2**. PLAL–CT and PLAH–CT films were initially amorphous. After the crystallization process, the total attainable crystallinity for PLAL (–CC and –NC) and PLAH (–CC and –NC) samples were around 29–33% and 50–43%, respectively, which increased with increasing optical purity of L-lactide content in the PLA matrix [55]. On the other hand, the X_C obtained from WAXD provided the overestimated values of 47–41% and 59–47% for PLAL (–CC and –NC) and PLAH (–CC and –NC), respectively. In this study, we used only the X_C obtained from MDSC to assess the fraction of the three-phase structure. The X_{RAF} values of PLAL–CC and PLAH–

CC (approximately 15%) were higher than those of PLAL–NC and PLAH–NC (approximately 2%). The specific *RAF* values ($RAF_{sp} = X_{RAF} / X_C$) were 52% for PLA–LCC, 32% for PLAH–CC, and approximately 6% for PLAL–NC and PLAH–NC. This finding indicates that the thicker RAF layers at the top and bottom of the basal planes of lamellar stacks of PLAL–CC and PLAH–CC referred to a higher degree of constraint and more defective crystals in the RAF compared with the thin layer RAF of PLA – NC [56,57].

Table 3.2 Thermal Properties Obtained from MDSC Analysis of PLA Film Samples.

	PLAL–CT	PLAH–CT	PLAL–CC	PLAH–CC	PLAL–NC	PLAH–NC
T_g, °C	57.9 ± 0.1	58.6 ± 0.1	59.8 ± 0.6	63.6 ± 0.3	67.1 ± 1.9	69.8 ± 0.1
T_{cc}, °C	99.3 ± 0.1	94.1 ± 0.3	-	-	-	-
T_{m1}, °C	146.4 ± 0.1	-	153.3 ± 0.3	168.6 ± 0.7	151.6 ± 0.4	165.5 ± 0.2
T_{m2}, °C	155.3 ± 0.1	170.3 ± 0.1	-	172.0 ± 0.2	-	169.9 ± 0.1
X_C	0.01 ± 0.02	0.02 ± 0.00	0.29 ± 0.02	0.50 ± 0.02	0.33 ± 0.03	0.43 ± 0.02
X_{RAF}	0.00 ± 0.01	0.00 ± 0.03	0.15 ± 0.03	0.16 ± 0.01	0.02 ± 0.02	0.03 ± 0.05
X_{MAF}	0.99 ± 0.00	0.97 ± 0.03	0.56 ± 0.01	0.35 ± 0.01	0.66 ± 0.05	0.54 ± 0.03
ξ_{T_α}, nm	3.7 ± 0.2	3.5 ± 0.4	2.1 ± 0.1	1.2 ± 0.1	1.8 ± 0.1	1.8 ± 0.1
T_α, ℃	58.4 ± 0.1	59.3 ± 0.1	59.4 ± 0.1	64.4 ± 0.6	68.3 ± 0.2	68.6 ± 0.1
δT, ℃	2.4 ± 0.1	2.6 ± 0.3	4.8 ± 0.1	10.1 ± 1.5	6.1 ± 0.5	5.1 ± 0.5

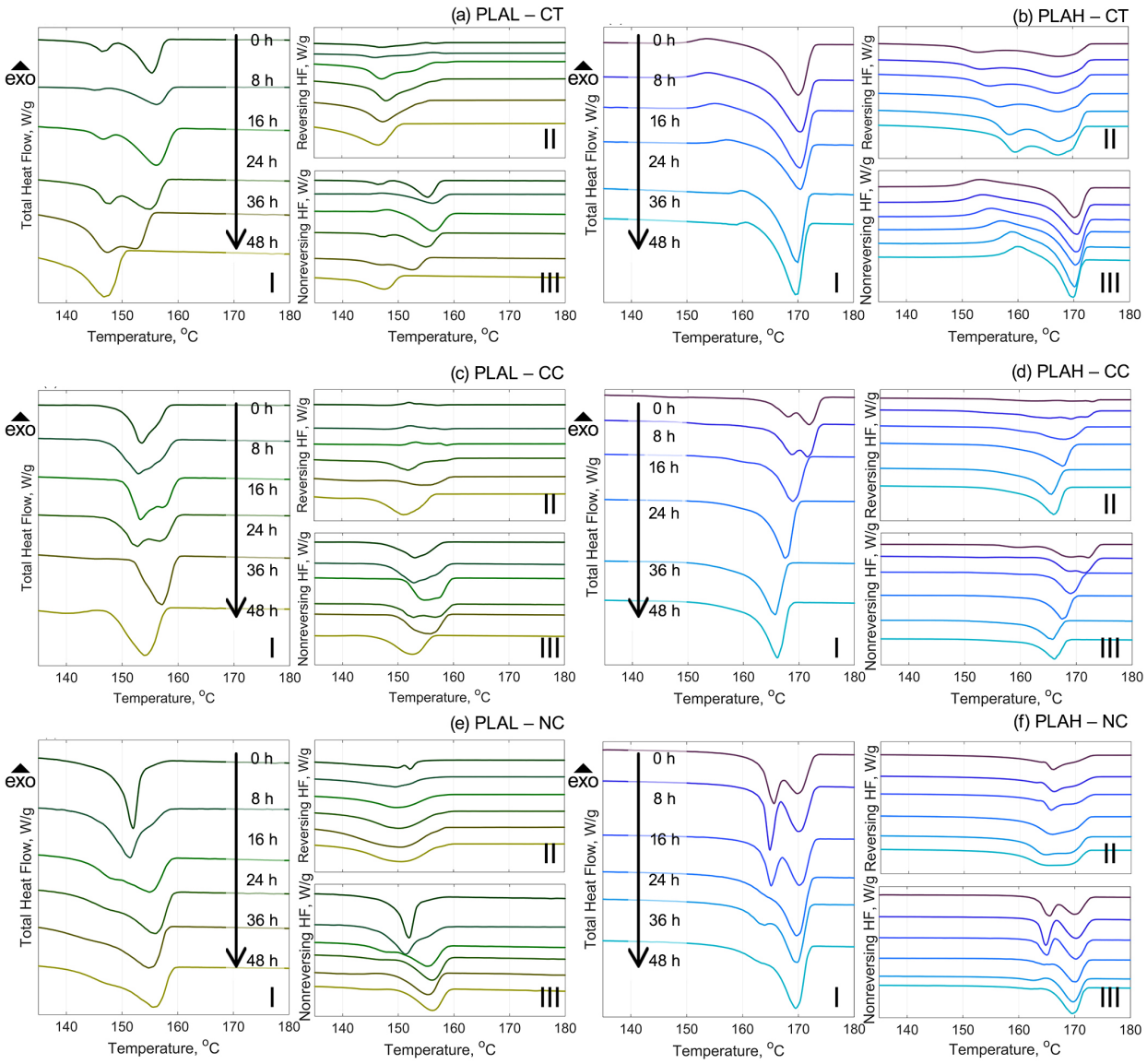

Figure 3.3 The MDSC heat flow curves (I, total heat flow; II, reversing heat flow; III, nonreversing heat flow) of PLA films during hydrolysis: (a) PLAL–CT, (b) PLAH–CT, (c) PLAL–CC, (d) PLAH–CC, (e) PLAL–NC, and (f) PLAH–NC. Thermograms are shifted along the vertical axis to improve understanding.

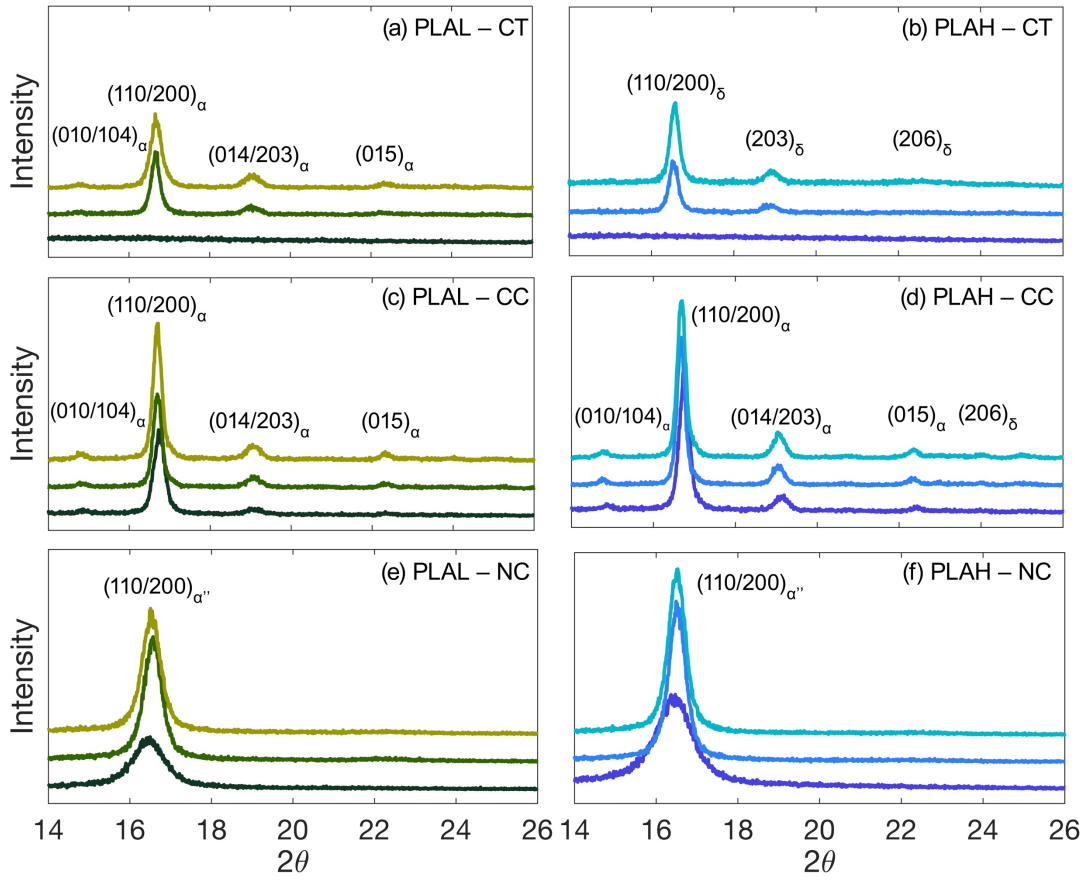

Figure 3.4 WAXD profile of PLA films during hydrolytic degradation: (a) PLAL–CT, (b) PLAH–CT, (c) PLAL–CC, (d) PLAH–CC, (e) PLAL–NC, and (f) PLAH–NC.

The changes in the three-phase structures of PLA films during hydrolysis were further investigated until the three phases could be effectively quantified; after that, one more set of data is reported with the X_{RAF} and X_{MAF} aggregated (e.g., 48 h for PLAL–CT; **Figure 3.5a**). The increase in the crystallinity of the films during hydrolysis can be related to the bulk erosion mechanism in which the water diffusion rate is much higher than the hydrolysis rate, allowing the water molecule to penetrate the polymer chain matrix. With the extra mobility of the PLA chains immersed in water [23], the chains rearrange into a more ordered crystalline structure. At the same time, the amorphous chains are hydrolyzed into shorter fragments, suggesting less entanglement and sufficient mobility to form new crystals. The increase in the crystallinity of the amorphous films (PLAL–CT and PLAH–CT) during

hydrolysis can be described by the Avrami model (Eq. (A3.1), Appendix 3D) (**Figure 3.5a, b** – dotted lines) while the crystallization growth of the initial semicrystalline films (PLA – CC, PLAH–CC, PLAL–NC, and PLAH–NC) can be described using the secondary crystallization by a root-time dependence model (Eq. (A3.2), Appendix 3D) (**Figure 3.5c–f** – dotted lines). The estimation of kinetic parameters of the crystallization from X_C data is presented in **Figure 3.5**. The statistical significance of the parameter estimation is provided in **Table A3.1**, Appendix 3D. The X_C of PLAL–CT and PLAH–CT increased dramatically during the initial 4 to 8 h after immersion in water and then kept increasing, as established by the Avrami primary crystallization process. The primary crystallization rate (K_p) of PLAL–CT was lower than that of PLAH–CT because the increasing amount of D-lactide in PLLA can slow down the crystal nucleation rate and crystal growth due to the segregation of the D-lactide units [27]. The Avrami exponent (n) values of 0.36 and 0.22 were estimated from PLAL–CT and PLAH–CT, respectively. Typically, the Avrami exponent of the isothermal crystallization process of PLA is between 2 and 4, representing the sum of the dimensionality and nucleation components [55,58]. Cheng [59,60] suggested that low values of the Avrami exponent can be attributed to changes in the radial growth rate over time, resulting from the restriction of crystal growth. The restriction of crystallization can arise from the high number of crystal nuclei and the formation of RAF between the crystals during crystallization [59–61]. Although the very low n value is not common, there are a few cases reported in the literature [23,60,62]. The lower value in the parameter n of PLAH–CT indicates more constraint due to greater nucleating sites compared with PLAL–CT.

The semicrystalline samples (PLAL–CC and PLAH–CC) had already achieved a certain amount of crystallinity after the cold-crystallization processes. The secondary crystallization of the semicrystalline samples can be developed from the formation of new crystallites in the space between existing lamellae or the thickening of existing lamellae [63].

The degree of crystallinity in the polymer systems can create a more tortuous pathway hindering the water molecules diffusing into the matrix [10]. The kinetic crystallization rates (K_s) of PLAL–CC and PLAH–CC were not significantly different, while the K_s of PLAL–NC was faster than that of PLAH–NC because PLAH–NC had the greater amount of initial pre-existing crystals (X_{pt}). The higher crystallinity could slow the diffusion of water molecules and subsequently slow the secondary crystallization of PLAH [64]. The maximum achievable crystallinity after hydrolysis of PLAL (–CT, –CC, and –NC) and PLAH (–CT, –CC, and –NC) samples reached approximately 54% and 65%, respectively, since the presence of higher D-lactide amounts in PLAL leads to generation of stereochemical defects within the polymer domain and, therefore, decreases the maximum attainable crystallinity in PLAL samples [55].

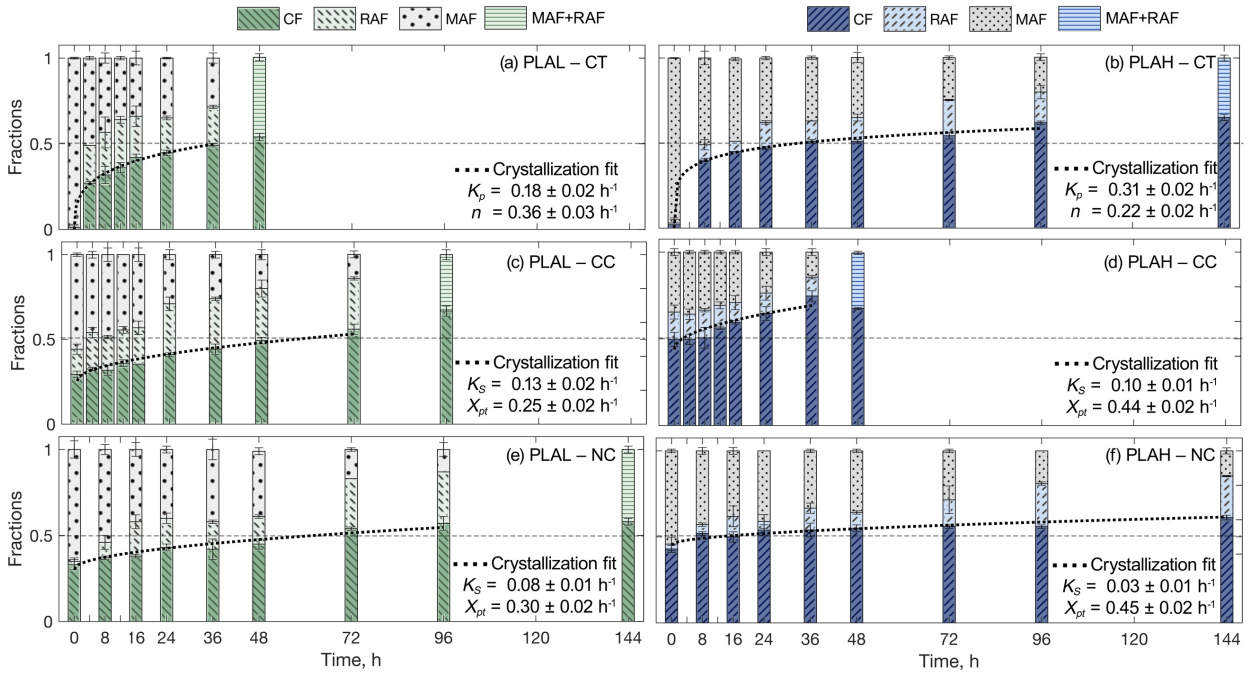

Figure 3.5 The changes in the three-phase structures of PLA films during hydrolytic degradation. The dashed horizontal lines indicate the guidelines of the phase fraction of 0.5. The dotted lines represent the best fit of crystallization kinetics: (a) PLAL–CT, (b) PLAH–CT, (c) PLAL–CC, (d) PLAH–CC, (e) PLAL–NC, and (f) PLAH–NC.

To study RAF evolution during the hydrolytic degradation, the X_{RAF} of each sample was evaluated as a function of hydrolysis time, as shown in **Figure 3.6**. The X_{RAF} of PLAL–CT (**Figure 3.6a**) increased dramatically from the initial stage (X_C and X_{RAF} = 0) and remained constant at around 25% during 4–12 h, and then leveled off until the end of hydrolysis which corresponds to the growth of α crystals, as indicated in **Figures 3.3a** and **3.4a**. The hydrolysis proceeded, the X_{RAF} of PLAL–CT was nearly constant, while the X_C increased. The X_{RAF} of PLAL–CC (**Figure 3.6c**) increased slightly from 15% to 30%, corresponding to the increase in the crystal thickness, as seen in the increase of the enthalpy value of fusion of T_{m2} (**Figure 3.3c**) and remained constant at 30%. PLAH–CC (**Figure 3.6d**) shows the initial X_{RAF} of 16%, which was similar to X_{RAF} of PLAL–CC. The X_{RAF} of PLAH–CC decreased slightly and remained constant at 11%. For PLAH–CT, PLAL–NC, and PLAH–NC (**Figure 3.6b, e, f**), the X_{RAF} gradually increased from 0% to 21%, 30%, and 16%, respectively, at 72 h after hydrolysis. According to the MDSC result (**Figure 3.3**), the increase of X_{RAF} could occur during the thickening processes of the crystal lamellae and the rearrangement of the δ (and the less ordered α'') crystals to the more ordered α structure, inducing the formation of X_{RAF} [50,56]. Righetti [24] reviewed the literature on the amorphous fractions of PLA and pointed out that the amount of RAF formation could be affected by the different forms of crystals. The α crystal, which has a close-packed arrangement, could lead to greater formation of RAF compared with the looser chain packing crystal forms. Moreover, the effect of the higher amount of D-lactide could lead to the higher X_{RAF} because the D-lactide can act as the stereodefect on the basal plane of the crystalline lamellae, so that all the PLAL films form more *RAF* than PLAH films.

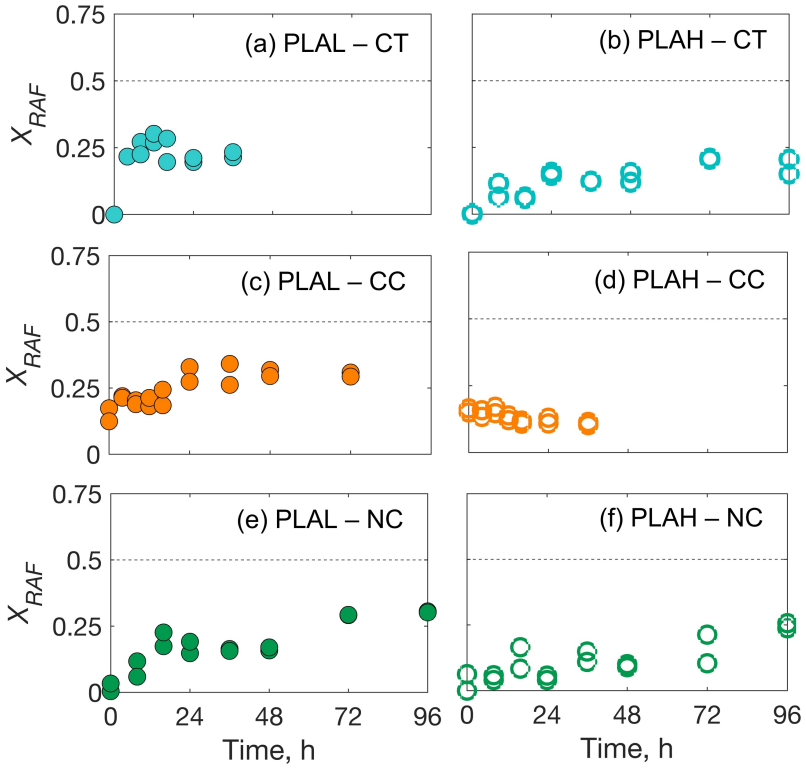

Figure 3.6 The plots of the evaluation of X_{RAF} versus the hydrolysis time: (a) PLAL–CT, (b) PLAH–CT, (c) PLAL–CC, (d) PLAH–CC, (e) PLAL–NC, and (f) PLAH–NC.

The cooperativity concept developed by Donth [65] provides information about chain mobility in the MAF region. The cooperative rearranging region (CRR) at the glass transition range is defined as the smallest subsystem of MAF that can rearrange itself independently into a different configuration under its T_g calculated from the MDSC measurement [66]. Examples of the calculation of CRR parameters of the PLAL–CT films, including CRR length (ξ_{T_α}), the T_g of the subvolume (T_α), and the mean temperature fluctuation (δT), are calculated using Eqs. (A3.3–A3.4) and shown in **Figure A3.4**, Appendix 3E. The experimental parameters obtained from the samples before hydrolysis are reported in **Table 3.2**. The ξ_{T_α} values of amorphous samples (PLAL–CT and PLAH–CT) were approximately 3.5–3.7 nm at the T_α of approximately 58.4–59.4 °C. After the cold-crystallization, the ξ_{T_α} values of PLAL–CC and PLAH–CC decreased to 2.1 and 1.2 nm, respectively, due to the suppression in the

mobility of MAF due to the increase of CF and RAF [67]. The C_p'' peaks of PLAL–CC and PLAH–CC shifted to the higher temperatures and became broader, as observed by an increasing T_α (59.4 and 64.4 °C) and δT (4.8 and 10.1 °C) compared with PLAL–CT and PLAH–CT, respectively. The temperature-related complex relaxation phenomenon could be connected to the different behavior of the MAF being confined in the inter- and intra-spherulite phases undergoing vitrification at the lower and higher temperatures, respectively [68]. After the crystallization process, the ξ_{T_α} values can considerably decrease due to the suppression in the mobility of MAF related to the increase of CF and RAF [67,69]. Moreover, the C_p'' peaks of cold-crystalline samples could be shifted to higher temperature and became broader compared to free amorphous region depending on the location that the MAF being confined. On the other hand, the ξ_{T_α} value of PLAL–NC and PLAH–NC was 1.8 nm at the higher T_α of approximately 68.5 °C, with slightly broad δT of 6.1 and 5.1 °C, respectively. The restriction of the MAF was related to the intra-oriented structure [54]. Additionally, the stretching could increase the tightness of RAF chains. The derivative of the complex heat capacity (C_p'') peaks of PLA films in the hydrolysis at 0 h and 24 h is shown in **Figure A3.5**, Appendix 3E, which became flat and broader due to the increase of crystallinity and degrading of amorphous chains after hydrolysis. Furthermore, the changes of ξ_{T_α} during hydrolysis is presented in **Figure A3.6**, Appendix 3E, showing the decreasing in ξ_{T_α} due to the rapid increase in crystallinity and spherulite growth taking up the whole amorphous space so that the ξ_{T_α} values of MAF become much smaller. For the crystallized PLA films (PLAL–CC, PLAH–CC, PLAL–NC, and PLAH–NC), the ξ_{T_α} values constantly decreased after hydrolysis due to the crystallization and hydrolysis of the MAF [68]. The ξ_{T_α} values of PLAH–CC during hydrolysis were much lower compared with those of the other samples.

The hydrolytic degradation of PLA with different L-lactide contents and crystallization methods was studied in unbuffered water at 85°C. The variation in the pH tracked during hydrolysis is presented in **Figure A3.7**, Appendix 3F. **Figure 3.7** illustrates the MWD of PLA films during hydrolysis. As the hydrolysis proceeded, the MWD peaks shifted to the lower molecular weight range and became broad. The peaks transformed from a monomodal distribution to bimodal distribution and were apparently located at Log M_w of approximately 3.5 and 3.9 for PLAL and about 3.6 and 4.0 for PLAH. The specific molecular weight peaks after hydrolysis correspond to the one- and two-folded PLA chains in the chain distributions of the crystalline residue. The two-folded crystalline residues could be hydrolyzed, resulting in only one peak crystalline residue at the end of hydrolysis. The crystalline thickness (L_c) of the one-fold of crystalline residue can be estimated according to the method used by Tsuji [70] as described in Eq. (A3.5), Appendix 3G. The L_c values of the crystalline residual after hydrolysis were 10.9, 11.0, and 9.8 nm for PLAL–CT, PLAL–CC, and PLAL–NC, respectively, which were lower than the L_c values of PLAH, which were 12.1, 12.5, and 11.0 nm for PLAH–CT, PLAH–CC, and PLAH–NC, respectively. This finding suggests that PLA with higher D-lactide could have a shorter L-unit sequenced segment, leading to a reduction of L_c. Moreover, the crystalline residue of PLAL–NC and PLAH–NC was thinner compared with the other films.

Figure 3.8 shows the change in normalized M_n ($\overline{M}_n$) of all PLA films during hydrolysis. The mathematical model described by Eqs. (3.8–3.12) was used to estimate the rate constants for the auto-catalytic hydrolytic degradation ($\overline{k}_{deg}$) by considering the reduction of M_n and the change in X_C. Generally, the hydrolytic degradation of PLA leads to cleavage of ester bonds preferentially in the amorphous region. To calculate the rate constant, the molecular chains in the MAF and RAF were assumed to be hydrolyzed at the same rate

of $\overline{k}_{deg}$ while CF was assumed not to be subjected to hydrolysis, neglecting the crystal modifications. The model considered the production of oligomer chains acting as a catalyst in the auto-catalytic hydrolysis reaction [40]. The estimated $\overline{k}_{deg}$ values of the PLA films shown in **Figure 3.8** indicate that for PLA films with lower L-lactide content, the $\overline{k}_{deg}$ value was highest in PLAL–CT (0.0124 h^{-1}), followed by PLAL–CC (0.0069 h^{-1}), and PLAL–NC (0.0045 h^{-1}). The statistical significance of the parameter estimation is provided in **Table A3.2**, Appendix 3G. As aforementioned, in this study, hydrolytic degradation of PLA film in water was assumed to proceed following a bulk erosion mechanism. PLAL–CC and PLAL –NC have lower hydrolysis rates since diffusion of water is hindered by the presence of the initial crystallinity. The hydrolysis of PLAL–CC was higher than that of PLAL–NC due to the higher amount of RAF, as presented in the X_{RAF} (**Figure 3.6**). Tsuji et al. [13] reported that the amorphous phase between the crystalline structure, now referred to as RAF, has more chain defects and also free ends, leading to an increase in the concentration of hydrophilic terminal groups, followed by an upsurge in the diffusion rate of water. Rio et al. [28] later showed that the RAF has a higher free volume than MAF, providing a higher water diffusion coefficient. Moreover, due to the preservation of the structural integrity of the chain networking from the melt-stretching process, it seems that the MAF of PLAL–NC was more resistant to hydrolysis.

In the case of PLA with higher L-lactide content, the $\overline{k}_{deg}$ of PLAH–CC (0.0070 h^{-1}) was much faster than the $\overline{k}_{deg}$ of PLAH–CT (0.0041 h^{-1}) and PLAH–NC (0.0022 h^{-1}). This finding is in contradiction to the result obtained from the lower L-lactide PLA. PLAH–CT had a surprisingly slower hydrolysis rate compared to PLAH–CC, which had much higher initial crystallinity. However, PLAH–CC had more X_{RAF} at the initial and early stages of the hydrolysis (before 24 h).

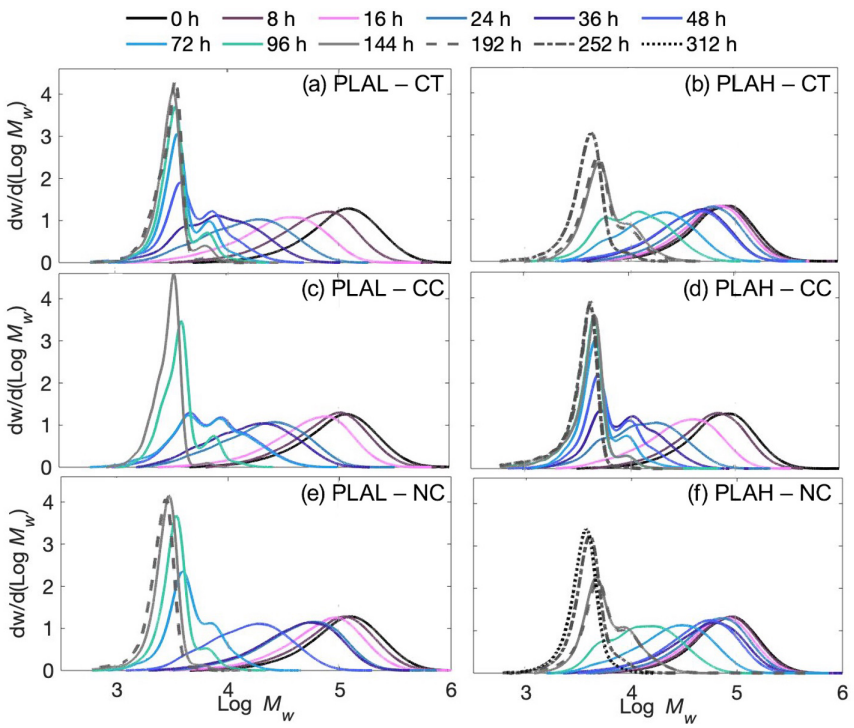

Figure 3.7 The molecular weight distribution of PLA film during hydrolysis: (a) PLAL–CT, (b) PLAH–CT, (c) PLAL–CC, (d) PLAH–CC, (e) PLAL–NC, and (f) PLAH–NC.

The initial RAF of the crystalline PLA film could have been more susceptible to hydrolysis than the RAF formation at the later stage, as shown in PLAH–CT. The high water diffusion and accumulation of hydrophilic groups in the RAF could counterbalance the effect of a high degree of crystallinity [25]. Accordingly, there was no significant difference in the $\overline{k}_{deg}$ between PLAL–CC and PLAH–CC. For PLAL–NC and PLAH–NC, the melt-stretching method can provide the higher crystallinity and less RAF and later influence the slower hydrolysis rate compared with the other PLA films. The melt-stretching method could suppress the formation of large crystallites and meanwhile promote nano-confined crystallization from the orientation of the mesophase [33]. This entanglement network could limit the diffusion of water molecules transporting in the perpendicular to the pre-stretching direction at the beginning of the hydrolysis and lead to high resistance to hydrolytic degradation.

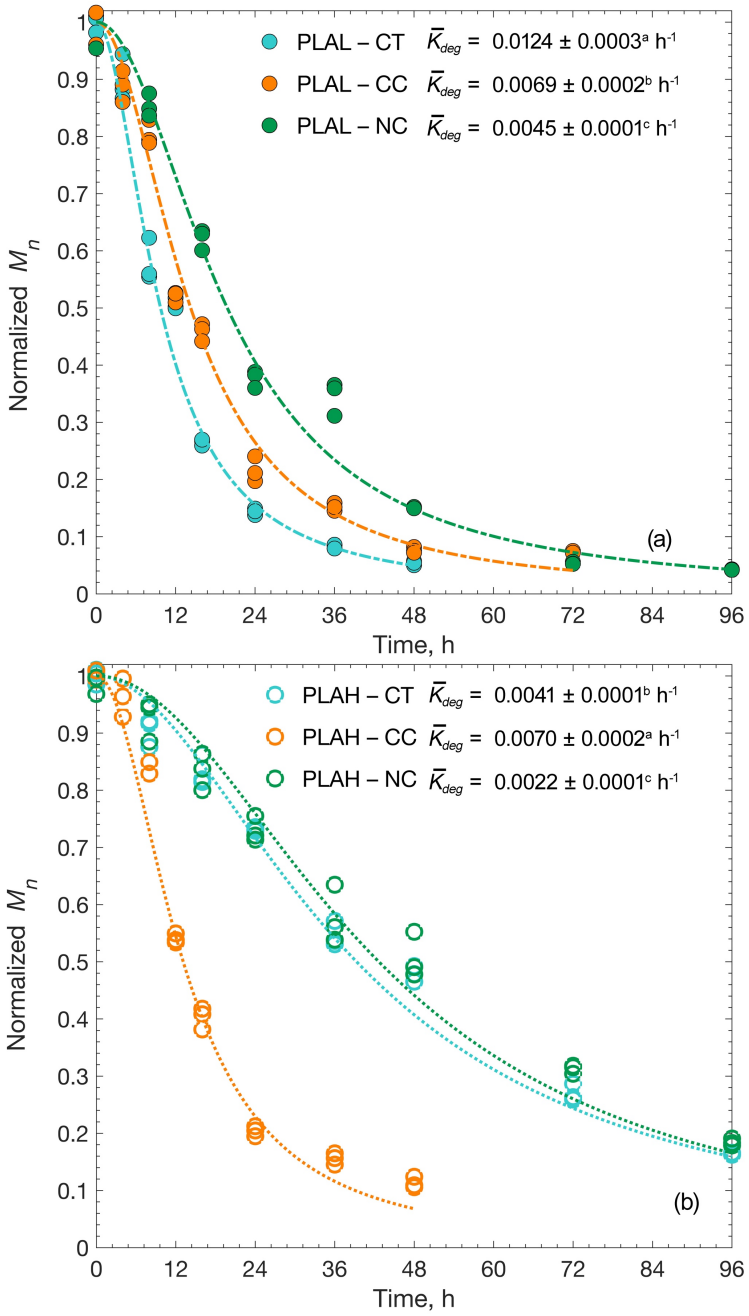

Figure 3.8 The normalized Mn during hydrolytic degradation: (a) PLAL, and (b) PLAH.

3.5 Conclusion

In this work, the effects of the crystalline behavior of amorphous and semicrystalline PLA films with different L-lactide contents and crystallization methods during the hydrolytic degradation were determined. The different amounts of L-lactide content affected the thermal properties and crystallization behavior. During hydrolysis, PLA films with higher L-lactide content (PLAH–CT, –CC, and –NC) had a higher attainable crystallinity than the films with lower L-lactide content (PLAL–CT, –CC, and –NC). The increasing D-lactide decreased the averaged L-lactide unit sequence length, interrupting the crystallization process, and increased the RAF formation. The different crystallization methods also affected the three-phase structure and phase behavior of PLA films. The results suggest that crystallinity has a significant effect on the hydrolysis of PLA by increasing the tortuous path of water molecules to diffuse through the PLA film matrix. Water diffusion in the amorphous matrix could affect the decrease in the hydrolysis rate, as observed in the crystalline PLA with lower L-lactide content (PLAL–CC and PLAL–NC) compared with the amorphous PLA film (PLAL–CT). Moreover, as the crystallization proceeded, the RAF also increased. The RAF domain has a higher free volume compared to MAF, and also has more folding chains, defects, and end chains, which increase the water diffusion and the concentration of hydrophilic terminal groups, leading to an augment of autocatalytic hydrolytic degradation [12–14]. The high initial amount of RAF could lead to rapid hydrolysis counterbalancing the high degree of crystallinity, as observed in PLAL–CC and PLAH–CC. For PLAL–NC and PLAH–NC, the melt-stretching method promotes the formation of nano-sized crystals without disrupting the chain network, leading to slow hydrolytic degradation. We expect that the promising study in the three-phase structure should be explored to broaden the hydrolytic degradation of PLA in the different media, for example, acidic, basic, and alcohol solutions.

3.6 Acknowledgements

L. W. thanks the Royal Thai Government for providing financial support for a Ph.D. fellowship. R. A. acknowledges the USDA National Institute of Food and Agriculture and Michigan State University AgBioResearch, Hatch project number MICL02665 for partial support of the study. S. T. acknowledges support from a grant from the Polymers program of the National Science Foundation (DMR-1905870). The authors thank Dr. Shi-Qing Wang (College of Polymer Science and Engineering, University of Akron) for providing insights on the crystallization process of the melt-stretching PLA films.

REFERENCES

[1] Tsuji H., Hydrolytic Degradation, in *Poly(Lactic Acid)*, Hoboken, NJ, USA: John Wiley & Sons, Inc., 2010, pp. 343–381.

[2] Codari F., Lazzari S., Soos M., *et al.*, Kinetics of the hydrolytic degradation of poly(lactic acid), *Polym. Degrad. Stab.*, vol. 97, no. 11, pp. 2460–2466, 2012, doi: 10.1016/j.polymdegradstab.2012.06.026.

[3] Tsuji H., Autocatalytic hydrolysis of amorphous-made polylactides: Effects of L-lactide content, tacticity, and enantiomeric polymer blending, *Polymer (Guildf).*, vol. 43, no. 6, pp. 1789–1796, 2002, doi: 10.1016/S0032-3861(01)00752-2.

[4] Rodriguez E. J., Marcos B., and Huneault M. A., Hydrolysis of polylactide in aqueous media, *J. Appl. Polym. Sci.*, vol. 133, no. 44, pp. 1–11, 2016, doi: 10.1002/app.44152.

[5] Tsuji H., Takai H., and Saha S. K., Isothermal and non-isothermal crystallization behavior of poly(l-lactic acid): Effects of stereocomplex as nucleating agent, *Polymer (Guildf).*, vol. 47, no. 11, pp. 3826–3837, 2006, doi: 10.1016/j.polymer.2006.03.074.

[6] Tsuji H., Okino R., Daimon H., and Fujie K., Water vapor permeability of poly(lactide)s: Effects of molecular characteristics and crystallinity, *J. Appl. Polym. Sci.*, vol. 99, no. 5, pp. 2245–2252, 2006, doi: 10.1002/app.22698.

[7] Tsuji H. and Ikarashi K., In Vitro Hydrolysis of Poly(L-lactide) Crystalline Residues as Extended-Chain Crystallites: II. Effects of Hydrolysis Temperature, *Polym. Degrad. Stab.*, vol. 85, no. 1, pp. 647–656, Jul. 2004, doi: 10.1016/j.polymdegradstab.2004.03.004.

[8] Tsuji H., Ikarashi K., and Fukuda N., Poly(L-lactide): XII. Formation, growth, and morphology of crystalline residues as extended-chain crystallites through hydrolysis of poly(L-lactide) films in phosphate-buffered solution, *Polym. Degrad. Stab.*, vol. 84, no. 3, pp. 515–523, 2004, doi: 10.1016/j.polymdegradstab.2004.01.010.

[9] Tsuji H. and Tsuruno T., Water vapor permeability of poly(L-lactide)/poly(D-lactide) stereocomplexes, *Macromol. Mater. Eng.*, vol. 295, no. 8, pp. 709–715, 2010, doi: 10.1002/mame.201000071.

[10] Duan Z. and Thomas N. L., Water vapour permeability of poly(lactic acid): Crystallinity and the tortuous path model, *J. Appl. Phys.*, vol. 115, no. 6, 2014, doi: 10.1063/1.4865168.

[11] Zhang N., Yu X., Duan J., *et al.*, Comparison study of hydrolytic degradation behaviors between α'- and α-poly(l -lactide), *Polym. Degrad. Stab.*, vol. 148, pp. 1–9, Feb. 2018, doi: 10.1016/j.polymdegradstab.2017.12.014.

[12] Tsuji H. and Ikada Y., Properties and morphology of poly(L-lactide): IV. Effects of structural parameters on long-term hydrolysis of poly(L-lactide) in phosphate-buffered solution, *Polym. Degrad. Stab.*, vol. 67, no. 1, pp. 179–189, 2000, doi: 10.1016/S0141-3910(99)00111-1.

[13] Tsuji H., Mizuno A., and Ikada Y., Properties and morphology of poly(L-lactide). III. Effects of initial crystallinity on long-term in vitro hydrolysis of high molecular weight poly(L-lactide) film in phosphate-buffered solution, *J. Appl. Polym. Sci.*, vol. 77, no. 7, pp. 1452–1464, 2000, doi: 10.1002/1097-4628(20000815)77:7<1452::AID-APP7>3.0.CO;2-S.

[14] Tsuji H. and Del Carpio C. A., In vitro hydrolysis of blends from enantiomeric poly(lactide)s. 3. Homocrystallized and amorphous blend films, *Biomacromolecules*, vol. 4, no. 1, pp. 7–11, 2003, doi: 10.1021/bm020090v.

[15] Huang Y., Chen F., Pan Y., *et al.*, Effect of hydrophobic fluoropolymer and crystallinity on the hydrolytic degradation of poly(lactic acid), *Eur. Polym. J.*, vol. 97, pp. 308–318, 2017, doi: 10.1016/j.eurpolymj.2017.09.044.

[16] Kawai T., Rahman N., Matsuba G., *et al.*, Crystallization and melting behavior of poly (L-lactic acid), *Macromolecules*, vol. 40, no. 26, pp. 9463–9469, 2007, doi: 10.1021/ma070082c.

[17] Wang H., Zhang J., and Tashiro K., Phase Transition Mechanism of Poly(l-lactic acid) among the α, δ, and β Forms on the Basis of the Reinvestigated Crystal Structure of the β Form, *Macromolecules*, vol. 50, no. 8, pp. 3285–3300, 2017, doi: 10.1021/acs.macromol.7b00272.

[18] Lotz B., Crystal Polymorphism and Morphology of Polylactides, in *Advances in Polymer Science*, vol. 279, 2017, pp. 273–302.

[19] Chen H. M., Shen Y., Yang J. H., *et al.*, Molecular ordering and α'-form formation of poly(l-lactide) during the hydrolytic degradation, *Polymer (Guildf).*, vol. 54, no. 24, pp. 6644–6653, Nov. 2013, doi: 10.1016/j.polymer.2013.09.059.

[20] Zhang J., Tashiro K., Tsuji H., and Domb A. J., Disorder-to-Order Phase Transition and Multiple Melting Behavior of Poly(L-lactide) Investigated by Simultaneous Measurements of WAXD and DSC, *Macromolecules*, vol. 41, no. 4, pp. 1352–1357, Feb. 2008, doi: 10.1021/ma0706071.

[21] Zhang X., Espiritu M., Bilyk A., and Kurniawan L., Morphological behaviour of poly(lactic acid) during hydrolytic degradation, *Polym. Degrad. Stab.*, vol. 93, no. 10, pp. 1964–1970, 2008, doi: 10.1016/j.polymdegradstab.2008.06.007.

[22] Naga N., Yoshida Y., Inui M., *et al.*, Crystallization of amorphous poly(lactic acid) induced by organic solvents, *J. Appl. Polym. Sci.*, vol. 119, no. 4, pp. 2058–2064, Feb. 2011, doi: 10.1002/app.32890.

[23] Iñiguez-Franco F., Auras R., Burgess G., *et al.*, Concurrent solvent induced crystallization and hydrolytic degradation of PLA by water-ethanol solutions, *Polymer (Guildf).*, vol. 99, pp. 315–323, Sep. 2016, doi: 10.1016/j.polymer.2016.07.018.

[24] Righetti M. C., Amorphous fractions of poly(lactic acid), *Adv. Polym. Sci.*, vol. 279, pp. 195–234, 2018, doi: 10.1007/12_2016_14.

[25] Sangroniz A., Chaos A., Iriarte M., *et al.*, Influence of the Rigid Amorphous Fraction and Crystallinity on Polylactide Transport Properties, *Macromolecules*, vol. 51, no. 11, pp. 3923–3931, Jun. 2018, doi: 10.1021/acs.macromol.8b00833.

[26] Fernandes Nassar S., Guinault A., Delpouve N., *et al.*, Multi-scale analysis of the impact of polylactide morphology on gas barrier properties, *Polymer (Guildf).*, vol. 108, pp. 163–172, 2017, doi: 10.1016/j.polymer.2016.11.047.

[27] Androsch R., Schick C., and Di Lorenzo M. L., Kinetics of Nucleation and Growth of Crystals of Poly(l-lactic acid), in *Synthesis, Structure and Properties of Poly(lactic acid)*, vol. 279, M. L. Di Lorenzo and R. Androsch, Eds. Cham: Springer International Publishing, 2018, pp. 235–272.

[28] del Río J., Etxeberria A., López-Rodríguez N., *et al.*, A PALS Contribution to the Supramolecular Structure of Poly(L-lactide), *Macromolecules*, vol. 43, no. 10, pp. 4698–4707, May 2010, doi: 10.1021/ma902247y.

[29] Urayama H., Kanamori T., and Kimura Y., Microstructure and thermomechanical properties of glassy polylactides with different optical purity of the lactate units, *Macromol. Mater. Eng.*, vol. 286, no. 11, pp. 705–713, 2001, doi: 10.1002/1439-2054(20011101)286:11<705::AID-MAME705>3.0.CO;2-Q.

[30] Jiang X., Luo Y., Tian X., *et al.*, Chemical Structure of Poly(Lactic Acid), in *Poly(Lactic Acid)*, Hoboken, NJ, USA: John Wiley & Sons, Inc., 2010, pp. 67–82.

[31] Saha S. K. and Tsuji H., Effects of molecular weight and small amounts of d-lactide units on hydrolytic degradation of poly(l-lactic acid)s, *Polym. Degrad. Stab.*, vol. 91, no. 8, pp. 1665–1673, 2006, doi: 10.1016/j.polymdegradstab.2005.12.009.

[32] Razavi M., Zhang W., Khonakdar H. A., *et al.*, Inducing nano-confined crystallization in PLLA and PET by elastic melt stretching, *Soft Matter*, vol. 17, no. 6, pp. 1457–1462, 2021, doi: 10.1039/d0sm02181d.

[33] Razavi M. and Wang S.-Q., Why Is Crystalline Poly(lactic acid) Brittle at Room Temperature?, *Macromolecules*, vol. 52, no. 14, pp. 5429–5441, 2019, doi: 10.1021/acs.macromol.9b00595.

[34] ASTM D4754-18, Standard Test Method for Two-Sided Liquid Extraction of Plastic Materials Using FDA Migration Cell, *ASTM Int. West Conshohocken, PA,* 2018, doi: 10.1520/D4754-18.

[35] Fischer E. W., Sterzel H. J., and Wegner G., Investigation of the structure of solution grown crystals of lactide copolymers by means of chemical reactions, *Kolloid-Zeitschrift und Zeitschrift für Polym.*, vol. 251, no. 11, pp. 980–990, Nov. 1973, doi: 10.1007/BF01498927.

[36] Pan J., *Modelling Degradation of Bioresorbable Polymeric Medical Devices*. Elsevier, 2015.

[37] Sevim K. and Pan J., A model for hydrolytic degradation and erosion of biodegradable polymers, *Acta Biomater.*, vol. 66, pp. 192–199, Jan. 2018, doi:

10.1016/j.actbio.2017.11.023.

[38] Gleadall A., Pan J., and Atkinson H., A simplified theory of crystallisation induced by polymer chain scissions for biodegradable polyesters, *Polym. Degrad. Stab.*, vol. 97, no. 9, pp. 1616–1620, 2012, doi: 10.1016/j.polymdegradstab.2012.06.023.

[39] Han X. and Pan J., A model for simultaneous crystallisation and biodegradation of biodegradable polymers, *Biomaterials*, vol. 30, no. 3, pp. 423–430, 2009, doi: 10.1016/j.biomaterials.2008.10.001.

[40] Han X., Pan J., Buchanan F., *et al.*, Analysis of degradation data of poly(l-lactide–co-l,d-lactide) and poly(l-lactide) obtained at elevated and physiological temperatures using mathematical models, *Acta Biomater.*, vol. 6, no. 10, pp. 3882–3889, Oct. 2010, doi: 10.1016/j.actbio.2010.05.015.

[41] Aliotta L., Gazzano M., Lazzeri A., and Righetti M. C., Constrained amorphous interphase in poly(l-lactic acid): Estimation of the Tensile elastic modulus, *ACS Omega*, vol. 5, no. 33, pp. 20890–20902, 2020, doi: 10.1021/acsomega.0c02330.

[42] Limsukon W., Auras R., and Selke S., Hydrolytic degradation and lifetime prediction of poly(lactic acid) modified with a multifunctional epoxy-based chain extender, *Polym. Test.*, vol. 80, no. September, p. 106108, Dec. 2019, doi: 10.1016/j.polymertesting.2019.106108.

[43] Nagendra B., Rizzo P., Daniel C., *et al.*, c-Perpendicular Orientation of Poly(L-lactide) Films, *Polymers (Basel).*, vol. 13, no. 10, p. 1572, May 2021, doi: 10.3390/polym13101572.

[44] Pethrick R. A., Polymer Structures, *Encycl. Condens. Matter Phys.*, no. 1992, pp. 355–362, 2005, doi: 10.1016/B0-12-369401-9/00697-5.

[45] Di Lorenzo M. L., Rubino P., Luijkx R., and Hélou M., Influence of chain structure on crystal polymorphism of poly(lactic acid). Part 1: Effect of optical purity of the monomer, *Colloid Polym. Sci.*, vol. 292, no. 2, pp. 399–409, 2014, doi: 10.1007/s00396-013-3081-z.

[46] Pan P., Zhu B., Kai W., *et al.*, Effect of crystallization temperature on crystal modifications and crystallization kinetics of poly(L-lactide), *J. Appl. Polym. Sci.*, vol. 107, no. 1, pp. 54–62, Jan. 2008, doi: 10.1002/app.27102.

[47] Yasuniwa M., Tsubakihara S., Iura K., *et al.*, Crystallization behavior of poly(l-lactic acid), *Polymer (Guildf).*, vol. 47, no. 21, pp. 7554–7563, Oct. 2006, doi: 10.1016/j.polymer.2006.08.054.

[48] Tsuji H., Ohsada K., and Arakawa Y., Stereocomplex- and homo-crystallization behavior, polymorphism, and thermal properties of enantiomeric random copolymers of l- and d-lactic acids from the melt, *Polymer (Guildf).*, vol. 228, no. June, p. 123954, 2021, doi: 10.1016/j.polymer.2021.123954.

[49] Androsch R., Di Lorenzo M. L., and Schick C., Crystal nucleation in random l/d-lactide

copolymers, *Eur. Polym. J.*, vol. 75, pp. 474–485, Feb. 2016, doi: 10.1016/j.eurpolymj.2016.01.020.

[50] Shan G. F., Yang W., Tang X. G., *et al.*, Multiple melting behaviour of annealed crystalline polymers, *Polym. Test.*, vol. 29, no. 2, pp. 273–280, 2010, doi: 10.1016/j.polymertesting.2009.11.011.

[51] Chen Y., Zhao L., Pan H., *et al.*, Impact of D-isomer content on the microstructure and mechanical properties of uniaxially pre-stretched poly(lactic acid), *Polymer (Guildf).*, vol. 186, no. August 2019, p. 122022, 2020, doi: 10.1016/j.polymer.2019.122022.

[52] Marubayashi H., Akaishi S., Akasaka S., *et al.*, Crystalline structure and morphology of poly(L-lactide) Formed under high-pressure CO2, *Macromolecules*, vol. 41, no. 23, pp. 9192–9203, 2008, doi: 10.1021/ma800766h.

[53] Takasaki M., Fukushi N., Yoshizawa M., *et al.*, Multiple Melting Behavior of High-Speed Melt Spun Polylactide Fibers, *J. Macromol. Sci. Part B Phys.*, vol. 56, no. 3, pp. 143–160, 2017, doi: 10.1080/00222348.2016.1273173.

[54] Xu R. J., Tian Z. Q., Xie J. Y., and Lei C. H., The structure transformation of pre-oriented polylactic acid film during uniaxial stretching at room temperature, *Polym. Cryst.*, vol. 2, no. 3, pp. 1–10, 2019, doi: 10.1002/pcr2.10072.

[55] Saeidlou S., Huneault M. A., Li H., and Park C. B., Poly(lactic acid) crystallization, *Prog. Polym. Sci.*, vol. 37, no. 12, pp. 1657–1677, 2012, doi: 10.1016/j.progpolymsci.2012.07.005.

[56] Androsch R. and Wunderlich B., The link between rigid amorphous fraction and crystal perfection in cold-crystallized poly(ethylene terephthalate), *Polymer (Guildf).*, vol. 46, no. 26, pp. 12556–12566, 2005, doi: 10.1016/j.polymer.2005.10.099.

[57] Di Lorenzo M. L. and Righetti M. C., Crystallization-induced formation of rigid amorphous fraction, *Polym. Cryst.*, vol. 1, no. 2, pp. 1–14, 2018, doi: 10.1002/pcr2.10023.

[58] Zhang B., Wang B., Chan J., *et al.*, Flow-Induced Dendritic ß-Form Isotactic Polypropylene Crystals in Thin Films, *Macromolecules*, vol. 49, no. 14, pp. 5145–5151, 2016, doi: 10.1021/acs.macromol.6b01123.

[59] Cheng S. Z. D., Kinetics of mesophase transitions in thermotropic copolyesters. 1. Calorimetric study, *Macromolecules*, vol. 21, no. 8, pp. 2475–2484, Aug. 1988, doi: 10.1021/ma00186a029.

[60] Cheng S. Z. D. and Wunderlich B., Modification of the Avrami treatment of crystallization to account for nucleus and interface, *Macromolecules*, vol. 21, no. 11cc, pp. 3327–3328, 1988.

[61] Grebowicz J., Cheng S. Z. D., and Wunderlich B., Kinetics of transitions involving condis crystals, *J. Polym. Sci. Part B Polym. Phys.*, vol. 24, no. 3, pp. 675–685, 1986, doi: 10.1002/polb.1986.090240313.

[62] Tsai W. C., Hedenqvist M. S., Laiback, *et al.*, Physical changes and sorption/desorption behaviour of amorphous and semi-crystalline PLLA exposed to water, methanol and ethanol, *Eur. Polym. J.*, vol. 76, pp. 278–293, 2016, doi: 10.1016/j.eurpolymj.2016.02.005.

[63] Marsh J. J., Turner R. P., Carter J., and Jenkins M. J., Thermal diffusivity and secondary crystallisation kinetics in poly(lactic acid), *Polymer (Guildf).*, vol. 179, no. July, p. 121595, Sep. 2019, doi: 10.1016/j.polymer.2019.121595.

[64] Drieskens M., Peeters R., Mullens J., *et al.*, Structure versus properties relationship of poly(lactic acid). I. Effect of crystallinity on barrier properties, *J. Polym. Sci. Part B Polym. Phys.*, vol. 47, no. 22, pp. 2247–2258, Nov. 2009, doi: 10.1002/polb.21822.

[65] Donth E., The size of cooperatively rearranging regions at the glass transition, *J. Non. Cryst. Solids*, vol. 53, no. 3, pp. 325–330, 1982, doi: 10.1016/0022-3093(82)90089-8.

[66] Saiter A., Delpouve N., Dargent E., and Saiter J. M., Cooperative rearranging region size determination by temperature modulated DSC in semi-crystalline poly(l-lactide acid), *Eur. Polym. J.*, vol. 43, no. 11, pp. 4675–4682, 2007, doi: 10.1016/j.eurpolymj.2007.07.039.

[67] Furushima Y., Ishikiriyama K., and Higashioji T., The characteristic length of cooperative rearranging region for uniaxial drawn poly(ethylene terephthalate) films, *Polymer (Guildf).*, vol. 54, no. 16, pp. 4078–4084, 2013, doi: 10.1016/j.polymer.2013.06.030.

[68] Delpouve N., Saiter A., and Dargent E., Cooperativity length evolution during crystallization of poly(lactic acid), *Eur. Polym. J.*, vol. 47, no. 12, pp. 2414–2423, 2011, doi: 10.1016/j.eurpolymj.2011.09.027.

[69] Lixon C., Delpouve N., Saiter A., *et al.*, Evidence of Cooperative Rearranging Region size anisotropy for drawn PET, *Eur. Polym. J.*, vol. 44, no. 11, pp. 3377–3384, 2008, doi: 10.1016/j.eurpolymj.2008.08.001.

[70] Tsuji H., In vitro hydrolysis of poly(L-lactide) crystalline residues as extended-chain crystallites. Part I: long-term hydrolysis in phosphate-buffered solution at 37°C, *Biomaterials*, vol. 25, no. 24, pp. 5449–5455, Nov. 2004, doi: 10.1016/j.biomaterials.2003.12.053.

APPENDIX 3A: OPTICAL PROPERTIES BY UV-VIS SPECTROSCOPY

Optical properties of amorphous PLA and crystallized PLA films after hydrolysis and two crystallization methods were analyzed by a UV-Vis spectrometer (Shimadzu Corporation, Kyoto, Japan) in the range of 200–800 nm.

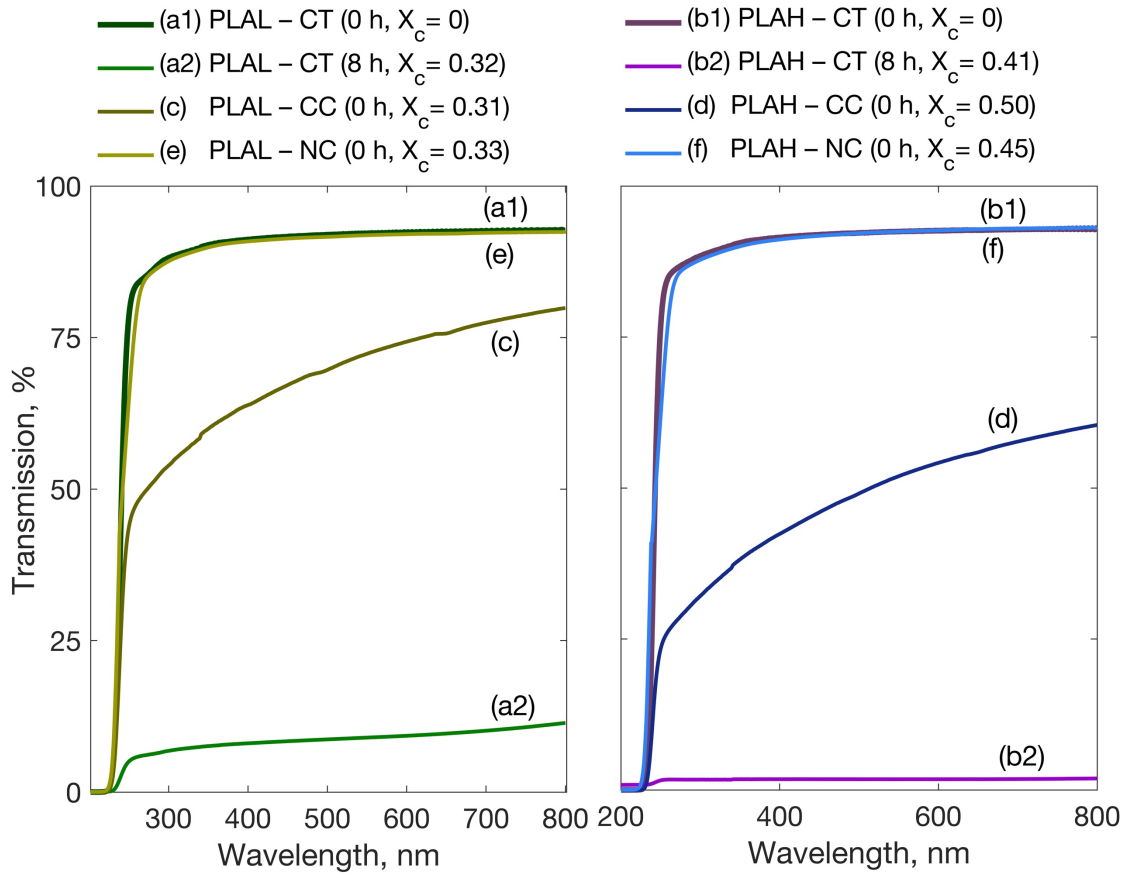

Figure A3.1 Light transmittance spectra of PLA films with different crystallization processes: (a1) PLAL–CT (0 h, X_c = 0), (b1) PLAH–CT (0 h, X_c = 0), (a2) PLAL–CT (8 h, X_c = 0.32), (b2) PLAH–CT (8 h, X_c = 0.41), (c) PLAL–CC (0 h, X_c = 0.31), (d) PLAH–CC (0 h, X_c = 0.50), (e) PLAL–NC (0 h, X_c = 0.33), (f) PLAH–NC (0 h, X_c = 0.45).

APPENDIX 3B: MDSC HEAT FLOW THERMOGRAMS OF THE PLA FILMS

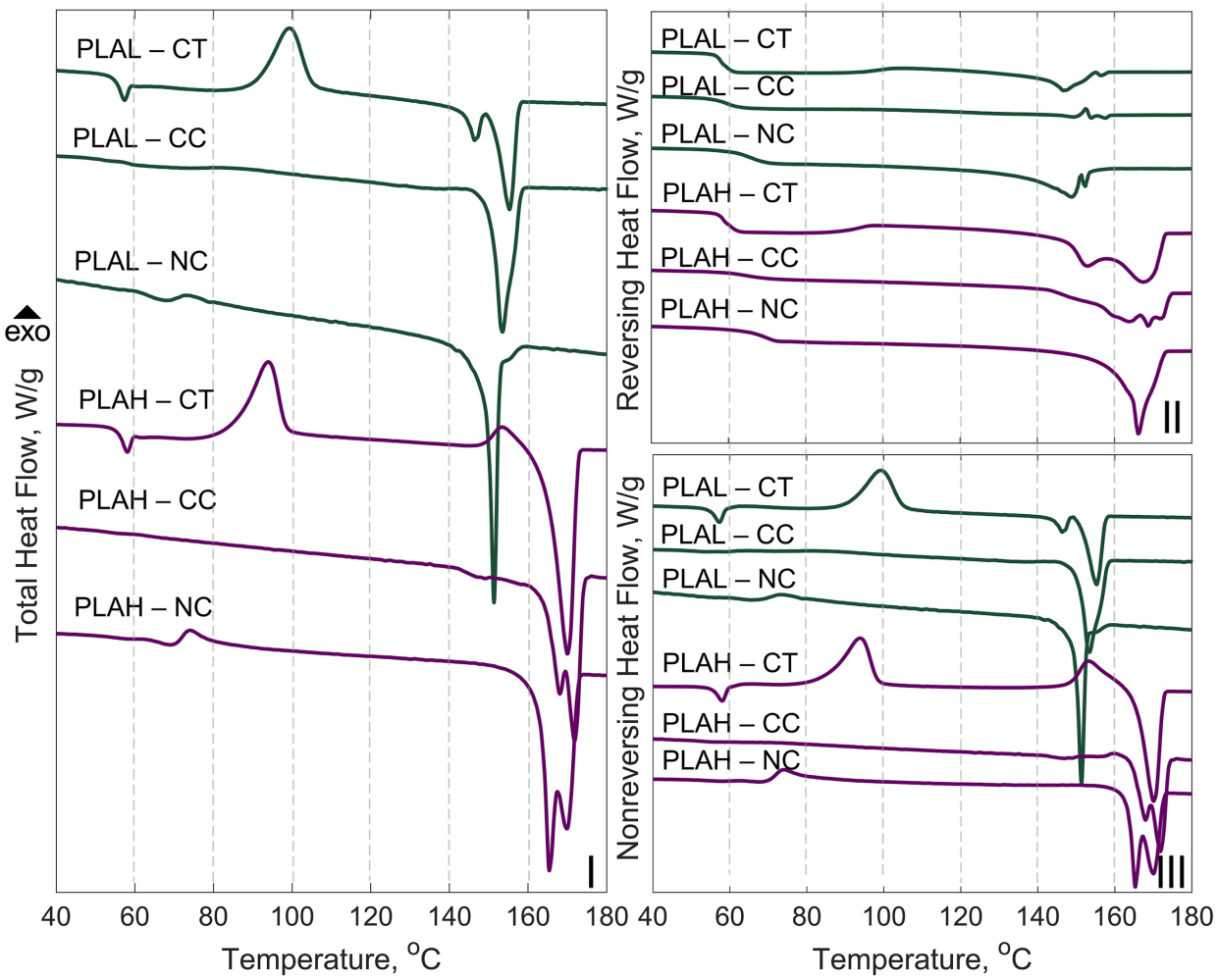

Figure A3.2 MDSC heat flow curves: (I) total heat flow, (II) reversing heat flow, and (III) nonreversing heat flow of the PLA films before hydrolysis.

APPENDIX 3C: DECONVOLUTION OF WAXD PROFILES OF PLA–NC

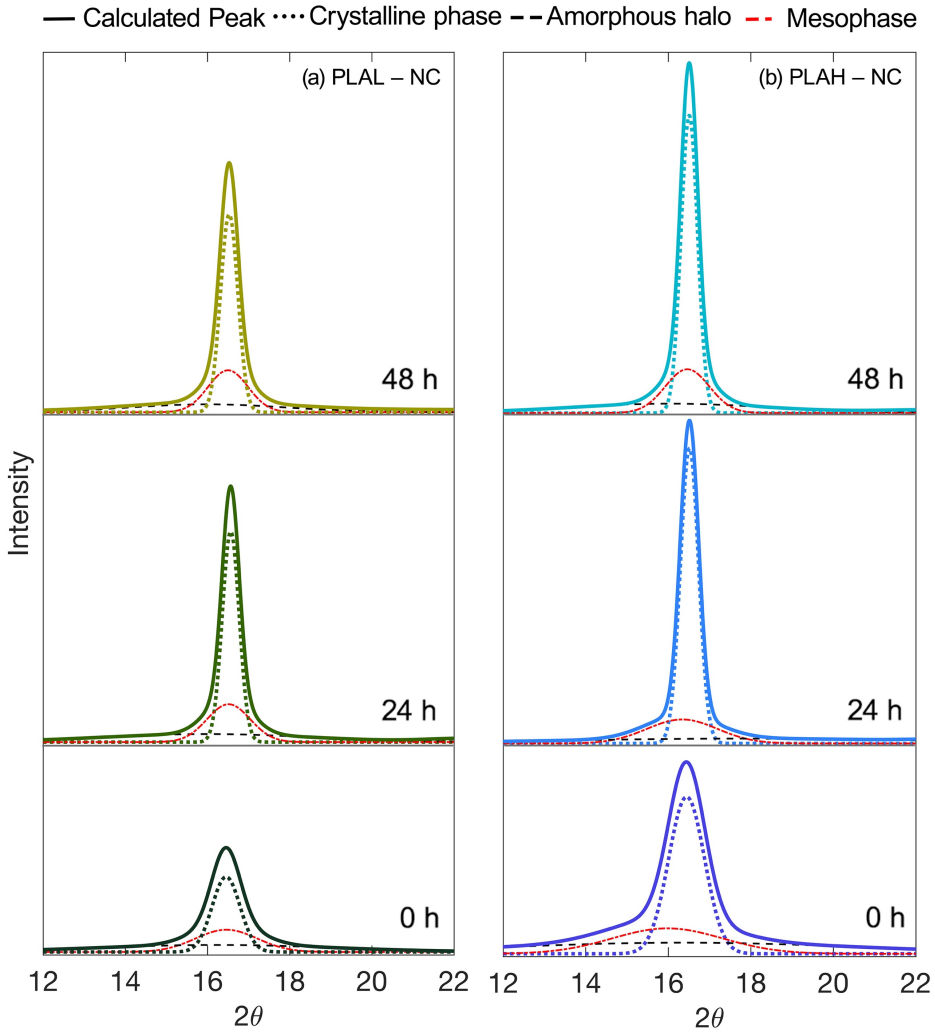

Figure A3.3 Deconvoluted WAXD peaks of PLAL–NC and PLAH–NC.

APPENDIX 3D: CRYSTALLIZATION KINETICS

The kinetics of isothermal crystallization of PLA during hydrolysis can be described in two consecutive processes. First, for the non-crystallized films, PLAH–CT and PLAL–CT, the primary crystallization process can be estimated using the Avrami equation:

$$X_c(t) = 1 - \exp\left(-K_p t^n\right) \quad \text{(A3.1)}$$

where $X_c(t)$ is the time-dependent fraction of crystallinity, K_p is the primary crystallization rate constant, t is the hydrolysis time, and n is the Avrami exponent indicating the mode of the dimension of crystal growth. Second, for the crystallized films, PLAH–CC, PLAH–NC, PLAL–CC, and PLAL–NC, the secondary crystallization equation following the root-time dependence model can be used as follows:

$$X_c(t) = X_{pt}\left(1 + K_s t^{1/2}\right) \quad \text{(A3.2)}$$

where $X_c(t)$ is more than the crystallinity at the end of the primary crystallization, X_{pt}; and K_s is the secondary crystallization rate constant.

Table A3.1 Rate Parameters for Primary and Secondary Crystallization of PLA Films.

Samples	Parameters	
Primary crystallization	K_p, h^{-1}	n
PLAL–CT	0.18 ± 0.02^{A1}	0.36 ± 0.03^{A}
PLAH–CT	0.31 ± 0.02^{B}	0.22 ± 0.02^{B}
Secondary crystallization	K_s, h^{-1}	X_{pt}
PLAL–CC	0.13 ± 0.02^{a}	0.25 ± 0.02^{a}
PLAH–CC	0.10 ± 0.01^{ab}	0.44 ± 0.02^{c}
PLAL–NC	0.08 ± 0.01^{b}	0.30 ± 0.02^{b}
PLAH–NC	0.03 ± 0.01^{c}	0.45 ± 0.01^{c}

[1] Within columns, different uppercase letters indicate significant differences between PLAL–CT and PLAH–CT, and different lowercase letters indicates significant differences between PLAL (–CC and –NC) and PLAH (–CC and –NC) ($\alpha < 0.05$).

APPENDIX 3E: COOPERATIVE REARRANGING REGION (CRR)

The characteristic volume of cooperativity at the dynamic glass transition temperature T_α ($\xi^3_{T_\alpha}$) and the number of monomer units in the CCR (N_α) can be determined from in-phase component ($C_p{}'$) of the complex heat capacity and out-of-phase component ($C_p{}''$) or the derivative of $C_p{}'$ obtained from the MDSC using the following equations:

$$\xi^3_{T_\alpha} = \frac{\Delta(1/C_p)}{\rho(\delta T)^2} k_B T_\alpha^2 \tag{A3.3}$$

$$N_\alpha = \frac{\rho N_A \xi^3_{T_\alpha}}{M_0} \tag{A3.4}$$

where C_p is the heat capacity at constant pressure. $\Delta(1/C_p)$ is $(1/C_p)_{glass} - (1/C_p)_{liquid}$ estimated from $C_p{}'$. T is the mean temperature fluctuation related to the dynamic glass transition obtained from the $C_p{}''$ Gaussian fit standard deviation. k_B and N_A, are the Boltzmann constant and the Avogadro number, ρ is the MAF density which is equal to 1.24 g cm^{-3}; and M_0 is the molar mass of PLA monomer unit, which is equal to 72 g mol^{-1}.

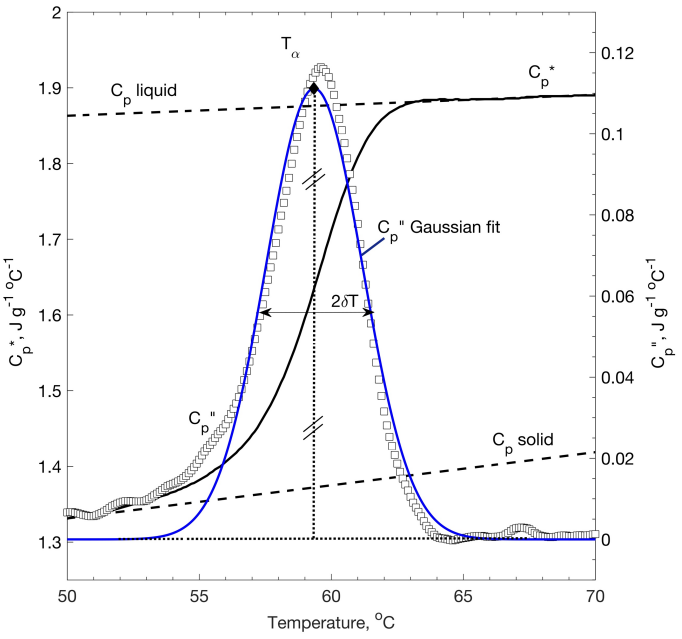

Figure A3.4 Example of $C_p{}'$ and $C_p{}''$ curves obtained by the heating scan of MDSC thermograms of PLA films. The blue line corresponds to the Gaussian fit of Cp″ used to calculate the ξ_{T_α}.

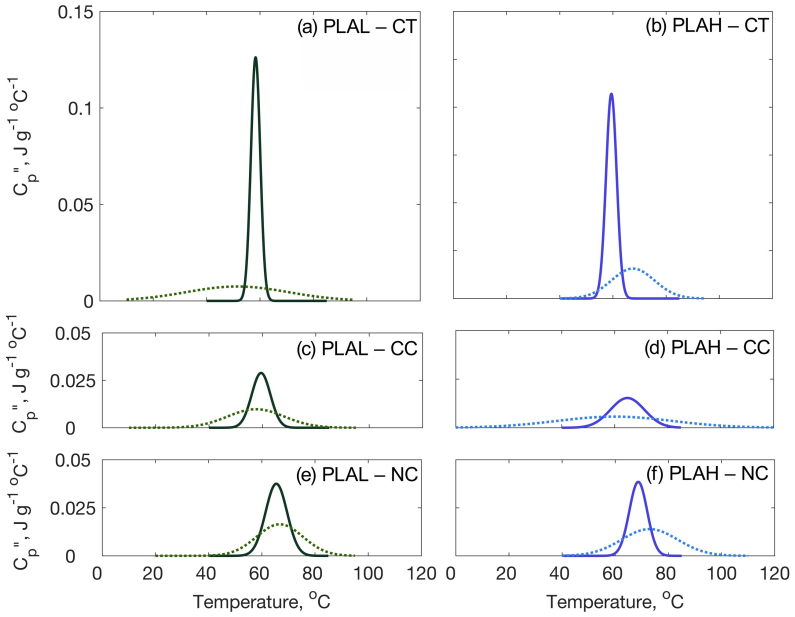

Figure A3.5 C_p'' curves obtained from MDSC of PLA films after 0 h (—) and 24 h (⋯) of hydrolysis: (a) PLAL–CT, (b) PLAH–CT, (c) PLAL–CC, (d) PLAH–CC, (e) PLAL–NC, and (f) PLAH–NC.

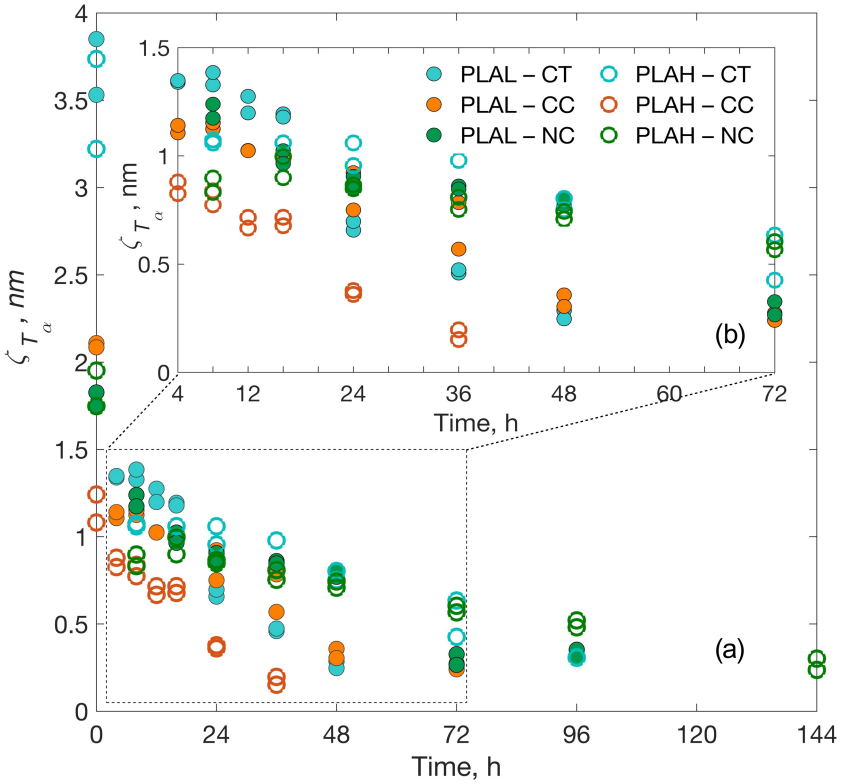

Figure A3.6 The CRR length evolution of PLA films during hydrolytic degradation.

APPENDIX 3F: *PH* MEASUREMENTS

The change in *pH* was measured during hydrolysis of collected samples in triplicate, as reported in **Figure A3.7.** The hydrolytic degradation in water was conducted initially at neutral *pH*. During the hydrolysis, the acidic products formed from the chain scission of PLA chains were released to the surface and the water.

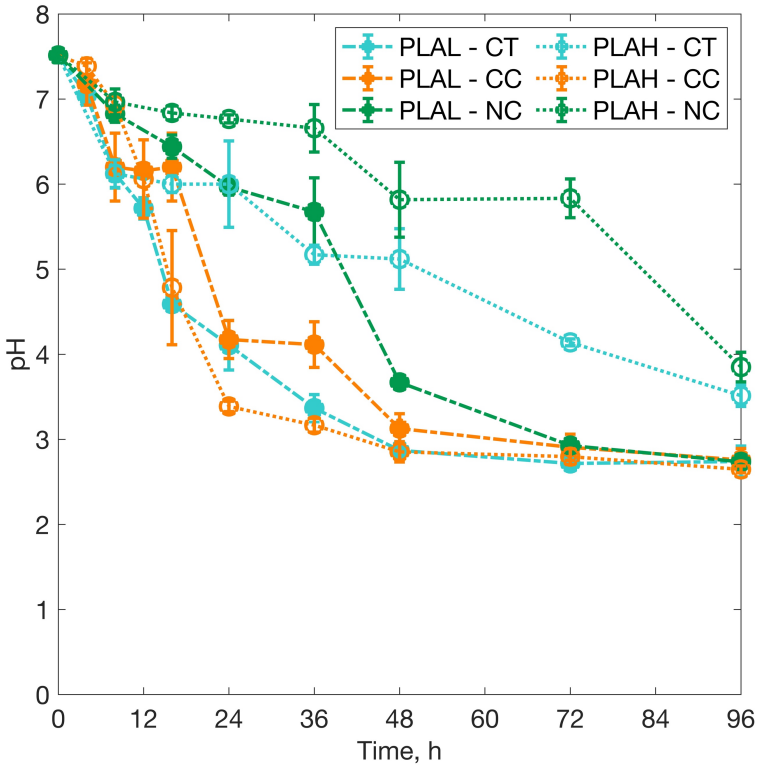

Figure A3.7 *pH* variation during hydrolytic degradation of PLA films.

APPENDIX 3G: THICKNESS OF CRYSTALLINE RESIDUE

The crystalline thickness of the PLA film after hydrolysis can be estimated from the specific molecular weight given below:

$$l_c(nm) = (0.288 \times M_n)/M_0 \quad \text{(A3.5)}$$

where M_n is the molecular weight of the crystalline residue after hydrolysis. The crystalline residue is assumed to be 10_3 helix with a length of 28.8 nm along the C-axis; and M_0(g mol^{-1}) is the molecular weight of the repeating unit of PLA, which is equal to 72.1 g mol^{-1}.

APPENDIX 3H: HYDROLYTIC DEGRADATION KINETICS

Table A3.2 Rates of Autocatalytic Hydrolytic Degradation ($\overline{k}_{deg}$) of PLA Films.

Samples	$\overline{k}_{deg}$, h^{-1}
PLAL–CT	$0.0124 \pm 0.0003^{Aa\ 1}$
PLAH–CT	0.0041 ± 0.0001^{Bb}
PLAL–CC	0.0069 ± 0.0002^{Ab}
PLAH–CC	0.0070 ± 0.0002^{Aa}
PLAL–NC	0.0045 ± 0.0001^{Ac}
PLAH–NC	0.0022 ± 0.0001^{Bc}

[1] Different uppercase letter indicates significant differences between samples with the same crystallization method, and different lowercase letters indicate significant differences between samples with the same % L-lactide ($\alpha < 0.05$).

CHAPTER 4: HYDROLYTIC DEGRADATION OF POLY(LACTIC ACID): UNRAVELING CORRELATIONS BETWEEN TEMPERATURE AND THE THREE PHASE STRUCTURES

4.1 Abstract

Hydrolysis significantly influences both the properties and degradability of poly(lactic acid), PLA. This work investigates the hydrolysis kinetics of PLA films as affected by degree of crystallinity and temperatures by considering the three-phase model structures (i.e., mobile amorphous, rigid amorphous, and crystalline). Molecular weight and three-phase fraction analyses were performed during hydrolysis to estimate the kinetic rates using phenomenological models. Results revealed that temperature significantly impacted PLA degradation, with distinct characteristics observed for each of these three phases. Above the glass transition temperature, the hydrolysis rates of PLA were comparable among samples with different crystallinity due to rapid water-induced crystallization of the amorphous phases, coupled with accelerated hydrolysis. In contrast, at below the glass transition temperature, the higher crystallinity sample exhibited a faster hydrolysis rate attributed to the presence of the rigid amorphous fraction. An increase in crystallinity introduced more defects due to limited mobility in the rigid amorphous fraction, influencing hydrolysis. The study provides valuable insights into the crucial relationship between temperature, crystallinity, and hydrolysis kinetics which are expected to be useful for predicting PLA degradation behavior during its intended applications and at its end of life.

4.2 Introduction

Poly(lactic acid), PLA, is a biobased and biodegradable polymer derived from natural resources, which can be entirely disintegrated and degraded under appropriate conditions such as industrial composting. To tackle the environmental challenges created by plastic pollution, PLA has emerged as one of the main biobased polymers versatile for various applications, especially as packaging materials, the disposal of which at their end of life has become a major environmental problem over the past few decades [1]. Many studies have been conducted to tailor PLA's properties and durability for specific applications while retaining its biodegradability after disposal [2,3].

Hydrolytic degradation is one of the crucial chemical reactions involving the breakdown of the PLA chains, affecting the deterioration of material properties and facilitating the initial abiotic-catalyzed biodegradation processes [2,4]. PLA hydrolytic degradation involves multiple steps: (1) diffusion of water molecules into the amorphous phase of the material; (2) chain scission of the ester bonds of amorphous chains, leading to a decrease of molecular weight and production of the oligomers and monomers; and (3) partial hydrolysis of crystalline fractions [5]. The kinetics of PLA are affected by material characteristics (i.e., crystallinity, DL-lactide ratio, and molecular weight) and environmental conditions (i.e., temperature and pH) [4,5].

Amorphous PLA can be transformed into an orderly structure under the favorable thermodynamic conditions or the influence of solvents [6]. The chains in the crystalline region are more hydrolysis-resistant than those in the amorphous regions due to limited interactions of water molecules in the tightly packed crystalline structure. Thus, hydrolysis predominantly occurs in the amorphous region, resulting in crystalline residues during the later stage of degradation [4]. However, the crystalline entities are not completely isolated from the amorphous regions [6]. The strong coupling between the two phases can result in a

separate phase in which the chains are restricted. This interphase is known as the rigid amorphous fraction (RAF), which refers to the continuum layer that undergoes devitrification/vitrification at a broad range of temperatures from above the glass transition of the mobile amorphous fraction (MAF) to the start of melting of the crystalline fraction (CF) [7–9]. The formation of RAF is influenced by the nature of materials and crystallization conditions [9–11], which, in turn affects the gas permeability [12,13] and mechanical properties [14] of the semicrystalline PLA.

Although the effect of crystallinity on the hydrolytic degradation of PLA has been extensively reported in the literature [15–22], the effect of RAF on the hydrolysis of PLA has not been widely explored. Tsuji and coworkers [15–17] investigated the hydrolysis of amorphous and melt-crystallized PLA films in phosphate-buffered solution (PBS) at 37 °C, and found that an increase in the degree of crystallinity can accelerate hydrolytic degradation due to the high density of carboxylic acid accumulating in the RAF region. Similarly, Huang et al. [18] reported that an increase in the degree of crystallinity resulted in a corresponding increase in the hydrolytic rate at 39 °C and 88% relative humidity (RH). Other researchers reported that the semicrystalline PLA samples showed higher resistance to hydrolytic degradation than the amorphous PLA under various hydrolysis conditions, such as in water at 50–58 °C [19–21] and NaOH solution at 50–70 °C [22]). These studies reported contradictory information about the role of the CF and MAF in the PLA hydrolysis kinetics. Furthermore, none of these studies evaluated the amount of RAF during the hydrolysis experiments.

The relationship between crystallinity and hydrolysis in PLA is complex and can depend on several factors. This present study aimed to develop a holistic understanding of the three-phase structure model–temperature relationship on the hydrolysis of PLA. Specifically, we investigated the effect of the crystallinity as well as rigid and mobile

amorphous phases on the hydrolytic degradation of PLA at 45 to 85 °C. PLA films were crystallized by melt-crystallization at 120 °C to develop different levels of the three-phase structure. The molecular weight of the samples and their three-phase structure were assessed during the hydrolysis. Finally, the kinetic constants of hydrolysis were estimated using modified phenomenological models. The results from this study can be useful for manipulating the hydrolytic properties and addressing end-of-life options of PLA for various applications.

4.3 Experimental section

4.3.1 Sample preparation

PLA resin, Ingeo™ 2003D thermoplastic extrusion-grade resin with L-lactic acid content of 95.7%, was provided by NatureWorks LLC (Minnetonka, MN, USA). The resins were dried at 50 °C for 12 h in a vacuum oven before processing in an extruder (Microextruder model RCP-0625, Randcastle Extrusion Systems, Inc., Cedar Grove, NJ, USA). The temperatures of feeding zone, transfer tube, and die were 195, 210, and 210 °C, respectively. The samples were first evaluated using a differential scanning calorimeter (DSC Q100; TA Instruments, New Castle, DE, USA), in isothermal mode at 120 °C to predetermine the melt-crystallization condition of the samples. The detailed method and results of the thermal study are described in **Figure A4.1**, Appendix 4A. Cast film was then pre-cut into 15 cm × 20 cm rectangular samples and fixed on a non-stick plate. For the amorphous PLA film (PLA–Q), the samples were heated at 180 °C for 8 min, and fast quenched in liquid nitrogen to avoid crystallization during cooling. To crystallize the PLA films, the samples were heated to 180 °C for 8 min and then cooled to a crystallization temperature of 120 °C, with holding times of 60, 90, and 180 min, respectively. The samples were then quenched in liquid nitrogen to prevent further crystallization. Fully crystallized film is henceforth referred to as PLA–MC–C, while PLA–MC–A and PLA–MC–B are partially crystallized films.

4.3.2 Hydrolysis experiments

Hydrolysis tests were conducted in HPLC-grade water (VWR, Radnor, PA, USA) at 45, 65, 75, and 85 °C under an unbuffered condition adapted from ASTM D4754–18 [23]. PLA film was cut into 2-cm diameter circles. Ten discs were stacked onto a stainless-steel wire with alternating glass beads and subsequently immersed into a vial containing 35 mL of water. The samples were periodically extracted throughout the testing periods at intervals based on hydrolysis temperatures. The samples were thoroughly rinsed with cold water and dried before analysis.

4.3.3 Three-phase fraction measurement

The three-phase fractions were measured by modulated differential scanning calorimetry (MDSC) technique (DSC Q100, TA instrument). The thermal analysis was performed under the heat-only condition with an oscillation (modulation) amplitude of 0.318 K, an oscillation period of 60 s, and an underlying heating rate of 1 °C min^{-1}. The technique separated the total heat flow into reversible (heat capacity-related) and non-reversing (kinetic) components. The heat flow and heat capacity data were obtained and analyzed using the Thermal Analysis Universal 2000 version 4.5A software.

The degree of crystallinity (X_C), the mobile amorphous fraction (X_{MAF}), and the rigid amorphous fraction (X_{RAF}) were determined by the following equations:

$$X_C = \frac{\Delta H_m - \sum \Delta H_c}{\Delta H_m^0} \tag{4.1}$$

$$X_{MAF} = \frac{\Delta C_p}{\Delta C_p^0} \tag{4.2}$$

$$X_{RAF} = 1 - X_{MAF} - X_C \tag{4.3}$$

where ΔH_m is the enthalpy of fusion from the integration of the heat flow in the melting region, $\sum \Delta H_c$ is the sum of the exothermic peak enthalpies, and ΔH_m^0 is the calculated melting

enthalpy of 100% crystalline PLA (139 J/g), which was determined using the method previously developed by Righetti et al. [24]. The determination of ΔH_m^0 is explained and shown in **Table A4.1**, Appendix 4B. ΔC_p is the measured heat capacity increment at T_g of the sample, and ΔC_p^0 is the heat capacity increment of 100% amorphous PLA, which was carefully measured from the PLA film treated by fast cooling from the molten state.

4.3.4 Wide-angle X-ray diffraction (WAXD)

Wide-angle diffraction analysis was conducted using an X-ray diffractometer (AXS D8, Bruker Co., Billerica, MA, USA) equipped with a global mirror filter Cu Kα radiation source operating at 40 kV and 100 mA. The diffractogram was recorded at room temperature within the 2θ range of 2° to 40° at a scanning rate of 0.24°min^{-1} with an increment of 0.01°. The X-ray beam was directed parallel to the film surface. Wide-angle diffraction analysis was used to determine the relative crystallinity for determination of ΔH_m^0 (**Table A4.1**, Appendix 4B) and investigate crystal modifications. The relative crystallinity was calculated from the ratio of the area under the crystalline peak to the total area of crystalline and amorphous peaks. Fityk 1.3.1 software [25] was used for background subtraction and diffractogram deconvolution using a Gaussian function.

4.3.5 Molecular weight measurement

The evolution of weight average (M_w) and number average (M_n) molecular weights, as well as the molecular weight distribution (MWD), were measured by size exclusion chromatography using Waters Gel Permeation Chromatograph (Waters Associates Inc., Milford, MA, USA) equipped with an isocratic pump (Waters 1515), an autosampler (Waters 717plus), a refractive index detector (Waters 2414), and a series of Styragel® columns (Styragel® HR-4, HR-3, and HR-2), maintained at 35 °C. HPLC-grade tetrahydrofuran (THF; Sigma-Aldrich, St. Louis, MO, USA) was used as the mobile phase solvent at a flux of 1 mL

min^{-1}. The molecular weights of PLA were evaluated using the universal calibration curve generated from a series of polystyrene standards (Shodex STANDARD SM-105, Showa Denko, Tokyo, Japan). The Mark-Houwink constants (K and a values) of PLA in THF at 35 °C were 0.0174 mL g^{-1} and 0.736, respectively, obtained from the literature [26]. The M_w, M_n, and overall MWD were analyzed using Waters Breeze™ 2 software. The multimodal MWDs were deconvoluted using the Fityk software for the later hydrolysis stage. The deconvolution involved fitting a Gaussian function to the log-normal distribution curves to identify the main population chains and crystalline residue peaks.

4.3.6 Mathematical models for the hydrolytic degradation

The hydrolytic degradation rates were determined using the modified models by Pan et al. [27]. These complete mathematical models encompass numerous equations, variables, and parameters, addressing aspects such as chain scission-induced crystallization, short-chain production and diffusion, and the impact of the catalytic effect, random and end scissions. A detailed description of the complete mathematical models applied for the degradation of PLA can be found elsewhere [27–31]. In the present study, we employed a subset of mathematical models introduced by Pan et al. [27] to investigate the impacts of noncatalytic and autocatalytic hydrolysis. We focused on utilizing readily available data such as molecular weight and crystallinity, aiming to evaluate the hydrolysis rate of the entire amorphous fractions (both MAF and RAF) by treating the crystalline fraction as non-hydrolysable. Parameter estimation was performed using advanced numerical methods facilitated by MATLAB software.

The hydrolytic degradation of PLA entails a chain scission of the ester bonds upon exposure to water molecules, leading to the fragmentation of the long chains. The rates of the hydrolysis reaction are given by Eq. (4.4):

$$\frac{\mathrm{d}R_s}{\mathrm{d}t} = k_1 C_E + k_2{}' C_E C_{H+} \tag{4.4}$$

where R_s represents the total mole concentration of chain scissions; k_1 and $k_2{}'$ are the rate constants for noncatalytic and autocatalytic hydrolysis, respectively; C_E represents the total ester bonds of the long chains in amorphous fractions, for both MAF and RAF; $C_{H+} = (k_a \frac{C_{ol}}{m\,(1-X_C)})^{0.5}$ represents the concentration of carboxylic acid end groups of the short chain, which are assumed to act as catalysts in the hydrolysis; C_{ol} represents the total ester units in all the oligomers and monomers with a length less than 8 units. In this study, an average degree of polymerization (m) of 4 units was employed. k_a is the acid disassociation constant of carboxylic end groups at a specific temperature which determines their ability to dissociate in a solution and characterizes their acidity. Accordingly, Eq. (4.4) can be rewritten as:

$$\frac{\mathrm{d}R_s}{\mathrm{d}t} = k_1 C_E + k_2 C_E \left(\frac{C_{ol}}{1 - X_C}\right)^{0.5} \tag{4.5}$$

where X_C is the crystallinity at time t evaluated from the crystallization kinetics from Eqs. (A4.5–A4.7), Appendix 4C. k_2 is related to k_a and m as follows:

$$k_2 = \frac{k_2{}' {k_a}^{0.5}}{m^{0.5}} \tag{4.6}$$

As hydrolysis progresses, the changes in C_E and C_{ol} can be described using the following equations:

$$C_E = C_{E_0} - C_{ol} - \omega\,(X_C - X_{C_0}) \tag{4.7}$$

$$C_{ol} = C_{E_0} \cdot \alpha \cdot \left(\frac{R_s}{C_{E_0}}\right)^{\beta} \tag{4.8}$$

where C_{E_0} represents the ester units in the amorphous phase before hydrolysis. It gradually decreases as hydrolysis proceeds due to the production of C_{ol} and the simultaneous formation of X_C. ω is the total ester bond of the crystalline phase. α and β are dimensionless

parameters. On the basis of the findings from Han et al. [29] and Sevim and Pan [31], α and β can be assigned as 0.4 and 1, respectively, implying that, after ten chain scissions, one short chain is produced.

The number average molecular weight (M_n) is typically determined by the summation of the weight of all polymer chains in a sample, considering both the amorphous and crystalline regions, while excluding the contribution of small oligomers that may be soluble in the hydrolysis media. This sum is then divided by the total number of chains in all species, which increases as chain scission progresses, with the exclusion of short chains. The calculation can be expressed as shown in Eq. (4.9):

$$M_n = \left(\frac{\left(C_{E_0} + \omega X_{C_0} - C_{ol}\right) M_0}{N_{chain_0} + R_s - \left(\frac{C_{ol}}{m}\right)} \right) \tag{4.9}$$

where N_{chain_0} is the total number of all chains before hydrolysis evaluated from the samples' initial density and molecular weight. The density measurement and the density of the samples can be found in **Tables A4.2** and **A4.3**, Appendix 4D. The rate constants, k_1 and k_2 can be determined through parameter estimation. Determining these rate constants could enable a comparison a comparison of the hydrolysis kinetics among PLA samples with different ratios of their three-phase structure and reflect their distinct kinetic behaviors of MAF and RAF.

The Vogel–Tammann–Fulcher (VTF) model describes the temperature dependence of reaction rates and relaxation times for amorphous or glassy materials. The VTF model is effective across a wide temperature range, where the relaxation times of the glassy solid deviate from the Arrhenius law particularly below T_g [32]. A detailed description of the VFT model for the degradation of PLA can be found elsewhere [33,34]. The VTF equation is given by Eq. (4.10):

$$k = k_0 exp^{-\frac{E}{R(T-T_0)}} \quad (4.10)$$

where k is the rate constant of noncatalytic and autocatalytic hydrolysis, k_0 is the pre-exponential factor, E is the pseudo-activation energy, R is the gas constant (8.314 J mol^{-1} K^{-1}), T is temperature expressed in Kelvin, and T_0 is the critical temperature point where the conformational entropy induced by segmental motion approaches zero, typically occurring at approximately 50 °C below T_g. Below T_0, the mobility and freedom of segmental motion in the polymer chains are significantly reduced.

4.4 Results and discussion

4.4.1 Initial thermal characterization of PLA films

The DSC thermograms of the amorphous and crystallized samples are shown in **Figure 4.1**. The T_g values of the samples increased slightly from 59.1 to 59.6 °C due to the increased crystalline fraction; however, the differences were not statistically significant. The exothermic peaks of the fully amorphous film (PLA–Q), and the partially crystallized films (PLA–MC–A and PLA–MC–B) occurred at approximately 94.4 °C due to the cold crystallization process of the amorphous fraction induced by the temperature increase. No cold crystallization event was observed for the fully crystallized film (PLA–MC–C) sample. Multiple endothermic peaks were observed in all samples suggesting the presence of different crystal modifications, lamellar thickness and/or perfection, and the melting−recrystallization −remelting phenomena during the heating scan [35]. The low T_m (T_{m1}) observed for the fully amorphous and partially crystallized films (PLA–Q, PLA–MC–A, and PLA–MC–B) could be attributed to the crystals forming during cold crystallization. The crystals obtained from melt-crystallization were observed in crystallized PLA at the mid-T_m (T_{m2}), at around 151.6 °C. On the other hand, the high-T_m (T_{m3}) could be attributed to the final melting of more stable crystals and reorganized crystal lamellae at a lower heating scan (<2 °C/min), during

which the molecules reorganized [36]. The final melting enthalpy for PLA–MC–C occurred at 157.3 °C, indicative of the formation of a more ordered structure as compared with the amorphous sample occurred at a slightly lower temperature of 155.1 °C (**Table 4.1**).

Figure 4.1b depicts the WAXD scans of the samples, revealing the crystalline patterns after baseline correction. The WAXD scan of the PLA–Q exhibited a broad distribution corresponding to the amorphous halo, indicating a lack of well-defined crystalline structure. The presence of these distinct patterns, including the prominent peaks at 2θ = 14.8° (010/104), 16.7° (110/200), 19.1° (014/203), and 22.3° (015), as well as the lower intensity peaks at 2θ = 12.4° (004/103), 20.7° (204), 27.4° (207/117), and 31.2° (217), provides compelling evidence that the three semicrystalline samples exhibited the dominant α-phase during the melt-crystallization process at a temperature of 120 °C. These distinctive WAXD peaks, corresponding to specific crystallographic planes, provide strong evidence of the prevalence of the α-phase in the samples [24,37].

The quantitative determination of the three-phase structure is presented in **Table 4.1**. The fully amorphous PLA–Q contained only the MAF. In contrast, by increasing the crystallization time from 60 to 180 min, PLA–MC–A, PLA–MC–B, and PLA–MC–C exhibited increasing crystallinity of 0.09, 0.18, and 0.24, respectively. The RAF was also present in these samples, with proportions of 0.05, 0.18, and 0.24, respectively. These results indicate that the formation of the RAF phase occurred concomitantly with crystal growth.

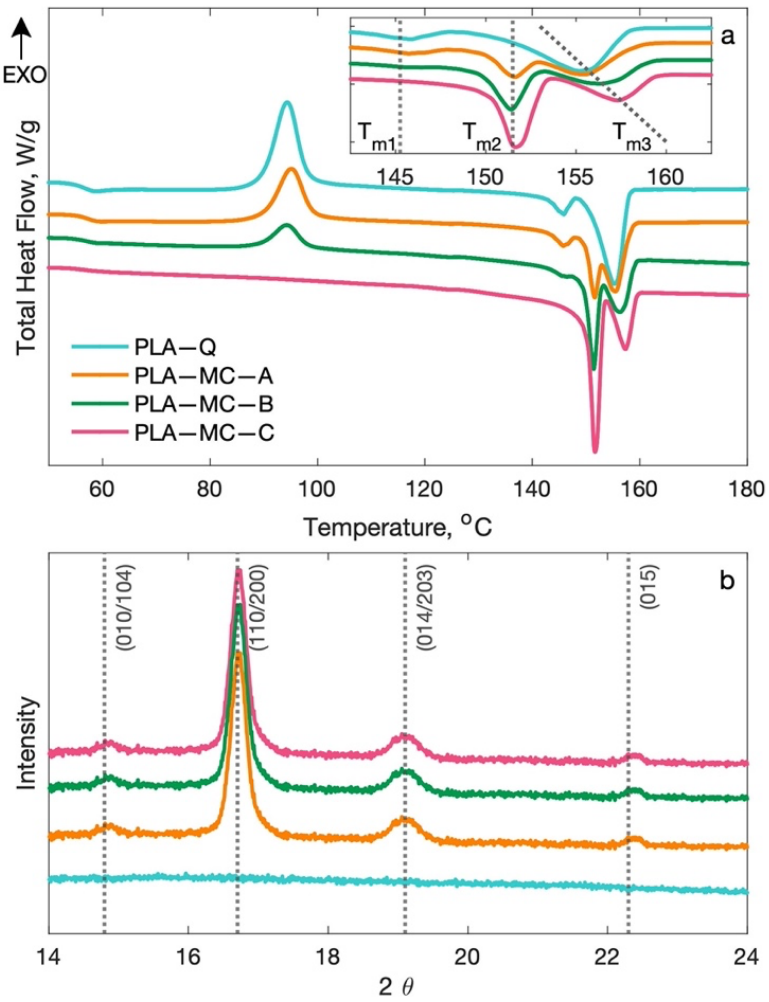

Figure 4.1 DSC thermograms (a) and WAXD profiles (b) of PLA film samples: PLA–Q, PLA–MC–A, PLA–MC–B, and PLA–MC–C. The inset in (a) shows an enlargement of the melting temperature region.

Table 4.1 Thermal properties of PLA film samples.

Sample	T_{m1}, °C	T_{m2}, °C	T_{m3}, °C	X_C	X_{RAF}	X_{MAF}
PLA–Q	145.8±0.1^{A}	–	155.1±0.1^{A}	0.00±0.00^{A}	0.00±0.00^{A}	1.0±0.00^{A}
PLA–MC–A	145.7±0.1^{A}	151.5±0.1^{A}	155.5±0.1^{A}	0.09±0.01^{B}	0.05±0.01^{B}	0.86±0.02^{B}
PLA–MC–B	145.9±0.5^{A}	151.7±0.5^{A}	157.0±0.1^{B}	0.18±0.01^{C}	0.18±0.01^{C}	0.64±0.01^{C}
PLA–MC–C	–	151.6±0.1^{A}	157.3±0.0^{B}	0.24±0.01^{D}	0.24±0.02^{D}	0.52±0.01^{D}

^{ABCD} Within a column, values with different uppercase letters are statistically different for each thermal property between samples (α = 0.05, Tukey's HSD).

Figure 4.2a shows the reversing heat capacity (Rev. C_p) signal of the samples as a function of temperature. The solid and liquid heat capacities were experimentally obtained by linear regression of the heat capacity below T_g and above T_g for fully amorphous samples or above T_m for semicrystalline samples, which serve as two reference baselines for quantitative thermal analysis [38]. PLA–Q contained only MAF, which relaxed entirely at T_g. In contrast, the C_p increment at T_g for semicrystalline samples (PLA–MC–A, PLA–MC–B, and PLA–MC–C) was successively reduced, suggesting the reduction of MAF. The temperature dependence of the solid amorphous fractions (MAF + RAF) is determined by Eq. (4.11) [10,39].

$$(X_{MAF} + X_{RAF})_{solid}(T) = 1 - X_c - \frac{Rev\ C_p(T) - C_{p_{solid}}(T)}{C_{p_{solid}}(T) - C_{p_{liquid}}(T)} \tag{4.11}$$

As shown in **Figure 4.2b**, the plot of amorphous fraction versus temperature reveals the differences in the molecular mobility of the MAF and RAF as a function of temperature. Below the T_g range, all the amorphous chains (MAF and RAF) are in a glassy state. At temperatures above the T_g, the entire MAF is altered from glassy to rubbery state, while RAF devitrifies as temperature increases and completely devitrifies before the melting of CF occurs. **Figure 4.2b** also reveals evidence of the decoupling fractions of MAF and RAF, affected by different temperature conditions.

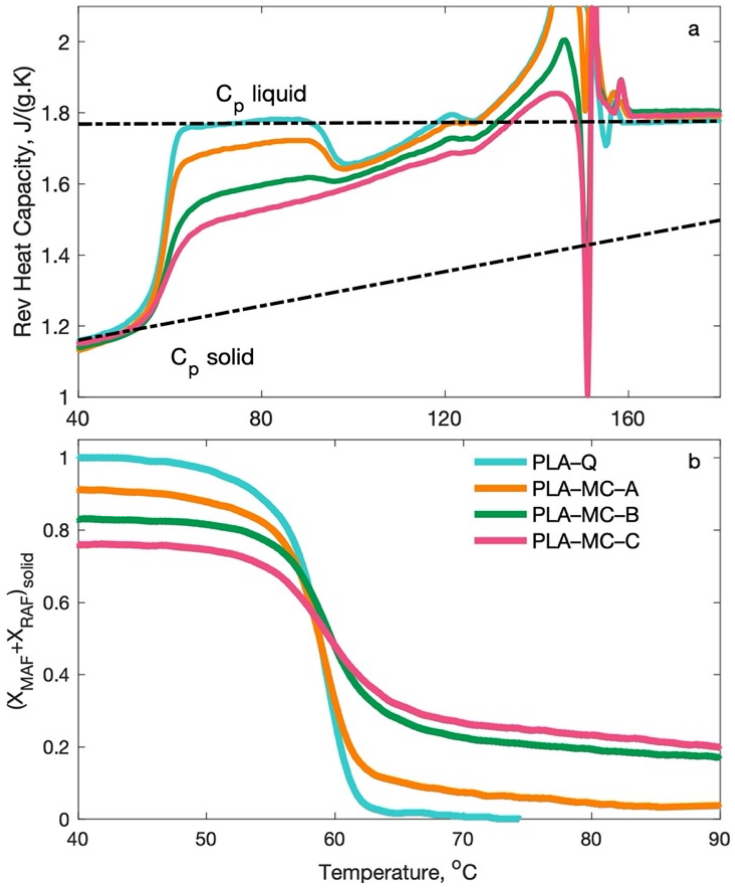

Figure 4.2 Temperature dependence of the reversible heat capacity (a) and the amorphous solid fractions (X_{MAF} + X_{RAF}) (b) of PLA samples, PLA–Q, PLA–MC–A, PLA–MC–B, and PLA–MC–C, before hydrolysis. The lower and upper dashed lines represent the baselines of solid and liquid heat capacities, respectively.

4.4.2 Characterization of PLA film during hydrolytic degradation

4.4.2.1 Thermal characterization

The hydrolysis experiments were conducted at 45, 65, 75, and 85 °C, encompassing the T_g of PLA, which is around 59 °C. However, when PLA films are immersed in water, water molecules can enhance chain mobility and increase the free volume in the amorphous phase. As a result, the T_g of PLA under immersion conditions is lowered than 53 °C as reported in the literature [34]. At 45 °C (below the T_g of the MAF), the PLA polymer was in a glassy state, where the mobility of amorphous chains was restricted. On the other hand, at 65, 75, and 85 °C (above the T_g), an increased mobility of the amorphous chains was observed.

The three-phase structures of PLA–Q, PLA–MC–A, PLA–MC–B, and PLA–MC–C were analyzed to determine the relative proportions of the CF, RAF, and MAF, without considering any mass changes during the hydrolysis process (**Figure 4.3**). The measurement process continued until a point where the heat capacity at T_g could be reliably determined to ensure accurate determination of the MAF content. The results indicate that during the hydrolysis at 45 °C, the three-phase structures of the samples remained constant for 1–90 d for all samples. This finding can be attributed to the limited mobility of the amorphous chains in both the MAF and RAF, which restricted their rearrangement into a more stable structure. The presence of initially long chains further hindered the crystallization process. However, on 120 d of hydrolysis, a significant decrease in MAF was observed, accompanied by an increase in CF, for PLA–Q and PLA–MC–A. This finding can be attributed to the hydrolysis of the shorter chains in the MAF with higher mobility, leading to the formation of new crystalline domains [40].

The hydrolysis-induced crystallization at 65, 75, and 85 °C progressed rapidly during the initial stages of hydrolysis, with PLA–Q being the fastest. For example, after 2 h at 85 °C, a substantial increase in the crystallinity of PLA–Q reached approximately 18%, accompanied by a corresponding rise in RAF of around 30%. In contrast, PLA–MC–C showed less pronounced changes in CF, similar to the hydrolysis at 45 °C. Crystallinity (X_C) values plotted in **Figure 4.3b, c, d**, representing the CF on a scale of 0 to 1, were used to evaluate the crystallinity kinetics of the samples during hydrolysis at temperature conditions higher than the T_g. A detailed explanation of the model used in this study is provided in Appendix 4C. The dashed lines (– –) in represent the model predictions of X_C based on Eqs. (A4.5–A4.7), Appendix 4C. At 45°C where the crystallization process was slow, the model was used primarily for parameterizing the hydrolysis rates. The crystallization process of PLA–Q followed the Avrami model, indicating a nucleation and growth mechanism (**Figure 4.3b**).

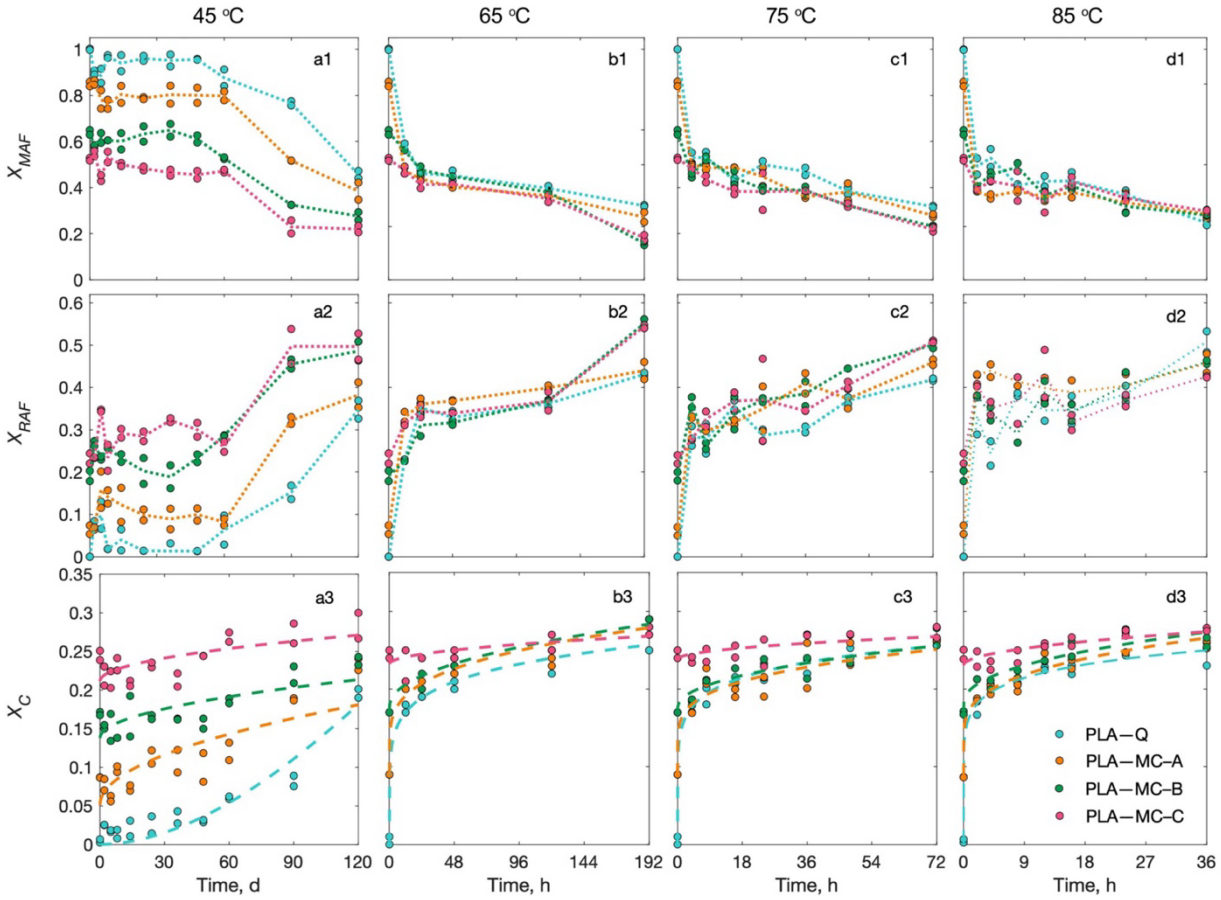

Figure 4.3 Changes in the three-phase structures of PLA films during hydrolytic degradation at 45 °C (a), 65 °C (b), 75 °C (c), and 85 °C (d) (columns), and X_{MAF} (1), X_{RAF} (2), and X_C (3) (rows). The dotted lines (···) connect the average values of X_{MAF} and X_{RAF}. The dashed lines (– –) represent the model predictions of X_C.

On the other hand, PLA–MC–C showed tendencies of secondary crystallization, suggesting the presence of additional crystallization mechanisms of existing crystals. The partially crystalline samples (PLA–MC–A and PLA–MC–B) showed a formation of new crystals and growth of existing crystals, indicating a dual and maybe more complex crystallization behavior. The rates of crystallization during hydrolysis were analyzed and modeled until a specific time point where all three phases could be reliably quantified. For example, at 192 h under 65 °C hydrolysis condition, the quantified fractions of MAF, RAF, and CF were 0.32, 0.26, and 0.42, respectively; beyond which, the MAF fraction was no longer detectable. **Table 4.2** summarizes the results of the Avrami exponent, *n*, as well as the

primary and secondary crystallinity rate constants, K_p and K_s, respectively, all estimated using Eqs. (A4.5–A4.7), Appendix 4C. The X_C values at the later stages for each sample were measured and compared with the values predicted by the crystallization model at earlier stages. The experimental X_C values after hydrolysis reached approximately 0.45, compared to the model prediction of 0.30. This discrepancy in crystallinity values may be attributed to the degradation of the amorphous regions, resulting in the formation of a crystalline residue and an overall increase in the crystalline fraction as the degradation process continued, which is not accounted for during early stage of crystallization [41].

Table 4.2 Crystallization kinetic parameters during hydrolysis for PLA at different temperatures.

Sample	T, °C	K_p, h^{-1}	n	K_s, h^{-1}
PLA–Q	65	$0.12 \pm 0.01^{A,a}$	0.17 ± 0.02^{A}	–
	75	$0.16 \pm 0.01^{B,a}$	0.14 ± 0.01^{AB}	–
	85	$0.18 \pm 0.01^{C,a}$	0.13 ± 0.01^{B}	–
PLA–MC–A	65	$0.06 \pm 0.01^{A,b}$	–	$0.04 \pm 0.02^{A,a}$
	75	$0.07 \pm 0.02^{A,b}$	–	$0.05 \pm 0.02^{AB,a}$
	85	$0.08 \pm 0.01^{A,b}$	–	$0.11 \pm 0.03^{B,a}$
PLA–MC–B	65	$0.01 \pm 0.01^{A,c}$	–	$0.04 \pm 0.01^{A,a}$
	75	$0.01 \pm 0.01^{A,c}$	–	$0.05 \pm 0.01^{AB,a}$
	85	$0.02 \pm 0.01^{A,c}$	–	$0.08 \pm 0.02^{B,ab}$
PLA–MC–C	65	–	–	$0.011 \pm 0.007^{A,b}$
	75	–	–	$0.015 \pm 0.005^{A,a}$
	85	–	–	$0.031 \pm 0.005^{B,b}$

[AB] Within a column, values with different uppercase letters are statistically different when compared within the same sample (α = 0.05, Tukey's HSD).

[ab] Within a column, values with different lowercase letters are statistically different when compared within the same temperature condition (α = 0.05, Tukey's HSD).

4.4.2.2 Molecular weight characterization

Figure 4.4a–d shows the MWDs of the samples during hydrolytic degradation in water at temperatures of 45 to 85 °C. Before the hydrolysis began, the MWDs of all samples had a similar overall profile with Mn ~71 kDa. The crystallinity of the initial long-chain PLA samples had no effect on the MWD characteristics compared to the fully amorphous sample. As the hydrolysis proceeded, PLA chains were cleaved into smaller segments, leading to a decrease in molecular weight, which resulted in a leftward shift of the MWDs on the graph, aligning with the lower molecular weight range. The MWD curves broadened over time and changed from a monomodal to bimodal or multimodal distributions, indicating the formation of two or multi-separate populations. This phenomenon has been reported extensively in the literature on the hydrolysis of PLA by researchers [16,42,43] with a general consensus that the presence of a crystalline fraction could enhance the chain scission reaction predominantly occurring at specific locations in the PLA chains, leaving behind more stable crystalline residues. In a previous work [44], we investigated the effects of different crystallization methods on the hydrolytic degradation of PLA samples with different L-lactide contents. We observed that both crystallization methods and chemical structures of PLA can impact the crystalline thickness as well as the specific MWD peak position of crystalline residues[44]. In addition, the specific MWD peaks can appear in more than one retention time, which may be attributed to one- or two-fold chains in the crystalline regions [16]. However, the present study focuses solely on melt-crystallization, and thus, the MWD peaks consistently appeared at two distinct retention times. These peaks are referred to as SP_L (specific peak at lower molecular weight) and SP_H (specific peak at higher molecular weight). During the later stage of hydrolysis, the intensity of SP_H decreased while SP_L increased. This could be attributed to chain scission occurring at the folding surface of the crystalline residue, as shown in **Figure 4.4d**.

Comparing the differences among the four samples, changes in MWD during hydrolysis at temperatures of 75 and 85 °C (**Figure 4.4c, d**) were similar. However, differences in the hydrolysis behavior were observed at the lower temperatures of 45 and 65 °C (**Figure 4.4a, b**). During the hydrolysis at low temperatures, the amorphous PLA–Q samples exhibited a slower degradation, while the highly crystalline PLA–MC–C samples evolved at a faster degradation rate than the other samples.

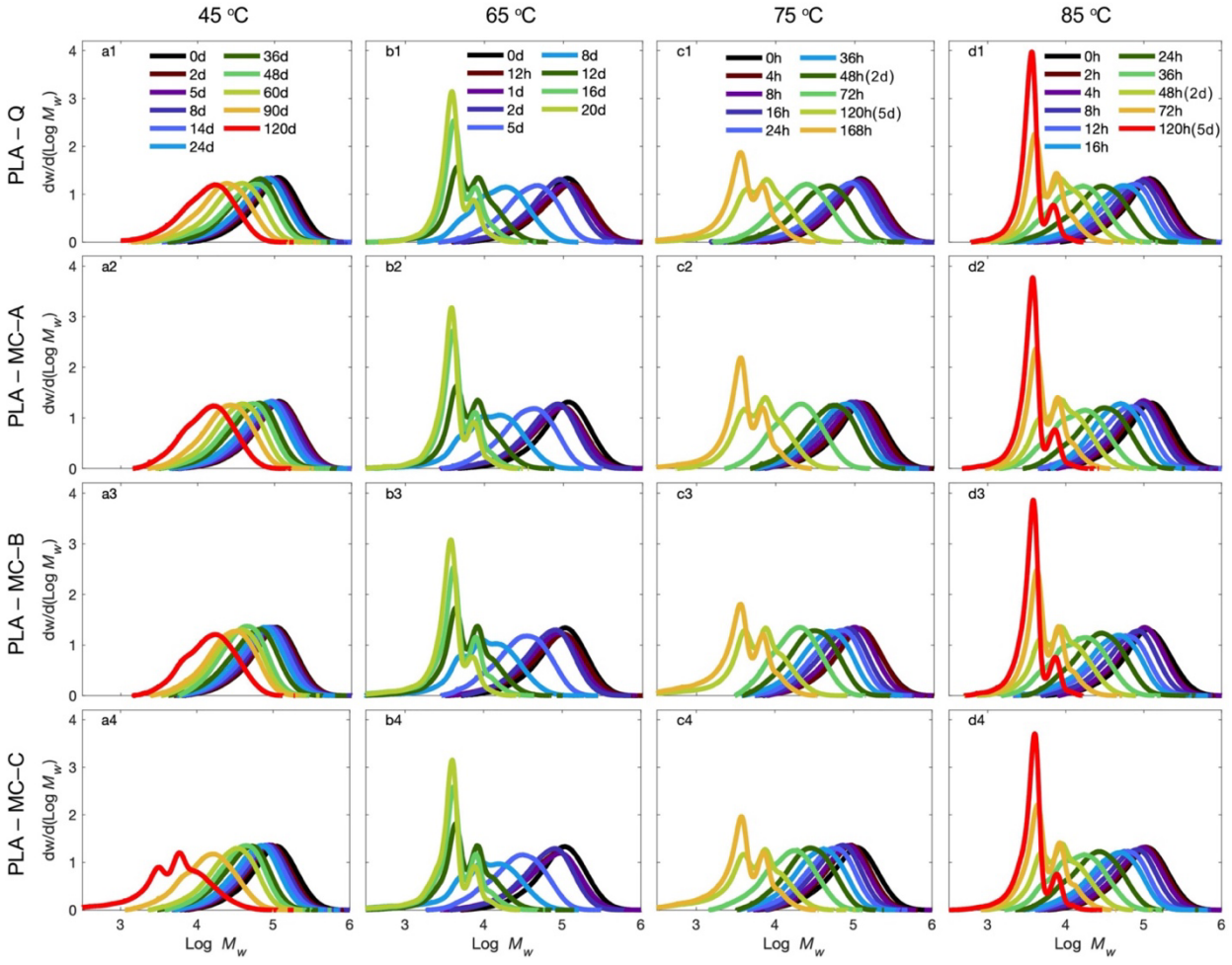

Figure 4.4 Molecular weight distribution during hydrolysis at 45 °C (a), 65 °C (b), 75 °C (c), and 85 °C (d) (columns) of PLA–Q (1), PLA–MC–A (2), PLA–MC–B (3) and PLA–MC–C (4) (rows).

Crystalline residues have been reported by researchers towards the later stage of hydrolysis due to the water-induced crystallization [41] and selective hydrolysis of the amorphous regions. To evaluate the kinetics of temperature-dependent hydrolysis, the deconvolution of MWD of specific peaks was carried out. **Figure 4.5a** shows examples of the deconvolution of the bimodal MWD for PLA–Q at 65 °C on 8, 12, 16, and 20 d. The deconvoluted peaks were assigned to one major population and the two narrow subpopulations due to SP_L and SP_H. The observed reduction in M_n of SP_L and SP_H, depicted in **Figure 4.5b,** aligns with previous studies on *in vitro* hydrolysis of crystalline residues by Tsuji and Ikarashi [45,46]. They reported a slow and linear decrease in M_n of crystalline residue over time. Additionally, the results show that the SP_L and SP_H at the end of the hydrolysis emerged at approximately 3.7 and 7.1 kDa, respectively. M_n of SP_L can be referred to as the molecular weight of a single chain of the one-fold in the crystalline region of PLA and can be converted to a lamellar thickness of approximately 11.69 nm. Accordingly, the measured lamellar thickness values for the present study were 11.50 nm for PLA–Q, 11.56 nm for PLA–MC–A, 11.69 nm for PLA–MC–B, and 11.99 nm for PLA–MC–C. On the other hand, SP_H can be referred to as a polymer chain with a length corresponding to the two-fold within the crystalline region, possessing twice the molecular weight of SP_L. The equation for thickness determination of the crystalline residue can be found in Eq. (A4.10), Appendix 4F**.** Further details and calculations regarding lamellar thickness can be found elsewhere in the literature [45–47].

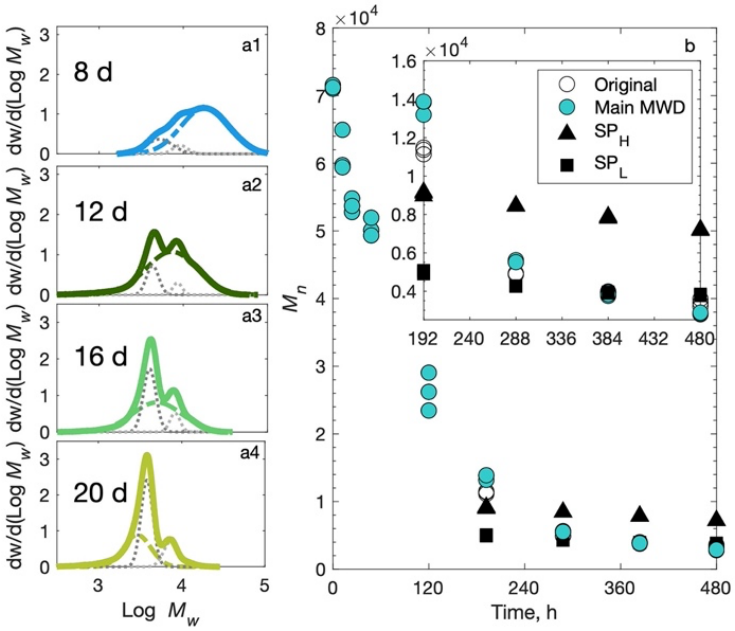

Figure 4.5 Deconvolution of MWD of PLA–Q during hydrolysis at 65 °C on 8, 12, 16, and 20 d (a1–a4) and the deconvoluted M_n as a function of time (b). The MWDs were deconvoluted to the main (—) and two specific (SP_L and SP_H) MWDs (···).

4.4.3 Estimation of hydrolysis rate constant

The hydrolysis rates were evaluated using simplified phenomenological models that considered both the molecular weight and crystallinity data. The M_n values were obtained from the original MWDs during the early stage of hydrolysis, while the deconvoluted main MWDs were from the later stage. The crystallization kinetics from **Table 4.2** were employed to simulate the time-dependent evaluation of the CF during hydrolysis. The RAF and MAF were being treated analogously as hydrolyzable fractions. A list of model parameters used for fitting the experimental data of hydrolytic degradation is provided in **Table A4.4**, Appendix 4E. **Figure 4.6** illustrates the normalized M_n as a function of hydrolysis time at various temperatures. The data points are accompanied by a model fitting based on Eq. (4.9). It shows that the normalized M_n among PLA samples with varying levels of crystallinity had minimal variation at lower temperatures (**Figure 4.6a, b, c**). Moreover, the difference in M_n at higher

temperature was not significant (**Figure 4.6d**). The phenomenological model offers a framework to treat the crystals as a nonhydrolyzable fraction within a polymer system, enabling the evaluation of rate constants associated with both noncatalytic (k_1) and autocatalytic (k_2) mechanisms for the hydrolyzable amorphous fractions (i.e., RAF and MAF). The noncatalytic hydrolysis of PLA involves the cleavage of ester bonds when exposed to water. In contrast, autocatalytic hydrolysis is facilitated by the carboxylic acid chain ends of oligomers [48]. The combination of these rate constants enhances the precision of the hydrolysis behavior representation and enables accurate predictions of the degradation trends over time. **Table 4.3** shows the rate constants of PLA samples as affected by temperature using Eqs. (4.5) and (4.9). At 45 °C, PLA–Q exhibited the slowest rate of noncatalytic hydrolysis (k_1), followed by PLA–MC–A, PLA–MC–B, and PLA–MC–C. Notably, samples with higher crystallinity, particularly PLA–MC–C, tended to display a significant increase in the rates of noncatalytic hydrolysis rate. Similarly, at 65 °C, PLA–MC–C also exhibited a faster noncatalytic rate than other samples. At 75 °C, the rate of hydrolysis in PLA–Q was comparable to that of PLA–MC–A, PLA–MC–B, and PLA–MC–C. Lastly, at 85 °C, although the group comparison of k_1 did not show significant differences, pairwise comparisons revealed significant differences between PLA–MC–C and PLA–Q. Interestingly, the autocatalytic rates (k_2) in the samples did not exhibit significant differences in all cases, except PLA–Q, which exhibited significantly higher autocatalytic rates at 85°C, suggesting that the degradation of the amorphous region tends to be accelerated by the oligomers produced during hydrolysis at the high temperature. Based on these findings, it could therefore be concluded that the T_g serves as a primary reference temperature for altering the hydrolysis reaction of PLA. At above the T_g, the PLA chains underwent reorganization and formed a crystalline structure, resulting in comparable hydrolysis rates among the samples. The hydrolysis stability of highly crystalline samples can be enhanced based on their specific

crystallization behavior. In contrast, below the T_g, the sample with higher crystallinity, PLA–MC–C, exhibited a faster hydrolysis rate compared to the other samples due to the immobilized chains of the RAF.

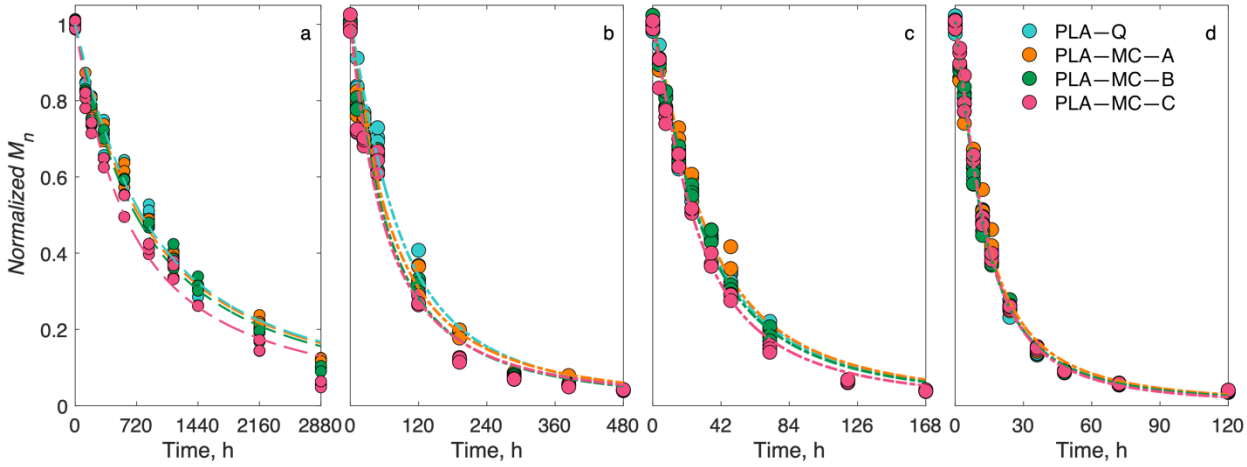

Figure 4.6 Normalized M_n during hydrolytic degradation of PLA samples at 45 (a), 65 (b), 75 (c), and 85 °C (d) by a model fitting based on Eq. (4.9).

Table 4.3 The rate constants k_1 (noncatalytic) and k_2 (autocatalytic) for PLA at different temperatures.

Treatments	Temperature			
	45 °C	65 °C	75 °C	85 °C
	k_1 ($\times 10^{-4} h^{-1}$)			
PLA–Q	0.0084 ± 0.0011 ^{A}	0.0696 ± 0.0157 ^{A}	0.2075 ± 0.0271 ^{A}	0.3985 ± 0.0402 ^{A}
PLA–MC–A	0.0099 ± 0.0011 ^{A}	0.1173 ± 0.0191 ^{AB}	0.1713 ± 0.0300 ^{A}	0.4195 ± 0.0589 ^{A}
PLA–MC–B	0.0113 ± 0.0015 ^{A}	0.1248 ± 0.0246 ^{AB}	0.1857 ± 0.0227 ^{A}	0.4260 ± 0.0333 ^{A}
PLA–MC–C	0.0156 ± 0.0019 ^{B}	0.1554 ± 0.0339 ^{B}	0.2116 ± 0.0256 ^{A}	0.3169 ± 0.0303 ^{A}
	k_2 ($\times 10^{-4} [mol^{-1} m^3]^{0.5} h^{-1}$)			
PLA–Q	0.0031 ± 0.0006 ^{a}	0.0636 ± 0.0089 ^{a}	0.1513 ± 0.0155 ^{a}	0.4182 ± 0.0245 ^{a}
PLA–MC–A	0.0025 ± 0.0005 ^{a}	0.0484 ± 0.0087 ^{a}	0.1386 ± 0.0170 ^{a}	0.3324 ± 0.0336 ^{b}
PLA–MC–B	0.0024 ± 0.0007 ^{a}	0.0492 ± 0.0110 ^{a}	0.1333 ± 0.0125 ^{a}	0.3343 ± 0.0125 ^{b}
PLA–MC–C	0.0024 ± 0.0008 ^{a}	0.0387 ± 0.0137 ^{a}	0.1366 ± 0.0132 ^{a}	0.3477 ± 0.0175 ^{b}

Within temperature columns, values of k_1 and k_2 with different uppercase and lowercase letters, respectively, are statistically different (α = 0.05 Tukey's HSD).

4.4.4 Influence of temperature on the hydrolytic degradation of PLA

The VTF equation was applied to model the temperature dependence of hydrolysis rates and relaxation times of the PLA samples. Vogel temperature (T_0) represents the temperature at which the sample deviates from following the Arrhenius behavior, which could serve as a critical temperature at which the samples undergo a transition in their behavior, including changes in chemical and physical processes, due to molecular mobility being influenced by the varying temperature conditions. [49]. In the study, to simplify the activation energy estimation process and avoid the complexities of nonlinear fitting, T_0 was set as 50 °C below its T_g [49]. **Figure 4.7** depicts the VTF plot, showing the natural logarithm of k_1 and k_2 plotted against the inverse of $T–T_0$. The slope of the plot represents the activation energy (E_a), while the intercept corresponds to the value of k_0. The specific values of E_a can be found in **Table 4.4**. Based on the estimated E_a values obtained from the noncatalytic hydrolysis rate constants of different samples, it can be observed that the amorphous and partially crystalline samples (PLA–Q, PLA–MC–A, and PLA–MC–B) had higher E_a values compared to the fully crystalline sample (PLA–MC–C). This suggests that the PLA hydrolysis rate is more temperature-dependent when there is a higher fraction of amorphous phase due to less ordered molecular structure and increased mobility of polymer chains. In contrast, crystalline PLA shows lower E_{ak1} values, indicating that hydrolysis rates are less influenced by temperature variation. Regarding the autocatalytic hydrolysis, the E_{ak2} values were not found to be significantly different among the samples, which suggests that the autocatalytic hydrolysis reaction was temperature independent across samples with different crystallinity.

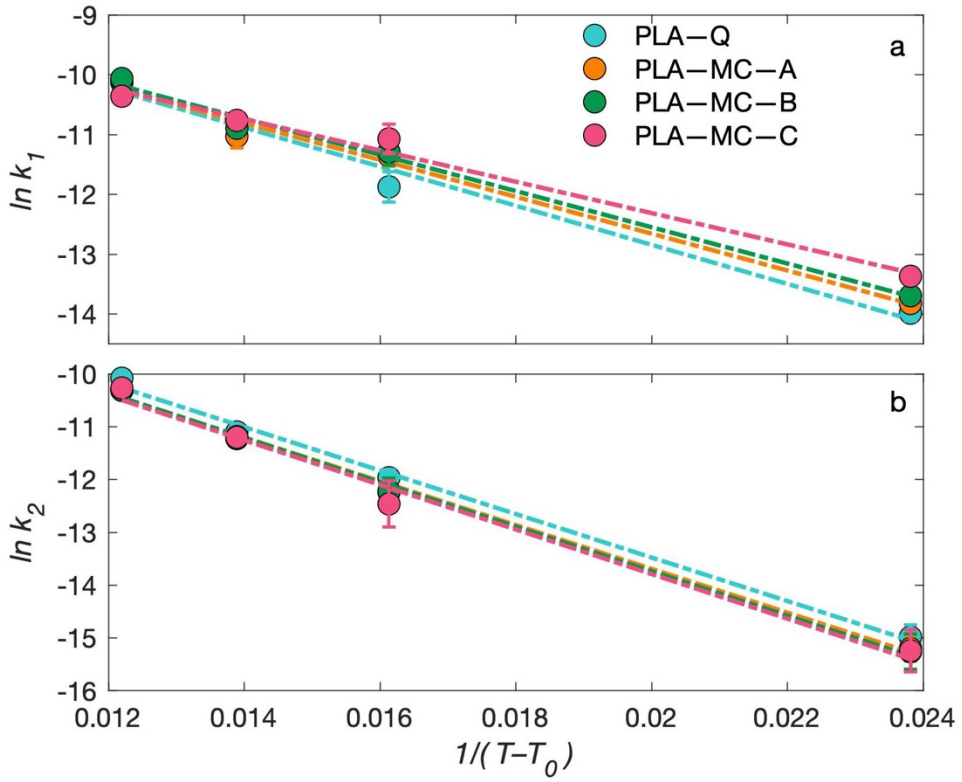

Figure 4.7 VTF plots of hydrolytic degradation of PLA different PLA samples at 45–85 °C for rate constants k_1 (a) and k_2 (b).

Table 4.4 Activation energies of rate constants k_1 (noncatalytic) and k_2 (autocatalytic) for PLA.

Sample	$E_{a_{k_1}}\ (J \cdot mol^{-1})$	$E_{a_{k_2}}(J \cdot mol^{-1})$
PLA–Q	2717 ± 133 ^{A}	3425 ± 100^{A}
PLA–MC–A	2560 ± 120 ^{A}	3446 ± 103 ^{A}
PLA–MC–B	2517 ± 99 ^{A}	3506 ± 113 ^{A}
PLA–MC–C	2176 ± 102 ^{B}	3511 ± 179 ^{A}

Within columns, values with different letters are statistically different (α = 0.05 Tukey's HSD) between samples.

4.4.5 Interpretation for real-world hydrolytic degradation

Hydrolytic degradation is a multifaceted phenomenon that depends on environmental conditions, material properties, and polymer characteristics [4]. In real-life scenarios, PLA hydrolysis has important implications when the polymers are exposed to water or moisture, leading to their breakdown and deterioration over time. However, the hydrolysis process is highly complex; phase structure analysis coupled with specific temperature conditions is crucial for obtaining meaningful insights into hydrolytic degradation.

An investigation of the three-phase structure of PLA films showed that the hydrolytic degradation of the polymer changes in the CF, RAF, and MAF. When PLA films are exposed to humid environments, the absorption of water molecules can facilitate the reorganization of PLA chains, forming a more ordered and crystalline structure. This effect is particularly pronounced at temperatures above T_g. Conversely, below T_g, the crystalline fraction remains unchanged for most of part the hydrolysis process due to the limited chain mobility. The crystallization process at low temperatures occurs after partial hydrolysis when the PLA chains become small enough to gain mobility and rearrange to form crystalline structures. In contrast, crystallization occurs at the beginning of the degradation process at elevated temperatures. It is noteworthy that the crystallization rate of PLA depends on their initial molecular morphology, including factors such as the pretreatment and crystallization processes. One fundamental rule in PLA hydrolysis is that the crystalline region had a slower hydrolysis rate than the amorphous regions [46,50].

The process of crystallization also leads to the formation of RAF, which acts as a boundary separating the MAF from the CF. As the CF increases, the RAF fraction also increases. The formation of RAF during PLA hydrolysis can lead to de-densification and an increase in free volume within the polymer matrix, leading to a decrease in density [51]. The study by Sangroniz et al. [12] reported that the CF and RAF could have inverse effects on the

diffusion coefficient of penetrants and transport properties of PLA. The interplay between CF and RAF in the hydrolysis of PLA can result in complex hydrolysis behavior, and their respective impacts on the degradation kinetics need to be carefully considered to elucidate the overall degradation behavior of PLA.

By considering the combined effects of temperature and the three-phase structure model, valuable insights can be gained into the kinetics of materials during hydrolytic degradation. Our findings indicate that at higher temperatures (up to 85 °C), samples with a higher crystallinity had a lower rate of hydrolysis compared to amorphous and partially crystalline samples. This observation highlights the significant role of the crystal structure at elevated temperatures, which provides increased resistance to water penetration and molecular degradation. Additionally, it is interesting to note that the RAF exhibits high molecular mobility and displays similar characteristics to the MAF. At 45 °C, which is below the *in-situ* T_g of PLA, an interesting observation was made that contradicts the findings at high-temperature conditions (e.g., 85°C). In PLA–MC–C, which exhibits a higher degree of crystallinity, the presence of the RAF becomes more prominent for PLA hydrolysis. PLA–MC–C demonstrated a faster rate of hydrolysis compared to their initial amorphous and partially crystalline counterparts. This finding suggests that the chains in RAF undergo full immobilization and maintain their de-densification effect. As a result, the PLA matrix develops more defects, making the material more susceptible to the hydrolysis processes. A similar phenomenon was observed at 65°C, which is above the T_g. This supports the notion that the RAF can be devitrified at temperatures higher than the T_g of the MAF. This unexpected trend suggests that the behavior of the three-phase structure of PLA during hydrolytic degradation can vary significantly depending on the temperature conditions. Unfortunately, measuring the amount of RAF during *in-situ* immersion tests at specific temperatures is currently not feasible. Further *in-situ* studies using alternative

characterization techniques can contribute to uncovering the three-phase behavior and provide a more comprehensive understanding of the degradation behavior of PLA.

4.5 Conclusion

Quantification of the phase structure allows for tracking the changes throughout the hydrolysis process, providing valuable insights into the relative amounts of the three-phase structure fractions. The results indicate that the degree of crystallinity significantly impacts the hydrolysis rate, with samples exhibiting higher crystallinity showing slower degradation compared to initially amorphous and partially crystalline samples depending on whether hydrolysis is conducted below or above the rubbery transition. By considering the qualitative aspect of the three-phase structure, this study reveals that temperature plays a crucial role in determining the behavior of the different phases within PLA. At higher temperatures, the crystalline regions exhibit increased stability and resistance to hydrolysis, which can be qualitatively observed through the kinetic rate of the sample with high crystallinity, while the mobility of the amorphous regions is influenced by the glass transition temperature. Moreover, the devitrification of the RAF can occur at temperatures below the glass transition, leading to dedensification effects and the creation of defects within the PLA matrix. The activation energy of each sample provides valuable insights into their sensitivity to temperature variation. In the case of the sample with higher crystallinity, it exhibits less sensitivity to temperature change, which can be attributed to the presence of defects and the limited mobility of the RAF within the material. As a result, the reaction rates at lower temperatures may increase and approach the rates observed at higher temperatures. Overall, this work enhances the understanding of the interplay between the three phase structures and environmental temperature in the hydrolytic degradation of PLA. The findings underscore the importance of considering both the quality and quantity of the phase structure when evaluating the degradation behavior of PLA. These insights are expected to be useful

during the design and development of more robust and durable PLA materials for packaging applications, as well as addressing PLA end-of-life scenarios such as chemical recycling and industrial composting for PLA.

4.6 Acknowledgements

W. L. would like to express gratitude to the Royal Thai Government for the financial support for a Ph.D. fellowship. R. A. acknowledges the USDA National Institute of Food and Agriculture and Michigan State University AgBioResearch, Hatch project number MICL02665 for partial support of the study.

REFERENCES

[1] Auras R., Harte B., and Selke S., An overview of polylactides as packaging materials, *Macromol. Biosci.*, vol. 4, no. 9, pp. 835–864, 2004, doi: 10.1002/mabi.200400043.

[2] Bher A., Cho Y., and Auras R., Boosting Degradation of Biodegradable Polymers, *Macromol. Rapid Commun.*, vol. 44, no. 5, 2023, doi: 10.1002/marc.202200769.

[3] Marano S., Laudadio E., Minnelli C., and Stipa P., Tailoring the Barrier Properties of PLA: A State-of-the-Art Review for Food Packaging Applications, *Polymers (Basel).*, vol. 14, no. 8, 2022, doi: 10.3390/polym14081626.

[4] Tsuji H., Hydrolytic Degradation, in *Poly(Lactic Acid)*, Hoboken, NJ, USA: Wiley, 2022, pp. 467–516.

[5] Gorrasi G. and Pantani R., Hydrolysis and Biodegradation of Poly(lactic acid), in *Advances in Polymer Science*, vol. 279, M. L. Di Lorenzo and R. Androsch, Eds. Cham: Springer International Publishing, 2017, pp. 119–151.

[6] Baltá-Calleja F. J. and Ezquerra T. A., Polymer Crystallization: General Concepts of Theory and Experiments, in *Encyclopedia of Materials: Science and Technology*, vol. 6, no. 10, Elsevier, 2001, pp. 7244–7252.

[7] Wunderlich B., Reversible crystallization and the rigid-amorphous phase in semicrystalline macromolecules, *Prog. Polym. Sci.*, vol. 28, no. 3, pp. 383–450, 2003, doi: 10.1016/S0079-6700(02)00085-0.

[8] Androsch R., Schick C., and Di Lorenzo M. L., Kinetics of Nucleation and Growth of Crystals of Poly(l-lactic acid), in *Synthesis, Structure and Properties of Poly(lactic acid)*, vol. 279, M. L. Di Lorenzo and R. Androsch, Eds. Cham: Springer International Publishing, 2018, pp. 235–272.

[9] Righetti M. C., Amorphous fractions of poly(lactic acid), *Adv. Polym. Sci.*, vol. 279, pp. 195–234, 2018, doi: 10.1007/12_2016_14.

[10] Esposito A., Delpouve N., Causin V., *et al.*, From a Three-Phase Model to a Continuous Description of Molecular Mobility in Semicrystalline Poly(hydroxybutyrate- co -hydroxyvalerate), *Macromolecules*, vol. 49, no. 13, pp. 4850–4861, Jul. 2016, doi: 10.1021/acs.macromol.6b00384.

[11] Di Lorenzo M. L. and Righetti M. C., Crystallization-induced formation of rigid amorphous fraction, *Polym. Cryst.*, vol. 1, no. 2, pp. 1–14, 2018, doi: 10.1002/pcr2.10023.

[12] Sangroniz A., Chaos A., Iriarte M., *et al.*, Influence of the Rigid Amorphous Fraction and Crystallinity on Polylactide Transport Properties, *Macromolecules*, vol. 51, no. 11, pp. 3923–3931, Jun. 2018, doi: 10.1021/acs.macromol.8b00833.

[13] Fernandes Nassar S., Guinault A., Delpouve N., *et al.*, Multi-scale analysis of the impact of polylactide morphology on gas barrier properties, *Polymer (Guildf).*, vol. 108,

pp. 163–172, 2017, doi: 10.1016/j.polymer.2016.11.047.

[14] Aliotta L., Gazzano M., Lazzeri A., and Righetti M. C., Constrained amorphous interphase in poly(l-lactic acid): Estimation of the Tensile elastic modulus, *ACS Omega*, vol. 5, no. 33, pp. 20890–20902, 2020, doi: 10.1021/acsomega.0c02330.

[15] Tsuji H. and Nakahara K., Poly(L-lactide): IX. Hydrolysis in acid media, *J. Appl. Polym. Sci.*, vol. 86, no. 1, pp. 186–194, 2002, doi: 10.1002/app.10813.

[16] Tsuji H. and Ikada Y., Properties and morphology of poly(L-lactide): IV. Effects of structural parameters on long-term hydrolysis of poly(L-lactide) in phosphate-buffered solution, *Polym. Degrad. Stab.*, vol. 67, no. 1, pp. 179–189, 2000, doi: 10.1016/S0141-3910(99)00111-1.

[17] Tsuji H., Mizuno A., and Ikada Y., Properties and morphology of poly(L-lactide). III. Effects of initial crystallinity on long-term in vitro hydrolysis of high molecular weight poly(L-lactide) film in phosphate-buffered solution, *J. Appl. Polym. Sci.*, vol. 77, no. 7, pp. 1452–1464, 2000, doi: 10.1002/1097-4628(20000815)77:7<1452::AID-APP7>3.0.CO;2-S.

[18] Huang Y., Chen F., Pan Y., *et al.*, Effect of hydrophobic fluoropolymer and crystallinity on the hydrolytic degradation of poly(lactic acid), *Eur. Polym. J.*, vol. 97, pp. 308–318, 2017, doi: 10.1016/j.eurpolymj.2017.09.044.

[19] Gorrasi G. and Pantani R., Effect of PLA grades and morphologies on hydrolytic degradation at composting temperature: Assessment of structural modification and kinetic parameters, *Polym. Degrad. Stab.*, vol. 98, no. 5, pp. 1006–1014, 2013, doi: 10.1016/j.polymdegradstab.2013.02.005.

[20] Zhang N., Yu X., Duan J., *et al.*, Comparison study of hydrolytic degradation behaviors between α'- and α-poly(l -lactide), *Polym. Degrad. Stab.*, vol. 148, pp. 1–9, Feb. 2018, doi: 10.1016/j.polymdegradstab.2017.12.014.

[21] Harris A. M. and Lee E. C., Heat and humidity performance of injection molded PLA for durable applications, *J. Appl. Polym. Sci.*, vol. 115, no. 3, pp. 1380–1389, Feb. 2010, doi: 10.1002/app.30815.

[22] Zhou Q. and Xanthos M., Nanoclay and crystallinity effects on the hydrolytic degradation of polylactides, *Polym. Degrad. Stab.*, vol. 93, no. 8, pp. 1450–1459, 2008, doi: 10.1016/j.polymdegradstab.2008.05.014.

[23] ASTM D4754-18, Standard Test Method for Two-Sided Liquid Extraction of Plastic Materials Using FDA Migration Cell, *ASTM Int. West Conshohocken, PA,* 2018, doi: 10.1520/D4754-18.

[24] Righetti M. C., Gazzano M., Di Lorenzo M. L., and Androsch R., Enthalpy of melting of α′- and α-crystals of poly(l-lactic acid), *Eur. Polym. J.*, vol. 70, pp. 215–220, Sep. 2015, doi: 10.1016/j.eurpolymj.2015.07.024.

[25] Wojdyr M., Fityk: A general-purpose peak fitting program, *J. Appl. Crystallogr.*, vol.

43, no. 5 PART 1, pp. 1126–1128, 2010, doi: 10.1107/S0021889810030499.

[26] Dorgan J. R., Janzen J., Knauss D. M., *et al.*, Fundamental solution and single-chain properties of polylactides, *J. Polym. Sci. Part B Polym. Phys.*, vol. 43, no. 21, pp. 3100–3111, 2005, doi: 10.1002/polb.20577.

[27] Pan J., *Modelling Degradation of Bioresorbable Polymeric Medical Devices*. Elsevier, 2015.

[28] Gleadall A., Pan J., and Atkinson H., A simplified theory of crystallisation induced by polymer chain scissions for biodegradable polyesters, *Polym. Degrad. Stab.*, vol. 97, no. 9, pp. 1616–1620, 2012, doi: 10.1016/j.polymdegradstab.2012.06.023.

[29] Han X., Pan J., Buchanan F., *et al.*, Analysis of degradation data of poly(l-lactide–co-l,d-lactide) and poly(l-lactide) obtained at elevated and physiological temperatures using mathematical models, *Acta Biomater.*, vol. 6, no. 10, pp. 3882–3889, Oct. 2010, doi: 10.1016/j.actbio.2010.05.015.

[30] Wang Y., Pan J., Han X., *et al.*, A phenomenological model for the degradation of biodegradable polymers, *Biomaterials*, vol. 29, no. 23, pp. 3393–3401, 2008, doi: 10.1016/j.biomaterials.2008.04.042.

[31] Sevim K. and Pan J., A model for hydrolytic degradation and erosion of biodegradable polymers, *Acta Biomater.*, vol. 66, pp. 192–199, Jan. 2018, doi: 10.1016/j.actbio.2017.11.023.

[32] Trachenko K., The Vogel-Fulcher-Tammann law in the elastic theory of glass transition, *J. Non. Cryst. Solids*, vol. 354, no. 32, pp. 3903–3906, 2008, doi: 10.1016/j.jnoncrysol.2008.05.021.

[33] Lyu S. P., Schley J., Loy B., *et al.*, Kinetics and time-temperature equivalence of polymer degradation, *Biomacromolecules*, vol. 8, no. 7, pp. 2301–2310, 2007, doi: 10.1021/bm070313n.

[34] Limsukon W., Auras R., and Selke S., Hydrolytic degradation and lifetime prediction of poly(lactic acid) modified with a multifunctional epoxy-based chain extender, *Polym. Test.*, vol. 80, no. September, p. 106108, Dec. 2019, doi: 10.1016/j.polymertesting.2019.106108.

[35] Shan G. F., Yang W., Tang X. G., *et al.*, Multiple melting behaviour of annealed crystalline polymers, *Polym. Test.*, vol. 29, no. 2, pp. 273–280, 2010, doi: 10.1016/j.polymertesting.2009.11.011.

[36] Di Lorenzo M. L., Calorimetric analysis of the multiple melting behavior of poly(L-lactic acid), *J. Appl. Polym. Sci.*, vol. 100, no. 4, pp. 3145–3151, 2006, doi: 10.1002/app.23136.

[37] Ma B., Wang X., He Y., *et al.*, Effect of poly(lactic acid) crystallization on its mechanical and heat resistance performances, *Polymer (Guildf).*, vol. 212, no. September 2020, p. 123280, 2021, doi: 10.1016/j.polymer.2020.123280.

[38] Pyda M. and Czerniecka-Kubicka A., Thermal properties and thermodynamics of poly(L-lactic acid), *Adv. Polym. Sci.*, vol. 279, pp. 153–193, 2018, doi: 10.1007/12_2017_19.

[39] Schick C., Wurm A., and Mohammed A., Formation and disappearance of the rigid amorphous fraction in semicrystalline polymers revealed from frequency dependent heat capacity, *Thermochim. Acta*, vol. 396, no. 1–2, pp. 119–132, 2003, doi: 10.1016/S0040-6031(02)00526-9.

[40] Tham W. L., Poh B. T., Mohd Ishak Z. A., and Chow W. S., Water Absorption Kinetics and Hygrothermal Aging of Poly(lactic acid) Containing Halloysite Nanoclay and Maleated Rubber, *J. Polym. Environ.*, vol. 23, no. 2, pp. 242–250, 2015, doi: 10.1007/s10924-014-0699-y.

[41] Iñiguez-Franco F., Auras R., Burgess G., *et al.*, Concurrent solvent induced crystallization and hydrolytic degradation of PLA by water-ethanol solutions, *Polymer (Guildf).*, vol. 99, pp. 315–323, Sep. 2016, doi: 10.1016/j.polymer.2016.07.018.

[42] Li S., Garreau H., and Vert M., Structure-property relationships in the case of the degradation of massive poly(α-hydroxy acids) in aqueous media - Part 3 Influence of the morphology of poly(l-lactic acid), *J. Mater. Sci. Mater. Med.*, vol. 1, no. 4, pp. 198–206, 1990, doi: 10.1007/BF00701077.

[43] Iñiguez-Franco F., Auras R., Dolan K., *et al.*, Chemical recycling of poly(lactic acid) by water-ethanol solutions, *Polym. Degrad. Stab.*, vol. 149, no. November 2017, pp. 28–38, 2018, doi: 10.1016/j.polymdegradstab.2018.01.016.

[44] Limsukon W., Auras R., and Smith T., Effects of the Three-Phase Crystallization Behavior on the Hydrolysis of Amorphous and Semicrystalline Poly(lactic acid)s, *ACS Appl. Polym. Mater.*, vol. 3, no. 11, pp. 5920–5931, Nov. 2021, doi: 10.1021/acsapm.1c01080.

[45] Tsuji H., In vitro hydrolysis of poly(L-lactide) crystalline residues as extended-chain crystallites. Part I: long-term hydrolysis in phosphate-buffered solution at 37°C, *Biomaterials*, vol. 25, no. 24, pp. 5449–5455, Nov. 2004, doi: 10.1016/j.biomaterials.2003.12.053.

[46] Tsuji H. and Ikarashi K., In Vitro Hydrolysis of Poly(L-lactide) Crystalline Residues as Extended-Chain Crystallites: II. Effects of Hydrolysis Temperature, *Polym. Degrad. Stab.*, vol. 85, no. 1, pp. 647–656, Jul. 2004, doi: 10.1016/j.polymdegradstab.2004.03.004.

[47] Tsuji H. and Miyauchi S., Poly(l-lactide): VI Effects of crystallinity on enzymatic hydrolysis of poly(l-lactide) without free amorphous region, *Polym. Degrad. Stab.*, vol. 71, no. 3, pp. 415–424, Jan. 2001, doi: 10.1016/S0141-3910(00)00191-9.

[48] Gleadall A., Pan J., Kruft M.-A., and Kellomäki M., Degradation mechanisms of bioresorbable polyesters. Part 1. Effects of random scission, end scission and autocatalysis, *Acta Biomater.*, vol. 10, no. 5, pp. 2223–2232, May 2014, doi:

10.1016/j.actbio.2013.12.039.

[49] Diederichsen K. M., Buss H. G., and McCloskey B. D., The Compensation Effect in the Vogel-Tammann-Fulcher (VTF) Equation for Polymer-Based Electrolytes, *Macromolecules*, vol. 50, no. 10, pp. 3831–3840, 2017, doi: 10.1021/acs.macromol.7b00423.

[50] Joziasse C. A. P., Grijpma D. W., Bergsma J. E., *et al.*, The influence of morphology on the (hydrolytic degradation of as polymerized and hot drawn poly(L-lactide)), *Colloid Polym. Sci.*, vol. 276, no. 11, pp. 968–975, 1998, doi: 10.1007/s003960050335.

[51] del Río J., Etxeberria A., López-Rodríguez N., *et al.*, A PALS Contribution to the Supramolecular Structure of Poly(L-lactide), *Macromolecules*, vol. 43, no. 10, pp. 4698–4707, May 2010, doi: 10.1021/ma902247y.

[52] Day M., Nawaby A. V., and Liao X., A DSC study of the crystallization behaviour of polylactic acid and its nanocomposites, *J. Therm. Anal. Calorim.*, vol. 86, no. 3, pp. 623–629, 2006, doi: 10.1007/s10973-006-7717-9.

[53] Lim L. T., Auras R., and Rubino M., Processing technologies for poly(lactic acid), *Prog. Polym. Sci.*, vol. 33, no. 8, pp. 820–852, 2008, doi: 10.1016/j.progpolymsci.2008.05.004.

APPENDIX 4A: DSC STUDY OF THE ISOTHERMAL CRYSTALLIZATION

The conditions for the isothermal crystallization of PLA by DSC were adapted from Day et al. [52] so that the appropriate crystallization time needed to achieve the desired crystallinity could be established. Film samples processed from the cast-film extruder were packed and sealed in a standard aluminum pan. The samples were heated to 180 °C at a heating rate of 5 °C min^{-1} for 8 min to erase the thermal history, and they were rapidly cooled at a heating rate of 20 °C min^{-1} to 122 °C, followed by a slow heating rate of 5 °C min^{-1} to achieve the crystallization temperature of 120 °C.

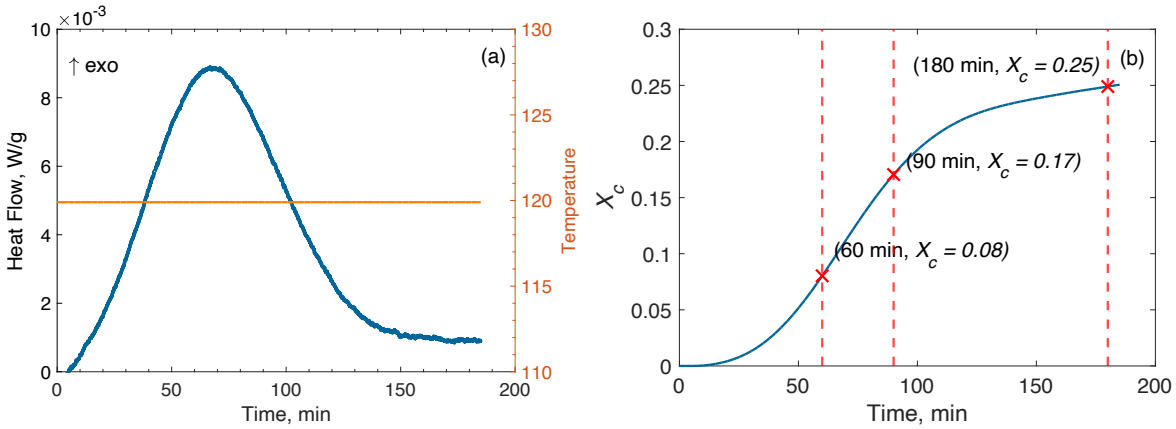

Figure A4.1 (a) DSC curve and (b) crystalline fraction of PLA film during DSC isothermal crystallization at 120 °C.

APPENDIX 4B: DETERMINATION OF THE ENTHALPY OF MELTING

The enthalpy of melting of 100% crystalline PLA (ΔH_m^0) of the α-crystals was determined using the method previously developed by Righetti et al. [24] based on DSC and wide-angle X-ray diffraction techniques. Analysis of the WAXD was conducted on a Bruker AXS D8 Advance X-ray diffractometer (Bruker Co.,) equipped with a Global Mirror Filter Cu Kα radiation source operating at 40 kV 100 mA. The diffractogram was recorded between a 2θ range from 2° and 40° at a rate of 0.24° min^{-1} and an increment of 0.01°. WAXD analysis was performed to provide the crystallinity and crystal modification. The enthalpies of crystallization of 100% crystalline can be expressed as Eq. (A4.1):

$$\Delta H_c^0\ (T_C) = \frac{\Delta H_c(T_C)}{X_{c_{(WAXD)}}} \tag{A4.1}$$

According to the temperature-dependence of the specific heat capacities of the solid and liquid, $\Delta H_c^0(T_C) = -\Delta H_c^0(T_C)$. The temperature evolution of enthalpy of melting of 100% crystalline was derived using the following Eq. (A4.2):

$$\Delta H_m^0\ (T) = \Delta H_m^0\ (T_C) + \int_{T_C}^{T} \left[C_p^l(T') - C_p^s(T')\right] dT' \tag{A4.2}$$

where C_p^l and C_p^s are the specific heat capacities for the liquid and solid states, respectively, fitted to the following linear function expressed as Eq. (A4.3):

$$\left[C_p^l(T') - C_p^s(T')\right] = 0.63 - 0.0028T\ (\mathrm{J\ g^{-1}\ K^{-1}}) \tag{A4.3}$$

By replacing equation S3 into S2, $\Delta H_m^0\ (T_m)$ can be determined by the following Eq. (A4.4):

$$\Delta H_m^0\ (T_m) = \Delta H_m^0\ (T_C) - 54.94 + \left(0.63\ T_m - 0.0014\ {T_m}^2\right) \tag{A4.4}$$

The values obtained from DSC and WAXD profiles are summarized in **Table A4.1**. So, the ΔH_m^0 of the α-crystals crystallized at 120 °C used in this work was 139 J g^{-1}, which is close to the ΔH_m^0 of the α-crystals of PLLA crystallized at 180 °C of 143 J g^{-1} reported by Righetti et al. [24].

Table A4.1 The value of the parameters to determine ΔH_m^0 of PLA.

Parameters	Source of characterization	Parameter value
ΔH_c(120 °C)	DSC	33.1 J g^{-1}
X_c	WAXD	0.253
ΔH_c^0 , ΔH_m^0 (120 °C)	Eq. (A4.4)	131 J g^{-1}
T_m	DSC	154 ℃
ΔH_m^0 (154 °C)	Eq. (A4.4)	139 J g^{-1}

APPENDIX 4C: CRYSTALLIZATION KINETICS

The kinetics of isothermal crystallization of PLA during hydrolysis can be described in two consecutive processes, the primary and secondary crystallization process.

First, for the fully amorphous film, PLA–Q, the primary crystallization process can be estimated using the Avrami equation:

$$X_c(t) = X_p = 1 - \exp\left(-K_p t^n\right) \tag{A4.5}$$

where $X_c(t)$ is the time-dependent fraction of crystallinity, X_p and K_p are the primary crystallinity and crystallization rate constant, t is the hydrolysis time, and n is the Avrami exponent indicating the mode of the dimension of crystal growth.

Second, for the fully crystallized film, PLA–MC–C, the secondary crystallization equation following the root-time dependence model can be used as follows Eq.(A4.6):

$$X_c(t) = X_s = X_{pt}(1 + K_s t^{1/2}) \tag{A4.6}$$

where X_{pt} is the crystallinity at the end of the primary crystallization. X_s and K_s are the secondary crystallinity, and crystallization rate constant.

Finally, for the partially crystallized films, PLA–MC–A and PLA–MC–B, the equations for primary and secondary crystallization equations are combined and presented as the following Eq. (A4.7):

$$X_c(t) = X_p + X_s = 1 - \exp\left(-K_p t^n\right) + X_{pt}(1 + K_s t^{1/2}) \tag{A4.7}$$

For the purpose of parametrization, the value of n in Eq. (A4.7) was obtained through the parametrization of Eq. (A4.5) for each temperature. This value represents the specific characteristic Avrami exponent of the crystals at each temperature.

APPENDIX 4D: DENSITY MEASUREMENT

The densities of films were measured at 23±0.1 °C by an auto density measurement system model 21-25 (Testing Machines, Inc., Delaware, USA). The density range of the column was formed by mixing two fluids, water and concentrated calcium nitrate solution. To achieve the densities of the three-phase structure, the density of fully amorphous sample can be defined as the density of MAF to determine those of CF and RAF as:

$$\frac{1}{\rho} = \frac{X_{MAF}}{\rho_{MAF}} + \frac{X_{RAF}}{\rho_{RAF}} + \frac{X_C}{\rho_{CF}} \quad \text{(A4.8)}$$

where ρ is the total density of the sample film; and ρ_{MAF}, ρ_{RAF}, and ρ_{CF} represent the density of the three phases, MAF, RAF, and CF, respectively, which are assumed to be constant. The density of each phase in shown in **Table A4.2**.

The densities of the samples were calculated and adjusted to compensate for the effects of the hydrolysis temperature. It is assumed that the density of the samples is dependent on temperature according to the following relationship:

$$\rho = \rho_0(1 - \alpha(T - T_0)) \quad \text{(A4.9)}$$

where ρ_0 is the reference density at temperature T_0 (23 °C) and α is the thermal expansion coefficient of PLA = 0.00007 °C^{-1} [53]. Adjusted densities of each sample are shown in **Table A4.3**.

Table A4.2 Density (g cm^{-3}) of MAF, RAF, and CF (at 23 °C).

ρ_{MAF}	ρ_{RAF}	ρ_{CF}
1.231±0.005A	1.229± 0.004A	1.312 ±0.002B

Table A4.3 Density (g cm^{-3}) of PLA samples (ρ_{PLA}) at the hydrolysis temperatures.

T, °C	PLA–Q	PLA–MC–A	PLA–MC–B	PLA–MC–C
23 (T_0)	1.231	1.237	1.244	1.254
45	1.229	1.235	1.242	1.252
65	1.227	1.233	1.240	1.250
75	1.227	1.232	1.239	1.249
85	1.226	1.231	1.238	1.248

APPENDIX 4E: PARAMETERIZATION FOR PHENOMENOLOGICAL MODELS

Table A4.4 A list of model parameters used for fitting the experimental data of hydrolytic degradation.

Model parameters	Unit	Value
N_{chain_0}	mol m^{-3}	ρ_{PLA}/M_n
C_{E_0}	mol m^{-3}	ρ_{PLA}/M_{n_0}; $M_{n_0} = 72$ g mol^{-1}
C_{ol_0}	mol m^{-3}	$C_{E_0}\times 10^{-12}$
ω	mol m^{-3}	ρ_{CF}/M_{n_0}
α	No unit	0.4
β	No unit	1
m	No unit	4

APPENDIX 4F: THICKNESS OF CRYSTALLINE RESIDUE

The crystalline thickness of the PLA film after hydrolysis can be estimated from the specific molecular weight given below, Eq. (A4.10) [46]:

$$l_c(nm) = (0.288 \times M_n)/M_0 \quad \text{(A4.10)}$$

where M_n is the molecular weight of the crystalline residue after hydrolysis. The crystalline residue is assumed to be 10_3 helix with a length of 28.8 nm along the C-axis; and M_0 is the molecular weight of the repeating unit of PLA, which is equal to 72 g mol^{-1}.

CHAPTER 5: THE HYDROLYTIC DEGRADATION MODELING FOR MOLECULAR WEIGHT DISTRIBUTION SIMULATION USING POPULATION BALANCE

5.1 Introduction

Hydrolytic degradation is a crucial chemical process that plays a vital role throughout the life cycle of poly (lactic acid) (PLA). The vulnerability of PLA to hydrolytic degradation has significant implications for its production phase, during application, or in its eventual disposal. The ideal scenario for PLA-based products involves not only maintaining their quality and performance over an intended period of use but also ensuring that they can be composted in an environmentally friendly manner within a relatively short timeframe. Understanding PLA hydrolytic degradation is vital for balancing between durability and degradability to maximize the utility and sustainability of PLA for various applications.

During hydrolysis, water molecules penetrate into amorphous regions and randomly cleave the ester bonds along the PLA chains, resulting in the formation of smaller PLA chains, oligomers, and monomers. The reaction can be catalyzed by H^+ ions, which may exist within the material. This includes the carboxylic end groups with a high degree of acid dissociation, contributing to the autocatalytic nature of the process [1,2].

All polymers are polydisperse composed of various polymer chains of different lengths. The diversity in chain length within a polymer material is represented as a molecular weight distribution (MWD). As a result, the molecular weight of a polymer is typically expressed as an average molecular weight, including number-average (M_n) and weight-average molecular weight (M_w), calculated from the molecular weights of all the chains in the sample. The degree of dispersion in the MWD is called polydispersity ($Đ$) [3]. The measurement approach for average molecular weight has found common usage for tracking molecular weight changes and kinetics in processes owing to its simplicity [4–8]. Nonetheless, this approach does not

furnish a comprehensive molecular weight distribution encompassing the entire polymer population, lacking a detailed molecular interpretation.

Researchers have investigated the kinetics of PLA hydrolytic degradation [9–14]. They observed that the MWD profiles of PLA evolve similarly during hydrolysis. Typically, in the initial stages of hydrolysis, there is a reduction in the molecular weight of PLA due to ester bond cleavage, leading to the shifting of MWD toward lower molecular weight. As degradation progresses, the MWD tends to broaden, indicating a wider range of chain length distribution within the polymer population. Finally, at the late hydrolysis stage, the MWD tends to split from an unimodal to a bimodal (or multimodal) distribution due to the differences in degradation rates and mechanisms of each component [10,15]. Additionally, the formation of crystalline regions may lead to scission at specific sites, resulting in nonhydrolyzable residues, also known as crystal residues [16].

Furthermore, distinct MWD profiles can also be observed prior to hydrolysis, and these profiles may undergo alterations due to factors such as the integration of a chain extender in neat PLA [8,17] or PLA/copolymer blends [18]. Merely focusing on average molecular weight and polydispersity index is inadequate to accurately elucidate the hydrolysis of PLA. Instead, determining the evolution in the entire MWD can offer a deeper mechanistic insight of the entire molecular system during hydrolysis. Moreover, it can provide more insight for focusing on and targeting specific subpopulations.

Perejon et al. [19] introduced an intriguing alternative for handling the kinetic analysis of complex processes. They proposed that complex processes involving several overlapping reactions could be separated into individual processes through peak deconvolution. Each of the individual curves contributes to its respective independent process in this approach. The deconvolution procedure was applied in degradation studies of PLA to fit the average molecular weight of the main peak to the first order of the kinetic reaction

[8,20,21]. However, the subpopulations were ignored when determining the rate constant. In contrast to the previous method, the entire MWD can be considered using the Monte Carlo approach, as found in previous studies, allowing for a more complete representation of the overall MWD during the hydrolytic degradation [22,23]. Alternatively, a population balance model was also employed to describe degradation systems, including the hydrolytic degradation of cellulose and hemicellulose [24,25], enzymatic chain-end scission of polysaccharides [26], and thermal degradation of poly(propylene carbonate) [27]. This model allows predicting the dynamics of distributed properties.

In this chapter, we introduce a population balance approach to explain how hydrolytic degradation occurs in PLA by using fundamental theory and potential hydrolysis pathway scenarios to create a simulation representing the entire MWD. The primary objective is to understand the kinetics of PLA hydrolysis comprehensively. To accomplish this, previously collected MWD data obtained from the study of PLA film degradation in water [28] were utilized. The methodology involved the application of a population balance model (PBM) and the high-order moment-conserving method of classes, as proposed by Alopaeus et al. [29] was used. Initially, the model was adopted as a simple representation, focusing on random scission, but later, it was refined to better align with experimental data. Subsequently, simulations of the MWD were conducted to predict the hydrolytic degradation under different scenarios.

5.2 Background of the study

The modeling of the hydrolytic degradation for PLA has been extensively studied to serve several significant purposes. It can be summarized into the following three main reasons [30]:

- To gain a comprehensive understanding of the underlying degradation mechanisms

- To consolidate data and compare the different materials' characteristics or conditions
- To predict the long-term material properties under accelerated conditions for practical implementation

The simplest way to monitor the hydrolysis process of PLA is to determine changes in the M_n versus the hydrolysis time, assuming that water molecules randomly hydrolyze the PLA ester bonds. Hydrolysis kinetics can be generally described by the pseudo-zero-order, first-order, and second-order kinetic models. **Figure 5.1** illustrates the experimental data of hydrolysis experiments conducted at 45 °C (**Figure 5.1a, b**) and 65 °C (**Figure 5.1c, d**) obtained from the previous experiments [28]. The pseudo-zero-order kinetics involves plotting the reciprocal of M_n against time to obtain a linear plot representing the basic noncatalytic hydrolysis. Alternatively, the first-order kinetic fitting shows the change in M_n over time, considering autocatalytic hydrolysis by the carboxylic end group [30].

Both zero and first-order models demonstrate a good fit with the M_n experimental data at 45 °C and 65 °C, with the coefficient of determination (R^2) values remained between 0.94 and 0.99. As mentioned in Farrar's review [30], the autocatalytic rate (k_2) typically gives the best fit under normal circumstances in the majority of the degradation studies of bioresorbable polymers [4,5,7,13,20,32]. Moreover, the impact of hydrolysis may lead to an increase in crystallinity and the loss of small oligomer chains during the process, which, in turn, is reflected in the data, deviating from the predicted trend.

As thoroughly discussed in Chapter 4, the phenomenological model provides an insight on the interplay between the noncatalytic and autocatalytic hydrolysis. The reduction of M_n and the increase in the total ester units of all the short chains per unit volume (C_{ol}) during hydrolysis at 45 °C and 65 °C are shown in **Figure 5.1e, f.** This model fits the experimental data well and offers a significant understanding of the underlying mechanisms.

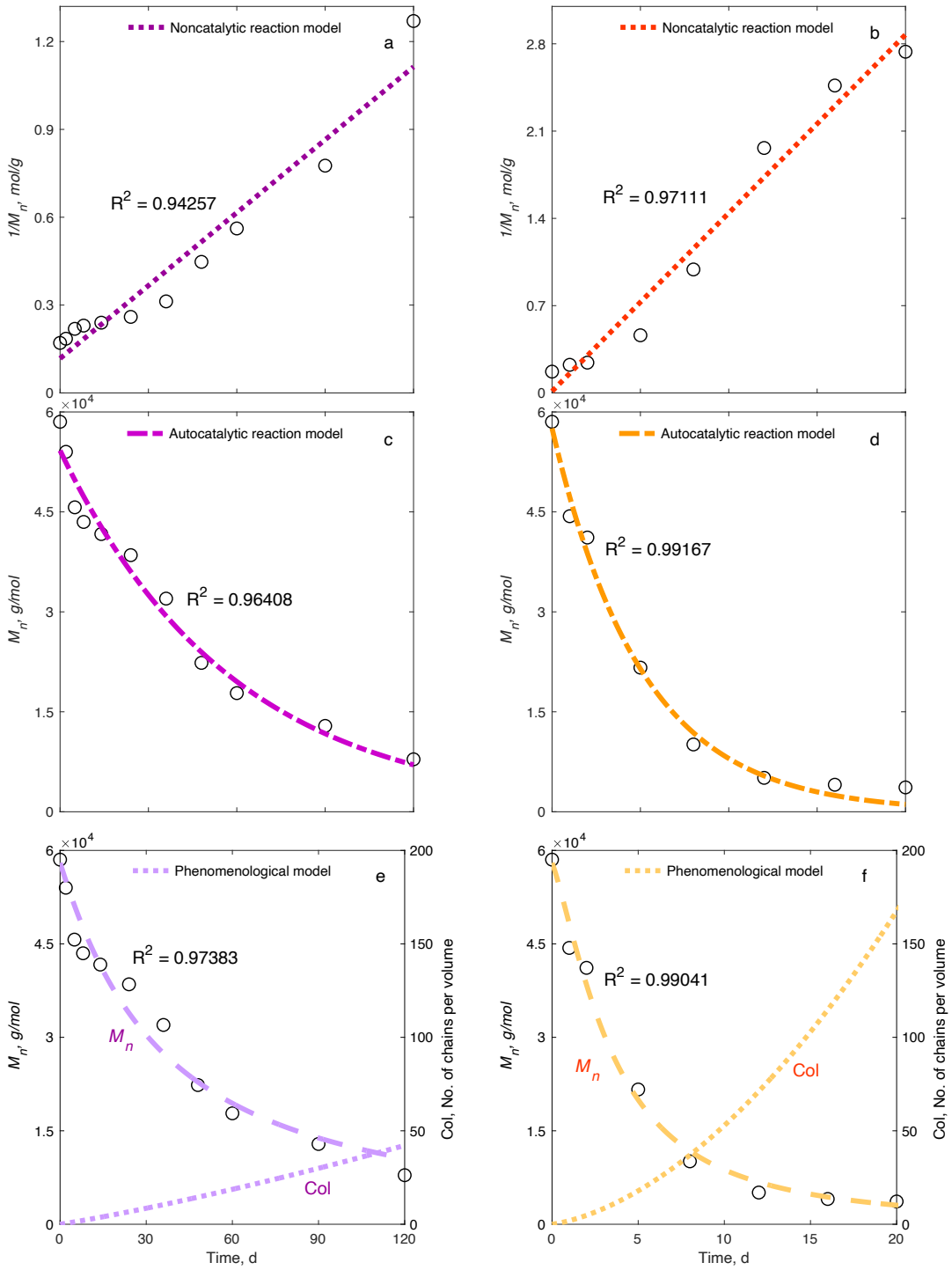

Figure 5.1 Changing in M_n vs hydrolysis time of PLA film in water at 45 °C (a, c, e) and 65 °C (b, d, f) fitting to the noncatalytic reaction, autocatalytic reaction, and phenomenological models. The symbol ○ represents the experimental M_n. The dashed and dotted lines represent the predicted M_n and C_{ol}, respectively.

Although the development of the phenomenological model can assist in fitting experimental data, polymers are macromolecules composed of chains, and for PLA, its degree of polymerization often exceeds 8 k units or 500 kDa. Relying solely on a single weight average to characterize the entire distribution may not provide a comprehensive understanding of the system. Modeling the MWD, however, can provide a holistic perspective and a broader understanding. **Figure 5.2** shows the entire MWD in the form of a plot of dw/d(log MW) versus log MW as a function of the hydrolysis time at 45 °C (**Figure 5.2a**) and 65 °C (**Figure 5.2b**). The line with arrows represents the prediction estimated from the phenomenological models showing the direction of the hydrolysis process. Notably, the reduction of M_n does not represent the changes in a broadening of polymer dispersity due to random chain scission [22,33].

Furthermore, shoulders are evident on the lower molecular weight side at 120 and 8 d for 45 and 65 °C, respectively, corresponding to the M_n values of approximately 7 kDa. For the 65 °C hydrolysis, the bimodal distribution becomes apparent in the later stages, indicating a significant difference between two or multiple separate populations. According to our previous work [28], this observation could be attributed to the rapid hydrolysis-induced crystallization occurring at temperatures above the T_g of PLA. Therefore, fitting the entire population's experimental data with standard MWD could make the prediction inaccurate.

It has been widely accepted that MWD analysis is crucial for the characterization and understanding of the hydrolysis process. Polymeric materials with different initial MWDs exhibit diverse behaviors during degradation, even when they possess the same initial average molecular weight [22]. The comprehensive analysis of MWD is therefore crucial. However, in many studies, the MWD is presented to offer an overview and comparison of the evolution of MWD for the samples of interest. Moreover, the determination of MWD towards the later stage of hydrolysis is lacking. This may be the result of selective degradation among

phases, which can occur in neat PLA [11,16,35] or its blends [36]. Additionally, under certain hydrolysis conditions, such as those in composts, it is practically not possible to retrieve the samples from the later stages due to the rapid disintegration of the material [37]. In the absence of this crucial information, a comprehensive analysis of the polymer's degradation progression could be hindered. It would be highly beneficial to explore the intricacies of the MWD for accurate prediction of the degradation of the low molecular weight chains and provide a comprehensive understanding of the transitional stages of their evolution.

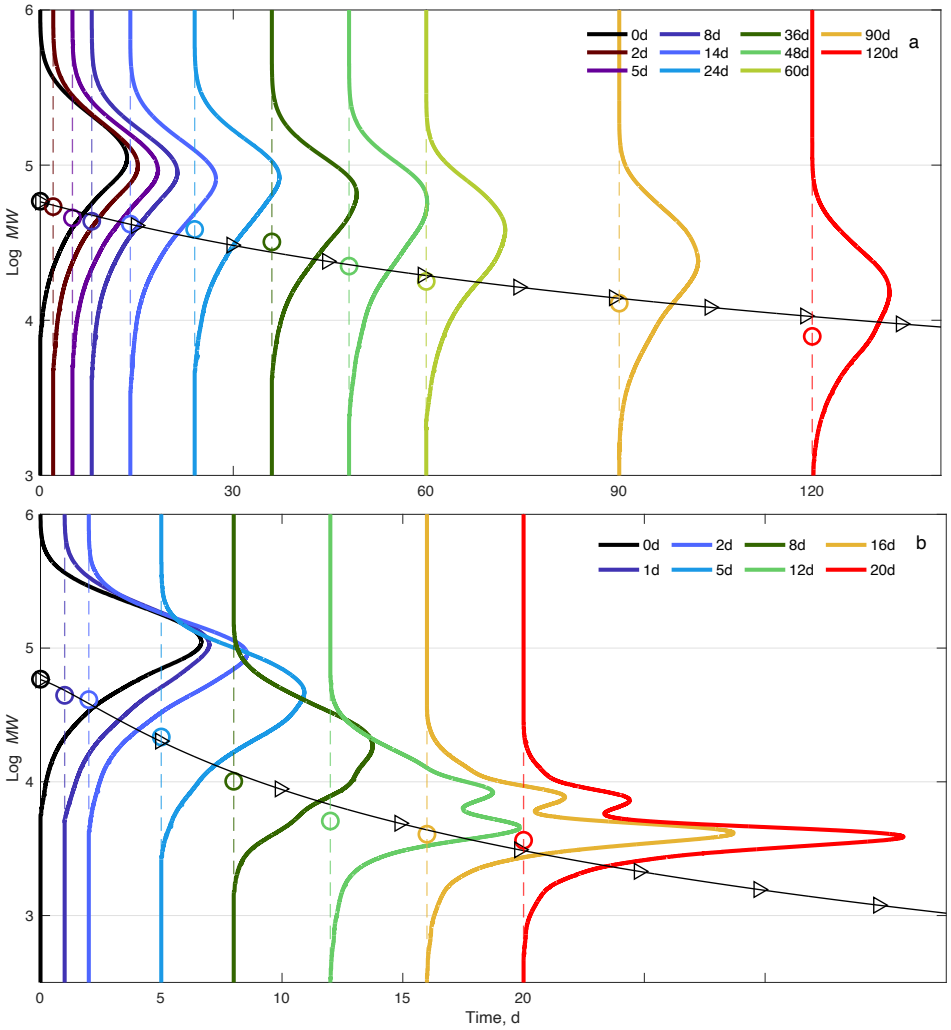

Figure 5.2 The MWD of hydrolytic degradation pathways of PLA film at 45 °C (a) and 65 °C (b). The symbol ○ represents the experimental M_n. The solid line represents the experimental MWD. The line with arrows indicates the prediction line showing the direction of the process.

5.3 Population balance model

In the context of PLA hydrolysis degradation, the system comprises a population of PLA chains with varying sizes, effectively described by MWD, dispersed within an environmental phase. The population balance within the hydrolysis system is designed to monitor the quantities of entities which could be defined as the length of the PLA chains. Chain scission events can lead to a reduction in molecular weight, and these events may encounter the birth processes that create short new chains and the death processes that eliminate existing long chains. These processes can be defined as source and sink terms, respectively. Importantly, the total number of monomer units and of mass conservation remain constant throughout the process [38].

During hydrolysis, random scission takes place at random locations along the polymer backbone, leading to a significant reduction in molecular weight [39]. The random chain scission of a polymer P with the molecular weight of x can be expressed as follows:

$$P(x) \xrightarrow{k_r} P(x') + P(x-x') \tag{5.1}$$

where $P(x)$ represents the polymer with a molecular weight of x undergoing chain scission, resulting in the formation of either $P(x')$ and $P(x-x')$ products. k_r is the rate constant of hydrolysis occurred via random chain scission. The rate of change of the macromolecule P can be mathematically represented within the framework of the population balance equation (PBE) as follows:

$$\frac{\partial P(\mathrm{x})}{\partial t} = -k_r(\mathrm{x})\,\mathrm{P}(x) + 2\int_x^{\infty} k_r(\mathrm{y})\,\Omega(x,y)\,P(y)\,dy \tag{5.2}$$

In Eq. (5.1) $\Omega(x,y)$ represents a stoichiometric kernel, which is used to describe the probability density function that characterizes the production of two moles of daughter particles with lengths x from the breakage of one-mole mother particle with a length of y.

According to McCoy and Madras [40], the stoichiometric kernel $\Omega(x,y)$ can determine the distribution of scission products as follows:

$$\Omega(x,y) = \Omega(y-x,y) = \frac{x^m(y-x)^m\,\Gamma(2m+2)}{\Gamma(m+1)^2\,(y)^{2m+1}} \tag{5.3}$$

where m is the dimensionless parameter indicated the degradation mechanisms. For random chain scission with $m = 0$, $\Omega(x,y)$ simplifies to $\Omega(x,y) = 1/y$, while the other forms of the chain scission can be found elsewhere [40].

Additionally, in the late stage of PLA hydrolysis, MWD exhibits a multimodal distribution, indicating the production or accumulation of the chains with specific molecular weights which can be expressed as follows:

$$P(x) \overset{k_s}{\rightarrow} S(x_s) + P(x - x_s) \tag{5.4}$$

where x_s represents the polymer chains with specific molecular weight, which can be set as monomers, oligomers, or chains of any predetermined length. k_s is a rate constant of specific chain scission. Subsequently, the rate of change of P, which is subject to both random and specific chain scission, can be adjusted as follows [41]:

$$\frac{\partial P(x)}{\partial t} = -k_r(x)\,\mathrm{P}(x) + 2\int_x^\infty k_r(\mathrm{y})\,\Omega(x,y)\,P(y)\,dy - k_s(x)\mathrm{P}(x) + \int_x^\infty k_s(\mathrm{y})\,\delta[x-(y-x_s)]P(y)dy \tag{5.5}$$

$$\frac{\partial P(x_s)}{\partial t} = \int_x^\infty k_s(\mathrm{y})\,\delta(x-x_s)\,P(y)\,dy \tag{5.6}$$

In Eq. (5.5), the polymer P with a molecular weight of x is associated with the process of breaking down of x to form x_s and the generating x from the coordinated chain x_s. The rate of change of $P(x_s)$ increases at the rate of k_s. The terms $\delta[x-(y-x_s)]$ and $\delta(x-x_s)$ represent stoichiometric kernels for specific chain scission, resulting in the production of x when x equals $(y-x_s)$ and x_s, respectively.

To solve these integrodifferential equations, the PBEs are transformed into a set of ordinary differential equations in their discretized forms. The discretized PBE, derived from the initial breakage model in Eq. (5.2), was utilized to analyze the change in the MWD during the random chain scission process of PLA using the method of category [29,42]. The adapted PBE designed for this purpose can be expressed as follows:

$$\frac{dY_i}{dt} = -k_r(L_i)\,Y_i + \sum_{j=i}^{NC}(k_r(L_j)\cdot\beta(L_i,L_j)\Delta L_i)Y_j \tag{5.7}$$

The source terms correspond to the chain scission of chains with size i, while the sink term accounts for the production of chains of size i from the fragmentation of larger polymers of size j. NC is the number of categories. Y_i is the concentration (dwt/dMW) of the PLA chain belonging to category i. For the combinations of random and specific chain scission, Eqs. (5.5)) and ((5.6)) can be transformed as follows:

$$\begin{aligned}\frac{dY_i}{dt} &= -k_r(L_i)\,Y_i + \sum_{j>i}^{NC}(k_r(L_j)\cdot\beta(L_i,L_j)\Delta L_i)Y_j \\ &\quad + \sum_{j>i}^{NC}[k_s(L_j)\cdot\delta[L_i-(L_j-L_s)]\Delta L_i)Y_j\end{aligned} \tag{5.8}$$

$$\frac{dY_s}{dt} = \sum_{j=i}^{NC}(k_s(L_j)\cdot\delta[L_i-(L_s)]\Delta L_i)Y_j \tag{5.9}$$

In addition to the method of category, the method of moment is used to transform the probability distribution based on sample data into moment equations and solve the resulting ordinary differential equations by providing approximations of some parameters of the particle size distribution [43,44].

The moments for weight distribution can be expressed in both continuous and discrete distribution as follows:

$$\mu_k = \int_0^{\infty} x^k\,Y(x)dx \tag{5.10}$$

$$\mu_k = \sum_{i=1}^{NC} Y_i M_i^k \tag{5.11}$$

where k is the order of moment, x is the continuous molecular weight, and M_i is the molecular weight of category i.

The moment method is also used for the continuous daughter distribution. The moment of category i, corresponding to the order of moment m(k), can be formulated as follows:

$$\mu_{\beta ki} = \int_{L_{i-}}^{L_{i+}} \beta\left(L_i, L_j\right) L_i^{m(k)} \, \mathrm{d}L_i \tag{5.12}$$

where L_{i-} and L_{i+} are lower and upper boundary for L_i, respectively. The term $\beta\left(L_i, L_j\right) \Delta L_i$ in Eqs. (5.7) and (5.8) refers to the contribution of breakage from category j into category i. It can be solved by a linear transformation between the moments μ and β table element as follow:

$$\mu_{\beta i} = [A] \left(\beta_i\left(v_i, L_j\right)\Delta L_i\right) \tag{5.13}$$

where $\mu_{\beta i}$ is the moment of MWD in Eq. (5.10) written in the matrix form. v_i, which replaces L_i, is a vector distributing from the breakage into category i. ΔL_i is the size of category i. [A] is a matrix, and its elements $a_{i,j}$ can be calculated from the following equation:

$$a_{i,j} = \mathrm{L}_{v_i(n)}^{m(n)}, \qquad n = 1, 2, \ldots, NM \tag{5.14}$$

Hence, the resulting moments are distributed among the categories represented in the vector v_i which can be obtained from the following equations:

$$v_i(n) = i - floor\left(\frac{NM}{2}\right); \; n = 1 \tag{5.15}$$

$$v_i(n) = v_i(1) + (n-1); \quad n = 2, \ldots, (NM-1) \tag{5.16}$$

$$v_i(n) = v_i(1) + \mathrm{NM} - 1; \quad n = NM \tag{5.17}$$

where NM is number of moments chosen for conservation and the function floor() rounds down to the nearest integer number, giving the greatest integer less than or equal to half of NM [45]. Finally, $\beta_i(v_i, L_j)\Delta L_i$ can be solved as:

$$\beta_i(v_i, L_j)\Delta L_i = [A]^{-1}\mu_{\beta i} \tag{5.18}$$

5.4 Experimental setup and data sources by Limsukon et al. [28]

5.4.1 Polymer sample preparation

The hydrolysis test on amorphous PLA film was carried out without buffering at 45 °C and 65 °C. Samples were collected at various time intervals during the testing period, and their MWD was analyzed using size exclusion chromatography (SEC) (Waters Associates Inc., Milford, MA, USA). The SEC unit was equipped with an isocratic pump (Waters 1515), an autosampler (Waters 717plus), a refractive index detector (Waters 2414), and a series of Styragel® columns (Styragel® HR-4, HR-3, and HR-2). Tetrahydrofuran was used as the mobile phase solvent at a flow rate of 1 mL min^{-1} and a controlled temperature of 35 °C. The evolution of MWDs was analyzed using the Waters Breeze™ 2 software based on the universal calibration curve generated from a series of Polystyrene standard-Shodex SM-105 supplied by Waters.

5.4.2 Data sources and analysis

Figures 5.3a and **5.4a** show the evolution of MWD of amorphous PLA film during the hydrolytic degradation experiments at 45 °C and 65 °C, respectively. The two conditions were selected in this study were based on the fact that these temperatures represent hydrolysis occurring below and above the glass transition temperature (T_g) of PLA (*c.* 52°C measured *in-situ*) [8]. The experiment conducted at 45 °C is anticipated to exhibit significantly delayed chain scission and a notably slower rate of solvent-induced crystallization than the experiment conducted at 65 °C [28]. Moreover, according to the MWD

results, the MWDs during the late hydrolysis stage at 45 °C remained unimodal for up to 120 d. In contrast, at 65 °C, they transitioned into a multimodal distribution, which became apparent after 8 d. The logarithmic molecular weight (*logMW*) and differential weight fraction $dw/d(logMW)$ were subsequently transformed into non-logarithmic terms of MW and dw/dMW for data modeling and processing, shown in **Figures 5.3b** and **5.4b**, respectively.

The initial MWD was discretized into 30 categories, representing a wide range of degrees of polymerization (DP). **Table A5.1**, Appendix 5A summarizes the discretized categories (L_i) of the initial MWD, including DP, category width (ΔL), molecular weight (MW), boundaries (L_{i-} and L_{i+}), and number concentration (Y_i). **Figure 5.5** shows the discretized initial MWD into 30 categories and their corresponding Y_i. Additionally, it includes M_n, which is calculated as the ratio of the first moment to the zeroth moment of the MWD using Eq. (5.10).

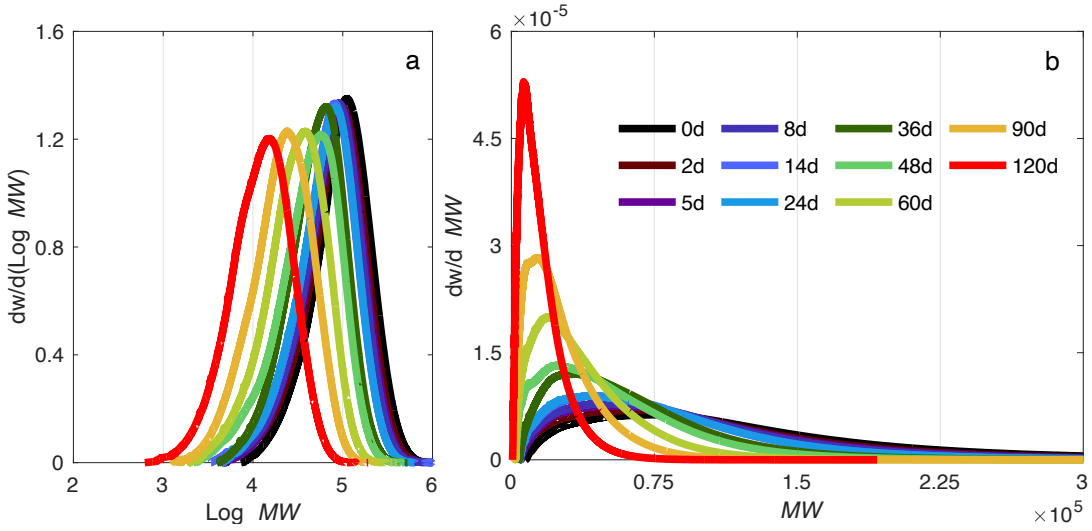

Figure 5.3 The MWD evolution during hydrolysis at 45 °C over a time range of 0 –120 d: $dw/d(logMW)$ vs *log MW* (a) and dw/dMW vs *MW* (b).

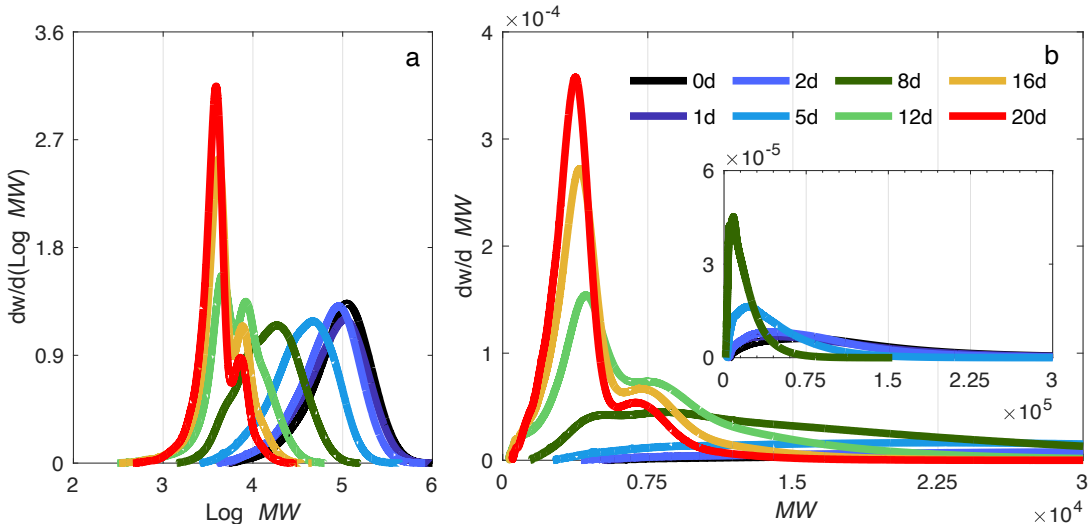

Figure 5.4 The MWD evolution during hydrolysis at 65 °C over a time range of 0 –20 d: *dw/d(logMW)* vs *log MW* (a) and *dw/dMW* vs *MW* (b). The insert in (b) shows a scaling down to overview the MWD of 0–8 d.

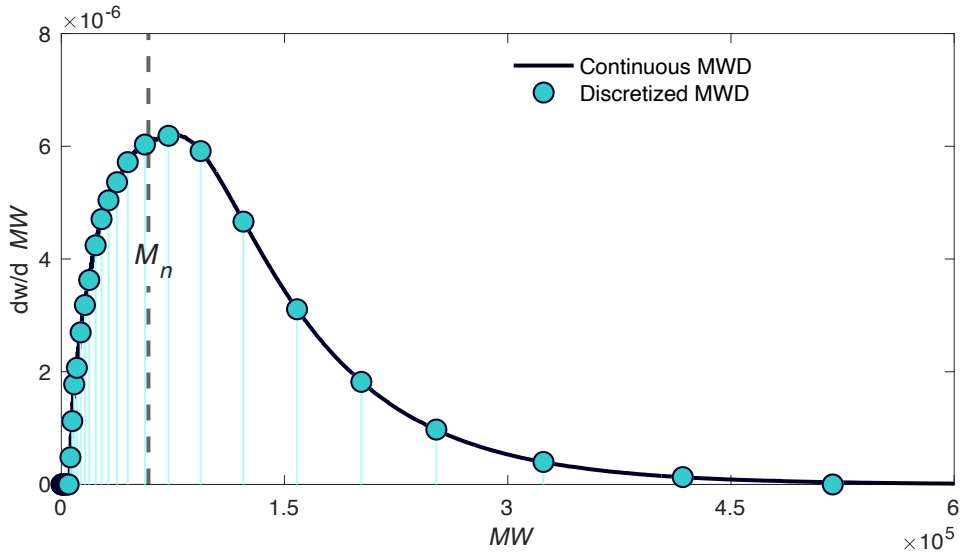

Figure 5.5 Categorized Initial MWD of PLA Before Hydrolysis.

The daughter size distribution, β table, for the 30 categories and three moments, is calculated using Eqs. (5.13–5.18), as shown in **Table A5.2**, Appendix 5B. This matrix element determines the birth terms of the breakage events. The β table is represented as the upper triangular matrix for the breakage of larger polymers L_j, forming smaller L_i for 30 categories. The detailed for calculation is described in Alopaeus et al. [29].

5.5 Results and discussion

The phenomenological kinetic models were fit with the experimental data of hydrolysis at temperatures of 45 °C and 65 °C as shown in **Figure 5.1e** and **f**. The resulting parameters were estimated and documented in **Table 5.1**, and were subsequently utilized within the population balance model. In the Case 1, the change in the total number of chain scissions is influenced by the noncatalytic reaction, expressed as:

$$\frac{d\overline{R_s}}{dt} = k_1 \cdot \frac{C_e}{C_{e0}}, \tag{5.19}$$

where C_{e0} and C_e are total number of ester units of all chain per unit volume at time initial and t. $\overline{R_s} = R_s/C_{e0}$ is number of chain scissions per unit volume normalized by C_{e0} . k_1 represents the noncatalytic rate constant. On the other hand, in the Case 2, the reaction is affected by both the noncatalytic and autocatalytic reactions, expressed as:

$$\frac{d\overline{R_s}}{dt} = k_2 \cdot \frac{C_e}{C_{e0}} + k_2{}' \cdot \frac{C_e}{C_{e0}} \cdot C_{H+} \tag{5.20}$$

where k_2 and $k_2{}'$ is the noncatalytic and autocatalytic rate constants, respectively. The concentration of H^+ in the model in the Case 2 is evaluated from the carboxylic end group of the short chains, which are produced as the hydrolysis proceeds. In our scenario, the production of the short chains was set so that after ten chain scissions, one short chain was produced. Lastly, in the Case 3, the rate constants were modified to match the experimental MWD and prediction and reflect the real hydrolysis situation. The specific degradation was set at category 7, corresponding to a DP of 53 and a molecular weight of 3,816 Da. This weight is considered the molecular weight of a one-fold PLA crystallite [35,46,47]. These crystallites signify that certain segments of the polymer chains tend to remain undegraded, pointing to crystalline residue forming from the chain scission at the specific chain length.

Table 5.1 The parameter estimation of the rate constants of hydrolytic degradation at 45 and 65 °C.

Case	45 °C	65 °C
1	k_1: 4.34×10^{-5} (d^{-1})	k_1: 5.04×10^{-4} (d^{-1})
2	k_2: 3.34×10^{-5} (d^{-1})	k_2: 1.48×10^{-4} (d^{-1})
	k_2': 4.39×10^{-6} $(\sqrt{\mathrm{m}^3}d^{-1})$	k_2': 1.52×10^{-4} $(\sqrt{\mathrm{m}^3}d^{-1})$
3	k_3: 3.34×10^{-5} (d^{-1})	k_3: 1.48×10^{-5} (d^{-1})
	k_3': 2.20×10^{-6} $(\sqrt{\mathrm{m}^3}d^{-1})$	k_3': 2.22×10^{-4} $(\sqrt{\mathrm{m}^3}d^{-1})$
	k_s: 3.34×10^{-5} (d^{-1})	k_s: 1.48×10^{-4} (d^{-1})

5.5.1 Hydrolytic degradation at 45 °C

Figures 5.6– 5.8 show the predicted evolution of the MWD of 30 categories over periods of hydrolysis from the population balance model. The k_1 of 4.34×10^{-5} d^{-1} was used in Case 1, while k_2 and k_2' of 3.34×10^{-5} d^{-1} and 4.39×10^{-6} d^{-1} were used in Case 2, respectively. The result suggests that the solely noncatalytic degradation model, Case 1, fits well at the beginning stage (**Figure 5.6a**), However, it leads to a deviation from the experimental data at the middle stage (**Figure 5.6b**), exhibiting faster predictions starting from 14 d and continuing to differ significantly from the experimental curves up to 48 d. The prediction MWD shows a faster degradation in the middle stage compared to the experimental data, seemingly to better fit the experimental data at the late stage (**Figure 5.6c**). In Case 2, the minor impact of autocatalytic degradation was considered. The results closely resembled those of Case 1, exhibiting a better fit during the early stages (**Figure 5.7a**). However, it led to a higher deviation in 24–90 d (**Figure 5.7b, c**), and exhibited a better fit at 90 d (**Figure 5.7c**). The influence of autocatalytic hydrolysis resulted in the initial delay

of the reduction in molecular weight. Moreover, the accumulation of short chains resulted in accelerating the process in the Case 2 compared to Case 1.

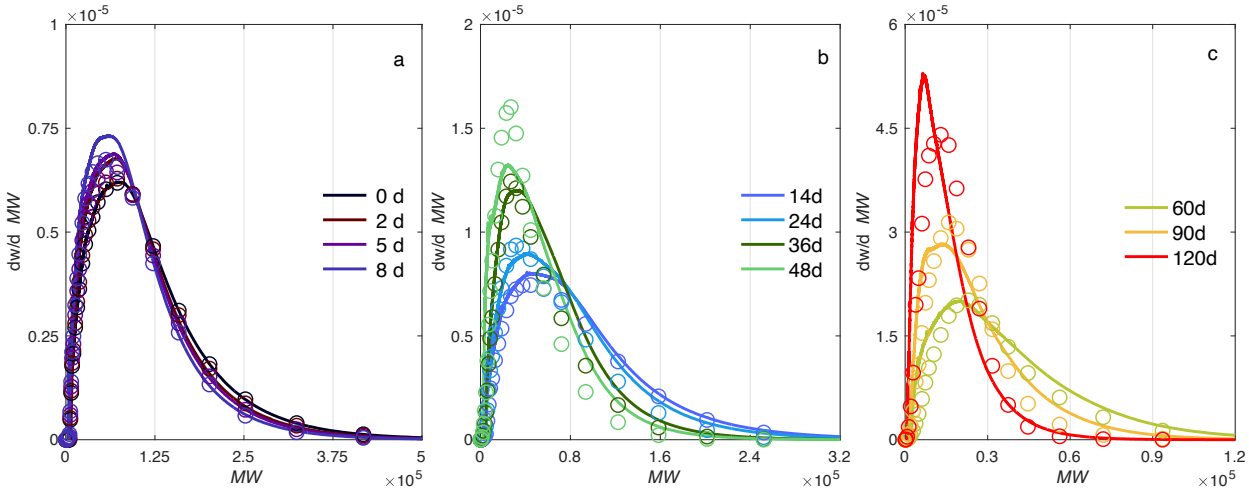

Figure 5.6 Comparison between the experimental (solid lines) and the predicted (symbol ○) MWDs following Case 1 during hydrolysis at 45 °C at the early stage, 0–8 d(a), the middle stage, 14–48 d (b), and the late stage, 60–120 d (c).

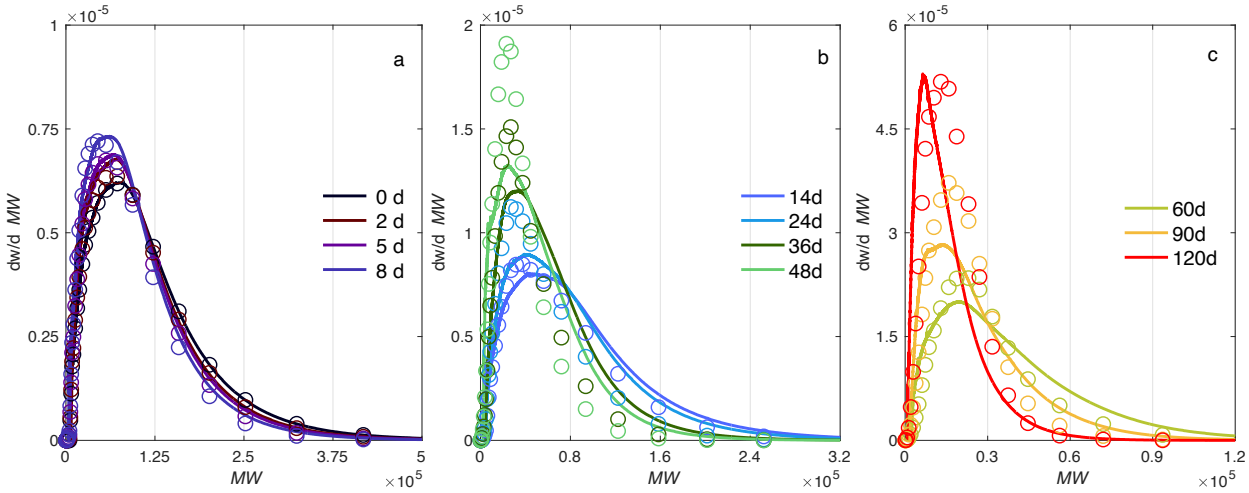

Figure 5.7 Comparison between the experimental (solid lines) and the predicted (symbol ○) MWDs following Case 2 during hydrolysis at 45 °C at the early stage, 0–8 d(a), the middle stage, 14–48 d (b), and the late stage, 60–120 d (c).

The scenario in Case 3 could be refined by adjusting the values of k_2 and $k_2{}'$ to k_2 and $0.5k_2{}'$, respectively. The specific degradation (k_s) was included in the late stage, becoming apparent after 60 d when a slight shoulder was observed. However, it shows the minimal effect due to the slow crystallization at the low temperature as reported in [28]. A value equal to the noncatalytic k_2 for k_s was employed to demonstrate the chain scission of the chains in category 7. The final prediction is shown in **Figure 5.8**.

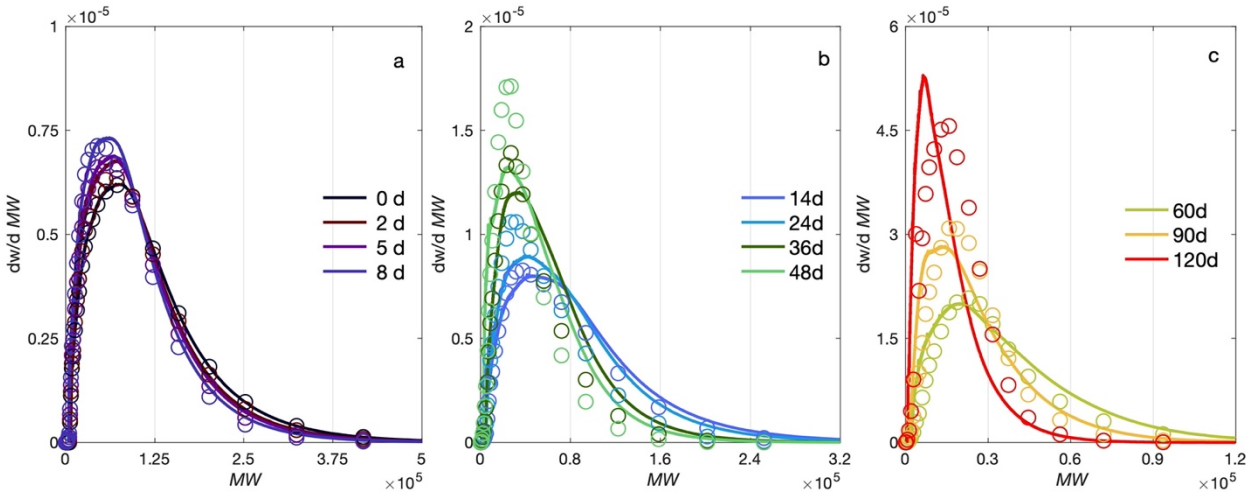

Figure 5.8 Comparison between the experimental (solid lines) and the predicted (symbol ○) MWDs following Case 3 during hydrolysis at 45 °C at the early stage, 0–8 d (a), the middle stage, 14–48 d (b), and the late stage, 60–120 d (c).

5.5.2 The hydrolytic degradation at 65 °C

Figures 5.9–5.11.illustrate the predicted MWDs of 30 categories throughout the various stages of hydrolysis at 65 °C, as determined by the population balance model. The corresponding rate constants are documented in **Table 5.1** (k_1= 5.04×10^{-4} d^{-1} for Case 1, k_2 and $k_2{}'$ = 1.48×10^{-4} and 1.52×10^{-4} d^{-1} for Case 2). For Case 1, the noncatalytic reaction model fails to adequately describe the experimental MWDs. Similarly, to the hydrolysis at 45 °C, the actual chain scission was slow at the beginning and significantly accelerated after 8 d at the middle stage (**Figure 5.9a, b**). Consequently, it ultimately deviates entirely from the actual MWD at the late stage of hydrolysis between 12 and 20 d.

The predicted MWDs exhibit a broad distribution, differing significantly from the multimodal distribution of the actual experimental MWDs (**Figure 5.9c**). On the other hand, the combination of noncatalytic and autocatalytic reactions in Case 2 provides a better fit in the first and middle stages compared to Case 1, as shown in **Figure 5.10a, b**. However, at the end of the hydrolysis, the predicted MWDs still provide a broader and unimodal distribution compared to the actual distribution (**Figure 5.10c**).

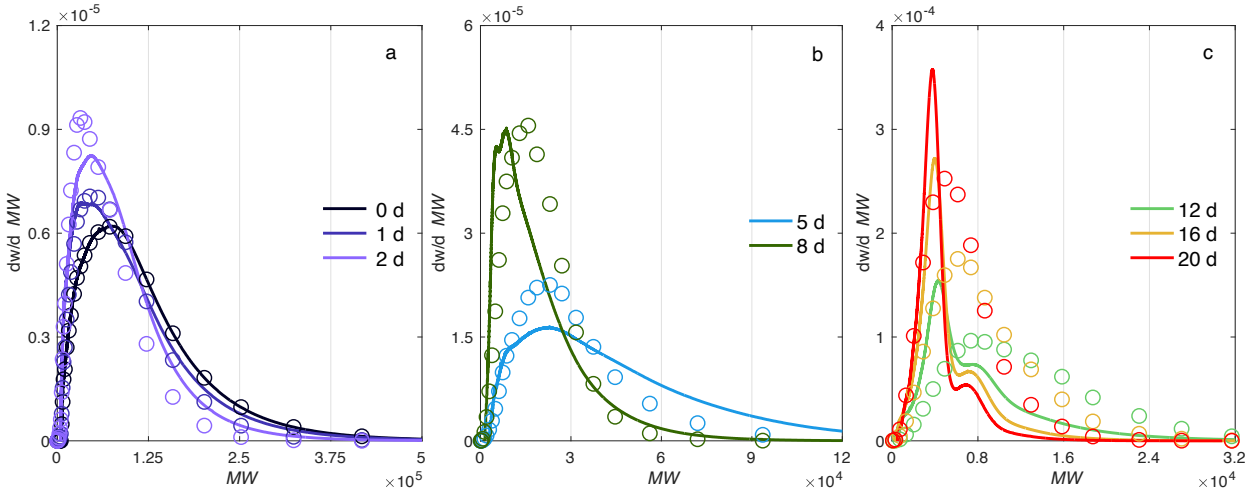

Figure 5.9 Comparison between the experimental (solid lines) and the predicted (symbol ○) MWDs following Case 1 during hydrolysis at 65 °C at the early stage, 0–2 d (a), the middle stage, 5–8 d (b), and the late stage, 12–20 d (c).

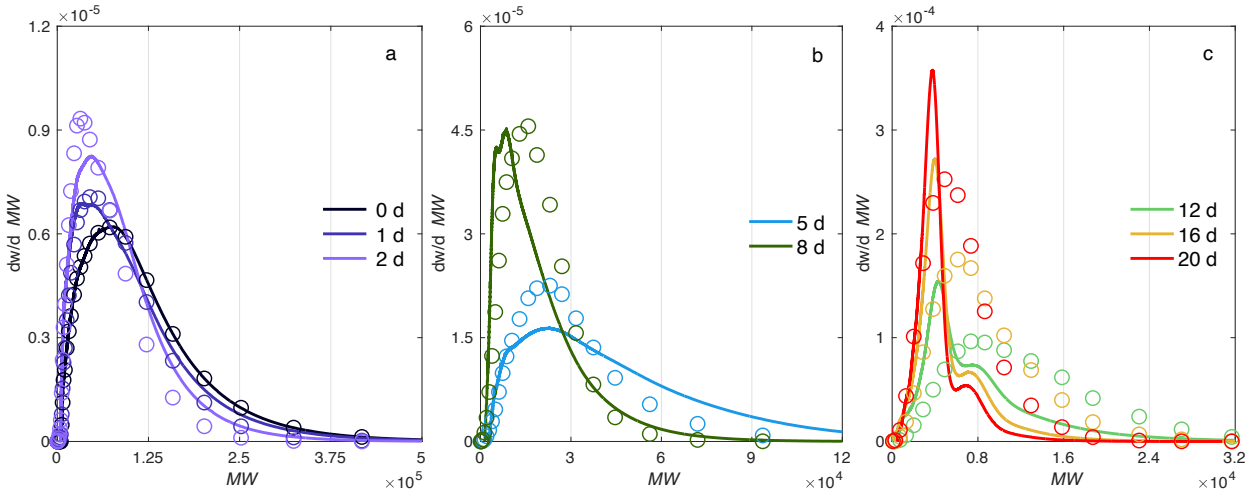

Figure 5.10 Comparison between the experimental (solid lines) and the predicted (symbol ○) MWDs following Case 2 during hydrolysis at 65 °C at the early stage, 0–2 d (a), the middle stage, 5–8 d (b), and the late stage, 12–20 d (c).

Hydrolysis at temperatures above T_g is generally more complex than at lower temperatures due to the rapid crystallization that can occur from the beginning of the hydrolysis process (approximately 20% within 2 d [28]). In the Case 3, the rate constants for population balance could be adjusted by altering k_2 and $k_2{}'$ to $0.1k_2$ and $1.5k_2{}'$, respectively, suggesting the strong autocatalytic hydrolysis. The specific chain scission at category 7 was set to start after 2 d to reach k_s of k_2 at 5 d due to the appearance of multimodal distribution at 8 d. As a result, the adjusted model shows a peak shape corresponding to the experimental MWDs and provides a better fit compared to cases 1 and 2 as shown in **Figure 5.11**.

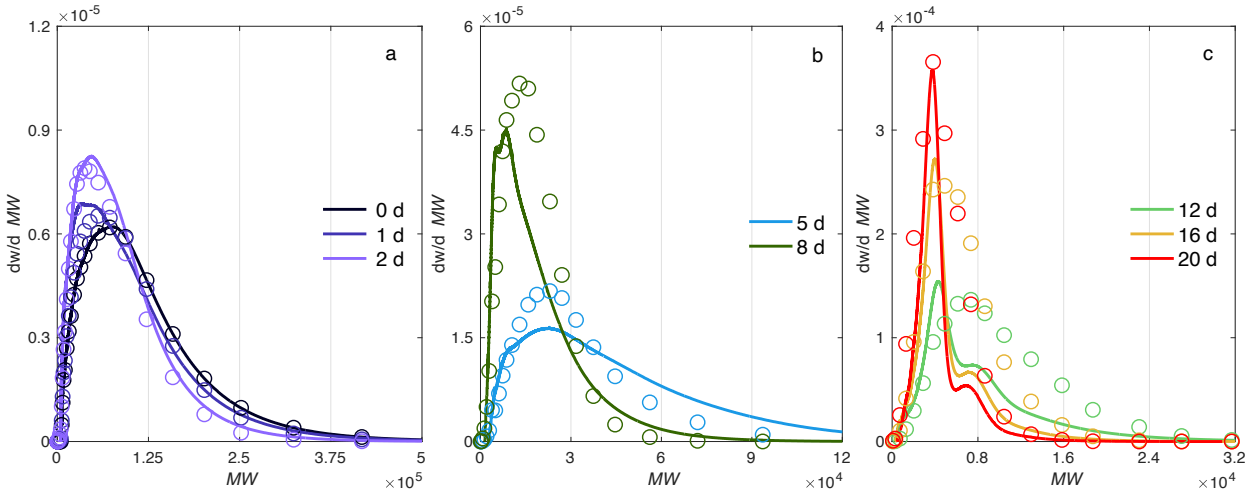

Figure 5.11 Comparison between the experimental (solid lines) and the predicted (symbol ○) MWDs following Case 3 during hydrolysis at 65 °C at the early stage, 0–2 d (a), the middle stage, 5–8 d (b), and the late stage, 12–20 d (c).

The hydrolysis PLA can be involved either solely or in a combination of noncatalytic and autocatalytic reactions depending on the various factors, especially the temperature. The k values obtained from fitting of M_n can assist in predicting the mechanism of PLA hydrolysis, as indicated by the trend lines and the delay in molecular weight reduction [48]. Nevertheless, the overall progression of the molecular weight distribution provides a comprehensive overview of the entire population of the system and serves as a critical indicator for evaluating the accuracy of the results and reinforcing the final conclusions.

5.5.3 Simulation for real-life hydrolytic degradation

In the previous section, the examination of the PLA hydrolysis system at 45 and 65 °C through the population balance model provided valuable insights into the real-life hydrolytic degradation process. Notably, the hydrolysis at 45 °C represents the typical scenario encountered in general applications below the T_g of PLA, illustrating the combination of noncatalytic and autocatalytic degradation processes. While the hydrolysis at 45 °C proceeds gradually and steadily, exhibiting an evolution of MWDs over time, the hydrolysis at 65 °C demonstrates a more rapid and complex degradation pattern.

Through the population balance model, we can effectively simulate the evolution of molecular weight distribution, offering practical applications in lifetime prediction scenarios. By tracking the molecular weight range of PLA beyond its entanglement molecular weight, which exceeds 10 kDa [49], we can predict the performance and longevity of PLA under different environmental conditions. **Figure 5.12** shows the entire MWD profile of hydrolysis at 45 for 120 d and 65 °C for 20 d using the model in Case 3. It can be used to study the MWD behavior in applications where degradation over time is a concern.

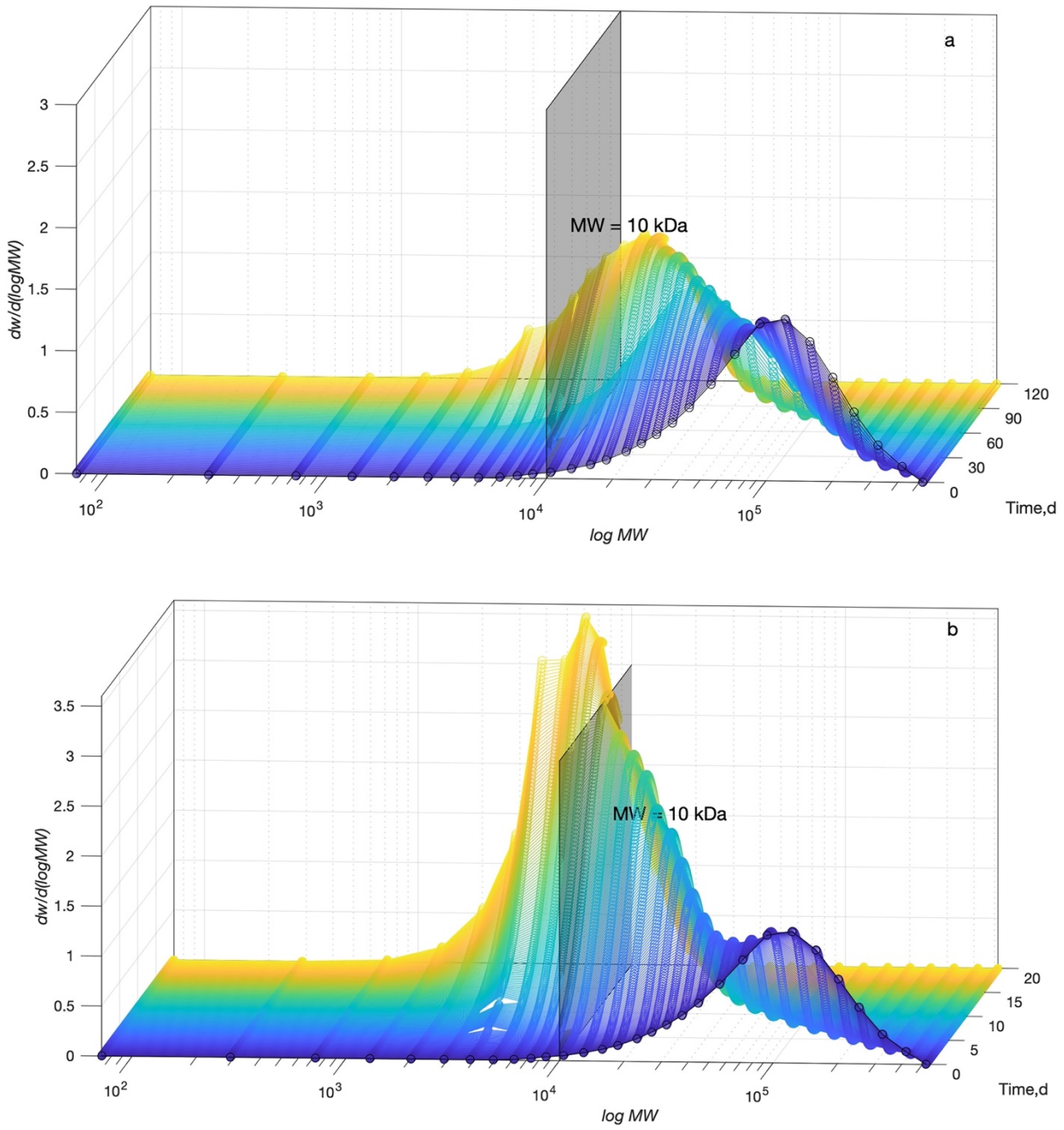

Figure 5.12 MWD profile during hydrolysis at 45 °C (a) and 65 °C (b). The vertical plane indicates the point where the molecular weight decreases beyond 10 kDa.

Moreover, the study can be used to unveil the crucial role of low molecular weights in biodegradation studies, elucidating the breakdown of long-chain PLA during the abiotic phase. The simulation highlights the abiotic hydrolysis process of PLA chains to reach a low molecular weight, allowing microorganisms to effectively break down the molecular chains under composting conditions [50,51]. As reported by Karjomaa et al. [50], PLA could undergo biodegradation under biodegradation tests at a molecular weight of 560–2880 at temperatures of 25 – 58 °C. **Figure 5.13** illustrates the predicted long-term molecular weight distribution profile over an extended time frame derived from the experimental data. The depicted time frame for the experiment at 45 °C is 180 d (**Figure 5.13a**), while the experiment at 65 °C spans 60 d (**Figure 5.13b, c**). This suggests that PLA film undergoes marginal degradation at the temperature below the T_g, referred to as mesophilic conditions of 20–45 °C, within a compost environment, under the predictions spanning over six months. Conversely, in the case of the 65 °C prediction, most of the molecular weight distribution progresses beyond the 3kDa threshold after approximately 20–30 d. Although still present at the final stage of hydrolysis, the resulting crystalline residue may undergo bioassimilation of the small fragments by microorganisms, followed by subsequent mineralization [51]. Both prognoses under these conditions correspond closely with the study performed by Mayekar et al. [37] proving the biodegradation performance of PLA film in mesophilic and thermophilic conditions.

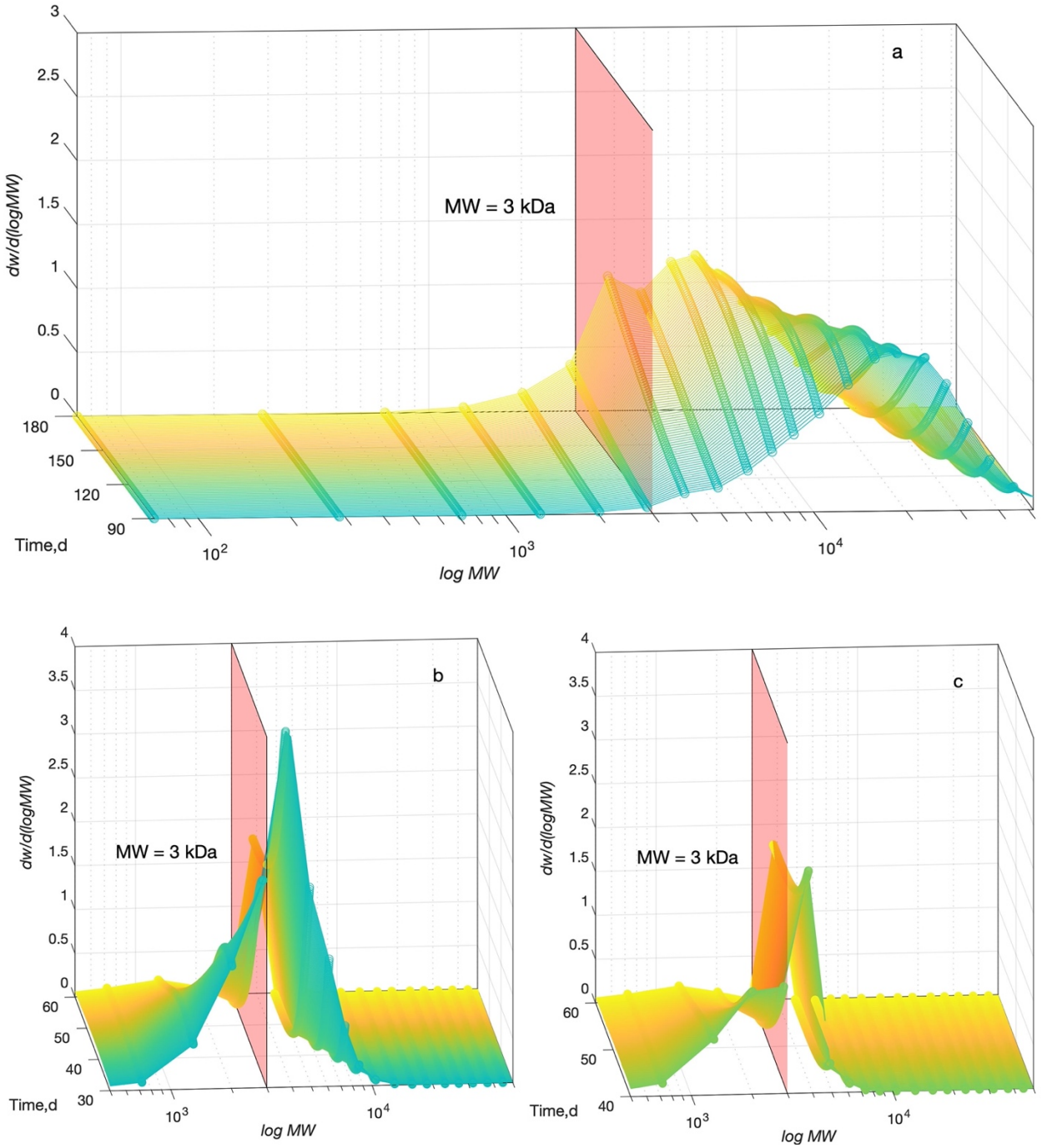

Figure 5.13 The long-term MWD profile during hydrolysis at 45 °C (a) and 65 °C (b–c). The vertical plane indicates the point where the molecular weight decreases beyond 3 kDa.

5.6 Conclusion

In this work, the population balance with the high-order moment-conserving method of classes framework, initially developed by Alopaeus et al. [29], was modified and effectively employed to elucidate the entire MWD during the hydrolytic degradation process of amorphous PLA film. The selection of the hydrolysis experiments at 45 °C and 65 °C served as representative examples illustrating the distinct hydrolysis conditions below and above the T_g of PLA. The method's performance can assist in rectifying the common issues and inaccuracies in estimating the MWD. The results also show an excellent agreement in distribution shape and the preservation of properties throughout the PLA hydrolysis process. Furthermore, the model adeptly captures essential hydrolysis mechanisms, such as noncatalytic and autocatalytic reactions. Ultimately, the simulation of the evolution of MWD was constructed for real-life hydrolytic degradation to provide comprehensive guideline insights and information for both material application and degradation practices.

Considering the findings from the population balance model for PLA hydrolysis, the subsequent phase would involve implementing the relationship of the evolution of crystallinity, which increases during hydrolysis, to refine the predictive capacity of the model. The rate of specific chain scission should be related to the increase in the amount of crystallinity, thus enabling a more comprehensive understanding of the PLA hydrolysis process and facilitating the enhancement of the model's predictive capacity.

REFERENCES

[1] Pan J. and Chen X., Modelling degradation of amorphous biodegradable polyesters: basic model, in *Modelling Degradation of Bioresorbable Polymeric Medical Devices*, no. 2008, Elsevier, 2015, pp. 15–31.

[2] Teixeira S., Eblagon K. M., Miranda F., *et al.*, Towards Controlled Degradation of Poly(lactic) Acid in Technical Applications, *C*, vol. 7, no. 2, p. 42, Apr. 2021, doi: 10.3390/c7020042.

[3] Haddleton D., Polymer chemistry, *Polym. Chem.*, vol. 1, no. 1, p. 13, 2010, doi: 10.1039/c000660m.

[4] Weir N. A., Buchanan F. J., Orr J. F., and Dickson G. R., Degradation of poly-L-lactide. Part 1: in vitro and in vivo physiological temperature degradation, *Proc. Inst. Mech. Eng. Part H J. Eng. Med.*, vol. 218, no. 5, pp. 307–319, May 2004, doi: 10.1243/0954411041932782.

[5] Weir N. A., Buchanan F. J., Orr J. F., *et al.*, Degradation of poly-L-lactide. Part 2: Increased temperature accelerated degradation, *Proc. Inst. Mech. Eng. Part H J. Eng. Med.*, vol. 218, no. 5, pp. 321–330, 2004, doi: 10.1111/j.1467-8500.1944.tb02025.x.

[6] Tsuji H. and Nakahara K., Poly(L-lactide): IX. Hydrolysis in acid media, *J. Appl. Polym. Sci.*, vol. 86, no. 1, pp. 186–194, 2002, doi: 10.1002/app.10813.

[7] Rodriguez E. J., Marcos B., and Huneault M. A., Hydrolysis of polylactide in aqueous media, *J. Appl. Polym. Sci.*, vol. 133, no. 44, pp. 1–11, 2016, doi: 10.1002/app.44152.

[8] Limsukon W., Auras R., and Selke S., Hydrolytic degradation and lifetime prediction of poly(lactic acid) modified with a multifunctional epoxy-based chain extender, *Polym. Test.*, vol. 80, no. September, p. 106108, Dec. 2019, doi: 10.1016/j.polymertesting.2019.106108.

[9] Tsuji H., Nakahara K., and Ikarashi K., Poly(L-Lactide): VIII. High-Temperature Hydrolysis of Poly(L-Lactide) Films with Different Crystallinities and Crystalline Thicknesses in Phosphate-Buffered Solution, *Macromol. Mater. Eng.*, vol. 286, no. 7, pp. 398–406, Jul. 2001, doi: 10.1002/1439-2054(20010701)286:7<398::AID-MAME398>3.0.CO;2-G.

[10] Rodriguez E., Shahbikian S., Marcos B., and Huneault M. A., Hydrolytic stability of polylactide and poly(methyl methacrylate) blends, *J. Appl. Polym. Sci.*, vol. 135, no. 11, p. 45991, Mar. 2018, doi: 10.1002/app.45991.

[11] Limsukon W., Auras R., and Smith T., Effects of the Three-Phase Crystallization Behavior on the Hydrolysis of Amorphous and Semicrystalline Poly(lactic acid)s, *ACS Appl. Polym. Mater.*, vol. 3, no. 11, pp. 5920–5931, Nov. 2021, doi: 10.1021/acsapm.1c01080.

[12] Iñiguez-Franco F., Auras R., Burgess G., *et al.*, Concurrent solvent induced crystallization and hydrolytic degradation of PLA by water-ethanol solutions, *Polymer*

(Guildf)., vol. 99, pp. 315–323, Sep. 2016, doi: 10.1016/j.polymer.2016.07.018.

[13] Harris A. M. and Lee E. C., Heat and humidity performance of injection molded PLA for durable applications, *J. Appl. Polym. Sci.*, vol. 115, no. 3, pp. 1380–1389, Feb. 2010, doi: 10.1002/app.30815.

[14] Tsuji H. and Ikada Y., Properties and morphology of poly(L-lactide): IV. Effects of structural parameters on long-term hydrolysis of poly(L-lactide) in phosphate-buffered solution, *Polym. Degrad. Stab.*, vol. 67, no. 1, pp. 179–189, 2000, doi: 10.1016/S0141-3910(99)00111-1.

[15] Li S., Garreau H., and Vert M., Structure-property relationships in the case of the degradation of massive poly(α-hydroxy acids) in aqueous media - Part 3 Influence of the morphology of poly(l-lactic acid), *J. Mater. Sci. Mater. Med.*, vol. 1, no. 4, pp. 198–206, 1990, doi: 10.1007/BF00701077.

[16] Tsuji H., Ikarashi K., and Fukuda N., Poly(L-lactide): XII. Formation, growth, and morphology of crystalline residues as extended-chain crystallites through hydrolysis of poly(L-lactide) films in phosphate-buffered solution, *Polym. Degrad. Stab.*, vol. 84, no. 3, pp. 515–523, 2004, doi: 10.1016/j.polymdegradstab.2004.01.010.

[17] Iñiguez-Franco F., Auras R., Ahmed J., *et al.*, Control of hydrolytic degradation of Poly(lactic acid) by incorporation of chain extender: From bulk to surface erosion, *Polym. Test.*, vol. 67, no. February, pp. 190–196, 2018, doi: 10.1016/j.polymertesting.2018.02.028.

[18] Ghalia M. A. and Dahman Y., Investigating the effect of multi-functional chain extenders on PLA/PEG copolymer properties, *Int. J. Biol. Macromol.*, vol. 95, pp. 494–504, 2017, doi: 10.1016/j.ijbiomac.2016.11.003.

[19] Perejón A., Sánchez-Jiménez P. E., Criado J. M., and Pérez-Maqueda L. A., Kinetic analysis of complex solid-state reactions. A new deconvolution procedure, *J. Phys. Chem. B*, vol. 115, no. 8, pp. 1780–1791, 2011, doi: 10.1021/jp110895z.

[20] Iñiguez-Franco F., Auras R., Dolan K., *et al.*, Chemical recycling of poly(lactic acid) by water-ethanol solutions, *Polym. Degrad. Stab.*, vol. 149, no. November 2017, pp. 28–38, 2018, doi: 10.1016/j.polymdegradstab.2018.01.016.

[21] Castro-Aguirre E., Auras R., Selke S., *et al.*, Impact of nanoclays on the biodegradation of poly(lactic acid) nanocomposites, *Polymers (Basel).*, vol. 10, no. 2, pp. 1–11, 2018, doi: 10.3390/polym10020202.

[22] Han X., Molecular and multi-scale modelling methods of polymer device degradation, in *Modelling Degradation of Bioresorbable Polymeric Medical Devices*, Elsevier, 2015, pp. 201–231.

[23] Hill A. and Ronan W., A kinetic scission model for molecular weight evolution in bioresorbable polymers, *Polym. Eng. Sci.*, vol. 62, no. 11, pp. 3611–3630, 2022, doi: 10.1002/pen.26131.

[24] Visuri J. A., Song T., Kuitunen S., and Alopaeus V., Model for degradation of galactoglucomannan in hot water extraction conditions, *Ind. Eng. Chem. Res.*, vol. 51, no. 31, pp. 10338–10344, 2012, doi: 10.1021/ie3000826.

[25] Ahmad W., Kuitunen S., Sixta H., and Alopaeus V., Population balance based modeling of changes in cellulose molecular weight distribution during ageing, *Cellulose*, vol. 22, no. 1, pp. 151–163, 2015, doi: 10.1007/s10570-014-0529-3.

[26] Kuen Y., Kirse C., Briesen H., *et al.*, Towards improved predictions for the enzymatic chain-end scission of natural polymers by population balances : The need for a non-classical rate kernel, *Chem. Eng. Sci.*, vol. 176, pp. 329–342, 2018, doi: 10.1016/j.ces.2017.10.027.

[27] Lin S., Yu W., Wang X., and Zhou C., Study on the thermal degradation kinetics of biodegradable poly(propylene carbonate) during melt processing by population balance model and rheology, *Ind. Eng. Chem. Res.*, vol. 53, no. 48, pp. 18411–18419, 2014, doi: 10.1021/ie404049v.

[28] Limsukon W., Rubino M., Rabnawaz M., *et al.*, Hydrolytic Degradation of Poly(lactic acid): Unraveling Correlations between Temperature and the Three Phase Structures, *Polym. Degrad. Stab.*, vol. 217, no. September, p. 110537, 2023, doi: 10.1016/j.polymdegradstab.2023.110537.

[29] Alopaeus V., Laakkonen M., and Aittamaa J., Solution of population balances by high order moment-conserving method of classes: reconstruction of a non-negative density distribution, *Chem. Eng. Sci.*, vol. 63, no. 10, pp. 2741–2751, 2008, doi: 10.1016/j.ces.2008.02.027.

[30] Farrar D., Modelling of the degradation process for bioresorbable polymers, in *Degradation Rate of Bioresorbable Materials: Prediction and Evaluation*, F. B. T.-D. R. of B. M. Buchanan, Ed. Elsevier, 2008, pp. 183–206.

[31] Lyu S. P., Schley J., Loy B., *et al.*, Kinetics and time-temperature equivalence of polymer degradation, *Biomacromolecules*, vol. 8, no. 7, pp. 2301–2310, 2007, doi: 10.1021/bm070313n.

[32] Mohd-Adnan A. F., Nishida H., and Shirai Y., Evaluation of kinetics parameters for poly(l-lactic acid) hydrolysis under high-pressure steam, *Polym. Degrad. Stab.*, vol. 93, no. 6, pp. 1053–1058, 2008, doi: 10.1016/j.polymdegradstab.2008.03.022.

[33] Emsley A. M. and Heywood R. J., Computer modelling of the degradation of linear polymers, *Polym. Degrad. Stab.*, vol. 49, no. 1, pp. 145–149, 1995, doi: 10.1016/0141-3910(95)00067-V.

[34] Rogošić M., Mencer H. J., and Gomzi Z., Polydispersity index and molecular weight distributions of polymers, *Eur. Polym. J.*, vol. 32, no. 11, pp. 1337–1344, 1996, doi: 10.1016/S0014-3057(96)00091-2.

[35] Tsuji H. and Miyauchi S., Poly(l-lactide): VI Effects of crystallinity on enzymatic hydrolysis of poly(l-lactide) without free amorphous region, *Polym. Degrad. Stab.*, vol. 71, no. 3, pp. 415–424, Jan. 2001, doi: 10.1016/S0141-3910(00)00191-9.

[36] Tabasi R. Y. and Ajji A., Selective degradation of biodegradable blends in simulated laboratory composting, *Polym. Degrad. Stab.*, vol. 120, pp. 435–442, 2015, doi: 10.1016/j.polymdegradstab.2015.07.020.

[37] Mayekar P. C., Limsukon W., Bher A., and Auras R., Breaking It Down: How Thermoplastic Starch Enhances Poly(lactic acid) Biodegradation in Compost─A Comparative Analysis of Reactive Blends, *ACS Sustain. Chem. Eng.*, 2023, doi: 10.1021/acssuschemeng.3c01676.

[38] Ramkrishna D. and Mahoney A. W., Population balance modeling. Promise for the future, *Chem. Eng. Sci.*, vol. 57, no. 4, pp. 595–606, 2002, doi: 10.1016/S0009-2509(01)00386-4.

[39] Pan J. and Chen X., Modelling heterogeneous degradation of polymeric devices due to short chain diffusion, in *Modelling Degradation of Bioresorbable Polymeric Medical Devices*, Woodhead Publishing Limited, 2015, pp. 89–109.

[40] McCoy B. J. and Madras G., Degradation Kinetics of Polymers in Solution: Dynamics of Molecular Weight Distributions, *AIChE J.*, vol. 43, no. 3, pp. 802–810, 1997, doi: 10.1002/aic.690430325.

[41] Kodera Y. and McCoy B. J., Distribution kinetics of plastics decomposition, *J. Japan Pet. Inst.*, vol. 46, no. 3, pp. 155–165, 2003, doi: 10.1627/jpi.46.155.

[42] Alopaeus V., Laakkonen M., and Aittamaa J., Solution of population balances with breakage and agglomeration by high-order moment-conserving method of classes, *Chem. Eng. Sci.*, vol. 61, no. 20, pp. 6732–6752, 2006, doi: 10.1016/j.ces.2006.07.010.

[43] Kostoglou M. and Karabelas A. J., Optimal low order methods of moments for solving the fragmentation equation, *Powder Technol.*, vol. 143–144, pp. 280–290, 2004, doi: 10.1016/j.powtec.2004.04.020.

[44] Mehta K. and Madras G., Dynamics of molecular weight distributions for polymer scission, *AIChE J.*, vol. 47, no. 11, pp. 2539–2547, 2001, doi: 10.1002/aic.690471116.

[45] Mathematics in School, The floor and ceiling functions, *Math. Sch.*, pp. 1–3, 2022, [Online]. Available: https://hdl.handle.net/2134/21435879.v1.

[46] Tsuji H., In vitro hydrolysis of poly(L-lactide) crystalline residues as extended-chain crystallites. Part I: long-term hydrolysis in phosphate-buffered solution at 37°C, *Biomaterials*, vol. 25, no. 24, pp. 5449–5455, Nov. 2004, doi: 10.1016/j.biomaterials.2003.12.053.

[47] Tsuji H. and Ikarashi K., In Vitro Hydrolysis of Poly(L-lactide) Crystalline Residues as Extended-Chain Crystallites: II. Effects of Hydrolysis Temperature, *Polym. Degrad. Stab.*, vol. 85, no. 1, pp. 647–656, Jul. 2004, doi: 10.1016/j.polymdegradstab.2004.03.004.

[48] Gleadall A., Pan J., Kruft M.-A., and Kellomäki M., Degradation mechanisms of bioresorbable polyesters. Part 1. Effects of random scission, end scission and

autocatalysis, *Acta Biomater.*, vol. 10, no. 5, pp. 2223–2232, May 2014, doi: 10.1016/j.actbio.2013.12.039.

[49] Cooper-White J. J. and Mackay M. E., Rheological properties of poly(lactides). Effect of molecular weight and temperature on the viscoelasticity of poly(l-lactic acid), *J. Polym. Sci. Part B Polym. Phys.*, vol. 37, no. 15, pp. 1803–1814, 1999, doi: 10.1002/(SICI)1099-0488(19990801)37:15<1803::AID-POLB5>3.0.CO;2-M.

[50] Karjomaa S., Suortti T., Lempi R., *et al.*, Microbial degradation of poly- (L-lactic acid) oligomers, vol. 3910, no. 97, pp. 333–336, 1998.

[51] Saadi Z., Rasmont A., Cesar G., *et al.*, Fungal Degradation of Poly(l-lactide) in Soil and in Compost, *J. Polym. Environ.*, vol. 20, no. 2, pp. 273–282, 2012, doi: 10.1007/s10924-011-0399-9.

APPENDIX 5A: THE EXPERIMENTAL DATA FOR INITIAL PLA FILM

Table A5.1 The discretized categories of the initial MWD.

Category, i	DP, L_i	Characteristic MW (g/mol)	ΔL_i	L_i-	L_i+	dw/dMw, Y_i
1	1	72	1	0.50	1.50	0
2	4	288	5	1.50	6.50	0
3	10	720	7	6.50	13.50	0
4	18	1296	9	13.50	22.50	0
5	28	2016	11	22.50	33.50	0
6	40	2880	13	33.50	46.50	0
7	53	3816	13	46.50	59.50	0
8	68	4896	17	59.50	76.50	0
9	85	6120	17	76.50	93.50	4.81E-07
10	102	7344	17	93.50	110.50	1.12E-06
11	120	8640	19	110.50	129.50	1.78E-06
12	145	10440	31	129.50	160.50	2.07E-06
13	180	12960	39	160.50	199.50	2.70E-06
14	220	15840	41	199.50	240.50	3.18E-06
15	260	18720	39	240.50	279.50	3.63E-06
16	320	23040	81	279.50	360.50	4.24E-06
17	375	27000	29	360.50	389.50	4.71E-06
18	440	31680	101	389.50	490.50	5.04E-06
19	520	37440	59	490.50	549.50	5.36E-06
20	620	44640	141	549.50	690.50	5.72E-06
21	780	56160	179	690.50	869.50	6.03E-06
22	1000	72000	261	869.50	1130.50	6.19E-06
23	1300	93600	339	1130.50	1469.50	5.91E-06
24	1700	122400	461	1469.50	1930.50	4.66E-06
25	2200	158400	539	1930.50	2469.50	3.11E-06
26	2800	201600	661	2469.50	3130.50	1.82E-06
27	3500	252000	739	3130.50	3869.50	9.74E-07
28	4500	324000	1261	3869.50	5130.50	4.00E-07
29	5800	417600	1339	5130.50	6469.50	1.31E-07
30	7200	518400	1461	6469.50	7930.50	0

Note: Categories 1 to 8 provides a dw/dMw of zero as well as category 30 showing the complete MWD related to the initial high MW before hydrolysis.

APPENDIX 5B: β TABLE ELEMENT FOR POPULATION MODEL OF HYDROLYSIS

Table A5.2 β table element of the daughter distribution for 30 categories.

i \ j	1	2	3	4	5	6	7	8	9	10	11	12	13	14	15	16	17	18	19	20	21	22	23	24	25	26	27	28	29	30
1	0	0.28	0.11	0.06	0.04	0.03	0.02	0.02	0.01	0.01	0.01	0.01	0.01	0.01	0.00	0.00	0.00	0.00	0.00	0.00	0.00	0.00	0.00	0.00	0.00	0.00	0.00	0.00	0.00	0.00
2	0	0	0.11	0.06	0.04	0.03	0.02	0.02	0.01	0.01	0.01	0.01	0.01	0.01	0.00	0.00	0.00	0.00	0.00	0.00	0.00	0.00	0.00	0.00	0.00	0.00	0.00	0.00	0.00	0.00
3	0	0	0	0.25	0.16	0.11	0.08	0.07	0.05	0.04	0.04	0.03	0.02	0.02	0.02	0.01	0.01	0.01	0.01	0.01	0.01	0.00	0.00	0.00	0.00	0.00	0.00	0.00	0.00	0.00
4	0	0	0	0	0.40	0.28	0.21	0.16	0.13	0.11	0.09	0.08	0.06	0.05	0.04	0.03	0.03	0.03	0.02	0.02	0.01	0.01	0.01	0.01	0.01	0.00	0.00	0.00	0.00	0.00
5	0	0	0	0	0	0.50	0.38	0.29	0.24	0.20	0.17	0.14	0.11	0.09	0.08	0.06	0.05	0.05	0.04	0.03	0.03	0.02	0.02	0.01	0.01	0.01	0.01	0.00	0.00	0.00
6	0	0	0	0	0	0	0.59	0.46	0.37	0.31	0.26	0.22	0.17	0.14	0.12	0.10	0.08	0.07	0.06	0.05	0.04	0.03	0.02	0.02	0.01	0.01	0.01	0.01	0.01	0.00
7	0	0	0	0	0	0	0	0.66	0.53	0.44	0.37	0.31	0.25	0.20	0.17	0.14	0.12	0.10	0.09	0.07	0.06	0.04	0.03	0.03	0.02	0.02	0.01	0.01	0.01	0.01
8	0	0	0	0	0	0	0	0	0.70	0.58	0.49	0.41	0.33	0.27	0.23	0.19	0.16	0.13	0.11	0.10	0.08	0.06	0.05	0.03	0.03	0.02	0.02	0.01	0.01	0.01
9	0	0	0	0	0	0	0	0	0	0.75	0.63	0.53	0.42	0.35	0.29	0.24	0.20	0.17	0.15	0.12	0.10	0.08	0.06	0.04	0.03	0.03	0.02	0.02	0.01	0.01
10	0	0	0	0	0	0	0	0	0	0	0.79	0.66	0.53	0.43	0.37	0.30	0.25	0.22	0.18	0.15	0.12	0.10	0.07	0.06	0.04	0.03	0.03	0.02	0.02	0.01
11	0	0	0	0	0	0	0	0	0	0	0	0.79	0.64	0.52	0.44	0.36	0.31	0.26	0.22	0.18	0.15	0.11	0.09	0.07	0.05	0.04	0.03	0.03	0.02	0.02
12	0	0	0	0	0	0	0	0	0	0	0	0	0.75	0.61	0.52	0.42	0.36	0.31	0.26	0.22	0.17	0.14	0.10	0.08	0.06	0.05	0.04	0.03	0.02	0.02
13	0	0	0	0	0	0	0	0	0	0	0	0	0	0.75	0.63	0.51	0.44	0.37	0.32	0.26	0.21	0.16	0.13	0.10	0.07	0.06	0.05	0.04	0.03	0.02
14	0	0	0	0	0	0	0	0	0	0	0	0	0	0	0.79	0.64	0.54	0.46	0.39	0.33	0.26	0.20	0.16	0.12	0.09	0.07	0.06	0.05	0.04	0.03
15	0	0	0	0	0	0	0	0	0	0	0	0	0	0	0	0.78	0.67	0.57	0.48	0.40	0.32	0.25	0.19	0.15	0.11	0.09	0.07	0.06	0.04	0.03
16	0	0	0	0	0	0	0	0	0	0	0	0	0	0	0	0	0.79	0.68	0.57	0.48	0.38	0.30	0.23	0.18	0.14	0.11	0.09	0.07	0.05	0.04
17	0	0	0	0	0	0	0	0	0	0	0	0	0	0	0	0	0	0.83	0.71	0.59	0.47	0.37	0.28	0.22	0.17	0.13	0.10	0.08	0.06	0.05
18	0	0	0	0	0	0	0	0	0	0	0	0	0	0	0	0	0	0	0.83	0.70	0.55	0.43	0.33	0.25	0.20	0.15	0.12	0.10	0.07	0.06
19	0	0	0	0	0	0	0	0	0	0	0	0	0	0	0	0	0	0	0	0.82	0.65	0.51	0.39	0.30	0.23	0.18	0.15	0.11	0.09	0.07
20	0	0	0	0	0	0	0	0	0	0	0	0	0	0	0	0	0	0	0	0	0.77	0.60	0.46	0.36	0.27	0.22	0.17	0.13	0.10	0.08
21	0	0	0	0	0	0	0	0	0	0	0	0	0	0	0	0	0	0	0	0	0	0.72	0.56	0.43	0.33	0.26	0.21	0.16	0.12	0.10
22	0	0	0	0	0	0	0	0	0	0	0	0	0	0	0	0	0	0	0	0	0	0	0.70	0.54	0.41	0.32	0.26	0.20	0.16	0.13
23	0	0	0	0	0	0	0	0	0	0	0	0	0	0	0	0	0	0	0	0	0	0	0	0.68	0.52	0.41	0.33	0.26	0.20	0.16
24	0	0	0	0	0	0	0	0	0	0	0	0	0	0	0	0	0	0	0	0	0	0	0	0	0.66	0.52	0.42	0.32	0.25	0.20
25	0	0	0	0	0	0	0	0	0	0	0	0	0	0	0	0	0	0	0	0	0	0	0	0	0	0.64	0.51	0.40	0.31	0.25
26	0	0	0	0	0	0	0	0	0	0	0	0	0	0	0	0	0	0	0	0	0	0	0	0	0	0	0.60	0.47	0.36	0.29
27	0	0	0	0	0	0	0	0	0	0	0	0	0	0	0	0	0	0	0	0	0	0	0	0	0	0	0	0.43	0.34	0.27
28	0	0	0	0	0	0	0	0	0	0	0	0	0	0	0	0	0	0	0	0	0	0	0	0	0	0	0	0	0.14	0.11
29	0	0	0	0	0	0	0	0	0	0	0	0	0	0	0	0	0	0	0	0	0	0	0	0	0	0	0	0	0	0.00
30	0	0	0	0	0	0	0	0	0	0	0	0	0	0	0	0	0	0	0	0	0	0	0	0	0	0	0	0	0	0

CHAPTER 6: OVERALL CONCLUSION AND RECOMMENDATIONS FOR FUTURE WORK

6.1 Overall conclusion

Hydrolytic degradation significantly impacts the properties of PLA over its lifecycle, especially under high humidity and elevated temperatures. This process can result in a reduction in molecular weight and the deterioration of specific properties. Conversely, it can also reduce the molecular weight to a level conducive to microorganisms' biodegradation during the composting process [1,2]. Therefore, comprehending the hydrolytic degradation of PLA is crucial for simultaneously enhancing its stability and biodegradability, thereby expanding its commercial utility. While extensive research has made significant progress in studying PLA hydrolysis under diverse surrounding media conditions and material parameters, some gaps still need to be explored. The primary objective of this dissertation was to examine the hydrolytic degradation of amorphous and semicrystalline PLA, aiming to clarify how the three-phase structure model influences the kinetic and mechanistic insights into the hydrolytic degradation of PLA.

Chapter 3 of this dissertation presented an efficient method for tracking the evolution of the three-phase structure (MAF, CF, and RAF) of PLA during the hydrolysis process. The investigation focused on understanding the influence of the three-phase structure, with a particular emphasis on RAF, which has often been absent in previous literature. The studies were designed to investigate two primary aspects: the effect of L-lactide content and crystallization methods, including cold crystallization and melt-stretching crystallization. The results revealed that different levels of L-lactide content influenced the thermal properties and crystallization behavior. An increase in D-lactide content led to a reduction in the average L-lactide unit sequence length, thereby interrupting the crystallization process and promoting RAF formation during crystallization. Furthermore, the selection of

crystallization methods affected the crystal quality and the three-phase structure quantity in PLA films. Melt-stretching crystallization was found to suppress the formation of large crystallites while promoting the growth of microcrystals. The combination of the designed parameters resulted in samples exhibiting specific crystallization features, such as the three-phase fractions and crystal modifications. The findings from the hydrolysis experiments suggest that the effect of crystallinity considerably decelerated the hydrolysis at 85°C. Amorphous PLA films with a higher L-lactide content underwent more rapid water-induced crystallization compared to those with lower L-lactide content and had slower hydrolysis rates. Among the samples, the melt-stretching crystalline samples, with a high CF and minimal RAF, demonstrated the lowest hydrolysis rates. However, for cold-crystallized samples, a higher initial amount of RAF, leading to rapid hydrolysis, effectively counterbalances the high degree of crystallinity observed in both cold-crystallization samples. This discovery prompted further investigation into the effect of the three-phase fractions through manipulating crystal properties in the subsequent chapter.

In Chapter 4, the hydrolysis kinetics of PLA films were examined, focusing on the influence of crystallinity levels and temperatures. By increasing the crystallization time, there was an observed increase in crystallinity, maintaining the dominant α-phase during the melt-crystallization process. The results indicated that temperature significantly affected PLA degradation, with distinct characteristics observed for these three phases. Above the T_g, the hydrolysis rates of PLA were similar among samples due to the rapid water-induced crystallization of the amorphous phases, resulting in accelerated crystallinity and degradation. Conversely, below and close to the T_g, samples with higher crystallinity exhibited faster hydrolysis rates. These findings highlight the significant impact of RAF under various temperature conditions. At higher temperatures, RAF shows less significance and exhibits similar characteristics to MAF. The crystal structure, on the other hand, can

contribute to lower hydrolysis rates. At lower temperatures, the chains in RAF underwent full immobilization and retained their defects. An increase in crystallinity introduced restricting mobility within the RAF and thereby influencing hydrolysis.

Chapters 3 and 4 provided valuable insights into the intricate relationship among temperature, crystallinity, and hydrolysis kinetics. Moreover, it contributes to resolving conflicting information regarding the roles of CF and RAF under diverse temperature conditions, thus aiding in predicting PLA degradation behavior during its intended applications and end-of-life stages.

Chapters 3 and 4 used the phenomenological model to fit experimental data, providing a comprehensive understanding of the interplay between noncatalytic and autocatalytic hydrolysis using the average molecular weights. The measurement approach for average molecular weight has found common usage for tracking molecular weight changes and kinetics in processes owing to its simplicity. In Chapter 5, the population balance was effectively employed to illustrate the entire MWD during the hydrolytic degradation process of amorphous PLA film. The selection of the hydrolysis experiments at 45 °C and 65 °C from Chapter 4 served as representative examples illustrating the distinct hydrolysis conditions below and above the T_g of PLA. Our predictions show a promising agreement in the weight location and distribution shape with the experimental MWDs. The evolution of the MWD by hydrolysis can be explained accurately by considering both noncatalytic and autocatalytic reactions, along with specific chain scission events of particular lengths. These phenomena were attributed to chain scission occurring at the folding surface of the crystalline residue. Ultimately, the simulation of the evolution of MWD was constructed for real-life hydrolytic degradation. For material application purposes, the simulation can track the molecular weight range of PLA beyond its entanglement molecular weight, enabling the prediction of the performance and longevity of PLA under various environmental conditions. In

biodegradation studies, the simulation highlights the abiotic hydrolysis process of PLA chains, resulting in a low molecular weight, which facilitates the effective breakdown of the molecular chains by microorganisms under composting conditions. This could provide comprehensive guideline information for both material applications and degradation practices.

6.2 Recommendations for future work

Considering the main findings from this study, several key areas should be further investigated to advance our comprehension of the effect of the three-phase structure model on hydrolysis of PLA. Specifically, the considerable influence of temperature conditions on RAF requires further investigation. Future research should prioritize a meticulous analysis through in-situ experiments to elucidate variations in both quantity and quality of RAF induced by temperature changes. Understanding the material properties requires consideration not just of the amount of RAF but also of its temperature-dependent characteristics. The dynamic mechanical analysis (DMA) technique could provide valuable insights, allowing for the determination of the T_g of RAF. According to the study conducted by Jiang et al. [3], DMA was used to determine the T_g of RAF in polypropylene during heating process. Applying DMA during the immersion for measuring *in-situ* RAF behavior during hydrolysis has the potential to yield valuable insights.

The results from this dissertation indicate that the choice of crystallization method can impact the three-phase structure during hydrolysis. Subsequent research efforts may focus on developing PLA structures that enhance crystallinity and reduce RAF, customizing distinct characteristics to improve barrier properties and stability for packaging and related applications. Furthermore, a comprehensive understanding of the three-phase structure's impact on hydrolysis could be extended to encompass its applicability to other polymeric materials, for example, poly[(R)-3-hydroxybutyrate], polystyrene, poly(ethylene

terephthalate), Nylon-6, and poly(butylene succinate), which can behave differently under various conditions [4–7].

Lastly, the dissertation has provided the foundational guideline for the population balance model for hydrolysis application. Further investigations could delve into the intricacies of the hydrolysis reactions, elucidating their underlying mechanisms and kinetics. Additionally, the application of inverse problem methods presents an opportunity to determine the hydrolysis rate directly from experimental data, aiming to achieve a more comprehensive understanding of the hydrolysis behavior.

REFERENCES

[1] Tsuji H., Hydrolytic Degradation, in *Poly(Lactic Acid)*, Hoboken, NJ, USA: John Wiley & Sons, Inc., 2010, pp. 343–381.

[2] Hamad K., Kaseem M., Yang H. W., *et al.*, Properties and medical applications of polylactic acid: A review, *Express Polym. Lett.*, vol. 9, no. 5, pp. 435–455, 2015, doi: 10.3144/expresspolymlett.2015.42.

[3] Jiang Q., Zhao Y., Zhang C., *et al.*, In-situ investigation on the structural evolution of mesomorphic isotactic polypropylene in a continuous heating process, *Polymer (Guildf).*, vol. 105, pp. 133–143, 2016, doi: 10.1016/j.polymer.2016.10.004.

[4] Righetti M. C. and Di Lorenzo M. L., Rigid amorphous fraction and multiple melting behavior in poly(butylene terephthalate) and isotactic polystyrene, *J. Therm. Anal. Calorim.*, vol. 126, no. 2, pp. 521–530, 2016, doi: 10.1007/s10973-016-5553-0.

[5] Ma Q., Pyda M., Mao B., and Cebe P., Relationship between the rigid amorphous phase and mesophase in electrospun fibers, *Polymer (Guildf).*, vol. 54, no. 10, pp. 2544–2554, 2013, doi: 10.1016/j.polymer.2013.03.019.

[6] Chen H. and Cebe P., Investigation of the rigid amorphous fraction in Nylon-6, *J. Therm. Anal. Calorim.*, vol. 89, no. 2, pp. 417–425, 2007, doi: 10.1007/s10973-007-8215-4.

[7] Saengbunkoet S., Kerddonfag N., Puekpoonpoal N., *et al.*, Structural evolution and related physical properties of machine direction oriented poly(butylene succinate-co-adipate) films, *Polymer (Guildf).*, vol. 249, no. February, p. 124859, 2022, doi: 10.1016/j.polymer.2022.124859.

APPENDIX: LIST OF PUBLICATIONS GENERATED FROM THIS DISSERTATION

Journal Articles

1. Limsukon W., Rubino M., Rabnawaz M., *et al.*, Hydrolytic Degradation of Poly(lactic acid): Unraveling Correlations between Temperature and the Three Phase Structures, *Polym. Degrad. Stab.*, vol. 217, no. September, p. 110537, 2023, doi: 10.1016/j.polymdegradstab.2023.110537.
2. Limsukon W., Auras R., and Smith T., Effects of the Three-Phase Crystallization Behavior on the Hydrolysis of Amorphous and Semicrystalline Poly(lactic acid)s, *ACS Appl. Polym. Mater.*, vol. 3, no. 11, pp. 5920–5931, Nov. 2021, doi: 10.1021/acsapm.1c01080.

Conferences

1. Limsukon, W. (presenter), Auras, R. Quantitative thermal analysis of the structural evolution of the during the hydrolytic degradation of poly(lactic acid). Poster presented at: Inspiring Plastics Profession (SPE) ANTEC®2023; March 2023; Denver, CO.
2. Limsukon, W. (presenter), Auras, R., Wang, S, Smith, T. Hydrolytic Degradation and Crystallization Behavior of Amorphous and Semicrystalline Poly(Lactic acid). Oral presented at: The International Association of Packaging Research Institutes (IAPRI) 2021; June 2021; Virtual.
3. Limsukon, W. (presenter), Auras, R. Effect of L-lactide content on the three-phase structure and hydrolytic degradation of poly (lactic acid). Poster presented at: Inspiring Plastics Profession (SPE) ANTEC®2021; May 2021; Virtual.